Fall August 2014

BEAM STEERING CONTROL SYSTEM FOR LOW-COST PHASED ARRAY WEATHER RADARS: DESIGN AND CALIBRATION TECHNIQUES

Rafael H. Medina-Sanchez
UMASS

BEAM STEERING CONTROL SYSTEM FOR LOW-COST PHASED ARRAY WEATHER RADARS: DESIGN AND CALIBRATION TECHNIQUES

A Dissertation Presented

by

RAFAEL H. MEDINA SANCHEZ

Submitted to the Graduate School of the
University of Massachusetts Amherst in partial fulfillment
of the requirements for the degree of

DOCTOR OF PHILOSOPHY

May 2014

Electrical and Computer Engineering

BEAM STEERING CONTROL SYSTEM FOR LOW-COST PHASED ARRAY WEATHER RADARS: DESIGN AND CALIBRATION TECHNIQUES

A Dissertation Presented

by

RAFAEL H. MEDINA SANCHEZ

Approved as to style and content by:

David J. McLaughlin, Chair

Stephen J. Frasier, Member

Ramakrishna Janaswamy, Member

Gopal Narayanan, Member

Christopher V. Hollot, Department Chair
Electrical and Computer Engineering

This dissertation is dedicated to my wife, Michelle,
my children Jeshua, Annia and Sharai,
and my wonderful parents Carmen and Rafael.

ACKNOWLEDGMENTS

Completing my dissertation has been a tremendous personal achievement, which would not have been possible without the support and contribution of many people. I would first like to express my deepest gratitude to my adviser Dr. David McLaughlin, who gave me the opportunity to be a part of CASA project and who supported in every moment the initiative of a "CASA phased array radar". I would like to thank Eric Knapp for his help in discussing the technical aspect of the project and overall guidance. I also wish to thank my good friend Jorge Salazar for developing the passive array and his enormous help in the assembly and testing of the phased array.

I would also like to extend my gratitude to Dr. Steve Frasier, Dr. Ramakrishna Janaswamy, and Dr. Gopal Narayanan for serving as my committee members. My special thanks to Dr. Frasier for his involvement and valuable contribution in the solid state radar group. I also want to thank Dr. Daniel Schaubert for teaching me all the technical background about phased array and for facilitating the anechoic chamber to measure the antenna.

I am thankful for the help and support of all members of CASA organization, Susan Lanfare, Janice Brickley, Marci Kelly, and Apoorva Bajaj, who provided all the technical and administrative support to the project.

My gratitude also goes to all members of the Microwave Remote Sensing Laboratory for all their support. My special thank to my friend Jorge Trabal for being a valuable source of information and discussion on radars. I thanks all my friends and colleagues from MIRSL, especially, Vijey Venkatesh, Krzysztof Orzel, Cristina Llop, Robert Palumbu, Razi Ahmed, Benjamin St. Peter, Mauricio Sanchez, Tony Hopf, Anthony Swochak, and Pei Sang. Thanks to Linda Klemyk and Tom Harley for their assistance in administrative activities and with laboratory equipments.

Most important, I would like to thank my family, because if it was not for them, I would never have made it this far. My wife Michelle and children Jeshua, Annia, and Sharai, for their love, support, encouragement, and sacrifices during all these years. My mother, Carmen, who believed in me and did everything she could to send me to a private university. I also thank her for giving me her love and instilling in me the importance of education and hard work. My father, Rafael, for helping my mother and always being present to help me with whatever I needed. How fortunate I am to have them in my life. I dedicate all my achievements to them.

The work presented in this dissertation was supported primarily by the Engineering Research Centers Program of the National Science Foundation under NSF Cooperative Agreement No. 0313747. Any opinions, findings, and conclusions or recommendations expressed in this material are those of the author and do not necessarily reflect those of the National Science Foundation.

ABSTRACT

BEAM STEERING CONTROL SYSTEM FOR LOW-COST PHASED ARRAY WEATHER RADARS: DESIGN AND CALIBRATION TECHNIQUES

MAY 2014

RAFAEL H. MEDINA SANCHEZ

B.E.E., UNIVERSIDAD TECNOLOGICA DE BOLVAR

M.Sc., UNIVERSITY OF PUERTO RICO MAYAGUEZ

Ph.D., UNIVERSITY OF MASSACHUSETTS AMHERST

Directed by: Professor David J. McLaughlin

Phase array antennas are a promising technology for weather surveillance radars. Their fast beam steering capability offer the potential of improving weather observations and extending warning lead times. However, one major problem associated with this technology is their high acquisition cost to be use in networked radar systems. One promising technology that could have a significant impact in the deployment of future dense networks of short-range X-band weather radars is the "Phase-Tilt Radar", a system that uses a one-dimensional phase scanned antenna array mounted over a tilting mechanism. This dissertation addresses some of specific challenges that arise in designing and implementing air-cooled, low-cost, one-dimensional phased antenna arrays for phase-tilt radars. The goal of this work is to develop methods that can lead to reduce the cost and enhance the performance of this type of systems.

Specifically, the thesis focuses on three concrete areas. The first one is on the development of a versatile low-cost beam steering system that can enable dual-polarimetric phased array radars to operate with high-frequency repetition pulses, difference pulsing schemes,

and modern scanning strategies. In particular, the dissertation will present the development of critical components and describes the concept of operations of the beam steering system.

The second area is to develop a calibration technique for small phased arrays. The work focused in finding the calibration settings for the array that best fit to the desired excitation. The technique provides lower random errors than conventional approaches, enabling the implementation of radiation patterns with sidelobes closer to the desired level. Additionally, the technique is extended to solve the gain-drift problem occurring in the two-way antenna pattern due to the temperature changes.

The third area studies the use of mutual coupling as signal injection technique to maintain the calibration of both array and radar. Future air-cooled phased array radars will require the use internal circuitry to calibrate the aspect of the radar that tends to change over time. In particular, this work is focused on developing low-cost calibration techniques to correct the antenna gain and radar constant from effects of temperature changes and element failures.

TABLE OF CONTENTS

LIST OF TABLES

Table **Page**

LIST OF FIGURES

Figure **Page**

CHAPTER 1

INTRODUCTION

1.1 Introduction

Long range S-band weather radar networks have been in use for many years, and although they have proved to be extremely useful for weather forecasting and warning service, their ability for observing severe and hazardous weather phenomena in the lower part of the atmosphere (< 2 Km) has been limited [1]. Part of the problem is caused by the Earth's curvature and terrain-induced blockage, which prevents these systems from observing more than 50% of atmosphere below 2 km altitude above ground level [2]. Another difficulty is that current systems provide slow volume scan update time and observations with low spatial resolution. In general, today's long-range radars cannot detect the formation and full vertical rotation of most tornadoes; also they cannot provide accurate estimation of precipitation near the ground.

The Engineering Research Center (ERC) for Collaborative and Adaptive Sensing of the Atmosphere (CASA) was established in 2003 with the vision of researching a new technology that could improve the observation, detection, and prediction of weather events at the lower atmosphere. CASA proposed a revolutionary technology, based on a dense network of short-range dual-polarized X-band weather radars, that can operate collaboratively and adaptively to sense the atmosphere [3]. The use of various short-range X-band radars can overcome the problems of blockage due to the Earth's curvature and enable high spatial and temporal resolution observations. The center proved the concept by installing four small radars in a research network in Oklahoma, each radar using a mechanically scanned antenna with a magnetron transmitter. The network served to demonstrate the technology of adaptive scanning and high-resolution observations of precipitation, providing scan update times at intervals of one minute or less. The next step in the evolution of this technology is to improve radars using active electronically scanned antennas (also called phased array

antennas). Advantages obtained from phased array radars (PAR) over the mechanically scanned radar include rapid beam steering, adaptive scanning, multifunction capability, and graceful degradation.

Phased arrays offer significant technical advantages compared to other types of radar systems. Their benefits have been extensively proved in military applications for many years. However, their use in civil applications has been limited because of their high cost. Although recent advancements in microwave technology have made phase-array components more affordable, there remains much more to be done in terms of reducing their cost and the cost of processes that are used to form arrays, if such technology is to be used in future networked radar systems. Because of phased array benefits, the weather radar community has recently started to invest time and resources into this technology. Currently, there is an ongoing project in the United States that involves multiple government agencies and academic institutions to study the possibility of updating multiple currently civilian radar systems (around 500 radars) with a single network of long range Multifunction Phased Array Radars (MPAR), reducing $3 billion in life cycle cost [4]. Preliminary studies indicates that the cost of a full MPAR system (single node) will be approximately $11.5 million [5]. Although the implementation of an MPAR network may bring many benefits, the system still has the limitation of providing of reduced coverage in the lowest 3 km of the atmosphere.

CASA offers an alternative approach to MPAR, the center visualizes that a dense network of 10,000 small phased array radars at 30 km radar spacing may be required to provide nationwide coverage at 30 km radar spacing. CASA argues that "such network have the potential to supplement, or perhaps replace large radars" [3]. However, for this concept to be economically feasible alternative, radars need to be built at dramatically lower cost than current phased array systems. A special challenge is to develop these radars commercially at a cost of U.S $50 k per unit (U.S $200 k four per node). To meet the cost criteria, different architectures for realizing electronically steered arrays have been evaluated including frequency-phase, phase-tilt and phase-phase technology. CASA demonstrated through a feasibility study [6] that both cost and performance requirements can be achieved using a phase-tilt radar. This type of system uses a one-dimensional phase antenna array mounted over a tilting mechanism. Such configuration will allow radars to perform elec-

tronic scanning in azimuth direction and mechanical scanning in elevation direction. Some of the features that this technology should have, includes small-aperture, low power, dual-polarization elements, low profile, and lightweight. Some established specification for these systems are described in Table 1.1. Their small size and low weight will allow them to be mounted on small towers having small footprints or used on existing infrastructures such as communication towers and rooftops, reducing potentially infrastructure costs.

Table 1.1: Key Radar specifications [7].

Parameter	Value
Operating frequency	9.3 GHz
Antenna size	1 m x 1 m
Antenna beamwidth	2^o x 2^o
Maximum range	30 km
Power	10 W to 100 W
Azimuth scan range	$\pm$ 45^o
Elevation scan range	0-56^o

The first part of this dissertation presents the development of a beam steering network that enables the development of low-cost, one-dimensional phased antenna arrays for future phase-tilt weather radars. Beam steering networks are systems that control the shape and direction of the formed beam by controlling the gain and phase of radiating elements. They are also the most expensive system in a phased array because they require the replication of the RF subunits that control the gain and phase of each element. The RF subunits are typically known as Transmit/Receive (T/R) modules, active components whose functions are controlled by amplifiers, phase shifters, and attenuators. Phased array systems are expensive because of the number and high cost of T/R modules populating the antenna. T/R module costs can make up about 50% of overall phase array costs [8, 6]. Another key component in the construction of beam steering networks is the RF distribution network. These components have the function of splitting/combining the signal that is transmitted/received from T/R modules. A beam steering system also requires communication interfaces and digital control units at level of T/R modules to translate the commands sent from the beam steering computer into control signals that can interpreted by attenuators and phase

shifters. One goal of this dissertation is to reduce cost and improve beam switching speed of phased array radars. This will be done by working in three areas. The first one is to use high levels of system integration and low cost manufacturing process. The second one is to design a low-cost high-speed communication interface capable of reducing interconnect complexity. The third one is to design a fast control architecture for T/R modules. In addition, cost is also reduced by using low-cost T/R modules that operate in alternate polarization.

The second part of the dissertation presents a calibration technique for small phased arrays. For successful beam shaping and beam steering in phased array radars, it is important to precisely set the gain and phase of each element. Precisely settings can only be obtained if the array is calibrated in advance. The purpose of the calibration is to compensate the amplitude and phase differences among radiation elements, while allowing the implementation of the desired excitation function. Amplitude and phase differences can occur due to natural variance of different RF hardware connected to each element. Also, amplitude and phase characteristic of T/R modules depend on temperature and usually tend to change in time. Calibration is necessary because it reduces the array errors, which in turn, leads to the implementation of radiation patterns with very low sidelobes. The smaller the array errors, the closer the implemented radiation pattern to the theoretical pattern will be. However, in practice, array errors are limited by the quantization errors and variance of bit error in both attenuators and phase shifters. Conventional calibration methods correct the problems associated with theses errors by using calibration look-up tables in T/R modules. Although these methods have been effectives in the calibration of arrays, they do not always provide the best settings to be set in the attenuators and phase shifters. The goal of the second part of the dissertation is to achieve calibration errors close to the theoretical minimal than can be achieved in an array. In turn, it will allow the implementation of more ideal radiation patterns. All the above will be done by means a calibration algorithm that will search for the attenuator and phase shifter settings that best fit to desired excitation. Techniques to predict the radiation patterns and to compensate the two-way antenna gain loss due to temperature changes are also presented.

The last part of the dissertation studies various techniques to monitor and calibrate phased array systems in the field. Phased array systems have long been recognized by their high reliability [9, 10, 6]. They can operate with a certain number of failed elements and support a wide range of temperatures. However, failures and temperature fluctuations are aspects that affect the performance of radars. The effect of failures is to reduce the effective radiated power and raise sidelobes, while temperature tends to produce fluctuations in the transmit power and receive gain of phased arrays. In order to avoid errors in the measurements, phased array radars use internal calibration procedures to maintain their calibration. Typically, internal calibration is performed using a calibration loop, a system based on directional couplers that can measure the individual characteristics of each element [11]. Other methods use mutual coupling measurements as calibration techniques [12, 13]. While the calibration loops tend to increase hardware complexity and cost of phased arrays, the mutual coupling techniques stand because their simplicity and low hardware requirement making them suitable for low-cost phased arrays. In the literature, mutual coupling techniques have been discussed as techniques to maintain the calibration of radiating elements and to diagnose failures. However, their use in the calibration of radar parameters have not been reported or covered. The goal of the last part of the dissertation is to develop low-cost methods to calibrate the antenna gain and radar constant from variations caused by temperature changes and element failures. This will be done by using two different methods, both based on results of mutual coupling measurements obtained from passive elements within the array aperture. Techniques to maintain the element calibrations and to predict the radiation pattern in the field are also presented.

1.2 Problem Statement

This research aims to address some of the unique and specific challenges that arise in designing and implementing air-cooled, low-cost, one-dimensional phased array antennas for short-range X-band weather radars. Specifically, the research concentrates on the design of a beam steering system, array calibration, and internal calibration of small low-power phased arrays. The main goal of this work is to present several various methods that simultaneously reduce cost and enhance the performance of phased array radar system. This

leads us to work on three main objectives: At first, develop a versatile low-cost beam steering control system that will enable operation of dual-polarimetric phased array radars with high frequency repetition pulses and modern scanning strategies (for example, beam multiplexing techniques [14]). Second, develop an optimal calibration method for small phased array having digital attenuators and phase shifters. The method will find the calibration settings for radiating elements that best fit to desired excitation, providing lower random excitation errors than conventional approaches. Finally, a study of the use of mutual coupling as signal injection technique to maintain both array and radar calibration will be investigated. The study will be focused in the gain calibration due to the effects of temperature changes and element failures. This research is the first step towards developing of low cost hardware and calibration techniques for a future networked radar system.

1.3 Dissertation Contributions

This section presents a list of the main contributions of this dissertation, highlighting three main areas. The first area is the design a beam steering control system for one-dimensional phased array antennas. The second area is a calibration technique for phased arrays. The third area is the internal calibration of phased array systems. The following items summarize the main contribution of this dissertation.

Versatile low-cost beam steering control system for one-dimensional phased array antennas

- Develop the requirements for the design of a one-dimensional phased array antenna for low-cost X-band weather radars.
- Design, implementation, and test of T/R modules for an analog beamformer network. The beamformer will enable the development of low-cost phase array antennas.
- Design of a backplane board to simplify the interconnection between T/R modules and other radar subsystem. The backplane includes two RF power distribution networks, a DC bias network, and a control and communication bus. The design reduces wiring complexity and cost of arrays by integrating various subsystem in a single board (which simplifies manufacturing process), and by using low cost PCB materials.

- Design and evaluation of a high-speed heavily loaded communication bus for the control of T/R modules. The bus is capable of driving up to 32 T/R modules in parallel using communication speeds up 100 Mbps.
- Design and evaluation of a versatile beam steering control system. The control architecture is based on a distributed beam steering system, which consists of a central controller and several element controllers at the level of each T/R module. The control differs from others architectures in that element controllers are controlled in parallel and synchronously by the central controller, and that element controllers do not use arithmetic units to compute the amplitudes and phases. The system has been designed to supports multiple pulsing schemes.

Calibration Technique for Phased Arrays

- Development of a calibration algorithm that finds the best available settings to implement the excitation function of a phased array. While conventional calibration technique only use the attenuator and phased shifter states that fit to ideal quantization states, the proposed technique takes advantage of the variance of attenuator and phased shifter states and use the discarded value from conventional technique to increase resolution of calibration data. The proposed method allows the implementation of radiation patterns with sidelobes that are closer to designed sidelobes.
- Development of a novel open loop calibration technique to compensate the two-way antenna gain from temperature changes. The method is suitable for air-cooled phase arrays with transmitters operating under compression. Compensation is performed in the receive array.
- Demonstrate experimentally the similarity between scanned gain of a phased array and embedded element pattern. It was shown that the scanned gain is affected by the ripples created the quantization errors, being more notable this effect in the receive array than the transmit array.
- Present a method to predict the radiation patterns of a phased array antenna by using calibration data and the embedded element pattern.

Internal Calibration of Low-Cost Phased Array Systems

- Demonstrate the use of a monitoring and calibration technique for elements of a phased array that is susceptible to temperature changes. The technique uses the inherent mutual coupling between active and passive elements as signal injection method to track and maintain the calibration of active elements. Because of the minimal hardware requirements and easy implementation, the technique is suitable for low-cost phased array system.
- Demonstrate a method to estimate the radiation patterns of a phased array from mutual coupling measurements. The technique is suitable to maintain the antenna patterns of fielded phased array radars, for example it can be used to estimate the sidelobe and beamwidth degradation after array maintenance or after diagnosing element failures.
- Development of a calibration technique based on mutual coupling measurements for maintaining the internal calibration of low-cost, air-cooled phased array radars. It was the first time that mutual coupling technique is used to calibrate the radar constant from variations in the antenna gain and transmit/receive power caused by temperature changes and failures. The technique eliminates the use of calibration networks and reduces cost of future arrays.
- Development of a calibration technique based on a deterministic model to maintain the radar calibration constant of low-cost, air-cooled phased array radars. The model that takes into account the temperature characteristics of T/R modules and the number of failed elements presents in array. The model has the advantage that mutual coupling measurements are not needed to calibrate the gain during precipitation measurement.

1.4 Dissertation Overview

This dissertation describes the design and implementation of a beam steering system for one-dimensional active phased array antennas, a system that will enable the development of low-cost solid stated weather radars. It also describes various techniques to calibrate and maintain the calibration of phased array systems. This thesis is organized as follows.

Chapter 2 presents a short description of the basic definitions used in the theory of linear phased arrays, beamformer network, and radar systems. The correction of the weather radar equation for use with one-dimensional phased array radars is also presented.

Chapter 3 describes the design and implementation of a low-cost and high-performance beam steering system for linear phased arrays. A short description of the system architecture of the CASA phased array antenna is given. This chapter also describes the array requirements by first describing the radar system requirements. The development of T/R modules and other array subsystems are also presented. The design of a low-cost hybrid backplane board that reduces wiring complexity and provides RF signal, bias voltages, and communication signal to T/R modules is described. The last section describes the design and implementation of a high-speed beam steering system. Details about system operation, serial communication, digital commands, and test are given.

Chapter 4 develops a technique to carry out the initial calibration of arrays. The technique is based on an algorithm that searches in the raw data of each element the best amplitude and phase settings that minimize the random errors in the excitation. This chapter provides the theory and experimental demonstration of the calibration technique in 64 element active phased array. The scanning performance of several array parameters including sidelobes, beamwidth, and beam positioning error are shown. In addition, a technique to calibrate the two-way antenna gain due to temperature changes is presented.

Chapter 5 presents several techniques based on mutual coupling measurements that can be used to maintain the calibration of phased array systems. These techniques are suitable for small low-cost phased array radars due to their reduced cost, easy implementation, and accuracy. This chapter evaluates the use and limitations of mutual coupling technique in the monitoring and calibration of radiating elements due to hardware variations and under the presence of temperature effects. Lastly, two calibration techniques for estimating and correcting the radar constant due to antenna gain variations are presented. Effects of temperature changes and T/R module failures on the antenna gain of a receive phased array antenna isalso studied.

Finally, chapter 6 summarizes the conclusions obtained in this work.

CHAPTER 2

FUNDAMENTALS OF PHASED ARRAYS

2.1 Introduction

Phased array antennas can adopt a number of different configurations, including linear, planar, and circular. This work focuses on linear active phased array antennas whose unit cell is formed by a subarray of radiating elements, each fed by a transmit and receive module that can provide amplitude and phase control. Linear phased arrays use the progressive phase excitation between the elements to scan the antenna beam electronically over one-dimension, while using the element amplitude distribution to control the pattern shape. The main advantages offered by phased arrays over conventional systems are increased scanning speed, high reliability, and multifunction capability. These advantages make the use of this technology the most logical choice for the next generation weather radars. The use of linear active phased arrays as a component of future low-cost weather radars is the major motivator of this work; consequently, this chapter is dedicated to explain the basic concepts related to the theory of linear phase arrays and how their characteristics can be used in a radar system.

2.2 Linear Array

Typical configurations used in arrays that perform electronically scanning in one dimension are shown in Figure 2.1. The array elements can be individual radiators, as shown in Figure 2.1a, or they can be subarray of radiators, as illustrated in Figure 2.1b. In general, the excitation of each array element is controlled in amplitude and phase by attenuators and phase shifters. In addition to the excitation control on each element, there is a relative phase shift between the waves arriving at the element due to their position in the space and the angle of arrival of the wave. Under the assumption that all radiating elements have the

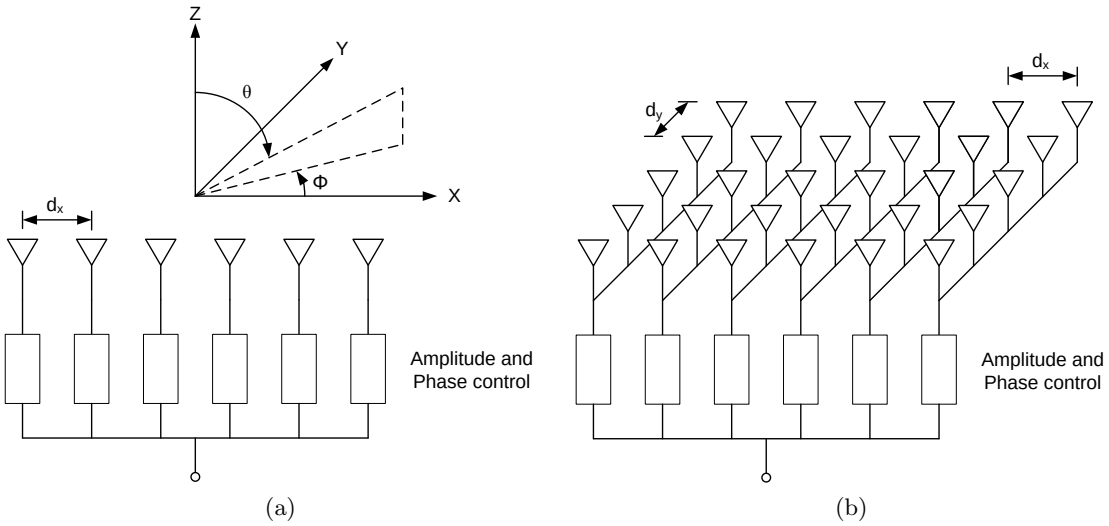

Figure 2.1: Array configuration of one-dimensional phased array antennas. a) Single elements. b) Columns of elements

same element pattern, the far-field array pattern is the summation over all N-elements of element patterns adjusted by the excitation control and incremental phase shift in space of each element, that is

$$f(\theta,\phi) = f_0(\theta,\phi)\sum_{n=1}^{N} V_n e^{jnkd_x sin(\theta)cos(\phi)} \tag{2.1}$$

where $f_0(\theta,\phi)$ is the common radiation pattern to all elements, V_n is the complex excitation assigned to each element, k is the free-space propagation constant at the operating frequency, and d_x is the element spacing in x-direction. The pattern $f(\theta,\phi)$ is maximum when the far-field contribution from the elements add in-phase. This occurs in the direction $(\theta_0, 0)$ by choosing the excitation coefficient , V_n to be

$$V_n = A_n e^{-jnkd_x sin(\theta_0)} \tag{2.2}$$

This implies that the attenuator and phase shifter at each element must be adjusted to set the amplitude A_n and phase $\alpha_n = -nkd_x sin(\theta_0)$. In general, the aperture amplitude distribution controls the beam shape of the pattern, while the phase distribution controls the pointing direction of the main beam.

2.2.1 Directive Gain

The directivity is the characteristic of an antenna that describes how much it concentrate energy in one direction in preference to radiation in other directions. By definition, the directivity is given as the ratio of the radiation intensity in a certain direction to the average radiation intensity, or

$$D(\theta,\phi) = \frac{U(\theta,\phi)}{U_{ave}(\theta,\phi)} = \frac{|f(\theta,\phi)|^2}{\frac{1}{4\pi}\int\int |f(\theta,\phi)|^2 sin(\theta) d\theta d\phi} \tag{2.3}$$

where $f(\theta,\phi)$ is the normalized field pattern of the antenna. Although the above expression gives the antenna directivity at any angular position, the maximum directivity is the value that is used to describe the directive of an antenna, which is defined as

$$D(\theta,\phi) = \frac{4\pi}{\int\int |f(\theta,\phi)|^2 sin(\theta) d\theta d\phi} \tag{2.4}$$

Also from 2.3 in 2.4, one can see that

$$D(\theta,\phi) = D|f(\theta,\phi)|^2 \tag{2.5}$$

For a linear array of N equally spaced isotropic elements, the maximum directivity [15] is given by

$$D_a = \frac{|\sum_{n=1}^{N} A_n|^2}{\sum_{n=1}^{N}\sum_{m=1}^{N} V_m V_n e^{j(n-m)kd_x sin(\theta_0)} sinc((n-m)kd_x)} \tag{2.6}$$

where $sinc(x) = sin(x)/x$. This expression shows that directivity is a function of the aperture amplitude distribution, the element spacing, and scan angle. In the particular case that the element spacing is close to $\lambda/2$ (λ= wavelength), the maximum directivity reduce to (for $\theta_0 = 0$)

$$D_a = \frac{|\sum_{n=1}^{N} A_n|^2}{\sum_{n=1}^{N} A_n^2} \tag{2.7}$$

The maximum value that can be obtained from above expression is N, and occurs when all elements have the same amplitude coefficient.

For large planar arrays with a separable aperture distribution, the directivity [16] is approximately given by the following expression

$$D_a(\theta_0) = \pi D_x D_y \cos(\theta_0) \tag{2.8}$$

where D_x and D_y are the directivities corresponding to linear arrays with isotropic elements in the x-direction and y-direction. When scanning to an angle θ_0, the directive gain is reduced to that of the projected aperture. It should be noted that this expression is valid only for array with not visible grating lobes.

2.2.2 Realized Gain

Theoretically, the realized gain is equal to the maximum directivity reduced by the radiation efficiency and losses due to impedance mismatches. However in practice, the realized gain is also affected by the inherent mutual coupling between elements. This effect modifies the element impedance and produces mismatch losses between T/R modules and elements. These losses can be taken into account in terms of the reflection coefficients seen into a typical element (i.e central element) when the entire array is excited [17, 16, 18]. In this case, the realized gain and directivity for a large phased array that scan in one dimension are related to each other as

$$G_r(\theta_0, 0) = \epsilon_r |f_0(\theta_0, 0)|^2 (1 - |\Gamma((\theta_0, 0)|^2) D_e D_a \tag{2.9}$$

where ϵ_r is the radiation efficiency, $f_0(\theta_0, 0)$ is the normalized field pattern form an isolated element, $\Gamma(\theta_0, 0)$ is the active reflection coefficient of a typical element, D is the array directivity, and D_e is the element directivity, defined as

$$D_e = \frac{4\pi d_x d_y}{\lambda^2} \tag{2.10}$$

in (2.9), the reflection coefficient varies as a function of the scan angle because the resulting impedance mismatch from the mutual coupling depends on the element excitation.

Now, considerer the case when a single element is excited and all other elements are terminated match loads. The array directivity is equal to unity. From 2.9, the realized gain reduces to

$$g_0(\theta_0, 0) = \epsilon |f_0(\theta_0, 0)|^2 (1 - |\Gamma((\theta_0, 0)|^2) D_e \tag{2.11}$$

This is the realized gain for a single element in a large array, sometimes called active element pattern or embedded element pattern. The above expression shows that the mutual coupling, which is implicit in the active reflection coefficients, alters the radiation power pattern of the isolated element. Comparison with (2.9) shows that

$$G_r(\theta_0, 0) = g_0(\theta_0, 0) D_a \tag{2.12}$$

If the array is large enough that the individual element pattern are approximately identica, then the expression shows that gain of the fully excited array is equal to gain of a single element augmented by the directivity of the array. Other way to represent the eq. 2.11 is substituting the element realized gain by the multiplication of normalized element pattern, the element directivity, and radiation efficiency, that is

$$G_r(\theta_0, 0) = g_{0n}(\theta_0, 0) \epsilon_r D_e D_a \tag{2.13}$$

where $g_{0n}(\theta_0, 0) = g_0(\theta_0, 0)/g_0(0, 0)$. This formula shows that the array realized gain depends on the shape of normalized element pattern, therefore if the element pattern has dips or nulls at particular angles, it can be concluded that the full array will have drops in gain when scanned to these angles.

2.2.3 Half-Power Beamwidth

The beamwidth is defined as the angular separation of the points where the main beam of the power pattern equals one-half. In a phase array, this parameter can be controlled by choosing the adequate element amplitude distribution. In general, the principal plane beamwidths of a rectangular array at broadside are given by

$$\theta_{3,br} = \frac{0.8858 B_x \lambda}{N_x d_x} \qquad (2.14)$$
$$\phi_{3,br} = \frac{0.8858 B_y \lambda}{N_y d_y}$$

where $\theta_{3,br}$ is the beamwidth on the $x-z$ plane, $\phi_{3,br}$ is the beamwidth on the $y-z$ plane, B_x and B_y are the beam broadening factors when tapered aperture distributions are used. While in a uniformly illuminated array this factor is equal to unity, in a -25 dB Taylor distribution the factor is equal to 1.2.

For other scan angles, the beamwidth increase approximately as $1/cos(\theta_0)$. In the case of a linear array having phase shifters along the x-axis, the beamwidth on the $x-z$ plane varies as

$$\theta_3(\theta_0) = \frac{\theta_{3,br}}{cos(\theta_0)} \qquad (2.15)$$

while the beamwidth in the orthogonal plane is constant.

2.2.4 Half-Power Beamwidth for Two-Way Patterns

The radiation patterns obtained from a phased array radar is not always same while transmitting and receiving in the direction of the target. For example, in transmit the array may use an uniform illumination for transmitting the maximum power available in transmitter, and then in receive use a tapered illumination for controlling the total sidelobes in the two-way pattern. In this case, the half-power beamwidth resulting from multiplication of two is given as

$$\theta_3^{2w} = \sqrt{\frac{\theta_{3tx}^2 \theta_{3rx}^2}{\theta_{3tx}^2 + \theta_{3rx}^2}} \qquad (2.16)$$

where θ_{3tx} and θ_{3rx} are the one way half-power beamwidth for transmit and receive patterns in the $x-z$ plane, respectively. Now, in an antenna that has similar patterns in transmit and receive, the beamwidth for one-way and two-way patterns are related as

$$\theta_3^{1w} = \sqrt{2}\theta_3^{2w} \qquad (2.17)$$

From 2.16 in 2.17, one can see that

$$\theta_3^{1w} = \sqrt{\frac{2\theta_{3tx}^2\theta_{3rx}^2}{\theta_{3tx}^2 + \theta_{3rx}^2}} \tag{2.18}$$

This is the equivalent half-power beamwidth that would be produced by a linear array when it transmits and receives with the same radiation pattern. Similarly, if θ_3 is substituted by ϕ_3, 2.18 can be used to determine the beamwidth in the orthogonal plane ϕ_3^{1w}.

2.2.5 Gain of Active Beamformers

Figure 2.2a depicts a linear array of N-elements configured in transmits. Considerer that each branch has a complex signal gain g_n and that N-way power divider is lossless and has equal phase in the output terminal. The power divider splits the input power in N equally portions, where the voltage coupling coefficients is $C = 1/\sqrt{N}$. Thus, the output power at each antenna element is $P_{oun,n} = g_n^2 P_{in}/N$. Now, the total power available in the antenna output is

$$P_{out} = \sum_{n=1}^{N} P_{out,n} = \sum_{n=1}^{N} \frac{g_n^2 P_{in}}{N} = \frac{P_{in}}{N} \sum_{n=1}^{N} g_n^2$$

Hence, the power gain for a transmit beamformer is given by

$$G_{BF,tx} = \frac{P_{out}}{P_{in}} = \frac{\sum_{n=1}^{N} g_n^2}{N} \tag{2.19}$$

In the case that all branches have the same signal gain g, the beamformer gain is equal to that of the single branch $G_{BF,tx} = g^2$.

Now, consider the case of linear array configured in receive, see Figure 2.2b. The total power received in the antenna aperture, P_{in}, is equally distributed among all array elements as P_{in}/N. The received voltage at each radiating element is $V_{in} = \sqrt{P_{in}/N}$. This signal is amplified and then coupled to the output port $V_{out,n} = g_n\sqrt{P_{in}/N}$. The combination of all power in the output yields

$$P_{out} = |\sum_{n=1}^{N} g_n \sqrt{\frac{P_{in}}{N}}|^2 = \frac{P_{in}}{N}|\sum_{n=1}^{N} g_n|^2$$

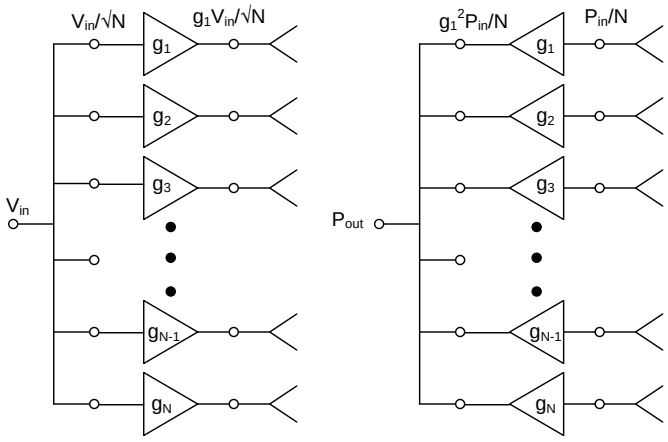

Figure 2.2: Beamformer networks. a) Transmit array. b) Receive array

the ratio of powers gives the total power gain, which is given as

$$G_{BF,rx} = \frac{P_{out}}{P_{in}} = \frac{|\sum_{n=1}^{N} g_n|^2}{N} \tag{2.20}$$

In the case that all branches have the same signal gain g, the beamformer gain is equal to that of the single branch $G_{BF,rx} = g^2$.

2.2.6 Total Power Gain of Active Phased Arrays

The power gain of an array is by definition associated to the array directivity and antenna efficiency. However, this concept does not consider that an active phased array has a gain associated to the array beamformer. The effect of this gain is to increase the radiation intensity in the space when the array is used as transmitter, or to increase the received power when the array is used as a receiver. Because of this effect, it results appropriate to redefine the antenna gain to take into account the beamformer gain.

Consider a transmit array as the one depicted in Figure 2.2a. The radiation pattern generated by an array having isotropic element at distance r is given by

$$f(\theta,\phi) = \frac{e^{jkr}}{4\pi r} \sum_{n=1}^{N} \frac{g_n V_{in}}{\sqrt{N}} e^{jnkd_x sin(\theta)cos(\phi)}$$

The maximum radiation intensity in the far-field will occur when all the fields radiated by the element are in phase. This values is proportional to

$$U_{max} = |f_{max}(\theta, \phi)|^2 = \frac{1}{4\pi r^2} \left(\sum_{n=1}^{N} \frac{g_n V_{in}}{\sqrt{N}} \right)^2$$

The maximum gain is obtained as

$$G_a = \frac{4\pi r^2 U_{max}}{P_{in}} = \frac{\left(\sum_{n=1}^{N} \frac{g_n V_{in}}{\sqrt{N}} \right)^2}{V_{in}^2} = \frac{\left(\sum_{n=1}^{N} g_n \right)^2}{N} \tag{2.21}$$

In the special case that all branches have the same gain g, the total gain is $G_a = Ng^2 = Dg^2$, since directivity is $D = N$ in an uniformly excited array. This result shows that the gain in an active phased array is augmented by the gain of the beamformer. (2.21) can also be obtained by multiplying the array directivity and the beamformer gain, that is

$$G_a = D_a G_{BF} \tag{2.22}$$

where D_a is given by (2.7) replacing $A_n = g_n$. Consequently, the total gain for a transmit array can be obtained using (2.7) and (2.19) in (2.22)

$$G_{a,tx} = \frac{\left(\sum_{n=1}^{N} g_{n,tx} \right)^2}{\sum_{n=1}^{N} g_{n,tx}^2} \frac{\sum_{n=1}^{N} g_{n,tx}^2}{N} = \frac{\left(\sum_{n=1}^{N} g_{n,tx} \right)^2}{N} \tag{2.23}$$

this is analogous to the expression given in (2.21).The above procedure can also be used to compute the gain for the receive array. But first, it should be note that in Figure 2.2b all radiating elements receive the same current. This means the array is receiving with an uniform illumination before the beamformer. Consequently it is assumed that $D = N$. Using this value and (2.20) in (2.22), one can see that

$$G_{a,rx} = N \frac{\sum_{n=1}^{N} g_{n,rx}^2}{N^2} = \frac{\left(\sum_{n=1}^{N} g_{n,rx}^2 \right)}{N} \tag{2.24}$$

giving a similar expression to that obtained in (2.21). Although the beamformer gains for transmit and receive array have been defined differently, the expression for the total gain are similar.

It should be pointed out that equations (2.21),(2.23), and (2.24) represent the ideal gain of an array and not the realized gain, which includes the term of impedance mismatch or element pattern. Since we know the effect of the beamformer gain is to increase the array gain, the realized gain in (2.13) can be written for transmit array and receive array as

$$G_{r,tx}(\theta_0, 0) = g_{0n,tx}(\theta_0, 0)\epsilon_r(D_e D_x D_y)G_{BF,tx} = g_{0n,tx}(\theta_0, 0)\epsilon_r G_{a,tx} \tag{2.25}$$

$$G_{r,rx}(\theta_0, 0) = g_{0n,rx}(\theta_0, 0)\epsilon_r(D_e D_x D_y)G_{BF,rx} = g_{0n,rx}(\theta_0, 0)\epsilon_r G_{a,rx} \tag{2.26}$$

where

$$G_{a,rx}(\theta_0, 0) = D_e D_y \frac{\left(\sum_{n=1}^{N} g_{n,rx}\right)^2}{N} \tag{2.27}$$

$$G_{a,tx}(\theta_0, 0) = D_e D_y \frac{\left(\sum_{n=1}^{N} g_{n,tx}\right)^2}{N} \tag{2.28}$$

The above expressions are given for a linear array with column of elements (see Figure 2.1b). In the cases of single radiating elements, D_y is unity.

2.3 Radar Systems

Radars are systems that are capable of measuring the distance, velocities, and transversal area of objects. Their working principle is based on the transmission of radio waves at a specific direction in the space and use the returned signal from the illumined scene to estimate the target properties. The time delay, frequency shift or signal amplitude are some of the signal characteristics that are used to measure the distance, velocities, and reflectivity of targets. There are various kinds of radar systems for different purposes. For weather sensing, the Pulsed-Doppler radar is the most popular system. These systems are used mainly to locate precipitation, calculate its motion, estimate its category (rain, snow, hail, etc.), and forecast its future position and intensity.

2.3.1 Radar Equation for Point Target Return

The radar equation provides a relationship between the transmitted power P_t, the characteristics of the target, and the receiver power at certain distance from the target. For a point scatter having backscatter cross section σ, the received power P_r at the receiver input is given [19] as

$$P_r = \frac{P_t g_t g_r \lambda^2 \sigma}{(4\pi r)^3 r^4 l^2} \tag{2.29}$$

where P_t is the transmit power, g_t is the transmit antenna gain, g_r is the receive antenna gain, λ is the wavelength at operating frequency, r is the target range, and l is the system loss. For mechanically steered radars with dish antennas, the above equation is valid for all scan angles in azimuth and elevation direction. Whereas for phased array radars, the equation is not completely true since the scan losses produced when the beam is electronically steered off-broadside.

To find the appropriate radar equation for a phased array radar that scans in one dimension, one must substitute (2.26) and (2.25) in (2.29), this yields

$$P_r(\theta_0) = \frac{P_t g_t(\theta_0, 0) g_r(\theta_0, 0) G_{a,tx} G_{a,rx} \lambda^2 \sigma}{(4\pi r)^3 r^4 l^2} \tag{2.30}$$

where the radiation efficiency of antenna has been include in the system losses. It should be also noted that P_t represents the input power in the transmit array and not the total transmit power delivered by the phased array as it is established in (2.29). Additionally, (2.30) shows that received power is a function of scan angle and the element pattern roll-off. It is obvious that to obtain accurate measurements with this formula, all system parameters must be measured accurately. Unfortunately, in practice, sometimes some of these parameters are not precisely known (i.e antenna characteristics and losses) and the radar must be calibrated to obtained the combined effect of these parameters. For example, rearranging terms, (2.30) can be written as

$$P_r(\theta_0) = \left(\frac{P_t G_{a,tx} G_{a,rx}}{l} \right) \left(\frac{g_t(\theta_0, 0) g_r(\theta_0, 0) \lambda^2 \sigma}{(4\pi r)^3 r^4 l^2} \right) \tag{2.31}$$

The first term on the right side of (2.31) contains radar parameters that are typically unknown and which contribution must be quantified. The purpose of the calibration is to determine the combined value of this first term. A classical approach of doing this is to measure the returned power from a reference target of known backscatter cross section and known range. Using (2.31), the first term can be computed as

$$C_s = \left(\frac{P_t G_{a,tx} G_{a,rx}}{l}\right) = \left(\frac{(4\pi)^3 r^4 P_r(\theta_0)}{g_t(\theta_0,0) g_r(\theta_0,0) \lambda^2 \sigma}\right) \tag{2.32}$$

where C_s is the system calibration constant. Note the measurement must be made when the array beam is pointing to the direction of the reference target.

2.3.2 Weather Radar Equation

The weather radar equation is an extension of the classical radar equation applied to a distributed target of many scattering elements. The equation is based on the measurement of the equivalent reflectivity factor Z of precipitation particles from the average received power that is returned by a volume target concentrated in the main beam. The expression is defined as

$$Z = \frac{1024 ln(2)}{c\pi^3} \left(\frac{\lambda^2 l}{P_t g_t g_r \tau \theta_3 \phi_3}\right) \left(\frac{\overline{P_r} r^2}{|K|^2}\right) \tag{2.33}$$

where Z is the radar reflectivity (mm^6/m^3),$\overline{P_r}$ is the average receive power (W), τ is the pulse width (s), c=3x108 m/s is the light speed, K=0.93 is the water dielectric constant, and θ_3 and ϕ_3 are the beamwidth of the one-way antenna pattern. Note that in this formula, the first term on the right side groups a set of constants, the second term groups the radar characteristics, and the third term groups the target characteristic.

The weather radar equation for a phased array radar that performs scanning in one-dimension is obtained by substituting (2.15), (2.25) and (2.26) in (2.33), giving

$$Z(\theta_0) = \frac{1024 ln(2) \lambda^2}{c\tau\pi^3} \left(\frac{l}{P_t G_{a,tx} G_{a,rx}}\right) \left(\frac{cos\theta_0}{g_{0n,tx}(\theta_0,0) g_{0n,rx}(\theta_0,0) \theta_{3,br} \phi_{3,br}}\right) \left(\frac{\overline{P_r} r^2}{|K|^2}\right) \tag{2.34}$$

This is the equivalent reflectivity factor obtained from the volume illuminated by the antenna at the scan angle θ_0. The third term in (2.34) represents the scan loss produced

by the normalized element pattern and beam broadening effect. When the array uses two different aperture illuminations in transmit and receive, the beamwidth $\theta_{3,br}$ and $\phi_{3,br}$ are the values obtained using (18). The second term represents the system calibration constant C_s. Finally, it should be pointed out that (34) corrects the reflective factor due to the scanning loss and broadening effects produced when beam is steered away from broadside, other effects as field projections [20, 21] are already included in the measured element pattern. For the case of a polarimetric radar that is tilted in elevation, the reflectivity factor of each polarization must be corrected by the effect of axis rotation.

The equ. (2.34) can also represented as

$$Z(\theta_0) = C_R \left(\frac{cos\theta_0}{g_{0n,rx}(\theta_0, 0) g_{0n,tx}(\theta_0, 0)} \right) (\overline{P_r} r^2) \tag{2.35}$$

where,

$$C_R = \left(\frac{1024 ln(2) \lambda^2}{c\tau\pi^3 |K|^2 \theta_{3,br} \phi_{3,br}} \right) \left(\frac{l}{P_t G_{a,tx} G_{a,rx}} \right) \tag{2.36}$$

is the radar constant, a combination of radar system parameters and physical constants that determines the proportionality factor between the reflectivity of a target at a given range and received power.

In general, the reflectivity factor is represented in logarithmic units dBZ, that is

$$\begin{aligned} Z[dBZ] &= \overline{P_r}[dBm] + C_R[dB] + 20log(r[km]) + 10log(cos\theta_0) \\ &\quad -10log(g_{0n,rx}(\theta_0, 0) g_{0n,tx}(\theta_0, 0)) \end{aligned} \tag{2.37}$$

This formula corrects the equivalent reflectivity of one-dimensional phased array radar. The results obtained by using this formula should be the same to the ones obtained from a mechanically steered weather radar (assuming zero tilt angle)

CHAPTER 3

BEAMFORMER AND BEAM STEERING CONTROL SYSTEM

3.1 Introduction

Phased array antennas are composed by many subsystems including radiating elements, TR modules, control electronic, communication interfaces, beam steering computer, RF distribution networks, DC manifold, cooling systems, built-in-test, etc. It is a common practice to design independently each subsystem in small modules, which are later used to construct subarray assemblies or build blocks (sometimes called tile or brick [15]) for the array. Typically, subsystems in a tile or brick construction are interconnected each other by mean cables (RF cables, ribbon cables, flex cables, etc). Example of type of construction in phased array that performs scanning only in azimuth plane are given in [22, 23, 24, 25, 26]. The advantage of this approach is that each subsystem can be tested for proper operation before the array integration, avoiding the installation of fail components. The disadvantage is that the lack of high integration between subsystems increases the fabrication and assembly process steps and increases wiring complexity and cost. Another approach for realizing the array assemblies is the fabrication of T/R packs (or panels), blocks that groups 4, 8, or 16 T/R modules with RF distribution networks and control electronic, all them fabricated in a high integrated PCB [27, 28]. This approach allows cost reduction of PCB and assembly, and minimize wiring interconnect. The disadvantage is that the system is expensive to maintain because to replace a failed module it is necessary to replace an entire T/R pack. Other disadvantage is that mutual coupling (leakage) between T/R modules limits the use of built-in test based on mutual coupling injection signal techniques [29].

This chapter describes the design of a low-cost beamformer network for CASA phased arrays which uses the concept of backplanes utilized in computer systems. Backplane architecture reduces wiring connections by allowing many daughter cards (T/R modules) to be

inserted in slots of a parallel bus. In this work, the backplane board includes all passive subsystems needed by the array, which includes RF distribution networks, DC manifolds, and communication buses. The design approach reduces cost by reducing the fabrication materials and simplifying the manufacturing process with the integration of various subsystem in a single board. In addition, T/R modules are fabricated in individual boards to reduce maintenance cost and provide low cost replacement parts. They also use their own enclosure to reduce the coupling between adjacent modules, which will allow the investigation of mutual coupling as a calibration technique.

Short-range phased array radars with adaptive and multifunction capabilities require flexible hardware that allows the system to adapt the scanning strategy according the target or weather events. It is desired to have systems that can support programmable pulse repetition frequency (PRF), pulse width, and dwell time, as well as support dual-polarization, beam-multiplexing, and adaptive scan. In order to support these capabilities, the beam steering control system must be fast enough to respond the commands sent by the beam steering computer, which implies the use of high-speed communication interfaces and microprocessor cores to calculate the attenuator and phase shifter settings that are required to implement each beam.

Different beam steering control architectures have been used in phased arrays [30, 31]. All them have in common the use of processing units to calculate the T/R module setting from a phase gradient (phase increment between element), element position and correction offsets (constant that corrects the hardware errors). Settings must be calculated for each beam; in a full polarimetric radar this might include the beams TV, TH, RH, and RV. Computation is performed either by a central processor or by element processors in T/R modules or subarray. However, there are some disadvantages associated with these approaches: They requires fast processing units that can add significantly to the array cost, the processing time to compute and transfer the settings to the attenuator and phase shifter imposes constraints to radar parameters (i.e. PRF and pulse width), and the transfer of digital commands during radar operation can interfere with RF signals. To overcome these limitations, a new beam steering control archicture based on look-up tables and state-machines was designed. The advantages of this system include: flexibility, reduce cost,

reduced wiring connection, high speed communication (higher that conventional system), minimize interference with RF signals, and allow high speed beam switching at very high PRFs and short pulse widths.

This chapter is organized as follow: Section 2 gives an overview of the array architecture proposed for CASA to developed phased array systems that meet the cost criteria for implementing low-cost low power X-band weather radars. Section 3 develops the system requirements for the beamformer network and beam steering control system of the array. Section 4 describes the design, implementation approach, and results of T/R modules. Section 5 explains the design and implementation of RF power distribution networks, communication bus, and power distribution system. The remaining sections describe the architecture of beam steering control system, as well as explain the communication and digital commands used to control the T/R modules.

3.2 System Overview

3.2.1 Antenna Array

A general discussion of the antenna array design is provided in [32]. The radiating aperture consists of a linear array of 72 vertical subarrays. The inner 64 subarrays are active elements that are fed by dedicated T/R modules that provide amplitude, phase, and polarization diversity. Additionally, the aperture has four passive subarrays at both edges that are used to reduce the edge diffraction effects and non-uniform mutual coupling. The vertical subarray used in the aperture consists of a linear array of 32 dual-linear-polarized aperture-coupled microstrip patch antennas that are interconnected by series-fed networks to each polarization port. The spacing between elements is 17 mm ($0.53\lambda_0$) in both azimuth and elevation. This value restricts the maximum scanning angle to $\pm$ 62.5^o in azimuth, where the first grating lobe is located. The aperture is fabricated as an array of 4 antenna tiles (panels) [6], each of which has 18 vertical subarrays in azimuth and 32 elements in elevation.

3.2.2 Antenna Architecture and Construction

Based on the general specifications of the phased array system that were settled on at an early stage, the aperture was divided in 4 Line Replaceable Units (LRU). Each LRU consists of an antenna panel having 16 active elements, a beamformer structure having 16 T/R modules, two RF manifolds, a power distributions system, and a serial communication bus. The decision of splitting the full array aperture into four LRUs is due to the limitation of fabrication process of the PCB (printed circuit board) and the maximum size of material used. Panel sizes are limited by manufacturing and assembly capabilities of PCB makers and PCB assemblers, respectively. Ultimately, the LRU size was chosen to maximize the material used in the antenna while meeting the requirements by standard PCB fabrication and assembly processes, which are key to reducing cost. The other key aspect that should be considered to reduce array fabrication costs is to use high levels of integration in both electronic components and array subsystems.

In order to reduce the cost and the interconnection complexity between T/R modules and other array subsystems, key components as RF manifolds, DC distribution systems, and serial communication buses of each LRU are fabricated into a multilayer PCB. The PCB design allows the T/R modules to plug directly into a shared high-speed communication bus and shared power and ground planes, eliminating the use of cables. The connection format is designed to provide DC, control, and RF signals on the same side of the T/R module. Although cables are not required to provide DC and control signals to T/R modules, the interconnections T/R modules and RF manifolds are still realized with conventional RF cables.

The beamformer architecture used in the linear active phased array is shown in Figure 3.1. The beamformer network is comprised of four beamformer structures, each having an array of 16 T/R modules and a backplane. The backplane has independent RF, digital, and DC bias section. The RF section is comprised of two passive corporate feed networks; one is used as a power divider and the other as a power combiner. The power divider ports interconnect the radar transmitter with all the transmit modules, while the power combiner ports interconnect the radar receiver with all the receive modules. The digital section consists of a scalable and parallel bus that interconnects the 64 T/R modules to

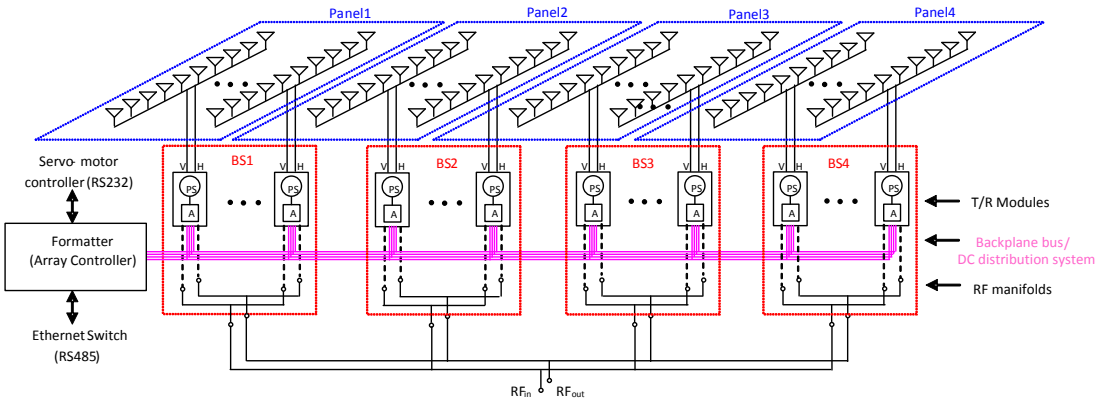

Figure 3.1: Beamformer architecture for linear active phased array.

a central array controller [33]. T/R modules are plugged to the backplane bus through a single multi-pin connector. This connector also allows T/R modules to receive the DC bias signals from the DC bias section, which consists of various power planes integrated in a multilayer PCB.

3.3 Array Requirements

3.3.1 T/R Modules Requirements

The requirements that modules should meet for this application are shown in Table 3.1. The key parameters of the transmitter design are a minimum transmit peak output power of 1 W with a maximum duty cycle of 30% at 9.36 GHz over a minimum of 80 MHz bandwidth. In the receiver chain, the goal are a minimum gain of 21 dB and less than 5 dB noise figure. The isolation between the antenna ports (H and V polarization) must be greater than 45 dB. This value is necessary to reduce the polarization errors that can be induced by the radar system at the polarization switch.

A high resolution control of the phase and gain is desirable to implement the array excitation function with low quantization errors. The required attenuator and phased shifter steps correspond to 6-bit quantization, the highest-resolution commercially available components. To achieve pattern with low sidelobe levels, the attenuator must have a minimum attenuation range of 10 dB.

Table 3.1: T/R module requerements.

Parameter	Value
Polarization	Alternate H and V
Transmit center frequency	9.36 GHz
Bandwidth	>50 MHz
Duty cycle	<30%
Pulse duration	1-60 uS
Transmit peak power	>1 W
Transmit gain	>21 dB
Receive gain	>21 dB
Noise figure	<5 dB
H-V isolation	>45 dB
Attenuator step	0.5 dB
Attenuation range	>10 dB
Phase shifter step	5.625^o
Phase shifter range	360^o

The use of commercial-off-the-shelf (COTS) devices with conventional PCB fabrication and assembly process is recommended in the design of the T/R modules to be able of developing this component at a cost of less than $500 [3, 34], including the packaging. Based on the array size and number of T/R modules, the design of individual units instead of a T/R array panel (several T/R modules) is required to ensure low cost replacement modules. Typically, the RF MMIC (microwave monolithic integrated circuit) devices are the dominant factor in the module cost, accounting for about 80% of the current module costs [8]. Similar proportion is obtained for T/R panels. In a small phased array radar with few failed modules, one finds that replacing the failed modules by T/R array panel is more expensive than replacing individual modules. Additionally, the use of individually packaged modules reduces the inherent mutual coupling between modules.

3.3.2 RF Power Distribution Network Requirements

RF distribution networks are key subsystems for feeding antenna elements or for collecting the power received by antenna elements. Usually, the RF power at the input port is distributed equally to an arbitrary number of outputs. The specifications for these components are the divider ratio, the phase and amplitude balance stability at the output ports,

the isolation between different output port and the return loss of each port. The divider ratio is specified typically as $1 : N$, where N is the number of output ports.

Various methods of feeding the array elements are discussed in [35]. The most common method is the parallel-feed network (also known as corporate feed network), which the array elements are combined into a network with transmission paths of equal electrical length. Equal transmission paths leads to equal amplitude and phase signals in the output. Corporate feed networks are generally preferred in phased arrays because they provide wide instantaneous bandwidth and good impedance match [36]. Based on these characteristics, this feeding method was chosen for this work.

The requirements that the corporate feed should meet for this applications are: A division ratio of 1:16, low insertion loss (<-10 dB), high isolation (<-30 dB), and low-cost.

3.3.3 Array Pattern Design

Weather radars require well designed antenna with very low sidelobes to reduce the error that may be introduced when the main beam point to a weak reflectivity and the sidelobes are illuminated by a strong reflectivity. The power received in the main beam is affected by the power received by the sidelobes, causing errors in the measurements. To reduce the errors, radars use antennas with sidelobes that are at least 25 dB below the main beam peak (the two-way sidelobes must be at least 50 dB or better below the main lobe peak). In a phase array antenna, a 50 dB sidelobe level is obtained when the transmit and receive aperture use the same tapered amplitude distribution, i.e. a 25 dB Taylor distribution. The problem of using a tapered amplitude distribution in the transmit aperture is that the radar cannot transmit at maximum power. The taper distribution limits power of the T/R modules, reducing the modules efficiency and the radar sensitivity. For instance, a 25 dB Taylor distribution generates a directivity loss of 0.43 dB and transmit power loss of 2.7 dB compared to an uniform distribution. Both terms cause a reduction in the radar sensitivity of 3.1 dB in one-way. In a phased array radar, the use of an uniform distribution in both transmit and receive apertures can maximize the radar sensitivity. The disadvantage is that it produces a two-way sidelobes of -26 dB.

The most simple and efficient solution for the problem of radar sensitivity and sidelobes is to use a uniform distribution in the transmit aperture and taper distribution in the receive array. This criteria allows the transmit array to transmit at maximum power and efficiency while the receive array can be used to reduce the two-way sidelobes. The question that arises is what is the best taper function for the receive array?. The question naturally occurs since the pattern multiplication from a uniform distribution and a highly tapered distribution for low sidelobe does not provide always the best two-way sidelobe level. Figure 3.2 shows the two-way sidelobes obtained by multiplying the radiation patterns of a uniform distribution with different Taylor distribution functions in a 64 element array. It shows peak and average values for different $\overline{n}$. The minimum sidelobe peak is -38.8 dB, which is obtained using a 24 dB Taylor distribution. An average SLL better than 50 dB is obtained when the designed SLL is specified in the range 20 dB and 34 dB. There is not an improvement in the two-way sidelobe peak for high values of the designed SLL. Figure 3.3 shows the pattern multiplication between a uniform distribution and a 24 dB $\overline{n} = 4$ Taylor distribution. Note the beamwidth is wider in the Taylor distribution. This beamwidth gets wider as the designed SLL is reduced, due to the energy removed from sidelobes is focused in the main beam. A designed SLL greater than 24 dB produces a radiation patterns whose a main beams are as wide as the location of the first sidelobe peak of the uniform distribution. The overlap between the main beam and first sidelobe peak in the pattern of a uniform distribution results in an increment in the two-way sidelobes, as is show in Figure 3.2.

3.3.4 Excitation Errors

The effect of the random excitation errors and failures on the antenna performance is to reduce the directivity gain and effective radiate power, and to raise the average sidelobe level and of some individual sidelobes. Theoretically, one can design the radiation pattern of an array with any sidelobe level as one desire. However, the random excitation errors limit the actual sidelobe level that one desires to achieve. The lower and closer the actual sidelobe level is to the designed sidelobe level, the smaller is the array error required. In practice, one can deteriorate the designed sidelobe level to achieve the desired sidelobe level with an acceptable error tolerance [37]. However, reducing the designed sidelobe level much

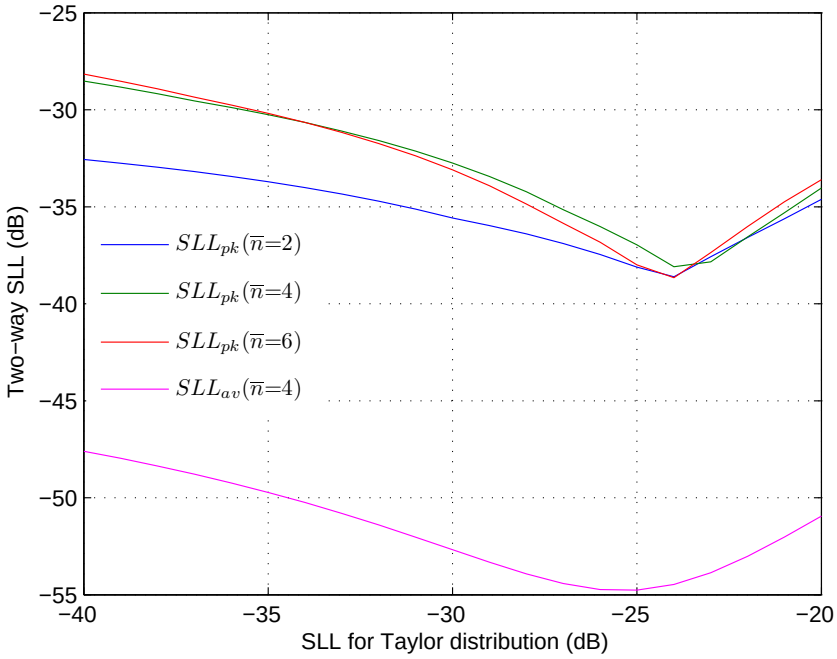

Figure 3.2: Two-way sidelobe level resulting from pattern multiplication of an uniform distribution and different Taylor distributions.

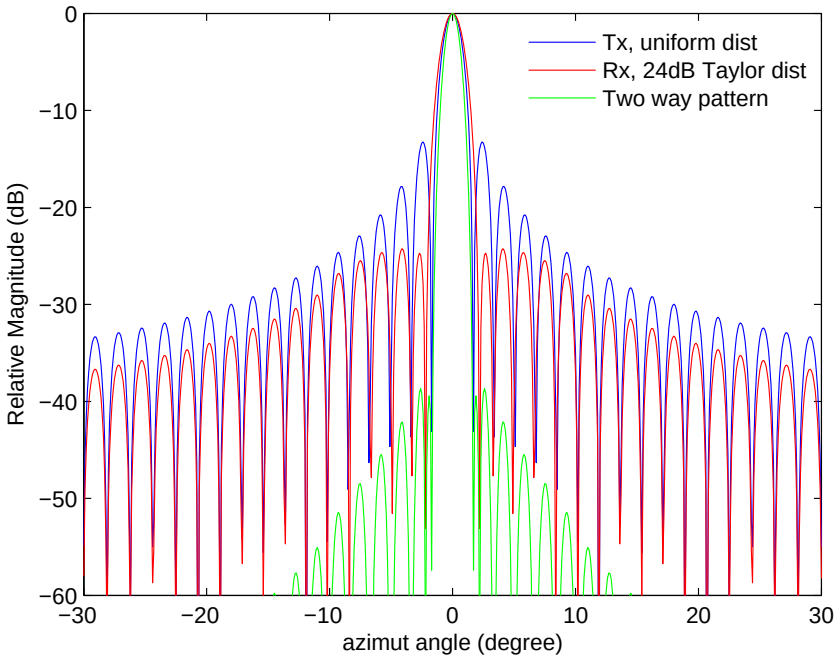

Figure 3.3: Optimal radiation patterns for a 64 element phased array antenna in transmit and receive to achieve low peak sidelobes.

in excess would increase dramatically the two-way sidelobe level of the radar. To keep low the two-way sidelobe level, the excitation errors must be low and the designed sidelobe level not so far from the desired value. For example, to implement a radiation pattern with a sidelobe peak of 24 dB the array may require a designed sidelobe or 25 dB. However, there is a probability that designed sidelobe level will exceed the desired value. This probability can be found from probability density function of the ensemble pattern, which is a Ricean distribution. The probability of individual sidelobes equal to or less than designed sidelobe level is given by [37, 15]

$$P(SLL < SLL_0) = \int_0^{SLL_0} \frac{2.SLL}{\overline{\Delta^2}} e^{\left(-\frac{SLL^2+SLL_0^2}{\overline{\Delta^2}}\right)} I_0\left(\frac{2.SLL.SLL_0}{\overline{\Delta^2}}\right).dSLL \tag{3.1}$$

where SLL_0 is the designed sidelobe at some given angle, I_0 the modified Bessel function of the first kind, and $\overline{\Delta^2}$ is the variance of the ensemble pattern sidelobe (also called the average sidelobe level). The variance for a linear array is given as

$$\overline{\Delta^2} = \frac{\Delta_a^2 + \Delta_p^2}{D_0} \tag{3.2}$$

where $\overline{\Delta_a^2}$ is the amplitude ratio variance normalized to unity, $\overline{\Delta_p^2}$ is the phase error variance in radians squared, and D_0 is the array directivity without error is given in (2.7) as

$$D_0 = \frac{|\sum_{n=1}^{N} A_n|^2}{\sum_{n=1}^{N} A_n^2} \tag{3.3}$$

where A_n is the excitation coefficient for the nth element. For a linear phased array antenna of 64 element having a 25 dB Taylor distribution, a directivity of 17.7 dB is obtained. The increase in the peak sidelobe level as a function of the array errors is shown in Figure 3.4. The curves are obtained from the cumulative probability function (3.1). For example, when the array error variance is $\overline{\Delta_a^2} = 0.001$ (the case when an attenuator of 0.5 dB resolution and 6 bit phase shifter are used) the peak sidelobe level is raised in less than 0.05 dB 50% of the time, less than 0.6 dB 90% of the time, less than 1.05 dB 99% of the time, and less than 1.5 dB 99.99% of the time. For higher error variances, the increase in the peak sidelobe level is

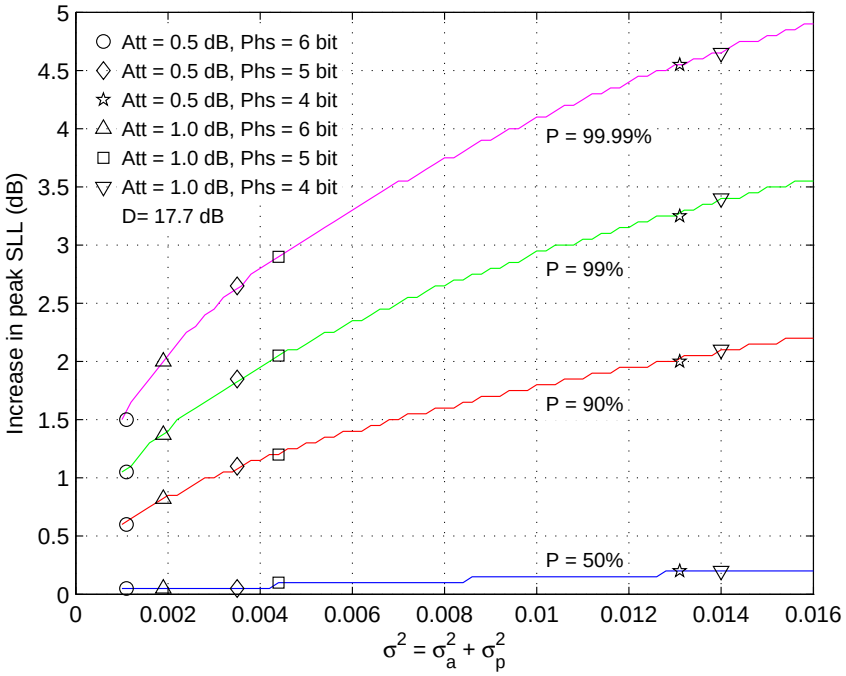

Figure 3.4: Increase in the peak sidelobe for a 64 element array using a 25 dB Taylor distribution.

much higher. The conclusion is that a linear phased array antenna of 64 elements requires an array error variance of 0.001 to be able to implement the radiation pattern with 25 dB peak sidelobes, with a probability of 99% that the sidelobe level will not exceed 24 dB. This error tolerance can be satisfied using digital attenuators with 0.5 dB resolution steps and 6-bit digital phase shifters. Similarly, the excitation errors can affect the sidelobes when an uniform distribution is used. Figure 3.5 shows the resulting increase in the first sidelobe (SLL_0=13 dB) for a 64 element array. The calculated directivity for this array is 18 dB. The results show in general a considerable reduction in the peak sidelobe in comparison to a 25 dB Taylor distribution, which is the result of using a larger directivity in the CDF of a Ricean distribution (3.1). For a phased array that uses digital attenuator with 0.5 dB step size and 6-bit digital phase shifter, the peak sidelobe is raised in less than 0.38 dB 99.99% of the time.

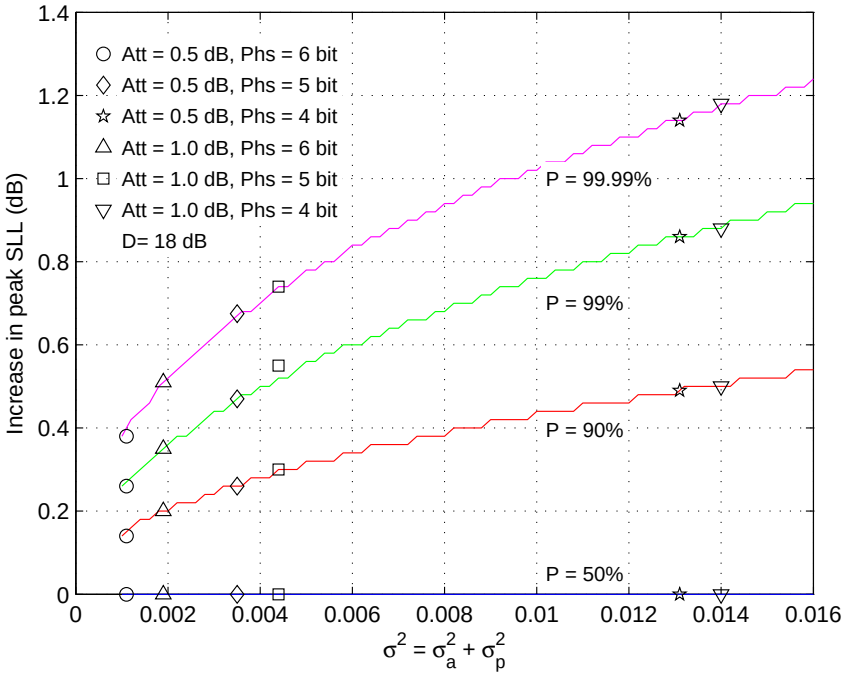

Figure 3.5: Increase in the peak sidelobe for a 64 element array using an uniform distribution.

3.3.5 Array Built in Test

In general, phased arrays are provided with Built-In-Test (BIT) functions, which continually monitor the integrity of all of the array elements in the operational environment. BITs are important components for diagnostic and calibration of arrays. Basically, a built-in-test measures the element characteristics using a test signal that is generated by an internal reference sources. Measurements are used to detect failures or hardware drift. To carry out the measurements, phased arrays must meet three requirements [38]: 1) the ability to turn on only one T/R module at a time, in either transmit or receive, with other elements are terminated in match loads, 2) separate transmit and receive beamforming networks, and 3) a method for injecting the test signal into or out of each module.

Three methods used to inject the test signals into or out all T/R modules are [39, 38]: RF coupler networks connected to test ports in the T/R modules, near-field antennas mounted around the periphery of the array, and inherent mutual coupling between elements. In the two first methods, the array requires additional hardware to implement the built-in-test, increasing the complexity and cost of the array. In contrast, in the mutual coupling

techniques the arrays use their owns elements to couple the test signals. Because of the minimum hardware requirements and cost, the mutual coupling as a built-in test signal injection technique is the recommended technique in this work.

3.3.6 Beam Steering Control System

Solid-state phased array radars with adaptive capabilities require flexible control features that allow changing the radar parameters during scanning operation, such as antenna scan patterns, pulse repetition frequency (PRF), pulse width, data collection rates, etc. Particularly, in short-range adaptive radar system, it is desired to have a PRF and pulse width that change depending on the situation and needs. A PRF of 1 to 5 KHz (to achieve an unambiguous range of 30 km) and pulse width of 1 μsec to 60 μsec are typical values for solid-states radars. To provide these values, the beam steering control system must be designed with high-speed microprocessors and high-speed communication interfaces that allow the T/R modules to update rapidly the calibration settings for the next beam. For example, a polarimetric weather radar operating in alternate mode and using 1 μsec pulse width (or beam switching) requests beam updates in less than 1 μsec. This implies that T/R module control signals must be updated in less than 1 μsec (beam update rates higher than 1 MHz) to switch from transmit beam (i.e. uniform illumination) to receive beam (i.e.taper illumination). The beam update time must include the beam processing time and command distribution time to all T/R modules. Beam steering control systems with this characteristic are not common. In fact, past work has demonstrated that response time of a beam steering system can be in the range of 5 μsec to 1 msec [40, 10, 41]

The main requirement is to design a low-cost beam steering control system for a dual-polarimetric radar that can support beam update rates of 1 MHz with minimum "dead time" (i.e. the finite time it take to update the T/R module controls for a new beam direction during which the radar is not transmitting or receiving). The system must also allow pulse-to-pulse beam switching, a characteristics that radars need to implement scanning strategies based on beam multiplexing techniques [14]. This technique requires that the beam location changes every single pulse; which implies that T/R modules settings must be updated every pulse.

The design of the beam steering control system must also include capabilities to control the element during the calibration. Most calibration techniques require that array has the ability to turn on only one module at a time, in either the transmit mode or the receive mode. This feature allows the measurements can be made in a single element while all other elements are off. During the calibration, the beam steering control system must be able to control all RF components of a T/R module, for example phase shifter, attenuator, T/R switch, and V/H switch. The control system must also include digital components such as memories and registers for storing calibrated data. It must also have the ability to control the write and read operation of memories and register.

To reduce the cost and wiring complexity in the system, a shared bus topology must be used to interconnect the digital sections of all T/R modules with the array controller. Typically this can be done by using communication interfaces the RS-485 standard and twisted pair cables (CAT5), which allow multidrop communications for up to 32 devices using speeds lower than 1 Mbps. Other alternative includes the use of LVDS standard and backplane buses. The advantage of using LVDS is that this standard is used in FPGA input/output pins, and it does not require external interfaces as the RS-485. Additionally, it works at speed much higher (up 200 Mbps) than RS-485. While backplane buses are low cost interfaces, designed typically with microstrip lines, that allow various LVDS devices can be interconnected in parallel. Based on these characterizes, it is recommended that the beam steering control system can be implemented over a LVDS backplane bus.

Two communications modes must be supported by the system: unicast and broadcasts. In unicast, the beam steering control system sends or receives commands to or from a single T/R module, for example during calibration mode, or when memory is written or temperature register is read. In broadcast, the beam steering control system sends the same commands to all T/R modules. This mode can be only used to update the beam commands stored in T/R modules.

3.4 T/R Modules

3.4.1 T/R Module Architecture and Design

Different T/R modules architectures can be found in the literature. However, the architecture selection should be closely related to the functionality required in the active aperture of the array in which it is used. An excellent overview of the performance and tradeoff analysis for different T/R modules architectures is given by [42]. In it, it is concluded that the common-leg architecture provides the best third-order-intercept (TOI) performance compared to other architectures, it also allows high-levels of integration at a lower cost. The third-order intercept point affects the ability of the radar to reject clutter. In a radar system, it is desired to provide a receiver with a high dynamic range [43]. This implies to have a high third-order intercept points at the same time have a low noise figure. Based on the conclusion in [42], the common-leg architecture was selected. However, some modifications were introduced in the architecture to satisfy some system requirements such as dual polarization and independent transmit and receive ports. The block diagram of the T/R module is given in Figure 3.6 (see full schematic and part list in Appendix A). A common 6-bit phase shifter and 6-bit attenuator with a gain block are used for receive and transmit channel. Two separated T/R switches connect the shared control circuitry to the transmitter and receiver blocks. These blocks in turn are connected to a PIN diode based high power diversity switch that provides transmit/receive and polarization diversity to the radiating elements. All RF circuits use GaAs MMICs from Hittite.

The Transmit channel consists of a 2 W power amplifier (PA HMC591LP5), a medium power amplifier (MPA HMC441LP3), a diversity switch, and the common control circuit. The bias-current of the amplifiers is controlled by MOSFET switches, which are controlled by the signal T (transmit). The amplifiers are turned off during the receive mode to reduce the temperature dissipation and eliminate any feedback loop. The details of the transmit channel analysis are given in Table 3.2. The table shows the gain, power in, power out, and 1 dB compression of each element of the transmitter. The input and output power are computed assuming that the power amplifier is operating at compression. It is projected an overall gain of 29 dB and 1 W of output power. Additionally, modules require 1 dBm input power to operate the power amplifier in compression.

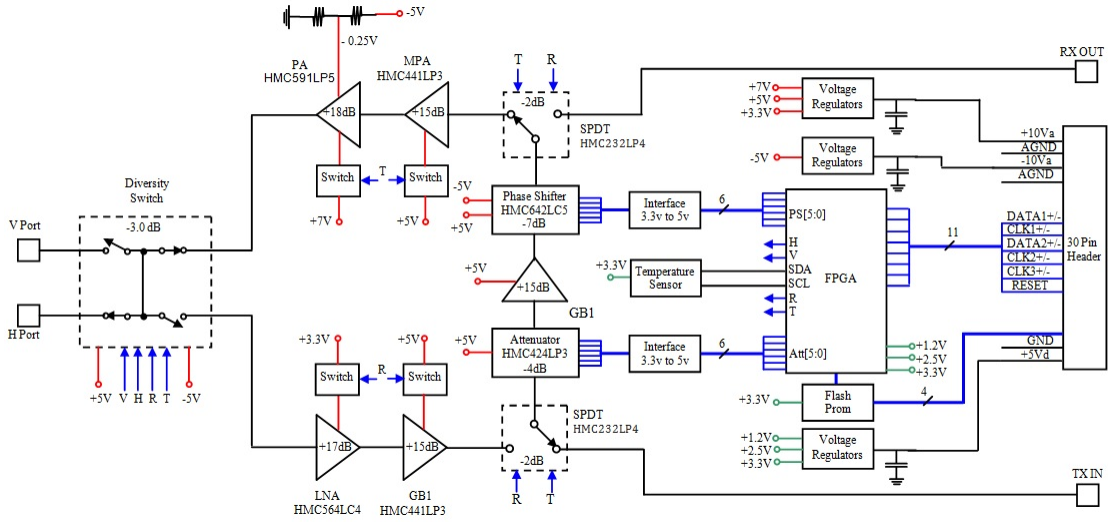

Figure 3.6: T/R module block diagram.

Table 3.2: Transmit channel performance

	Comp. performance		Cumulate module performance			
Component	Gain (dB)	P_{1dB} (dBm)	Gain (dB)	P_{in} (dBm)	P_{out} (dBm)	P_{out} (W)
Switch	-2	22	-2	1	-1	0.0008
Attenuator	-4	22	-6	-1	-5	0.0003
Gain block	15	18	9	-5	10	0.01
Phase shifter	-7	28	2	10	3	0.002
Switch	-2	22	0	3	1	0.0013
Medium power amp	15	18	15	1	16	0.0398
Power Amplifier	17	32	32	16	33	1.9953
Diversity switch	-3	40	29	33	30	1

The Rx block consists of a diversity switch, a low noise amplifier (LNA HMC564LC4), a gain block (GB1 HMC441LP3), and the common control circuit. The low-noise amplifier offers a high dynamic range with a gain of 17 dB and noise figure of 1.5 dB. The 45 dB isolation of the diversity switch provides receive protection during the 1-Watt transmit pulse. Additionally, the MOSFET switches controlling the bias-current of the amplifiers provide additional protection during transmit mode. The details of the receive channel analysis are given in Table 3.3. The table shows the gain, noise figure, and the input third order of intercept of each element used in the receiver. The total receiver channel has gain of

Table 3.3: Receive channel performance

	Component performance			Cumulate module performance		
Component	Gain (dB)	NF (dB)	TOI_{out} (dBm)	Gain (dB)	NF (dB)	TOI_{in} (dBm)
Diversity switch	-3	3	-	-3	3	-
Low noise amp	17	1.8	25	14	4.8	8
Gain block	15	4.5	29	29	4.9	9.86
Switch	-2	2	50	27	4.9	24.86
Attenuator	-4	4	45	23	4.91	22.83
Gain block	15	4.5	29	38	4.92	9.47
Phase shifter	-7	7	41	31	4.94	24.46
Switch	-3	2	50	28	4.96	17.46

29 dB and 4.95 dB of noise figure. The channel input TOI point is about 8 dB at maximum gain (attenuator set to zero).

In addition to the RF circuit, the T/R module has a digital control circuit that interfaces the module with the commands sent from array controller [33]. The functionality of this control circuit is implemented in a FPGA, some of its functions are:

1. To provide a fast serial interface to communicate with command from the array controller.
2. To provide memory interface to store the calibration data.
3. To provide interface to control the attenuator, phase shifter, LNAs bias, power amplifier bias, and transfer switch.
4. To monitor the temperature from a temperature sensor
5. To provide T/R module timing.

Since the T/R module is integrated with analog and digital components, it requires separate power supplies to avoid mixing analog and digital signals. T/R modules are primarily powered by +10 V, +5 V and -10 V power supplies that are provided from very low-impedance power planes in the backplane board. These voltages are regulated to appropriate DC levels on the T/R module according the specifications of the components. Separate ground and power planes for analog and digital signals distribute the voltages across the module, avoiding in this way the coupling and noise interference among these signals. Figure 3.6 shows in detail the voltage levels used by each component. All components

are directly connected to the power planes, except the amplifiers used in the transmitter and receiver blocks. The drain bias voltages for these amplifiers are driven by load switches, which in turns are controlled by the T/R signal generated by a digital controller.

3.4.2 Diversity Switch Design

Early on in the design of the T/R module, it became apparent that PIN diodes were the most appropriated switching element available. GaAs (Gallium Arsenide) MMIC switches that could drive 2 W were not commercially available. For that reason, a large signal GaAs Pin diode diversity switch is proposed. The switch uses a star configuration of 4 Single-Pole Single-Throw (SPST) switches [44]. A characteristic of microwave SPST switches is that diodes are spaced by quarter-wavelength transmissions, which help to increase the isolation when multiplex diodes are used.

Each pole is independently controlled by a bipolar control signal, as illustrated in Figure 3.7a. The entire switch incorporates a total of 10 GaAs PIN diodes: two diodes at each arm to increase the isolation between ports, and an additional diode in the polarization switches to terminate the ports in a load of 50 Ω when they are switched off. Matched loads are needed in the ports to terminate the radiating array element at its characteristic impedance during the antenna calibration. The bias networks were designed with two radial microstrip radial stub and high impedance microstrip lines, see Figure 3.7b.

An important aspect of the switch design is that its implementation differs from the conventional approaches because the diode cathodes are not directly connected to grounded vias. When diodes are directly grounded with vias, the insertion loss of the switch tends to increase by the impedance of the vias, especially at high frequencies. To avoid this problem, the diode cathodes are directly connected to microstrip lines that are previously grounded to zero potential. To keep a low insertion loss, the reactance of equivalent impedance seen from diode anodes is cancelled out by using microstrip radial stubs, which are also part of the bias networks. Designing these networks is the most critical part of the switch.

The switch was designed, optimized and simulated in a 2D electromagnetic simulator. The optimization focused in the tuning of the microstrip radial stubs that cancel out the diode reactance. An empirical model of the PIN diode in the simulator was used. To reduce

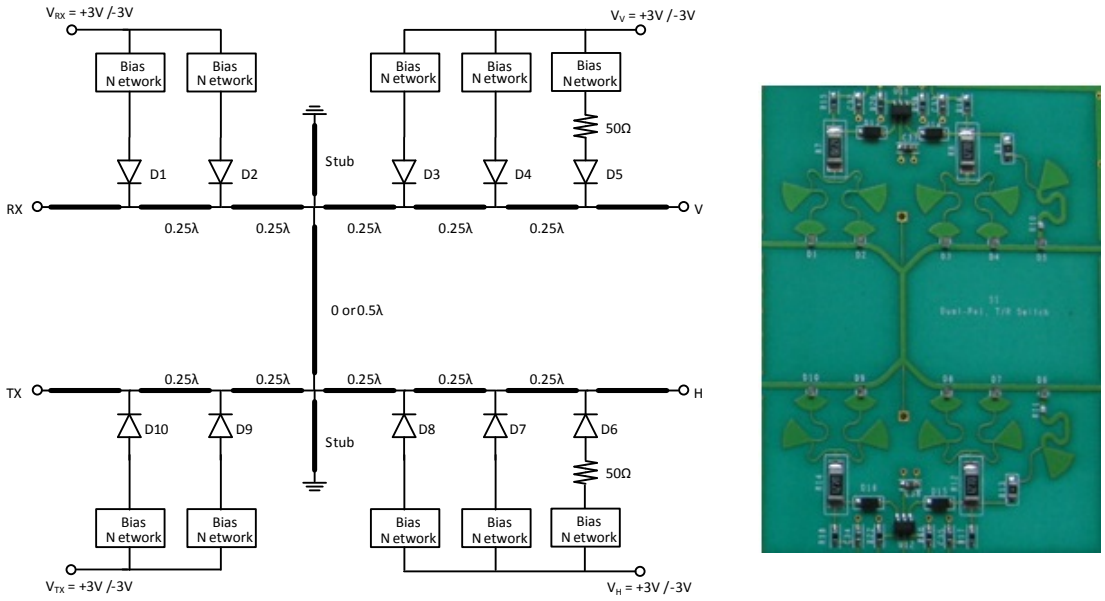

(a) (b)

Figure 3.7: Pin diode diversity switch. a) Schematic. b) Implementation.

risk of failure because the fabrication tolerances, it was necessary to create different designs, each having different tuning/bias networks. A PCB array having different switch designs was fabricated and tested. The circuit having the best performance was chosen for the T/R module design. Figure 3.8 shows the switch performance in the frequency range 8 - 12 GHz. Figure 3.8a shows the measured insertion loss and return loss when poles TX and V are on. A 3.2 dB insertion loss at 9.36 GHz and return loss better than -10 dB are obtained. Similarly, Figure 3.8b shows the measured insertion loss and return loss when poles RX and H are on. In this plots an insertion loss of 3.4 dB and return loss better than -10 dB is obtained. In Figure 3.8c and 3.8d are shown the isolation and return loss for the poles V and H when one is on and the other is off. The isolation is better than 40 dB in the range 9.3 - 11 GHz. In figure 3.8e and 3.8f are shown the coupling (insertion loss) between the antennas poles and the unable channel (off). A coupling better than 40 dB was measured in the range 9.3 - 11 GHz.

In addition to S-parameter measurements, power measurements were realized to determine the power operation range. Measurements were realized with a power meter and a

signal generator with a 10 W power amplifier. Results shown that the diversity switch has a high 1dB compression point, being able to hand 10 W without introducing any distortion.

3.4.3 Control Electronics and Interfacing

The control logic is implemented in a Field Programmable Gate Array (FPGA). This component generates the control signals for the attenuator, phase shifter, T/R switches, and amplifier's load switches from commands that are sent from the array controller. In addition, the module is equipped with an I2C temperature sensor, whose temperature register can be read from the FPGA through dedicated lines. The on-board FPGA, a Xilinx Spartan-3E XC3S100E FPGA, is locally programmable with an external flash Programmable Read-Only Memory (PROM). As a part of the control logic, the FPGA internal memory is configured as a look-up table, where calibrated settings for the attenuator and phase shifter are stored. The memory, registers and I/O ports of the FPGA are remotely controlled from an external FPGA-based array controller, which translates the user commands from the host computer to control and timing signals for the radar system. The communication (25 Mbps data transfer) between the Array Controller and the T/R module is realized through five differential transmission lines, which include CLK1, DATA1 and CLK3 as differential inputs to the module, CLK2 and DATA2 as differential outputs from the module, as it is shown in Figure 3.6. CLK2 and DATA2 allow the array controller to read the memory, the attenuator, phase shifter, and temperature register of the T/R module. While CLOCK3 has different purposes, it works as a trigger signal when the array controller request to update the attenuator and phase shifter or work as advancing clock to read a sequence command table on the FPGA. The sequence table contains information to access the look-up table for a predetermined beam position and transmit-receive sequence (TV, TH, RH, and RV). The resulting output data of each sequence is used to update the attenuator, phase shifter, and T/R switches.

3.4.4 Module Implementation and Fabrication

The printed circuit boards (PCB) for T/R modules were panelized in 2x2 arrays during the manufacturing process, allowing them to be easily populated and soldered using

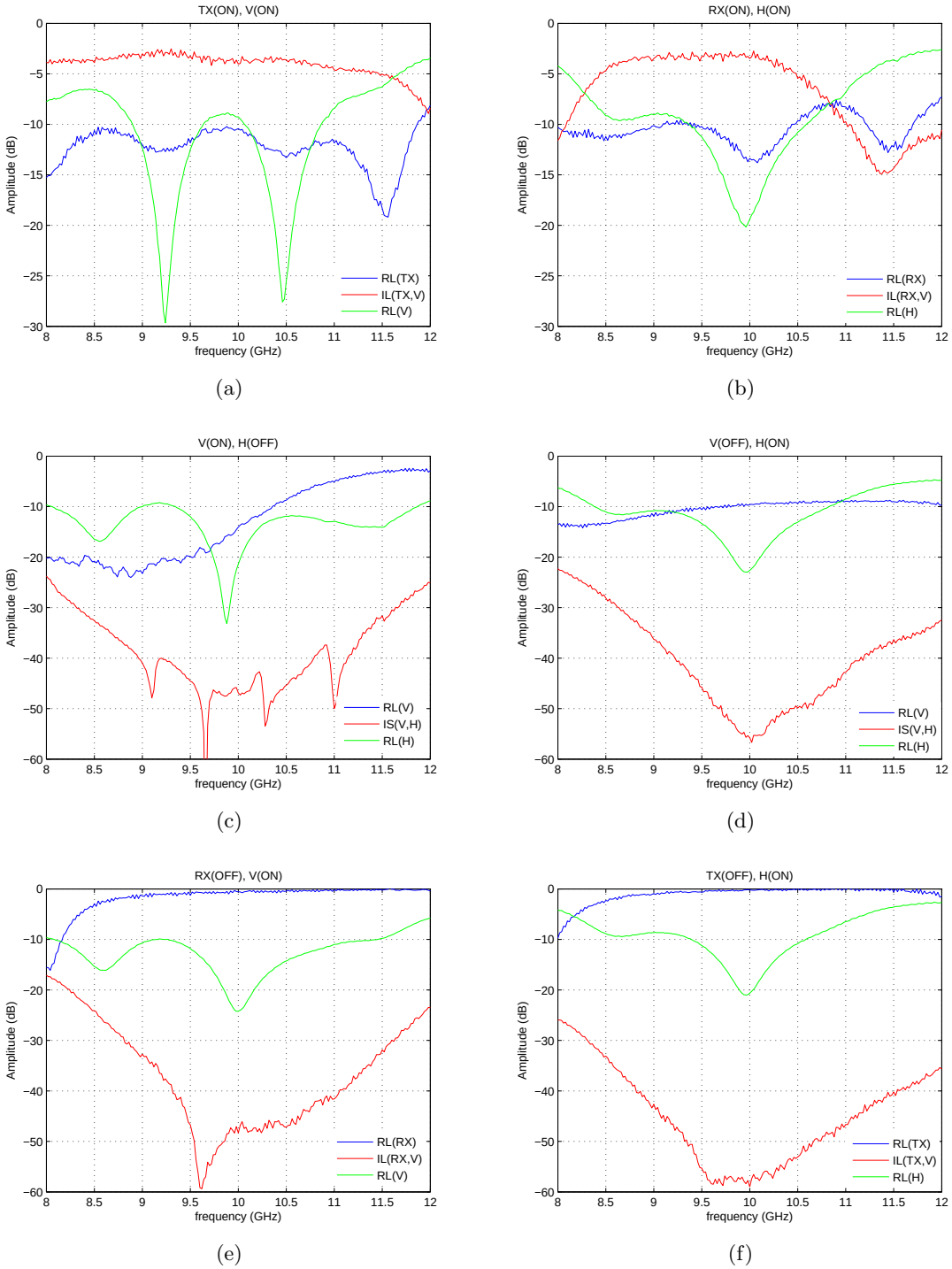

Figure 3.8: Diversity switch performance as a function of frequency.

standard processes. In addition, arrayed PCBs can help to reduce cost because they fewer fabrication steps which speeds the assembly. A picture of a fully populated T/R module is shown in Figure 3.9. The PCB comprises six circuit layers fabricated on a hybrid construction of Rogers 4350 and FR4, see Figure 3.10 . A laminate of 10 mil Rogers 4350 in the *TOP* layer is used to implement the RF and digital sections. The remaining layers, four FR4 laminates including the bonding adhesives, are used to implement the analog and digital ground/power planes, and to distribute the control signals. The PCB is designed to have low thermal impedance from the power amplifier footprint through the board mounting plate, which works as a heat spreader. A thermal patch isolates the PCB from the baseplate avoiding that vias and transmission lines be short-circuited.

In Figure 3.9, the RF components are COTS plastic-packaged GaAs microwave monolithic integrated circuits (MMICs). The large square containing microstrip lines and radial stubs to the right of the module is the high power diversity switch. The area inside the gold square to the left of the module corresponds to the digital components and interfacing section. The two ports at the right side of the module are SMP sub-miniature connectors that connect to the radiating element via short coaxial cables. The two ports at the left side are SMA connectors that connect the TR module to two separate RF manifolds. All components except the connectors were placed on the board using pick and place machine. The module with enclosure weights 140 g and has a dimension of 6.6 cm x 11.2 cm.

3.4.5 Measurements

One of the challenges of producing phased-array antennas is the large number of T/R modules that must be tested during the development phase or prototype production. In addition, the testing of a single module is a labor intensive that generally involves hundreds or thousands of measurements under different conditions. The use of automated equipment is a requirement to reduce cost and time while keeping a standardized process. Based on this need, an automated test station was specifically designed for this project. The test station is based on a PNA series Network Analyzer from Agilent that is remotely controlled via LAN (local area network) from a host computer. Figure 3.11 shows the schematic diagram of the measurement equipment setup for the T/R module evaluation. The entire

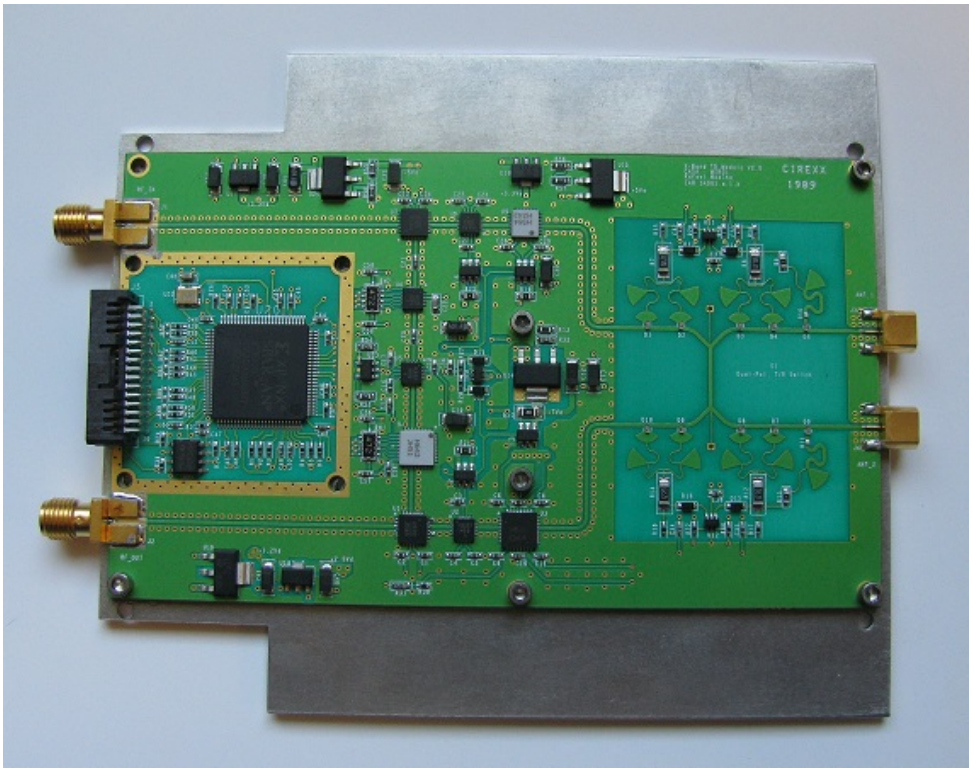

Figure 3.9: Photograph of the implemented T/R Module.

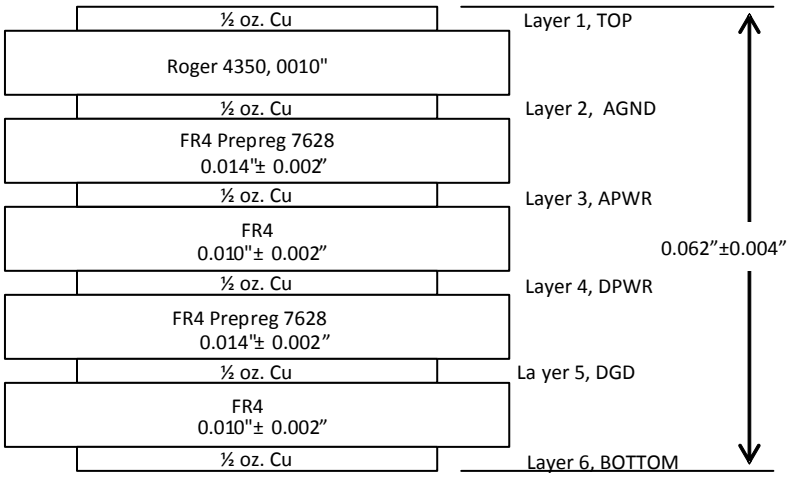

Figure 3.10: PCB cross section.

characterization process is controlled from the host computer by mean of a Graphical User Interface that was developed in the C language. The system only allows measurements of pulsed S-parameters and power at only one temperature. However, measurements can be repeated at other temperatures after manually abjusting the module temperature with a cold plate. The process starts by first heating up the module with a pulse of 30% duty cycle, once the steady-state temperature is reached, module parameters are measured at several frequencies.

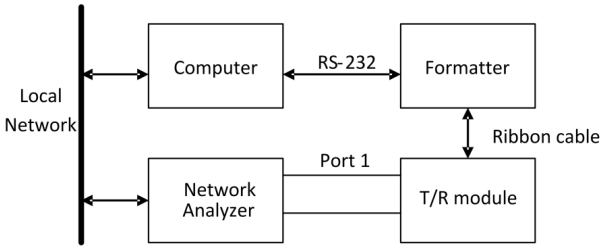

Figure 3.11: Measurement equipment setup for the T/R module evaluation.

3.4.6 Test Results

Table 3.4 summarizes the module performance at the operating temperature. The values were obtained from a group of 64 T/R modules at the frequency of 9.36 GHz. Measurements are made with zero insertion attenuation and phase. According the results, the modules present a transmit peak output power of 30.9 dBm, a noise figure of 5.5 dB, and an isolation between H and V ports of 45 dB. Although the noise figure exceeded in 0.5 dB the desired value, the key parameters meet the module design requirements. On the other hand, gains and return losses (RL) were obtained from small signal measurements. The average performance for these parameters is shown in the Figure 3.12. From gain measurements, it can be estimated that the modules have a bandwidth of about 1GHz.

Figure 3.13 shows the typical transmit output power and power efficiency of one module as a function of the input power. The minimum input power to reach the 1 dB compression point and maximum module efficiency are 5 dBm and 12% respectively. The low efficiency is a consequence of using a linear power amplifier having an efficiency of 20%, it is also

Table 3.4: T/R module performance summary at 9.36GHz.

Parameter	H-Pol	V-Pol
Transmit gain (dB)	24.5	24.7
Transmit peak power (dBm)	30.9	30.8
Transmit input 1 dB compression (dBm)	5	5
Transmit input return loss (dB)	-15.5	-15.6
Tx small signal gain variation over temperature (dB/^{o}C)	0.09	0.09
Receive gain (dB)	27.3	27.1
Receive input 1dB compression	-15.7	-15.2
Minimum noise Floor (dB)	5.4	5.6
Receive input return loss (dB)	-12.7	-11.8
Receive output return loss (dB)	-12.9	-13
Rx gain variation over temperature (dB/^{o}C)	0.016	0.016
Isolation between RF_{in} and RF_{out} ports (dB)	78	78
Isolation between V and H port (dB)	47.4	46
Phase shifter step (degrees)	5.531	5.531
RMS phase error (degrees)	1.49	1.49
Attenuator step (dB)	0.476	0.476
RMS attenuation error (dB)	0.161	0.161
Transmit and receive settling time (μsec)	<2	<2
Overall module efficiency	12%	12%

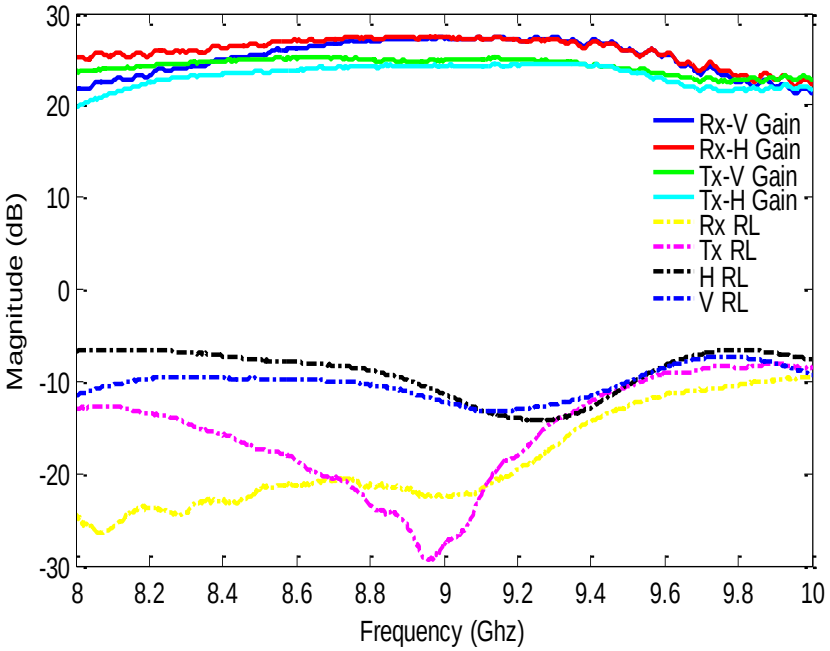

Figure 3.12: Average gain and return losses for 64 modules.

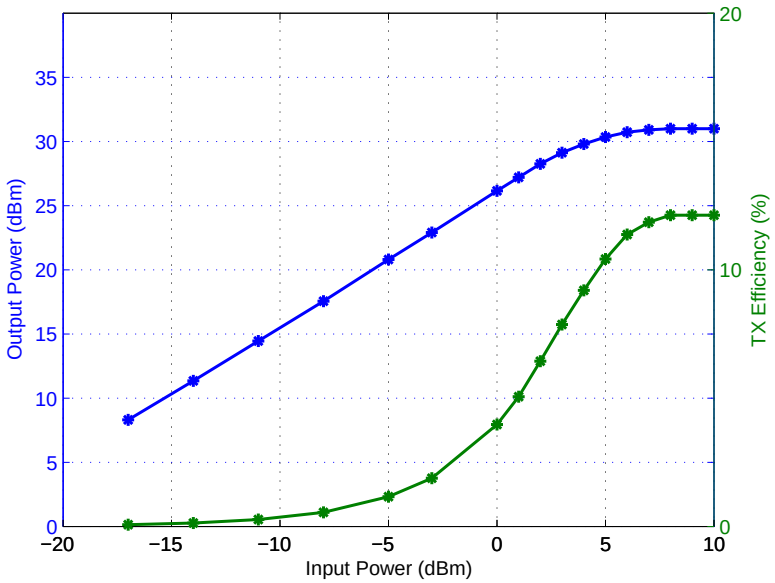

Figure 3.13: Transmit peak output power and module efficiency versus input power.

because insertion loss produced by the diversity switch and low efficiency of DC linear voltage regulators.

The small signal gain/phase and Tx saturation power performance are shown in Figure 3.14 as a function of temperature. Measurements are normalized to the operating temperature of 32 ^{o}C. The gain and phase in the Rx channel decay at a rate of 0.016 dB/^{o}C and 0.6 deg/^{o}C respectively. The results show that these variations can be compensated with one attenuation step and 3 phase shifting steps in the temperature range. In contracts, the gain in the Tx channel decay a faster rate, 0.09 dB/^{o}C, with a similar phase variation, 0.6 deg/^{o}C. For large signal excitation, the relative saturation power (loss) increases at a rate of 0.018 dB/^{o}C.

The typical gain and phase performance versus the attenuator and phase shifter states of one receive module at 9.36 GHz are shown in Figure 4.4 (Chapter 4). The plots comprise of a set of 64 curves, each representing the response at a specific attenuation state. The results show that the gain is affected by the insertion loss of each phase shifter state. Similar effect is observed in the phase, but its value is only affected by the insertion phase of the attenuator. For example, at zero phase state, the module phase varies from 0^{o} to -50^{o} when

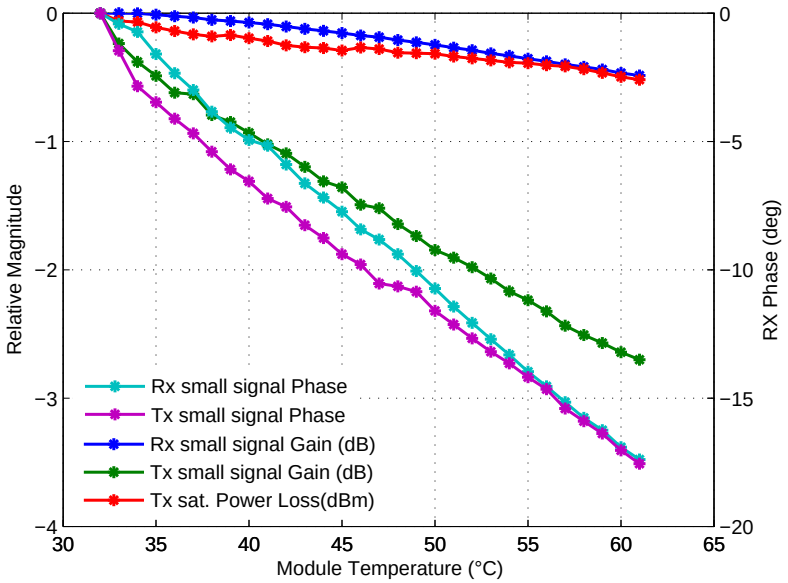

Figure 3.14: Relative gain/phase performance and saturation power loss versus module temperature.

the attenuator is adjusted from zero to maximum attenuation. This effect can be corrected by using calibration techniques and by storing the corrected settings in the module memory. Ultimatly the calibration should be done for different temperatures. Results could be used, for instance, to compensate the gain/phase deviation due to the temperature, as it is shown in Figure 3.14. On the other hand, the step size (resolution) for the attenuator and phase shifter as a function of component state for a typical T/R module is shown in Figure 3.15. The attenuator presents a non-uniform attenuation step versus states; the mean step and standard deviation are 0.457 dB and 0.161 dB, respectively. Similar behavior is obtained with the phase shifter, which has a mean phase step of 5.54^o and standard deviation of 1.49^o.

Measurements were also performed in the time domain to determine the settling time of T/R modules. Settling time is the time required for the output to reach the steady-state within a given error bound following some input stimulus. For this test, a signal generator connected to module input and a microwave Schottky diode detector connected to the module output were used. The diode voltage was measured with a high-speed digital oscilloscope. Figure 3.16a shows the typical switching characteristic of a T/R module for a

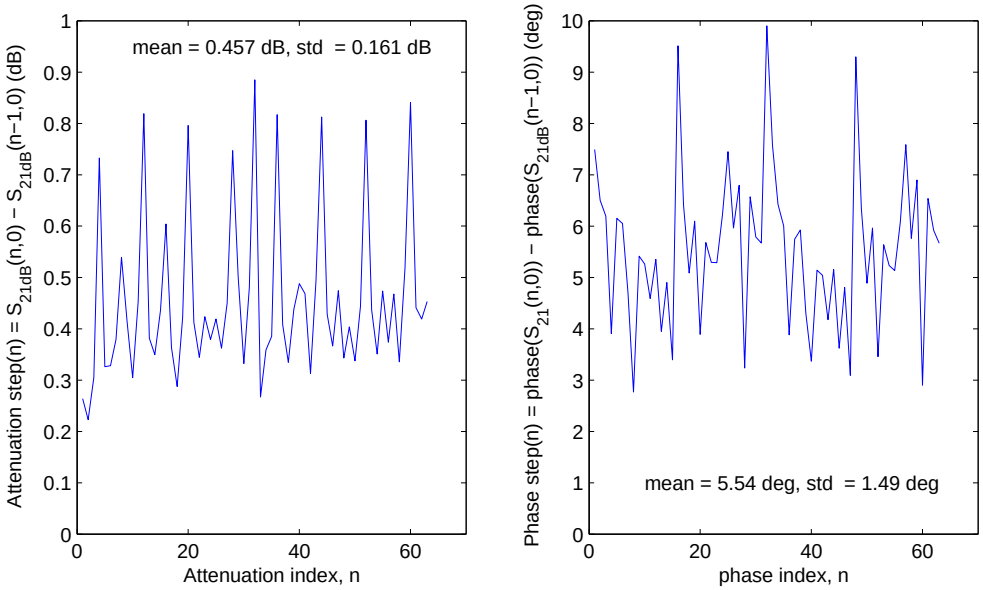

Figure 3.15: Resolution step as a function of component states. Left: Attenuator. Right: Phase shifter

pulse of 100 μsec. The green signal represents the control signal applied to either transmit channel or receive channels and yellow signal is the IF signal measured at the channel output. The voltage demodulated by the diode detector during rise time for both transmit and receive channel are shows in figure 3.16b and 3.16c, respectively. The settling time in both cases is about 2 μsec. This values is important because it can indicate the maximum PRF that can be implemented by the radar. For example, assuming the minimum pulse width of the radar is τ_{pw}= 1 μsec and maximum duty cycle is limited at DC= 30% to protect the T/R module power amplifier of excessive heating. It is obvious that the waveform must be transmitted until the settling time has elapsed to avoid the amplitude modulation that could created by the variable gain. Therefore, the transmit channel will be enable by the time τ_{st}+ τ_{pw}= 2μsec+1 μsec= 3 μsec. The minimum pulse repetition interval is obtained as

$$PRI = \frac{\tau_{st} + \tau_{pw}}{DC} = \frac{2\mu S + 1\mu S}{0.3} = 10\mu S$$

using this value one can find the maximum PRF is 1/PRI = 100 kHz. The wide PRF-range enable the system to work in a widely range of radar applications including weather and

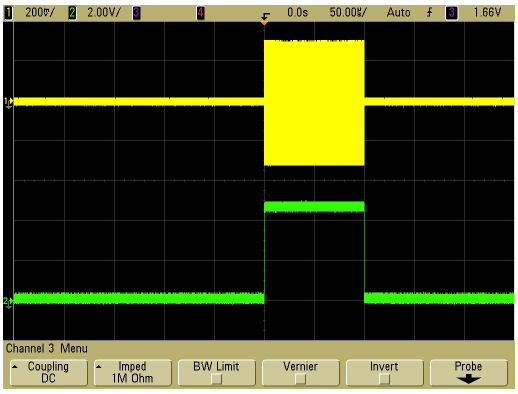

(a)

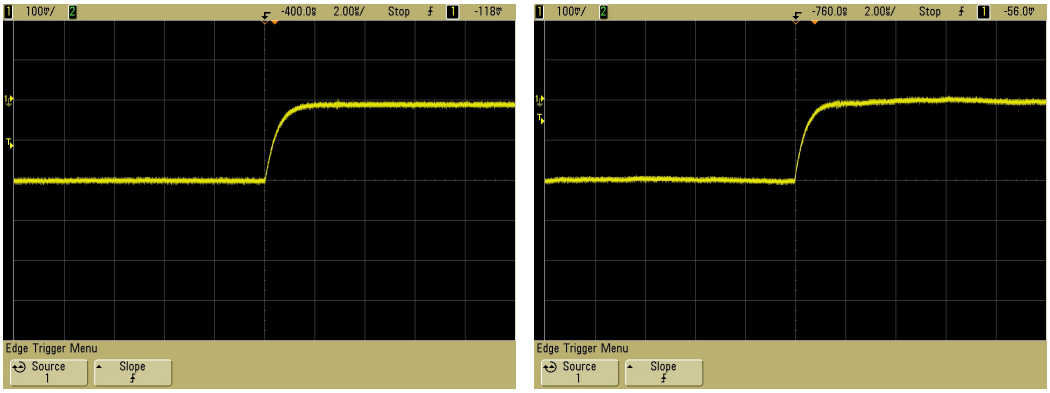

(b) (c)

Figure 3.16: Typical switching characteristics of a T/R module.a) RF and DC bias pulse. b) RF pulse at the transmitter output. c) RF pulse at the receiver output.

airborne surveillance. On the other hand, Figure 3.16c suggests the radar gain in receive must be calibrated during the settling time to observe targets close to the radar.

3.5 Backplane Board

3.5.1 Description

The backplane is the interface between TR modules and other radar subsystems. All RF signal distribution lines, DC bias signal, and digital bus that connect the T/R modules with the transceiver, power supplies, and array Controller are located in this board. The array system uses four backplanes to interface the 64 T/R modules with other radar subsystems. Figure 3.17 depicts how the radar subsystems are interconnected through the backplane and what sections are integrated in it. The RF, digital and DC bias sections are implemented in

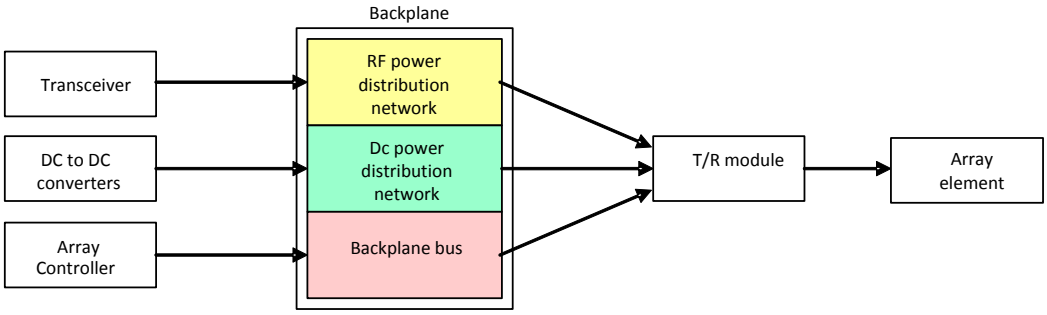

Figure 3.17: Backplane subsystem.

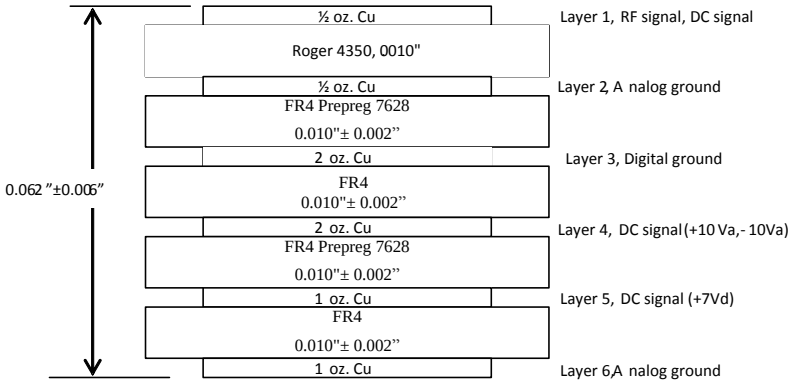

Figure 3.18: Backplane PCB cross section.

a multilayer hybrid PCB fabricated on FR4 and Roger 4350 material. Figure 3.18 shows the board layout structure and the layers assigned to each subsystem. Each section is complete isolated each other by ground planes. The RF and DC power distribution networks partially share the top layer because both the RF connectors and DC bias connectors are assembled on it. The cost model for the backplane is described in Appendix B.

Figure 3.19 shows the front and rear view of the backplane and how the beamformer structure is assembled. In Figure 3.19a, the from view shows the backplane's top layer where the RF manifold are designed. The rear view shows the header connector array that forms the backplane bus. In Figure 3.19b, the T/R module header connector is plugged to backplane bus, while the RF connectors are connected to RF manifold with RF semi-rigid cables. Note that the corporate feeds are enclosed in a metallic lid in order to eliminate any radiation or coupling with other subsystems. The whole RF power distribution network is

shown in Figure 3.20. Two 1:4 power dividers are needed to connect the outputs from the 4 power combiners and inputs of the 4 power dividers, respectively.

3.5.2 Corporate Feed Network

3.5.2.1 Design and Implementation

Typical components used in the design of corporate feeds are the microstrip T-junction, Wilkinson power divider, and rat-race coupler [18]. T-junctions and Wilkinson power divider are three-port networks that can split the power equally. T-junctions are passive components of simple design that are characterized by a poor performance. Wilkinson power dividers are also simple components which solve the matching and poor isolation problem of T-junctions. The drawback of these two components is that both are lossy components. On the other hand, rat-race couplers (also known as hybrid ring coupler) are lossless four-port networks that provide ports with very good return loss and high isolation. Compared with thee-port networks, the rat-race couplers are larger structures, but they provide a better performance. Based on the system requirements, such as low insertion loss and high isolation, the rat-race coupler was chosen for this design.

A rat-race coupler consists a $3\lambda_0/2$ ring of microstrip line with line impedance of 70.71 Ω an 4 microstrip lines of 50 Ω spaced at intervals of $\lambda_0/4$ as shown in Figure 3.21a. The input power at port 1 splits and travels both ways round the ring. At ports 2 and 3 the signal arrives in phase and adds whereas at port 4 it is out of phase and cancel. Ports 2 and 3 are in phase with each other, while port 4 is terminated in a resistive load of 50 Ω. A 1:16 corporate feed is designed by connecting several rat-race couplers in cascade at ports 2 and 3 as is shown in Figure 3.21b. Fifteen couplers are needed in total. Note that 50 Ohms terminations at port 4 of each coupler are grounded by radial stubs and that half of the corporate feed is symmetrically opposite to the other half. Theoretically, the insertion loss in a 1:16 power divider is 10log10(1/16)=-12 dB.

The corporate feed is implemented in a 10 mil Roger 4350 material, its design was simulated in 2D electromagnetic simulator. Simulated results indicated a good amplitude and phase balance among output ports. A photography of the fabricated 1:16 corporate feed network is shown in Figure 3.22. The ports are connected to surface mount SMA

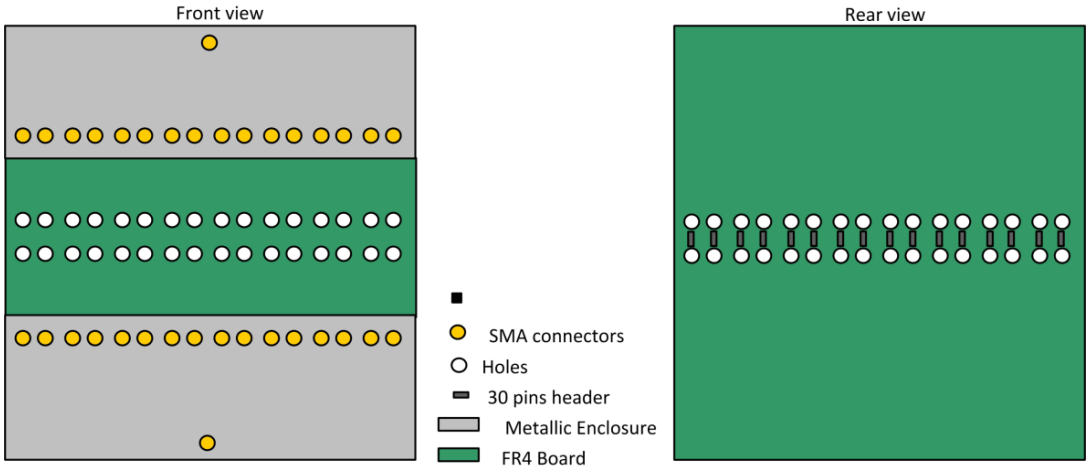

(a)

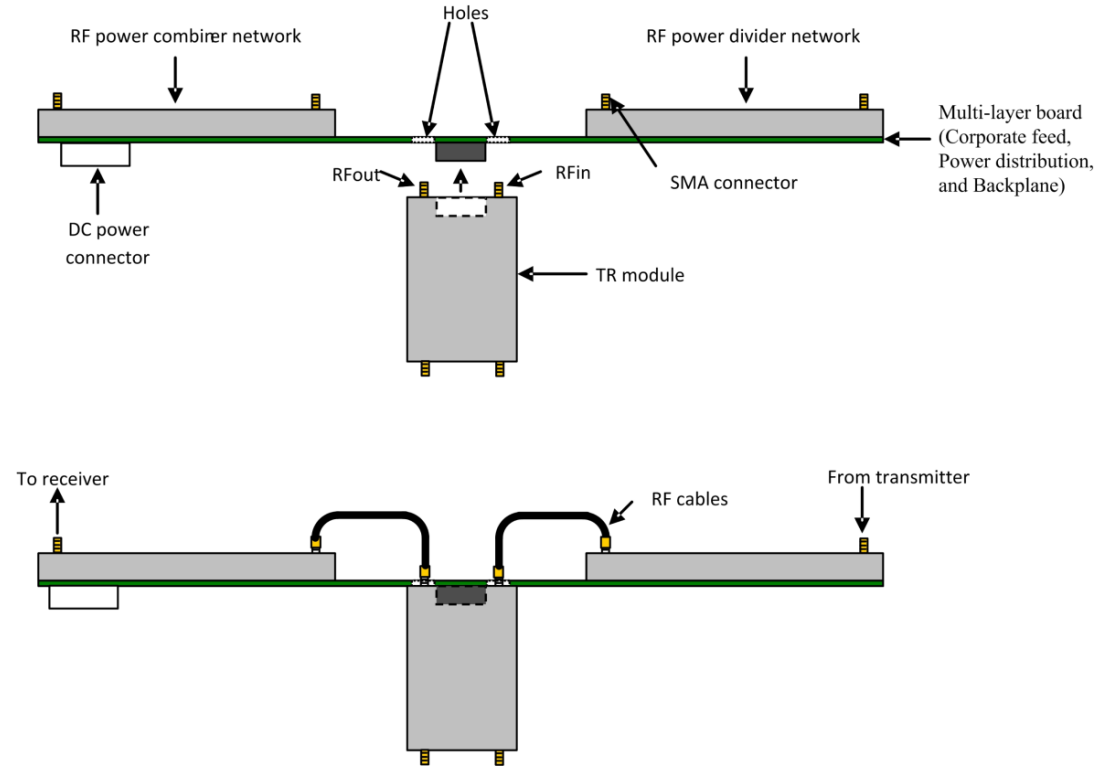

(b)

Figure 3.19: Backplane board and Beamformer structure. a) Front and rear view of backplane board. b) Beamformer assembly

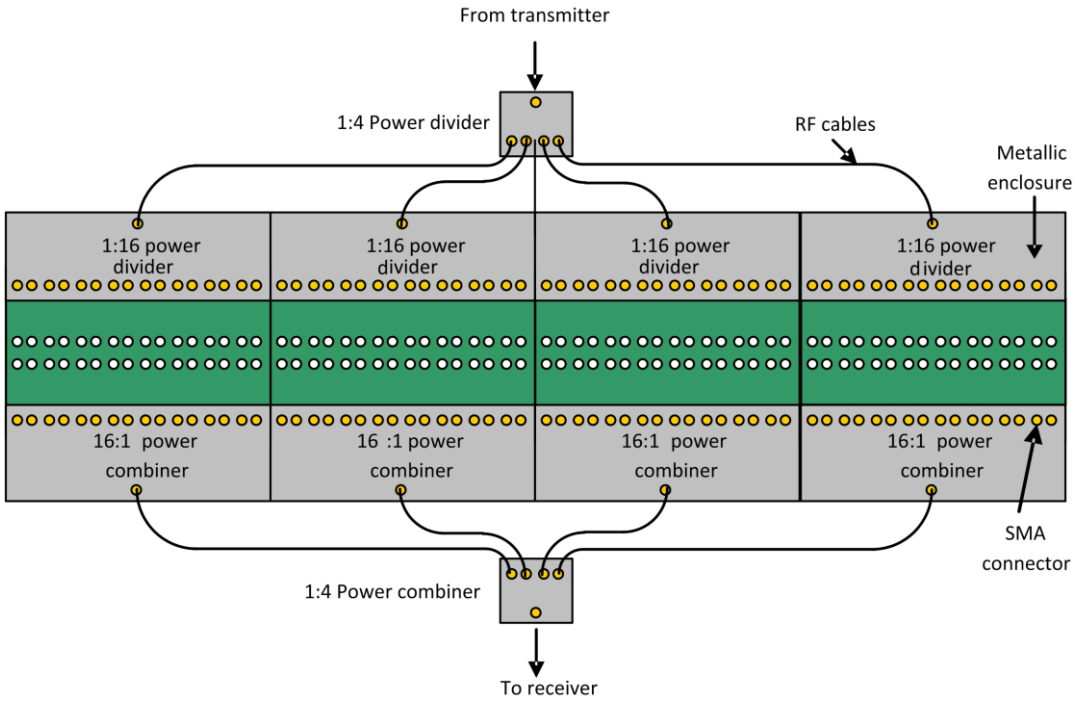

Figure 3.20: RF power distribution network.

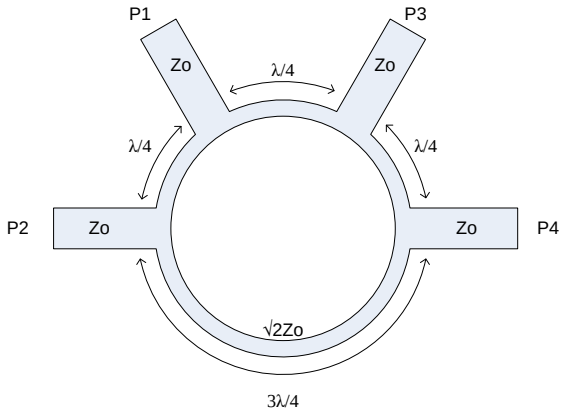

(a)

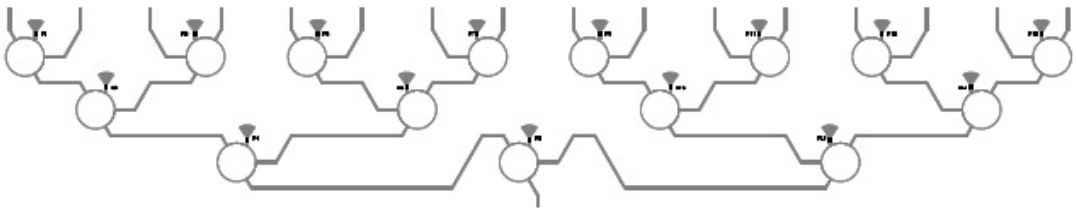

(b)

Figure 3.21: Component and schematic circuit of the RF power distribution network. a) Rat-race coupler. b) 1:16 corporate feed.

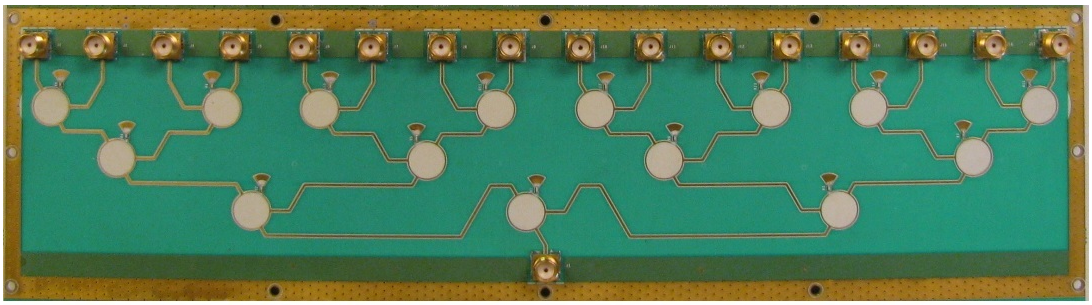

Figure 3.22: Corporate feed layout.

connectors, and the peripheral is surrounded by a gold-color ground plane that allows the attachment of a conducting lid that can be placed over the PCB to provide isolation.

3.5.2.2 Results

Measurements were made using a two port vector network analyzer in the frequency range from 9.06 GHz to 9.66 GHz. Each output port was measured while the other ports were terminated in 50 Ohms loads. The return loss for each of the 17 ports is depicted in Figure 3.23. In average, the return loss is lower than -10 dB. The amplitude and phase insertion loss for each of the 16 branches is depicted in Figure 3.24. In Figure 3.24a, the insertion loss is -16.6 dB at 9.36 Ghz and there is approximately 0.3 dB spread in insertion loss among output ports. A increment of 4.6 dB with respect to theoretical insertion loss was obtained. This value is attributed to losses in the transmission lines and SMA connectors. In figure 3.24b, there is approximately a 7^o spread in the insertion phase.

3.5.3 Backplane Bus

3.5.3.1 Design

Backplanes have been widely used in high-speed communication and computer system because they are low cost and reliable system. However, their use in phased array antennas has been unknown or it has not been reported. A backplane is an interconnect system that allows the parallel connection of various digital cards (PCBs) to a shared bus. They should be designed properly to guarantee signal integrity and high-speed performance. To meet these high performance standards, the buses use differential signaling over a pair of mi-

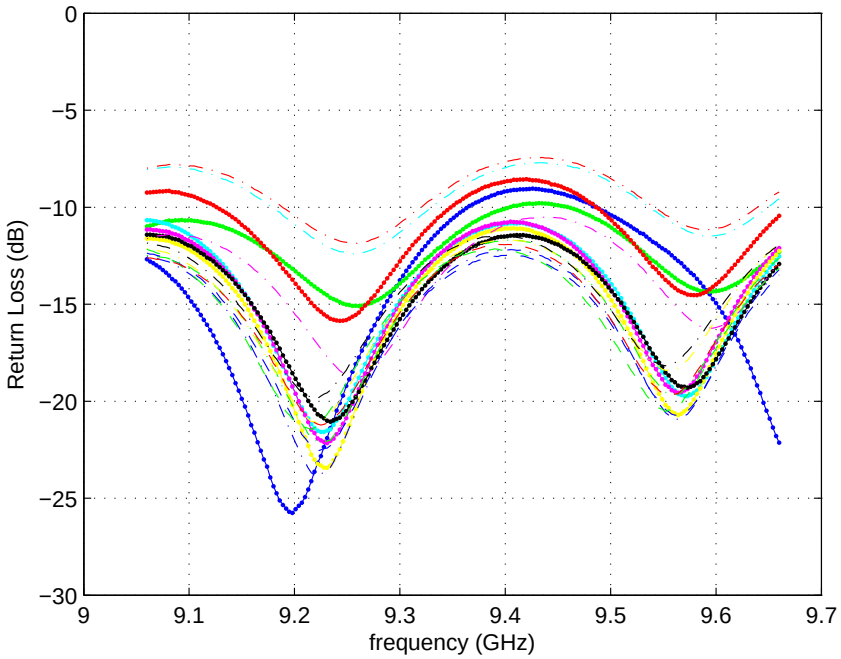

Figure 3.23: Return loss for each input port of a 1:16 corporate feed.

crostrip lines (or striplines) as method for transmitting information. Differential signaling is the preferred method because they are much more immune to noise than single-ended signaling, which uses a single transmission line. For high-speed backplane system, low-voltage differential signaling (LVDS) is the technology of choice. LVDS is a standard that allows high-speed data transfers, low power consumption, and low electromagnetic interference.

The performance of a backplane is strictly related with elimination and reduction of reflections caused by impedance mismatches between the bus and load impedances. Reflections affect the signal integrity and reduce the speed with which data can be transmitted. Designing of the proper microstrip line pairs and using the best matching terminations in a backplane are key for a good performance. A general discussion of basic design considerations for backplanes is provided in [45]. Other aspect related to backplane designs is the bus topology. Two common topologies are LVDS multidrop and LVDS multipoint [46]. In a multidrop topology, there is a single driver and multiple receivers over the bus length. The communication is unidirectional. While the multidrop topology has multiple

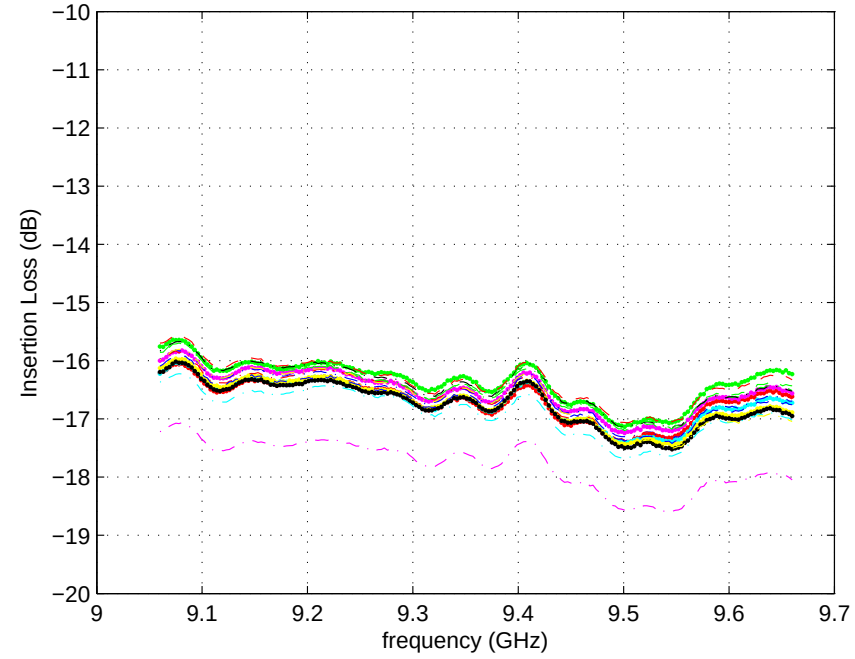

(a)

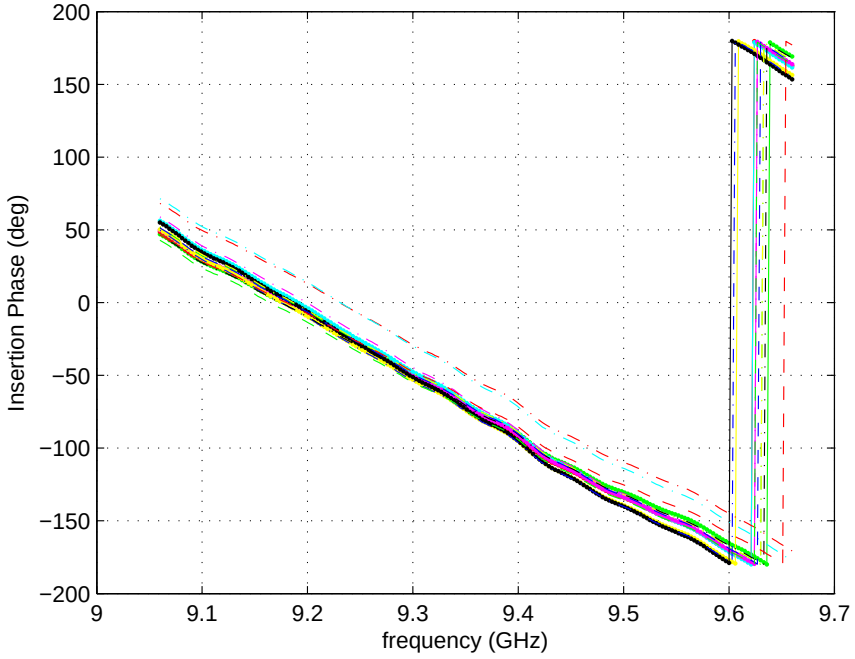

(b)

Figure 3.24: Insertion loss and insertion phase measured at each branch of a 1:16 corporate feed. a) Insertion loss. b) Insertion phase.

signal drivers and receivers, all sharing a single bus. This configuration allows bidirectional communications.

For simplicity, in this project, a multi-drop topology for the communication and beam-steering control system was chosen. The backplane bus that connects the array controller with T/R modules uses five transmission line pairs (buses). Three buses are used to transmit data (ones bus) and clocks (two buses) from the array controller to T/R modules; each of these buses can be represented as shown in the top in Figure 3.25. There also two buses to transmit data and clock from the T/R modules to array controller. In this case, each bus can be represented as shown in the lower part in Figure 3.25; where each driver is a tree-states transmitter. Normally all driver outputs are set to high impedance and only the driver that responds to array controller commands can transmit over the bus. A general diagram of the bus topology used in the array system is depicted in Figure 3.26. The configuration used two arms, each having two backplanes in cascade with 32 T/R modules connected in parallel. Two repeater/buffer boards connected at the end of each arm are used to extend the connection between the beamformer structure and the array controller. Ultimately, the three buses transfering data and clock toward T/R modules are connected in parallel in the array controller. While the two buses coming from T/R modules are multiplexed into a single data line. The advantage of this topology is that all T/R modules are connected in parallel at the Array controller using a simple, high speed, and low cost communication bus.

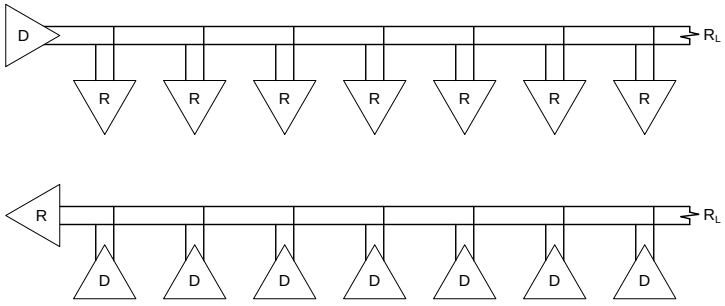

Figure 3.25: Multidrop topology.

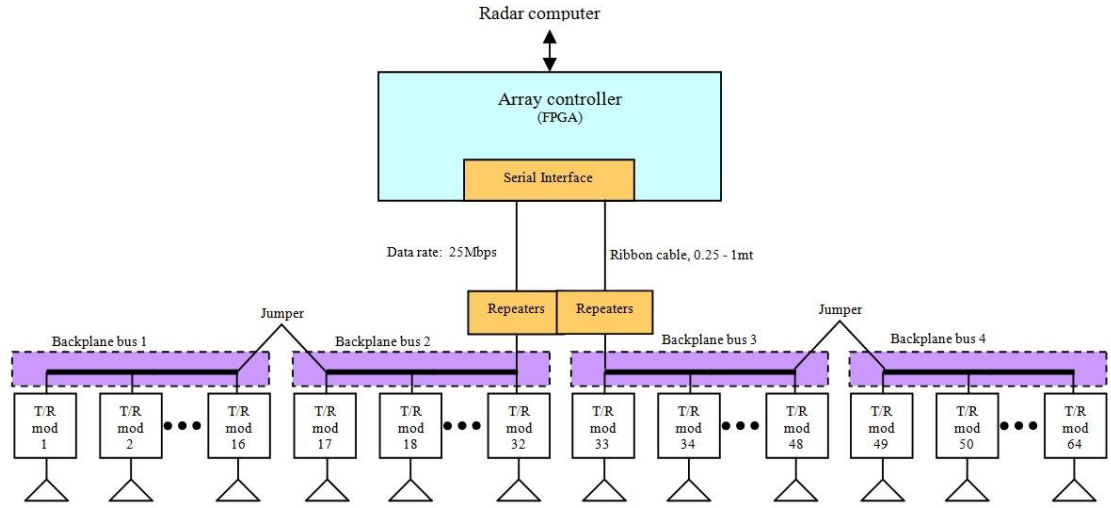

Figure 3.26: Communication architecture topology for linear phased array antenna.

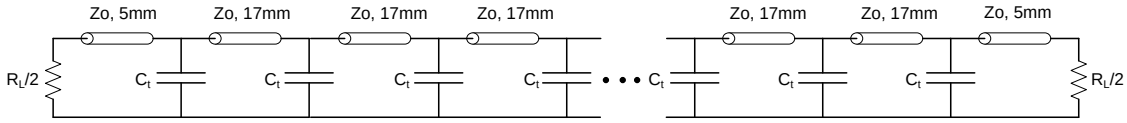

Figure 3.27: Equivalent circuit for a backplane bus.

The primary goal of this design is to implement a 100 Mbps multipoint backplane that can be scalable and allow interconnect 32 modules in parallel. To design the microstrip lines, the equivalent electrical circuit of backplane bus is used. Figure 3.27 shows the equivalent circuit of Figure 3.25, where an equivalent capacitive load (C_t) replaces the receivers (or drivers) and stubs (transmission line pairs that connect the devices to backplane connectors). The spacing between T/R modules is equal to radiating element spacing, 17 mm, and it is assumed that all connectors are populated with T/R modules. When the microstrip line is loaded with the devices and stubs, the distributed capacitance of the receivers and stubs affects the characteristic impedance of the line. The net result is that the effective (loaded line) impedance will be lower than the characteristic impedance of the line. The effective impedance of the loaded line is given as

$$Z_0(loaded) = \sqrt{\frac{L}{C + NC_t/H}} \tag{3.4}$$

where N number of devices,H is the total length of transmission line, L and C are inductance and capacitance per unit length of the microstrip line. These values are given in [47] as

$$\begin{aligned} C &= \frac{0.67(\epsilon_r + 1.41)}{ln\left(\frac{5.68h}{0.8w+t}\right)} \quad \text{in pF/in} \\ L &= \frac{CK^2}{12(\epsilon_r + 1.41)} ln\left(\frac{5.68h}{0.8w+t}\right) \quad \text{in nH/in} \end{aligned} \tag{3.5}$$

where ϵ_r is the relative permittivity of the material, t is the thickness of the material, w is the trace width of the microstrip, t is the trace thickness, k=87 for $15 < w < 25$ mils, or k=79 for $5 < w < 15$ mils. The value of the termination resistor at each end of the line depends on the effective impedance of the line. Its values is chosen as $R_L = 2Z_0(loaded)$

The microstrip line was implemented in the top layer of the backplane having a 10 mil Roger 4350 material with ϵ_r=3.48 and t=0.5 mils, see figure 3.18. The design equation for the trace width for a microstrip line is given by [47] as

$$w = 7.475he^{\frac{-Z_0\sqrt{\epsilon_r+1.41}}{87}} \tag{3.6}$$

The microstrip impedance without the loading effect is designed to be 70 Ω. Therefore, the trace width is

$$w = 7.475 * 10 * e^{\frac{-70\sqrt{3.48+1.41}}{87}} \approx 12\ mils$$

When this value is used in (3.5) and (3.6), one find that C= 1.86 pF/in and L= 8.92 pH/in. Since the material used in top layer in both backplane and T/R modules are the same, the distributed capacitance can be used to calculate the capacitance of the stub (C_{stub}) connecting the device to the bus. The stub is the transmission line that connects the module's FPGA to the header connector, which is approximately 0.5 inches. Therefore, C_{stub}=0.5 in*1.86 pF/in= 0.93 pF. On the other hand, the capacitance associated to FPGA input port in differential mode can be obtained from the manufacturer's specification sheet. This value is about 8 pF. The total equivalent capacitance for the device and stub is summed C_t=0.93+8=8.93 pF.

With all the connector filled (32 connector), the total length of the backplane is approximately 32*1.7 cm/2.54 = 21.41 inches. The effective impedance of the loaded microstrip line is obtained from (3.7) as

$$Z_0(loaded) = \sqrt{\frac{8.92}{1.86 + 32 * 8.93/21.41}} = 24.22\ \Omega \tag{3.7}$$

To reduce the reflections at the ends, the termination resistor should be close to the effective differential impedance of backplane. That is $R_L = 2Z_0(loaded) = 2 * 24.22 = 48.44\Omega$. Finally, this values was rounded to 50 Ω. Also, as part of the design, PSPICE simulations using the equivalent circuit of the backplane were performed. The purpose of the simulation was to verify signal integrity at different speeds. Simulations indicated that the backplane bus can work perfectly up 100 Mbps.

3.5.3.2 Implementation

Figure 3.28 shows a photograph of the front view of the backplane, the board face where the buses are implemented. There are five microstrip line pairs with termination pads at the ends. The two black connectors at the ends are used to connect either repeater boards or jumper cables. While the connector for the T/R modules are installed in the rear side plane. A photograph of a partially assembled beamformer structure is shown in Figure 3.29.

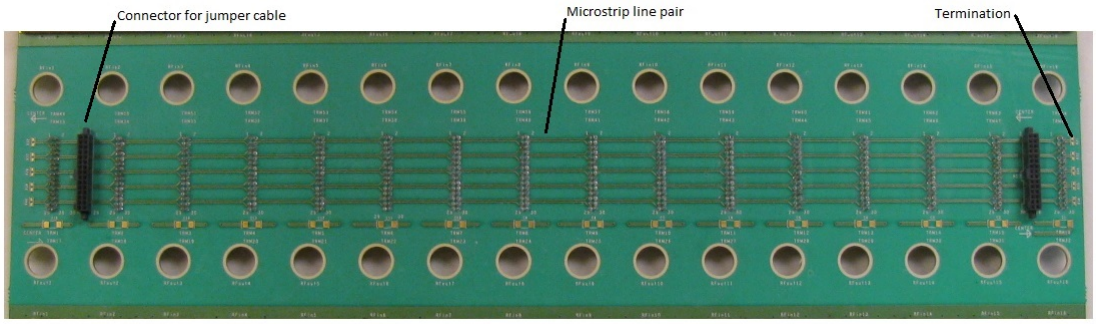

Figure 3.28: Backplane bus layout.

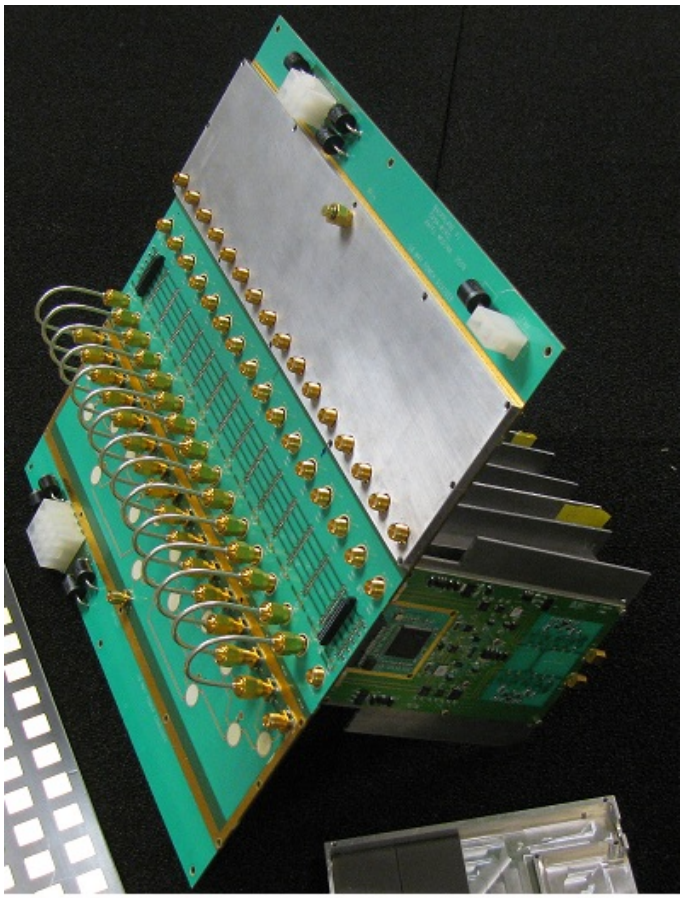

Figure 3.29: Assembled beamformer structure.

3.5.3.3 Measurements

Testing consisted of measuring waveforms on the buses of two fully loaded backplanes connected in cascade with a short ribbon cable. The data were clocked over the backplane at a frequency of 25 Mbps. Single and differential waveforms for the input receiver are shown in Figure 3.30. Measurements were made at the termination resistor. The differential waveform (V) was calculated by the oscilloscope from the non-inverting receiver input waveform (Vp) and inverting receiver input waveform (Vn). The three waveform show a little undershoot or overshoot and small load reflections. The differential waveform have substantial noise margins with respect to the receiver thresholds of ± 10 mV. An eye diagram for the differential waveform is shown in Figure 3.31. The jitter is about 1 nsec while the eye rise time and eye fall time are about 5 nsec.

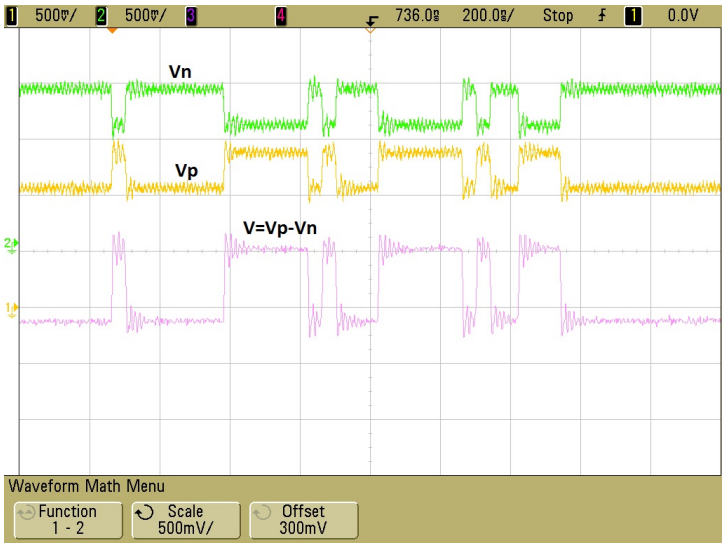

Figure 3.30: Serial data transmission in a backplane at 25 Mbps.

3.6 Beam Steering Control System

3.6.1 Architecture

A phased array with 64 elements, each having a T/R module with 16 control signals (6 bit phase shifter, 6 bit digital attenuator, transmit signal, receive signal, H polarization, and V polarization), require of 16x64= 1024 control signals to switch the beam. Because of the large amount of wiring that must be supplied to all T/R modules, the only practical solution to reduce cost and wiring complexity is to use serial communication. The serial transmission of this amount of data in a short time would require a large bandwidth and the use of well designed high-speed serial interfaces that might increase the system costs. Fortunately, the bandwidth problem can be avoided if a distributed beam steering control system is used. In this type of system, the beam steering computer broadcasts phase gradients (for azimuth and elevation) to all T/R module digital controllers, which generate phase and amplitude settings that are needed to implement the beam [40, 48, 30, 49, 31]. The phase setting is computed from the phase gradient, the element position in the array, and phase correction constant of that particular element. While the amplitude, it is obtained typically from a look up table. An example of phase calculation from phase gradients in the T/R modules is given in [49]. The calculation of a 6-bit phase setting is carried out using a FPGA. The time taken to broadcast a 36 bit phase gradient over 10 Mbps network (3.6 μsec) and to compute

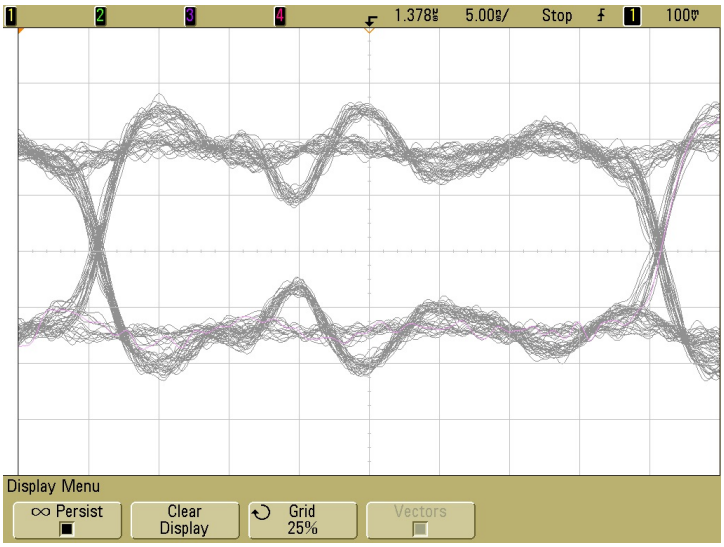

Figure 3.31: Eye diagram for bus LVDS backplane at 25 Mbps.

the phase (2.12 μsec) was about 5.7 μsec. The problems with this implementation are that the phase calculation is performed every transmit and receive pulse, and the computational cost in time to generate each beam might be too large for adaptive short range radars (using alternate polarization and beam multiplexing technique), which require short pulses (i.e. 1 μsec)

Rather than attempting to compute the phase with a digital controller, the BSCS developed in this work uses calibrated look-up tables to translate beam commands into calibrated phase and amplitude settings. The look-up tables are unique for each T/R modules. They store the phase shifter and attenuator states for each scan angle at all operation modes. The advantages of this technique are: 1) The time taken to translate the command into calibrated settings is much lower than the time taken to compute the calibrated setting with a processor, 2) Digital controllers are simpler to design. Figure 3.32 shows a block diagram of the key logic modules developed for the BSCS. The system consists of a network of custom state machines (digital controllers) implemented in the T/R module FPGAs, instead of microprocessor core. State machines have the advantage of responding immediately and in parallel to a large number of timing signals. The system is totally synchronous because a global clock controls all operations. T/R modules are controlled by means of 16-bits

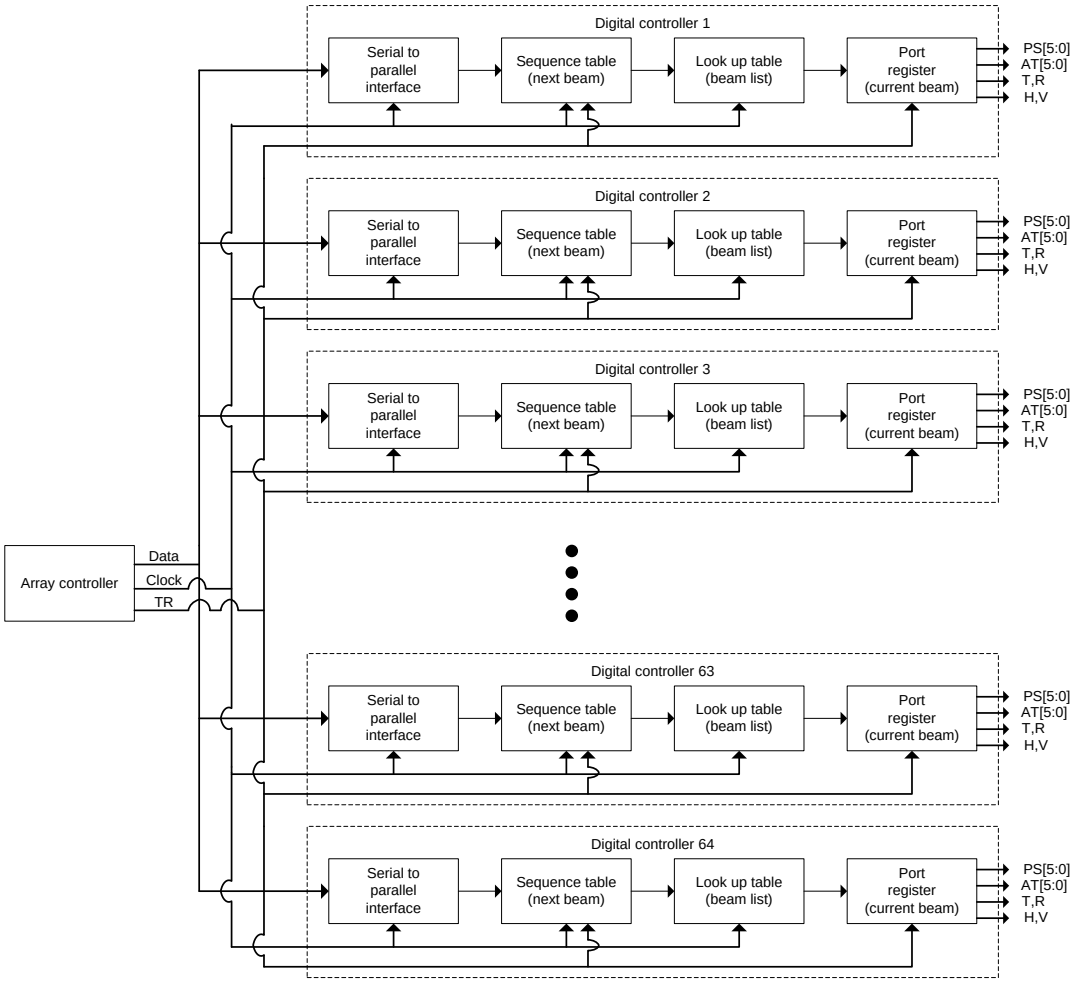

Figure 3.32: Block diagram of the key logic modules used in beam steering control system.

commands and by a TR signal (called "CLK3" signal in the T/R module). The digital controller includes a serial to parallel interface that passes the received commands to a 16 line parallel bus in the FPGA. A programmable sequence table stores the next sequence of beams that must be implemented by the array. A look-up table then translates the beam commands to calibrated settings. A port register stores the settings for the current beam and generates control signals to RF components (attenuator, phase shifter, T/R switches, V/H switch, amplifiers). The beam switching and timing are controlled at the rising edge (transition for low to high level) of the TR signal. This signal also serves as "advance signal", which allows the next beam command can be read from the sequence table.

In order to understand the concept of operation behind the BSCS, let's consider a specific example. Suppose that the radar system is performing dual polarization measurements with the sequence TH, RH, TV, RV, TH, RV, TV, and RH. A timing diagram illustrating this operation mode is shown in Figure 3.33. For the nth scan angle, the array controller generates a serial stream by concatenating 8 beam commands. The beam command includes a bit for array channel (TR), a bit for polarization (HV), and several bits to represent the scan angle as an integer binary number ($beamID$). The relationship between $beamID$ and scan angle is explained in chapter 4 (see equation 4.19). The sequence table for this operation mode is defined in Table 3.5. Four different beams or radiation patterns must be implemented by the beamforming network: two transmit beams (TH and TV) and two receive beams (RH and RV). The serial stream having the sequence table is broadcasted from the array controller to all T/R modules during the dead time between two dwell periods. Each digital controller accepts the commands and stores them in a 8 words (16-bits) memory (sequence table). Once this operation is completed, the read pointer points to the first location of the sequence table, reading the first beam command. The command bits are supplied in parallel to the corresponding input terminals of the look-up table, which translates the beam commands to calibrated settings. The output data returned by the look-up table contains the setting for the next beam including the bits T, R, H, V, PS[5:0], and AT[5:0]. These bits are described in Table 3.6. The data will be hold by the look-up table until the rising edge on the TR signal, at which point the data is latched in the output port. Simultaneously, the read pointer of the sequence table advances one position for each rising edge on the TR signal, reading the next beam command. Therefore, the first pulse on the TR signal allows the transmit beam $b0$ to be implemented, and the same time, it allows the next calibration setting (receive beam $b1$) to be read from the lookup table, as shown in Figure 3.33. When the second pulse on the TR signal arrives, the receive beam $b1$ is implemented and the next calibration settings is read. This procedure is repeated until the last command in the sequence table is read (receive beam $b1$), at this point the read pointer of the sequence table is returned to point to the first location on the sequence table, starting a new loop. The loop will run indefinitely until the sequence table is updated with a new beam sequence.

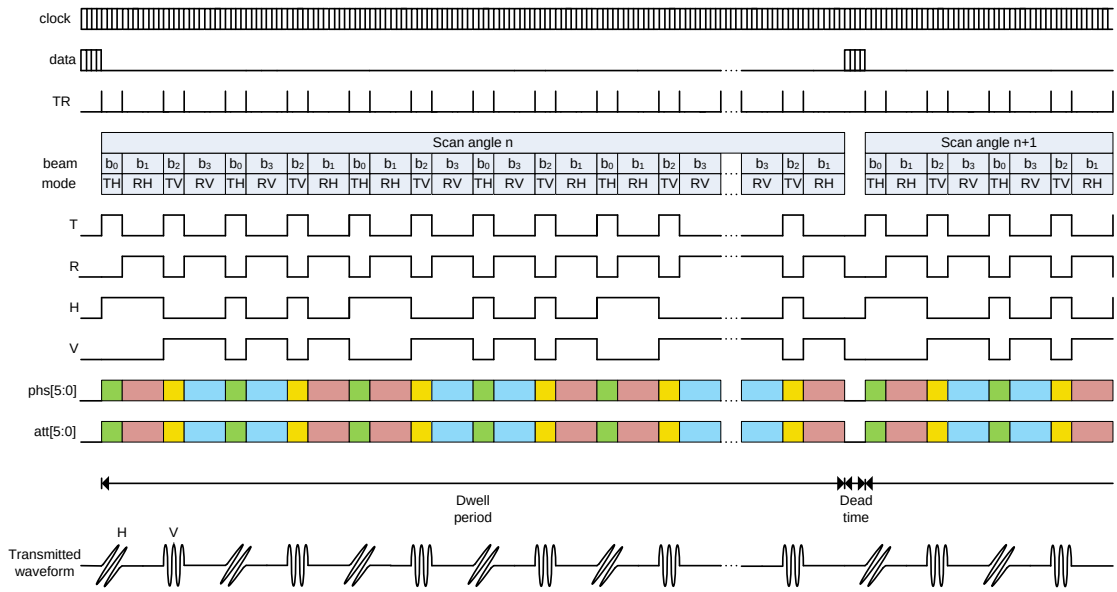

Figure 3.33: Timing diagram of representative command/response sequence.

The communication and control architecture of the beam steering control system has been designed to operate with clock signals up to 100 MHz. However, the clock was fixed to 25 MHz to get a low bit error rate (BER) in the serial communication. At this clock speed, the sequence table is transmitted in the order of 6 μsec. A short-range radar operating in alternate polarization and using 3 kHz PRF with 30 pulses of integration per channel, has a dwell time of 4x30/3000= 40 msec. For this radar, the dead time to update the

Table 3.5: Data structure of sequence table

	Beam command			
sequence	TR	HV	Scan angle	beam index
TH	1	1	beamID	b0
RH	0	1	beamID	b1
TV	1	0	beamID	b2
RV	0	0	beamID	b3
TH	1	1	beamID	b0
RV	0	0	beamID	b3
TV	1	0	beamID	b2
RH	0	1	beamID	b1

Table 3.6: Digital controller interface signals.

Port	Width	Type	Signal	Description
DATA1	2	input	differential	Serial data line input
CLK1	2	input	differential	Serial clock line input
DATA2	2	output	differential	Serial data line output
CLK2	2	output	differential	Serial clock line output
CLK3	2	input	differential	Serial TR line input (TR signal)
RST	1	input	single	Reset line input
T	1	output	single	Transmit channel enable
R	1	output	single	Receive channel enable
H	1	output	single	Horizontal polarization enable
V	1	output	single	Vertical polarization enable
PS	6	output	single	Phase shifter control bits
AT	6	output	single	Attenuator control bits
SDA	1	bidirectional	single	I2C serial data line
SCL	1	output	single	I2C serial clock line

sequence table is about $6/40\text{x}10^3*100 = 0.015\%$ of the dwell period, which denotes a very small fraction of time.

3.6.2 Interfacing Signals

The input and output signals used by the digital controller are defined in table 3.6. The signals DATA1, CLK1, DATA2, CLK2, CLK3, and RST are supplied by the backplane bus (see Figure 3.6). DATA1 and CLK1 are signals generated by the array controller. DATA2 and CLK2 are signals generated by the T/R modules when the array controller request status information. The CLK3 signal (or TR signal) controls the beam switching in the array and controls the signals generated by the output port. The RST signal is generated by the array controlled, when it is set to 1, the state-machines and registers in all T/R module are restarted.

The controller has an output port that generates the signals: T, R, H, V, PS, and AT . These signals control the RF devices in the T/R module (see Figure 3.6)

3.6.3 Serial Communication

The communication system uses a serial data bus and a serial clock bus to transfers data between the digital transmitters and receivers. The transmitter has a parallel-to-serial interface that accepts 16-bit parallel data and then shifts it out bit by bit in an especial

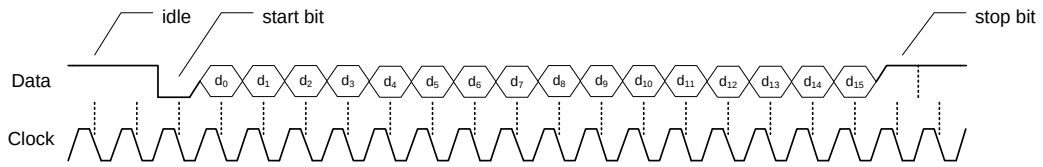

Figure 3.34: Transmission of a 16-bit word.

protocol. The data is transmitted with the least significant bit first. The receiver has a serial-to-parallel interface that accepts serial data and then converts it to 16-bit parallel data. There is one clock pulse for each data bit that is transmitted, see Figure 3.34. The serial data bus is logically high when it is idle. The transmission starts with a start bit, which is 0, followed serially by a 16-bit word, and ends with a stop bit, which is 1. At the receiver, each bit is sampled on the middle of each bit period using the falling edge of the clock signal. A transition on the serial data bus from idle to a low level is interpreted as the beginning of communication.

3.6.4 Digital Command

T/R modules are controlled by means of commands that are based on 16-bit words. There are two types of commands: broadcast and unicast. The broadcast commands control simultaneously all T/R modules using a common command, for example when a new sequence table is loaded. On the contrary, the unicast commands are used to establish a direct point-to-point communication between the array controller and a specific T/R module, allowing the attributes of a particular module can be set or read. The digital controllers accept four unicast commands: write port, write address register, write memory, and read temperature register. The T/R module controller requires a 7-bit address to enable a read or write operation. The first word in unicast, is the addressing commands, which comprises a mandatory one in the most significant bit (this bit in 1 means a uncast communication), followed by 6 reserved bits (all bits are set in 1), a 6-bits module address (AD_5-AD_0), a 2-bits register address (M_1 and M_0), and ends with a write/read select bit in the least significant bit (refer to Table 3.7). The reserved bits can be used to extend the number of T/R module addresses, allowing up to 4096 possible modules. The register address is

defined in Table 3.8. The bit (M_1 and (M_0 are used for addressing the internal registers and memory. The WR select bit set the operation mode, 1 = write and 0 = read.

Table 3.7: First word in unicast command

	First word in unicast command (addressing command)										
	UB bit	Reserved	Module address						Register address		WR bit
bit	b_{15}	$b_{14} : b_9$	b_8	b_7	b_6	b_5	b_4	b_3	b_2	b_1	b_0
value	1	1	AD_5	AD_4	AD_3	AD_2	AD_1	AD_0	M_1	M_0	WR

Table 3.8: Register address

Register address		
M1	M0	Description
0	0	Address register
0	1	Memory
1	0	Port
1	1	Temperature register

3.6.4.1 Unicast Commands

3.6.4.1.1 Write Port. It is possible to update the signals that control the RF components (T, R, H, V, PS[5:0], and AT[5:0]) by writing a 16-bit word in the port register and sending one pulse (during one clock cycle) into the signal CLK3 once write port command has been completed. The word is loaded in the port at the CLK3's rising edge. The write command uses two words, see Table 3.9. The first word is the addressing command and the second word is the binary value to be assigned the port. The bits in the second word are described in Table 3.6. A timing diagram of the serial sequence used to write the port of a T/R module is shown in Figure 3.35. The write port command has been implemented to control individually the T/R module functions during the array calibration. Calibration techniques require typically that only one element can be controlled while all other elements are off.

3.6.4.1.2 Write Memory. The FPGA of each T/R module has a 4096 x 16 bit internal memory that can be used for storing calibration look-up tables. Details regarding the

Table 3.9: Write Port Command.

bit	b_{15}	b_{14}	b_{13}	b_{12}	b_{11}	b_{10}	b_9	b_8	b_7	b_6	b_5	b_4	b_3	b_2	b_1	b_0
1st word	1	1	1	1	1	1	1	A_5	A_4	A_3	A_2	A_1	A_0	1	0	1
2nd word	H	V	T	R	PS_5	PS_4	PS_3	PS_2	PS_1	PS_0	AT_5	AT_4	AT_3	AT_2	AT_1	AT_0

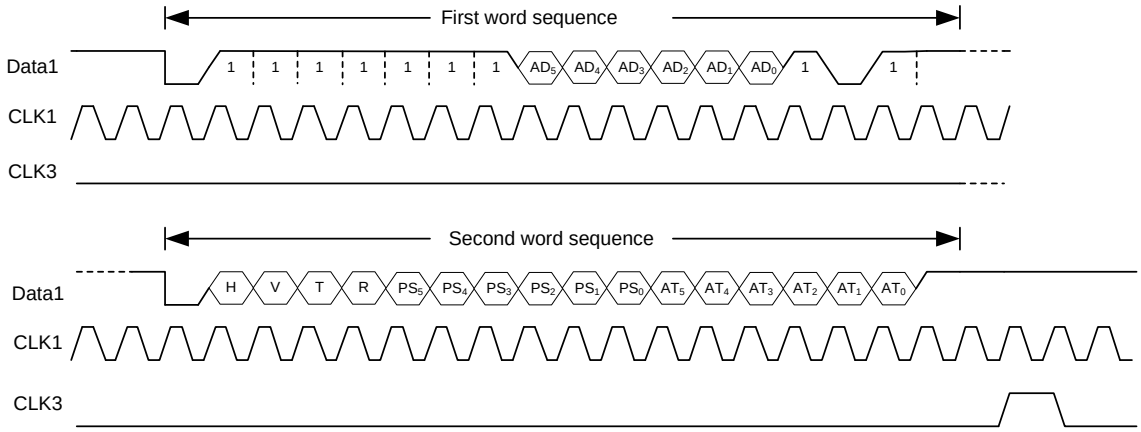

Figure 3.35: Transmission of write port command.

look-up table organization are given in chapter 4. The memory write operation requires an addressing command, followed by a 16-bit word that contains the number of words (N<=4096) to be written in the memory, and a serial stream having the data (N words) to be stored in the memory. The write memory command is defined in Table 3.10. The number of words is represented by a 10-bits command, allowing for 4096 possible values. The data to be stored in the memory contains control bits for the T/R module at different scan angles and operation modes. Once the write operation is complete, the T/R module returns the same data to the array controller. The returned data can be used to detect communication errors. A timing diagram of the serial sequence used to write the controller memory is shown in Figure 3.36 .

3.6.4.1.3 Write Address Register. The internal memory is accessed by commands that are stored in the sequence table or by commands that are stored in an address register. The write address register command allows the memory of each individual T/R module

Table 3.10: Write memory command.

bit	b_{15}	b_{14}	b_{13}	b_{12}	b_{11}	b_{10}	b_9	b_8	b_7	b_6	b_5	b_4	b_3	b_2	b_1	b_0
1st word	1	1	1	1	1	1	1	A_5	A_4	A_3	A_2	A_1	A_0	0	1	1
2nd word	0	0	0	0	0	0	L_9	L_8	L_7	L_6	L_5	L_4	L_3	L_2	L_1	L_0
3rd word	H_0	V_0	T_0	R_0	$PS_0[5:0]$						$AT_0[5:0]$					
(n+3)th word	H_n	V_n	T_n	R_n	$PS_n[5:0]$						$AT_n[5:0]$					
(N+3)th word	H_{N-1}	V_{N-1}	T_{N-1}	R_{N-1}	$PS_{N-1}[5:0]$						$AT_{N-1}[5:0]$					

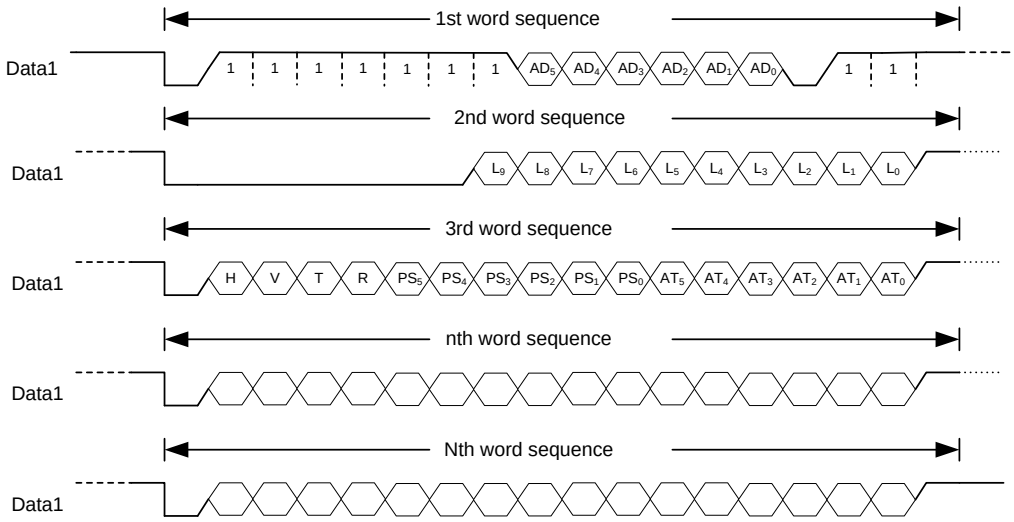

Figure 3.36: Transmission of write memory command.

can be accessed without affecting the status of other T/R modules. To set a calibration setting that is stored in the memory, the write address register command must be sent to T/R module followed by one pulse of the signal CLK3. This pulse is necessary to load the data read from the memory into the output port. The command comprises two words, the first word is the addressing command, and the second word is the memory address to be accessed, see details in Table 3.11. Because the number of memory locations is 4096, the memory address bits (MA_{11}-MA_0) has been limited to 12 bits. Figure 3.37 shows the timing diagram of write operation in the memory address register of a T/R module. Once the write operation is complete, the T/R module returns the same data to the array controller.

Table 3.11: Write address register command.

bit	b_{15}	b_{14}	b_{13}	b_{12}	b_{11}	b_{10}	b_9	b_8	b_7	b_6	b_5	b_4	b_3	b_2	b_1	b_0
1st word	1	1	1	1	1	1	1	A_5	A_4	A_3	A_2	A_1	A_0	0	0	1
2nd word	0	0	0	0	MA_{11}	MA_{10}	MA_9	MA_8	MA_7	MA_6	MA_5	MA_4	MA_3	MA_2	MA_1	MA_0

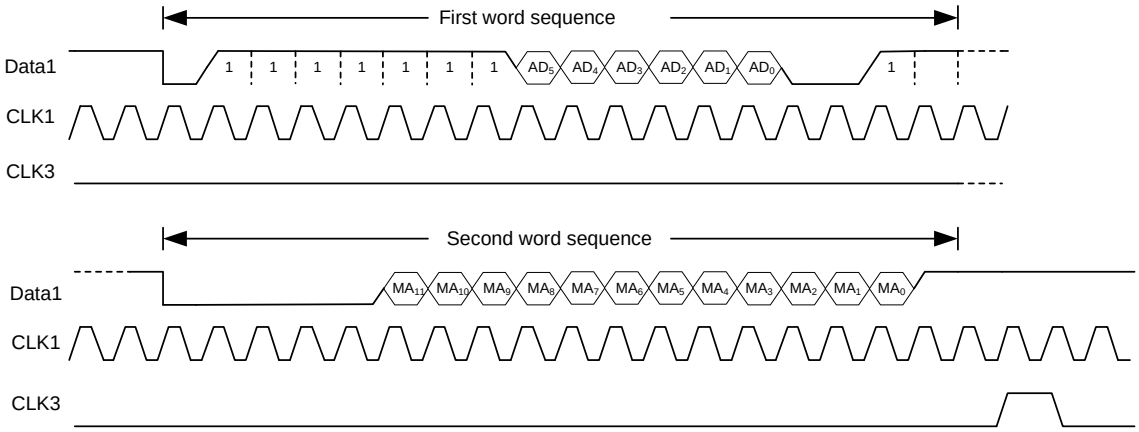

Figure 3.37: Transmission of write address register command.

3.6.4.1.4 Read Temperature Register. T/R modules have a temperature register that continuously is updated with real-time information from a temperature sensor installed in the T/R module. This register can be read by means of the read temperature command. The read operation starts with a 16-bit command word that is sent from the array controller throughout the serial lines DATA1 and CLK1. Once this operation is completed, the T/R module returns back two command words throughout the serial DATA2 and CLK2. The serial stream includes the addressing command sent originally by the array controller and a word having the 8-bits temperature data. The read temperature command is defined in Table 3.12. A timing diagram of the serial sequence used to read the temperature register from a T/R module is shown in Figure 3.38. Note that the serial lines DATA1 and CLK1 transmit a single word and thatthe serial lines DATA2 and CLK2 transmits two words.

Table 3.12: Read temperature register.

bit	b_{15}	b_{14}	b_{13}	b_{12}	b_{11}	b_{10}	b_9	b_8	b_7	b_6	b_5	b_4	b_3	b_2	b_1	b_0
1st word	1	1	1	1	1	1	1	A_5	A_4	A_3	A_2	A_1	A_0	1	1	0
2nd word	0	0	0	0	0	0	0	0	T_7	T_6	T_5	T_4	T_3	T_2	T_1	T_0

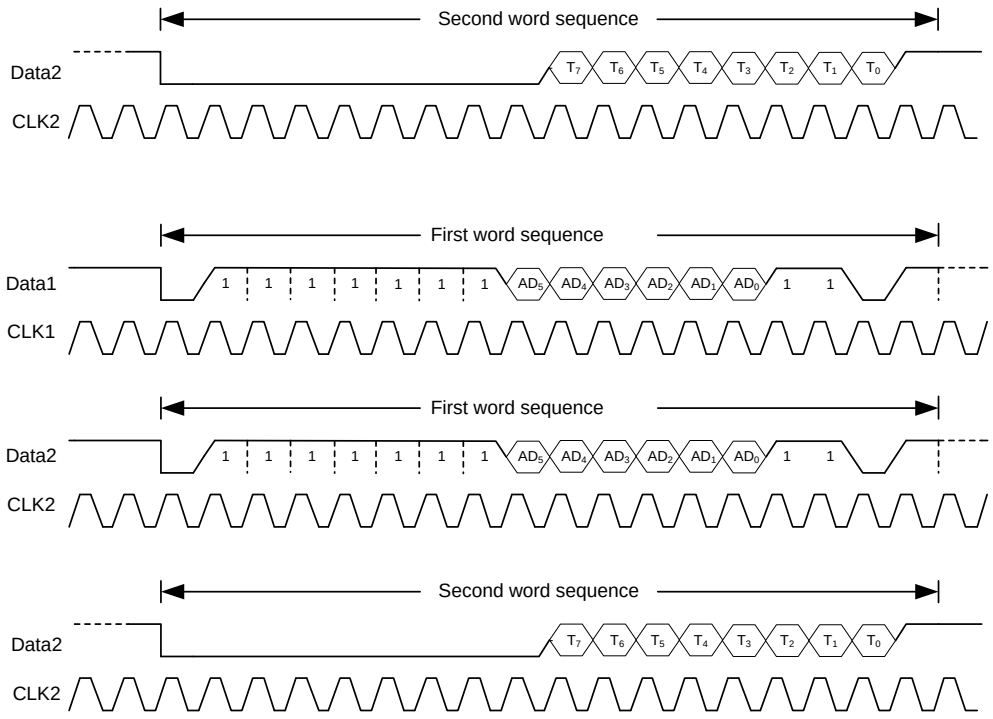

Figure 3.38: Transmission of read temperature command.

3.6.4.2 Broadcast Command

3.6.4.2.1 Write Sequence Table. The sequence table stores the list of beams that the array must implement for a time interval. The beam sequence comprises 8 states: 4 transmit states and 4 receive states. Two consecutive states, including a transmit state and a receive state, is called a cycle. The write sequence table command comprise 9 words, see Table 3.13. Note the most significant bit of each word starts in 0; this indicates that a broadcast command has been sent from the array controller. The first 8 words contain the beam commands to be implemented by the array, and the last word defines the number of pulses per cycles (L) in a sequence. The beam commands are formatted as memory

Table 3.13: Write sequence table.

bit	b_{15}	b_{14}	b_{13}	b_{12}	b_{11}	b_{10}	b_9	b_8	b_7	b_6	b_5	b_4	b_3	b_2	b_1	b_0
1st word	0	0	0	0	$MA_0[11:0]$											
2nd word	0	0	0	0	$MA_1[11:0]$											
3rd word	0	0	0	0	$MA_2[11:0]$											
nth word	0	0	0	0	$MA_{n-1}[11:0]$											
8th word	0	0	0	0	$MA_7[11:0]$											
9th word	0	0	0	0	0	0	0	0	L_7	L_6	L_5	L_4	L_3	L_2	L_1	L_0

address bits (MA_{11}-MA_0), which indicate the physical location of a calibration setting in the look-up table. The number of pulses per cycle is 8-bits wide allowing for 256 possible pulses. Depending on how the sequence table and number of pulses per cycle is defined, different pulsing schemes can obtained. Some examples of pulsing schemes are indicated in Tables 3.14 - 3.19. The phased array can be configured to operate using single polarization (HH or VV or HV or VH), dual polarization (HH and VV, or HH and HV, or VV and VH), and quad-polarization (HH, VV, HV, and VH). Where HH is the horizontally polarized transmitted energy and horizontally polarized received energy, VV is the vertically polarized transmitted energy and vertically polarized received energy, HV is the horizontally polarized transmitted energy and vertically polarized received energy, and VH is the vertically polarized transmitted energy and horizontally polarized received energy.

Figure 3.39 shows the timing diagram of write operation for the sequence table. Once the sequence table is written, the CLK3 rising-edge must sent to set the new calibration settings for the next beam in the output ports (see also Figure 3.33). CLK3 signal causes the modules to toggles between transmit and receive states.

Table 3.14: Sequence table for Single polarization.

State	T/R	H/V	Beam	pulses/cycle
1	T	H	beamID	1
2	R	H	beamID	
3	T	H	beamID	1
4	R	H	beamID	
5	T	H	beamID	1
6	R	H	beamID	
7	T	H	beamID	1
8	R	H	beamID	

Table 3.15: Sequence table for dual pol - dual PRT.

State	T/R	H/V	Beam	pulses/cycle
1	T	H	beamID	1
2	R	H	beamID	
3	T	H	beamID	1
4	R	H	beamID	
5	T	V	beamID	1
6	R	V	beamID	
7	T	V	beamID	1
8	R	V	beamID	

Table 3.16: Sequence table for dual pol - dual PRF

State	T/R	H/V	Beam	pulses/cycle
1	T	H	beamID	n_{f1}
2	R	H	beamID	
3	T	H	beamID	n_{f2}
4	R	H	beamID	
5	T	V	beamID	n_{f1}
6	R	V	beamID	
7	T	V	beamID	n_{f2}
8	R	V	beamID	

Table 3.17: Sequence table for fully polarimetric- single PRT (alternate pulse)

State	T/R	H/V	Beam	pulses/cycle
1	T	H	beamID	1
2	R	H	beamID	
3	T	H	beamID	1
4	R	V	beamID	
5	T	V	beamID	1
6	R	H	beamID	
7	T	V	beamID	1
8	R	V	beamID	

Table 3.18: Sequence table for fully polarimetric -alternate dwell

State	T/R	H/V	Beam	pulses/cycle
1	T	H	beamID	n
2	R	H	beamID	
3	T	H	beamID	n
4	R	V	beamID	
5	T	V	beamID	n
6	R	H	beamID	
7	T	V	beamID	n
8	R	V	beamID	

Table 3.19: Sequence table for single polarization - beam multiplexing

State	T/R	H/V	Beam	pulses/cycle
1	T	H	beamID0	n
2	R	H	beamID0	
3	T	H	beamID1	n
4	R	H	beamID1	
5	T	H	beamID2	n
6	R	H	beamID2	
7	T	H	beamID3	n
8	R	H	beamID3	

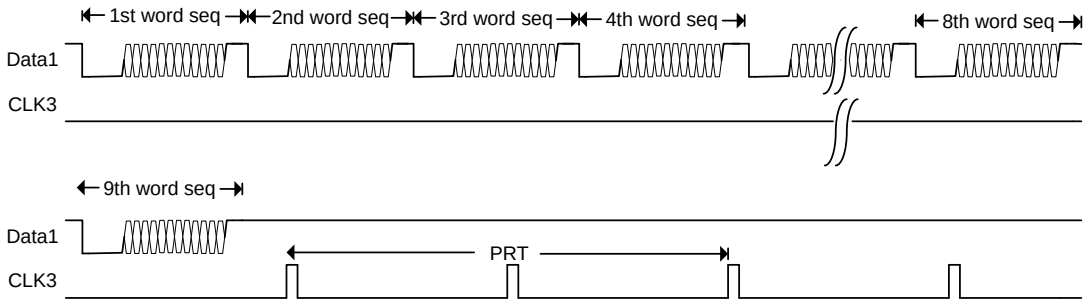

Figure 3.39: Transmission of sequence table.

3.6.4.3 T/R Module Digital Controller

The conceptual block diagram of the T/R module digital controller is shown in Figure 3.40. It consists of six major components: serial interface, command controller, sequence table, sequence counter, lookup table, and I2C interface. All other blocks are used for storing temporary values or for interfacing. The controller is implemented in a Xilinx Spartan-3E XC3S100E FPGA using the Verilog language.

3.6.4.3.1 Serial Interface. The serial interface comprises of a receiver and a transmitter. The receiver receives serial data (DATA1) and serial clock (CLK1) from two LVDS input buffers, which convert from differential to single end signaling. A serial-to-parallel shift register is used to convert the serial data to 16-bit parallel data. The receiver stores the recovered word in a 16-bit buffer and generate a flag signal that indicates when a word has been received. The transmitter is implemented with a parallel-serial shift register. The serial output data is sent to a LVDS output buffer, which converts the signal from single-

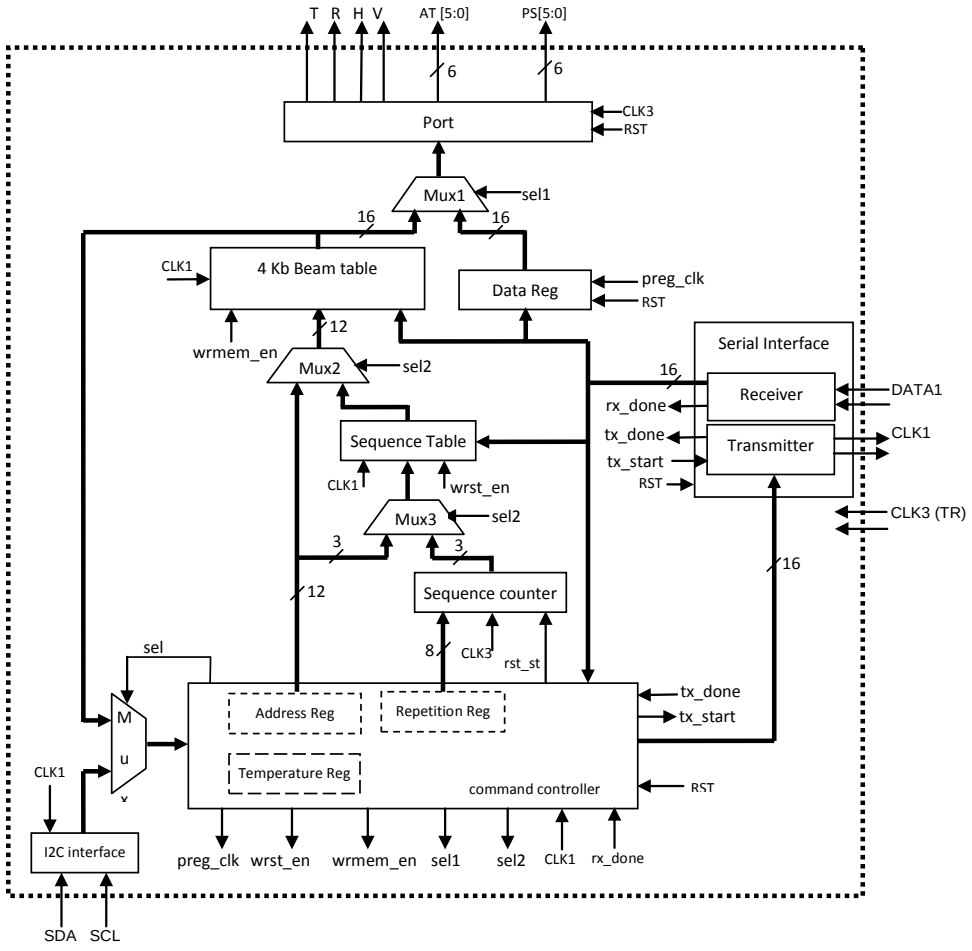

Figure 3.40: Internal structure of the digital controller core.

ended to differential signaling. The flow charts for the serial receiver and serial transmitter interface are shown in Figure 3.41.

3.6.4.3.2 Command Controller. The command controller handles the data traffic between the array controller and various registers and memory tables in the T/R module controller. It reads the data from the serial interface, and based upon clocking and received commands, the command controller generates control signals for controlling the operation of the lookup table, sequence table, port register, memory address register, and temperature register. The flow chart for the command controller is shown in Figure 3.42. When the controller receives unicast commands, it decodes the T/R module address from the

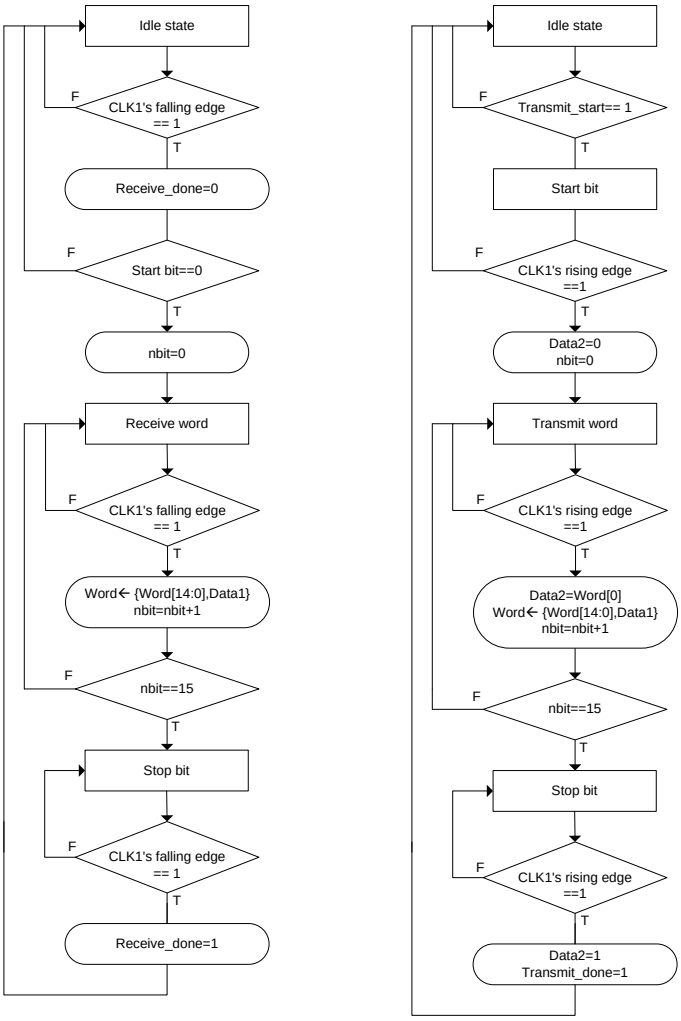

Figure 3.41: Serial receiver and transmit interface flow chart.

addressing command and compare it to the one saved in a local register. If addresses are different, the next command words are omitted. Otherwise, the local controller accepts the next command words, addressing the data to a register or a memory table according the decoded register address bits (M1 and M0, see table 4). Depending on these bits, different operations can be realized:

- If a command of write port is accepted, the command controller generates the $preg\_clk$ signal to stores the 2nd word in a temporal register (Data register), see Figure 3.40. It also sets the selection signal ($sel1$) of the multiplexer $MUX1$, allowing the output port to route the values from the temporal register. The data is passed to the port

register when the CLK3's rising edge arrives. Once the write operation in the output port is completed, the controller sends the addressing command and port data to the serial transmitter, which transmits them back to the array controller.

- If a command of write memory is accepted, the command controller sets the selection signal ($sel2$) of the multiplexer $MUX2$ controlling the memory address bus to route the values from the address register. It also sets the selection signal ($sel1$) of the multiplexer $MUX1$ controlling the output port to route the values from the memory output lines. For the first memory word, the address register is set to point to 0. Then, for each received word, the command controller generates the $wrmem\_en$ signal (write memory enable) to write the words in the memory; subsequently, it increases the address register by 1. Once the write operation in the memory is completed, the controller sends sequentially the addressing command, memory data length, and memory data to the serial transmitter, which transmits them to the array controller.
- If a command of write address register is accepted, the command controller stores the 2nd word in the address register. It also generates the $sel1$ signal and $sel2$ signal to read the memory from the address register and route the memory output data to the input of the port register. Then, it sends the address command and address register data to the serial transmitter to transmit them back to the array controller.
- If a command of read temperature is accepted, the command controller reads the temperature register from the I2C controller, which periodically updates the temperature value from a external sensor using the SDA line and SCL line. The temperature registers is 8-bit wide. Once the temperature read operation is completed, the controller sends the addressing command and temperature value (formatted in a 16-bit word) to the serial transmitter to respond to the request from the array controller.

On the other hand, when the command controller receives a broadcast commands, which is write sequence table, it sets the address register to zero and sets the selection signal ($sel2$) of the multiplexer $MUX3$ that controls the addresses bus of the sequence table memory to route the values from the address register. Then, for each beam command word that is received, the command controller generates a pulse of the $wrst\_en$ signal (write sequence

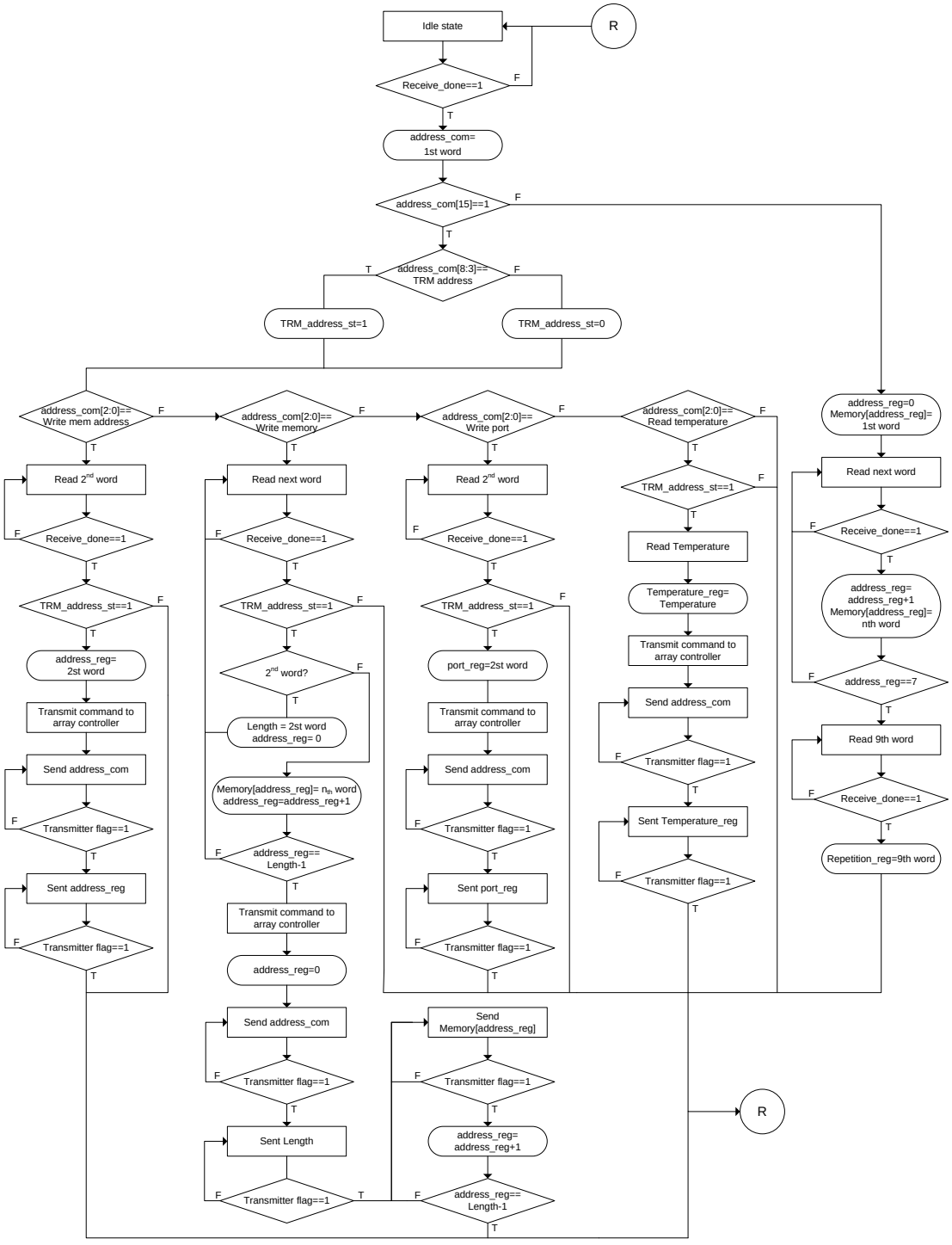

Figure 3.42: Command controller flow chart.

table enable) to write the words in the sequence table memory while the address register is incremented by 1. The 9th command word (last command word) is stored in the repetition register. Once the write operation is completed, the controller resets the sequence counter to zero, subsequently it generates the $sel2$ signals to switch the control of the sequence table to a sequence counter, and generates the $sel1$ signal to pass the data from the look-up table to the port.

3.6.4.3.3 Sequence Table and Sequence Counter. The sequence table is implemented in a 8 x 16 bit memory which is used to store beam commands. Its output lines control the addressing of the calibration look-up table. The sequence table address bus is controlled initially by the address register during writing operation, but each time this operation is completed, the control is passed to the sequence counter. A repetition register determines how the sequence counter is operated, using single or double loop. When the repetition registers is 1, the counter operates as a single loop, the count start at 0 and increases monotonically to 7 and wraps around, each increments is controlled by the CL3's rising edge. When the repetition register is set to the binary number n (for $n_{10}<256$), the counter operates as a double loop, it counts from 0 to 1 and wrap around n times, each increment is controlled by the CL3's rising edge. Then, the counter passes to counts from 2 to 3 and wrap around n times. Same procedure is repeated by numbers 4-5 and 6-7. Once the cycle has been completed, the counter is returned to zero and the process is repeated indefinitely.

3.6.4.3.4 Look-up Table. The look-up table is based on a 4096 x 16 bit random access memory (RAM). The memory stores calibration settings as a function of the memory address, which in turn, is also a function of scan angle (beamID), channel bit (TH), and polarization bit (VH), see chapter 4 for more details. Tables are pre-calculated and stored in the radar computer after the array calibration. Then they are stored in the memory during the radar initialization phase. The data read from memory is controlled by means of beam commands that are supplied by the address register (when an memory address command is used) or by the sequence table (when the write sequence table command is used).

The resulting output data is sent for storing to the port register throughout of multiplexer $Mux1$.

3.6.4.3.5 I2C Interface. The T/R module has a low cost digital temperature sensor (TC74) that can provide temperature measurements in the range of -40^{o}C to +125 ^{o}C using 8-bit digital words. The sensor is a two-wire serial output devices that is compatible with I2C interface. In order to communicate with this sensor, the T/R module controller has implemented an open core I2C interface [50]. Communication between devices is realized at 100 Kbps using the serial data line (SDA) and serial clock line (SCL). All transfers take place under the control of the T/R module controller, acting as the Master, while the TC74 always operates as a slave. The interface also includes and I2C controller, which generates the commands to access and to read the digital sensor. The controller is programmed to read the sensor's temperature each second. Measurements are stored in a 16-bit temperature register, which outputs are connected to command controller.

3.6.5 System Integration and Test.

After measuring each individual component of the array, the four LRUs were assembled and tested individually to check out electrical operation and communication. The communication test was performed with the LRU connected to the array controller. A computer was used to generate random unicast commands that were sent to T/R modules. The returned commands from T/R modules were then compared with the original commands to check out the bit error rate and to verify the bus backplane operation. After passing the communication test, the electrical performance of each LRU was measured to verify interconnection between corporate feeds and T/R modules. Then the array was built to check out the design concepts and calibration. Figure 3.43 shows a photograph of the beamformer network assembled in the array.

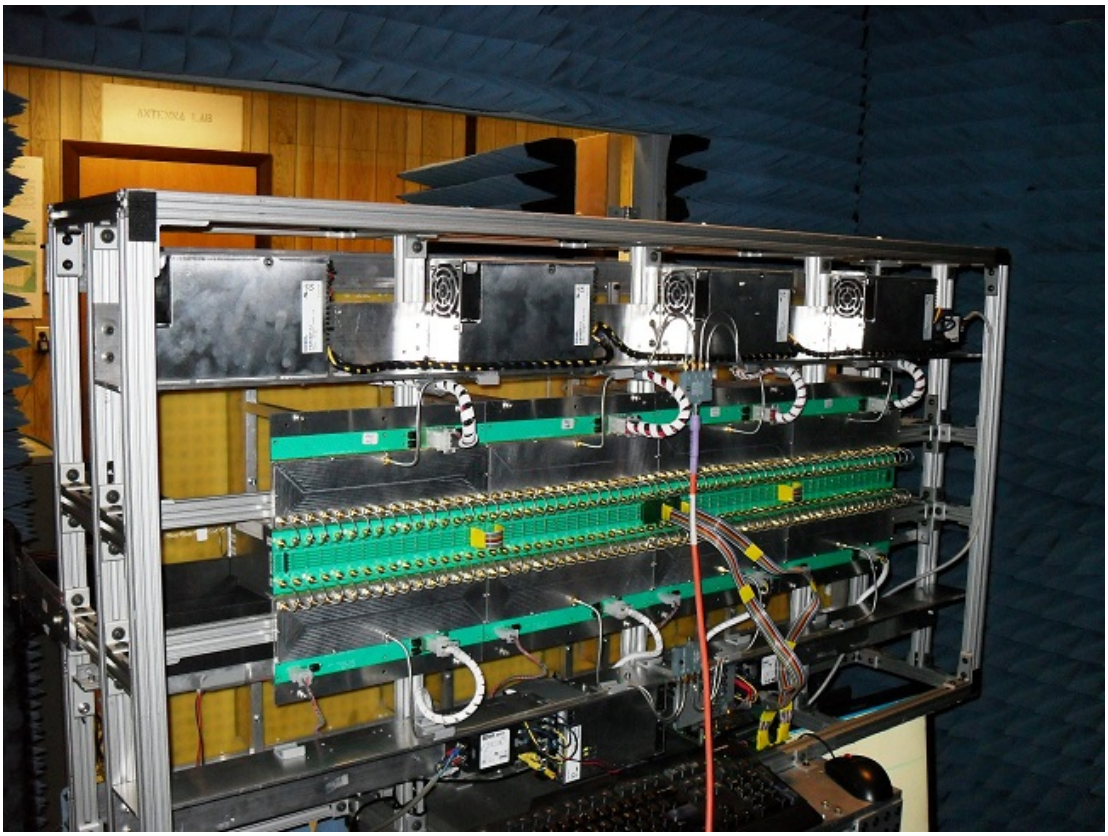

Figure 3.43: Photo of the beamformer network mounted in the antenna frame.

CHAPTER 4

ARRAY CALIBRATION

4.1 Introduction

Active phased array antennas are usually complex systems that are composed of a large number of electronically controlled radiating elements. Beams are formed by adjusting the amplitude and phase of the signal emitted (or received) from each radiating element, and by coherently adding the corresponding signals of each element in the desired direction. To achieve the desired shape and direction of the beam, the electrical differences in the paths of RF signals that feed the radiating elements must be calibrated before applying the amplitude and phase settings. Electrical differences are originated by natural variances in the T/R modules, cables, RF manifold, etc. The procedure used to compensate these differences is known as array alignment or calibration. While the details of this procedure vary from system to system, the main goal is the same, to find the proper element calibration settings that both compensate the hardware differences and implement the desired excitation function. There are different techniques to find what the element calibration settings should be, depending on the application and the characteristic of the array. The most common and simple technique is the one based on measurements of the radiation pattern at broadside of each radiating element [10, 51, 52, 53]. Measurements are made by placing a near-field probe in front of each element while other elements terminated in matched load. Resulting data is used to determine the radiated offset vector, which represents the inherent disparity in the amplitude and phase between elements. These offset vectors are then used to equalize the amplitude and phase of element patterns without altering the element patterns shape.

There are also techniques to compensate the element pattern differences at all angular positions from variations caused by mutual coupling and edge diffraction effects [54, 55]. These techniques require full measurement of radiation patterns from all elements. Patterns are then used to extract calibration coefficients that cancel out the mutual coupling and

edge diffraction effect. The advantage of this method is that theoretical patterns with ultra low sidelobes and deep nulls can be achieved. Drawbacks are that high resolution attenuators and phased shifters are needed; it is difficult to implement in a large array because of the number of measurements; and it requires large far field range facilities with special algorithms to extract the calibration coefficients.

All of above techniques are restricted to arrays whose elements can be examined individually, in other words, arrays that have the ability to individually turn on and off each element. This property increases the isolation between the element under test and inactive elements, minimizing the errors due to radiation effects from other elements. In contrast, arrays whose elements are simultaneously turned on and off, need special techniques to measure each individual element. The most relevant technique in this category is the rotation element field vector (REV) method [56]. In this method, the relative amplitude and phase of each element are obtained from absolute power measurements. To obtain these values, the phase shifter in the element under test is stepped through all its states, while phase shifters in the inactive elements are held in the same state. In this fashion, the measured power as a function of the phase shifter states describes a sinusoidal behavior. The complex gain is obtained from three parameters of this sinusoidal function: the maximum power, the minimum power, and the phase shift corresponding to the maximum power. The main disadvantage of this method is that it is time consuming; many measurements must be made to obtain the amplitude and phase of a single element.

Another aspect related with the calibration of phased arrays is the element characterization, which is a procedure that consists in measuring the amplitudes and phases of each element as a function of attenuator and phase shifter states. Characterization is important because attenuators and phase shifters are nonlinear components, and measurements allows to know the existing relationship between the commanded states and implemented amplitude and phase of an radiating element. For analog devices, this relationship is found by fitting the data in curves. Models are used to create calibrated states that are later stored in memory look-up tables at the T/R modules [53, 54]. Because the characterization and modeling of analog components are consuming processes for large arrays, digital attenuator and phased shifter are preferred component to build phased arrays. Digital devices present

a better response between the commanded state and implemented state, making them easy to use. However, they are not perfect components and need some level of calibration to achieve low excitation errors. For example, attenuators and phase shifters have an insertion phase and insertion loss, respectively, that changes with the commanded state. For that reason, characterization is still need for correcting these shifts.

Typically, element characterization is performed in planar near-field antenna test facility. During this process, a sampling probe is positioned in front of each radiating element, with only that element enabled in either transmit or receive. The amplitude and phase is measured through all attenuator and phase shifter states that can be controlled from a T/R module [38]. After characterization, the data is calibrated to correct for component variances, insertion loss and insertion phase shift that are naturally created by phase shifters and attenuators, respectively. The calibrated data is then stored into memory-based look-up tables in the T/R modules [25, 57, 58]. Look-up tables translate the ideal commands sent from the beam steering computer into corrected commands. Disadvantages of this procedure are: the unacceptable time that is needed to measure the whole array, and calibrated settings do not provide the most optimal weights for implementing excitation functions with low RMS errors. It is known that excitation errors are theoretically limited by the quantization errors. It will be shown in this chapter that the quantization errors due to the attenuator and phase shifter are increased by the variance of the insertion loss and insertion phase of these components, limiting the possibility of reaching RMS errors close to the theoretical minimum value and getting a best array performance. Calibration is necessary because it reduces the array errors, which in turn, leads to the implementation of radiation patterns with very low sidelobes. The smaller the array errors, closer the implemented radiation pattern to the theoretical pattern will be.

This chapter develops mathematically and demonstrates experimentally a calibration method that takes advantage of the variance in the amplitude and phase characteristics of T/R modules to implement the desired excitation coefficients with low RMS errors. The goal is to reach quantization errors close or better than the theoretical minimum value. These low errors are important in small and medium size phased array radar to achieve very low sidelobe levels. The proposed method is used in the calibration of a linear phased

array testbed. The procedures to calibrate the transmit array operating in compression and receive array using a taper illumination are described. It is shown that after calibrating, it is possible to predict the radiation pattern and scanning performance. Additionally, the method is modified to make it more robust and allow the calibration of phased array antennas at different temperatures. In particular, it is described how the two-way antenna gain drift due to the temperature variation can be corrected. This method overcomes the difficulties of correcting the gain drift in transmit arrays operating in compression. The evaluation of the relevant features of the phased array testbed such as beam pointing error, beamwidth, peak sidelobes, scanned gain, active element pattern is presented.

4.2 Theory

4.2.1 Array Alignment

It is known from array theory, that the radiation pattern characteristics of an uniformly spaced antenna array can directly be synthesized by selecting properly the excitation of its radiating elements. Sidelobe level, null position, or beamwidth are some input parameters used to design the array excitation. Theoretically, the far-field radiation pattern is expressed as the product of a common element pattern multiplied by an array factor. While in an ideal array, the element patterns are considered to be the same, in real arrays, the element patterns differ from each other because its environment. Effects as mutual coupling, edge diffraction, mismatch, and variations in elements themselves, affect the embedded element radiation patterns from their original patterns (i.e. isolated pattern). An embedded element pattern is the radiation pattern obtained when a single element is driven and the surrounding elements are terminated in the generator impedance. For a N-elements linear array, the exact computation of its radiation pattern can be expressed as [59]

$$f_a(\theta,\phi) = \sum_{n=1}^{N} f_n(\theta,\phi) v_n e^{jk\widehat{r}.\widehat{r_n}} \tag{4.1}$$

where $f_n(\theta,\phi)$ is the far-field embedded element pattern, v_n is the complex excitation coefficient (or illumination) for the nth element, k is the free-space propagation constant, $\widehat{r}$ is the unit radial vector from the coordinate origin in the observation direction, and $\widehat{r_n}$, is a

position vector from the origin to the center of the nth element. For a large uniform array, where the number of inner elements is much greater than the number of edge elements, it is reasonable to assume that element radiation patterns are alike because they see an identical environment. This assumption allows the definition of an array element factor that accounts for the all varying effects in the array, which is called average embedded element pattern or average active element pattern, $f_{av}(\theta, \phi)$. Using this term, the overall array radiation pattern (4.1) can be written as [59]

$$f_a(\theta, \phi) = f_{av}(\theta, \phi) \sum_{n=1}^{N} v_n e^{jk\widehat{r}.\widehat{r_n}} \tag{4.2}$$

This expression corresponds with concept of principle of pattern multiplication used in array theory [60]. All calibration needs to do is to compensate for hardware imperfections in the elements and permit the desired excitation coefficients v_n to be implemented.

In order to carry out the array calibration, a set of vector offsets or calibration coefficients that describe the disparity of amplitudes and phases among elements need to be determined from measurements of the system. The introduction outlined the conventional technique to perform this calibration, which consists in measuring the transfer function of each element separately by using an external near-field antenna (NF probe) placed in front of the element under test. This can be seen in the example of a linear array depicted in Figure 4.1. It is assumed here that the probe is linearly polarized and that both array and probe are connected to a vector network analyzer, having their input impedances perfectly matched to the characteristic impedance of the system. The gain or insertion loss of each element is measured using the scattering parameter S_{21} (forward transmission), which is the voltage transfer function between the array and reference NF probe. Depending on the array configuration, separate transmit and receive parameters may have to be determined.

Let's consider that the nth element is driven by the excitation and other elements are terminated in matched load. The measured transfer function can be considered to be made up of a T/R module normalized complex gain, $W_n(att, phs)$, which depends on the attenuator and phase shifter states, att and phs respectively; the combined effects of RF manifold, RF cables, connectors, radiating element, and the T/R module gain when the

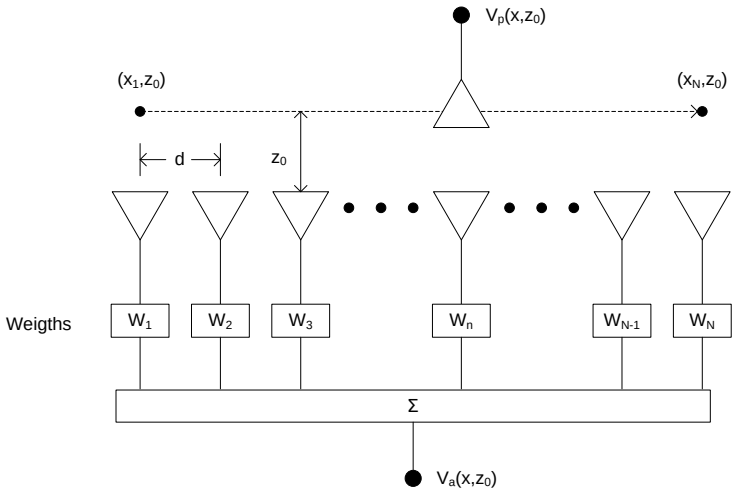

Figure 4.1: Array calibration performed with a near field probe measurement system.

attenuator and phase shifter are set to its digital reference, or the state zero, denoted by the complex quantities u_n; and the free space coupling between the radiating element and sensing probe, denoted by C_n. Thus, the measured transfer function can be expressed as

$$S_{21}^{q}(n, att, phs) = C_n u_n^q W_n^q(att, phs) \tag{4.3}$$

where the superscript q denotes the operation mode on the driven element. For single polarization, q = R (receive) or T (transmit). If the array elements are designed with horizontal (H) and vertical polarization(V), then q denotes any four modes: RH, RV, TH and TH. For a large array, it can be assumed that the free space coupling between the radiating elements and probe is identical and that it does not vary with the probe position, that is, $C_1 = C_3 = C_3 = ... = C_n = C$. In addition, it is defined that the normalized gain, with the attenuator and phase shifter in the state zero, is $W_n(0,0) = 1$. Hardware differences between array elements can be observed when all modules are set to state zero, on this case (4.3) reduces to

$$S_{21}^{q}(n, 0, 0) = C u_n^q \tag{4.4}$$

It is immediately noticed that the measured transfer functions will not be similar if there are hardware differences in the RF path of each radiating element, that is, $u_1^q \neq u_2^q \neq$

$u_2^q ... \neq ... u_N^q$. These random variations must be compensated with the attenuators and phase shifters such that the desired excitation can be implemented. Since the calibration is simply a matter of making S_{21} the same for all radiating elements, it is desirable to adjust the amplitudes and phases of all array elements with respect to the element that presents the lowest transfer function in the array in state zero, which is denoted by the index n_{ref}. This assumption theoretically allows the implementation of excitation coefficients with zero random errors. Subsequently, the relative errors between the elements n and n_{ref} is computed as follow

$$K^q(n_{ref}, n) = \frac{S_{21}^q(n_{ref}, 0, 0)}{S_{21}^q(n, 0, 0)} = \frac{u_{n_{ref}}^q}{u_n^q} \tag{4.5}$$

The quantity $K^q(n_{ref}, n)$ is the vector offset between the elements n and n_{ref}. This vector, when used as complex multiplier, make the complex gain of the element n looks like the complex gain in the element n_{ref}. Consequently, consider the vector offset has been determined by the above method, and desired array excitation for the nth element is given by the complex coefficient v_n. To implement the excitation function and correct for hardware differences between elements, the attenuator and phase shifter have to be set to some state att and phs such that

$$W_n^q(att, phs) = K^q(n_{ref}, n) v_n^q \tag{4.6}$$

Note that magnitude and phase of $W_n^q(att, phs)$ corresponds to the insertion loss and insertion phase that need to be set by the attenuator and phase shifter to achieve the desired excitation. To carry out the calibration in conventional arrays, both amplitude and phase offsets are stored in tables for use by the array control computer. Details about the implementation of this calibration can vary from system to system, but the concept is the same in all of them, the array control computer computes the phase steering commands for each element and adds the phase offsets stored in the calibration table to the phase commands that are sent to T/R modules. Analogically, attenuator commands are generated from the amplitude offsets and excitation coefficients that are stored in look-up tables. One

example of computation of required states for the attenuators and phase shifters is given in [22]. In it, the phase shifter states for the nth element is computed as follow

$$phs(n) = mod\big(\frac{\Delta P(n) + round(n\Psi)}{LSB_p}, 2^p\big) \tag{4.7}$$

where $\Delta P(n)$ is the phase offset in degrees, LSB_p is the phase shifter Least Significant Bit in degrees, p is the number of bits of the phase shifter,

$$\Psi = \frac{180}{\lambda_0} d.sin(\theta_0) \tag{4.8}$$

is the phase increment in degrees between elements, d is the spacing between elements, θ_0 is the desired beam steering angle, and λ_0 is the wavelength. While the attenuator states for the nth element is computed as follow

$$\begin{aligned} att(n) &= -round\big\{\frac{\Delta A(n) + A(n)}{LSB_a}\big\} \\ att(n) &= att(n) - min(att(n)) \end{aligned} \tag{4.9}$$

where $\Delta A(n) = 20log10(|W_n^q(att, phs)|)$, is the amplitude offset in dB, $A(n) = 20log10(|v_n^q|)$, is the excitation coefficient in dB , and LSB_a is the attenuator Least Significant Bit in dB.

4.2.2 Element Calibration

Unfortunately, conventional attenuators and phase shifters have electrical characteristics that deviate from those of the ideal components. Unless these deviations are compensated, the implemented excitation function will not be optimal because of the random errors, decreasing the ability to create patterns with very low sidelobes. In fact, the states obtained from (4.7) and (4.9) are raw states that should not be directly applied to phase shifters and attenuators to avoid high quantization errors. In practice, active elements are characterized through all attenuator and phase shifter states, then the data is processed to remove the deviations between ideal and measured states [38, 51]. In active arrays using analog attenuators and phase shifters, the characterization is important because these components are

typically nonlinear; and it is necessary to know the existing relationship between the raw states and implemented states of elements. In this case, the relationship is found by fitting the data in curves. Then, these curves are used to create calibrated states that are later stored in memory look-up tables at the T/R modules [61, 53].

On the other hand, digital attenuators and phased shifters are preferred component to build phased arrays. Digital devices present a better response between raw states and implemented states, making them easy to use. However, because they are not perfect components, they need some level of calibration if one wants to achieve low excitation errors. For example, attenuators have an insertion phase characteristic and attenuation bit error that change with attenuation states. Similarly, phase shifters have an insertion loss characteristic and phase bit error that change with phase states. Examples of these variations from a typical T/R module at 9.36 GHz are depicted in Figure 4.2. Measurements correspond to a 0.5 dB step digital attenuator and 5.625^o step digital phase shifter. In the attenuation bit error versus attenuation states characteristic of Figure 4.2, the attenuation error gradually increases as a function of the attenuation state. This is because in the calculation an ideal step of 0.5 dB is assumed. However, the attenuation step obtained from the slope of normalized attenuation versus attenuation states characteristic is 0.456 dB. In the attenuator insertion phase versus attenuation states characteristic, there is a gradual variation in phase. This arises because the implementation of the attenuator circuits, higher attenuations use more concatenated attenuation sections and longer circuit paths. On the other hand, in the phase error versus phase shifter states characteristic of Figure 4.2, it is shown that the phase error is uniformly distributed between -2^o and 10^o, with a mean of 3.8^o. However, this mean is brought to zero in the calculation if the measured phase step of 5.531^o is used instead. In the phase shifter insertion loss versus phase state characteristic, it is shown that the insertion loss varies across all phase states is in the same order of magnitude than the attenuator resolution step. Hence, it became clear that the characterization is necessary to determine the actual LSBs or resolution steps of attenuators and phase shifters, which values are slightly different from the value specified by the manufacture.

Typically T/R modules have electrical characteristics as shown in Figure 4.2, all calibration need to do is to remove as much of these variances as possible. Past examples of

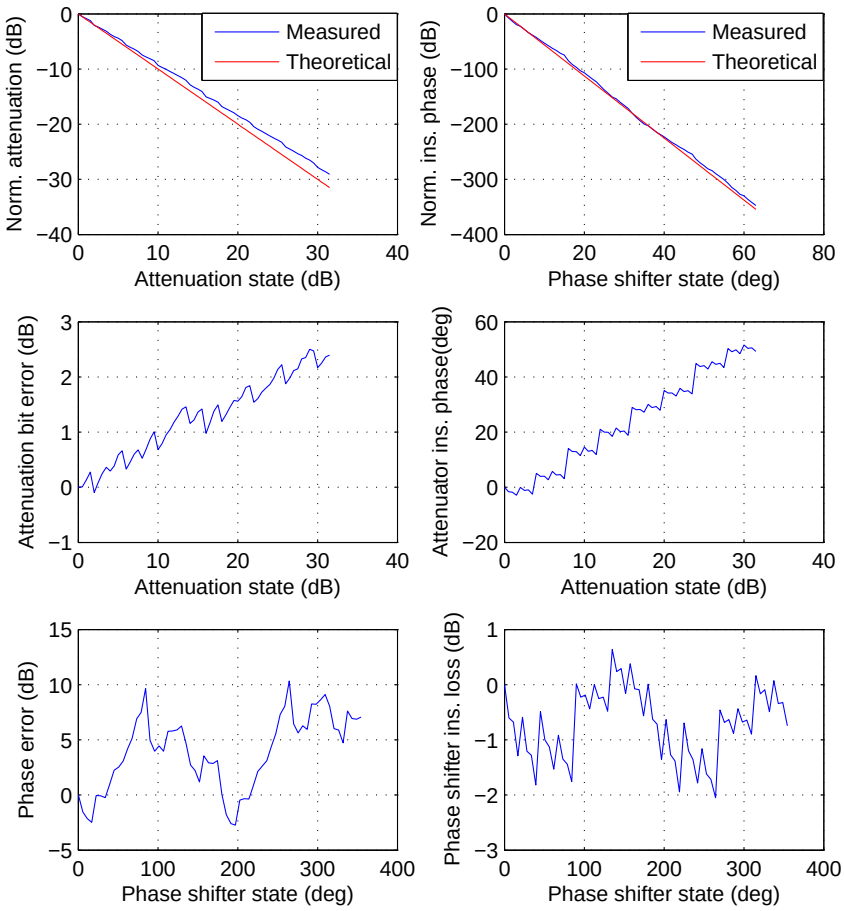

Figure 4.2: Attenuator and phase shifter performance in a X-band T/R module.

how to perform this calibration are given in [57, 62, 58]. In [57], the attenuator and phase shifter states are calibrated separately by adjusting the measured data to linear models that represent the theoretical states of each component. In this work, two separate algorithms for amplitude and phase corrections are presented. Unfortunately, this approach cannot correct the effects of phase and insertion loss shift created by attenuators and phase shifters, respectively. In [62], a nearest state algorithm is used to correct simultaneously both attenuator and phase shifter performances. The algorithm is mentioned but not covered in this work. Nevertheless, it can be assumed that the algorithm works similarly as the nearest neighbor algorithm, which can find the closest points to a desired point in the

measured data. This process is represented algorithmically in Figure 4.3. The attenuator and phase shifter states of a T/R module are adjusted such as the norm between the measured complex gain, $S_{21}^{q}(n, att, phs)$, and theoretical complex gain is minimized. The optimization problem can be written as

$$x_{min} = \min_{att,phs} \parallel S_{21}^{q}(n, att, phs) - 10^{-LBS_a.att_{raw}} e^{LSB_p.phs_{raw}} \parallel \tag{4.10}$$

This expession provides a set of values for att and phs that allows the implementation of desired complex gain given by att_{raw} and phs_{raw}. In practice, the translation from raw states to calibrated states is performed using a two-dimensional look-up table stored in the internal memory of each T/R module.

The comparison between uncorrected and corrected gain/phase maps of a typical X-band T/R module based on a 6-bit 32 dB digital attenuator with attenuation steps of 0.5 dB, and a 6-bit digital phase shifter that provides 360^o phase coverage with phase shift steps of 5.625^o are shown in Figure 4.4 and Figure 4.5. After characterization, it is found that LSBa and LSBp are 0.456 dB and 5.531^o, respectively. These values are then used in (4.10) to find the calibrated states that correct the gain and phase variations. Finally, the lower attenuator states in the calibrated data are discarded in order to have a uniform gain characteristic and implement states with low calibration errors. In Figure 4.5, the corrected gain map has a very uniformly distributed pattern through all attenuator and phase shifter states. It should be noted the attenuation range was reduced from 64 to 60 states in order to improve the gain characteristic at the lower attenuation states, where it's almost impossible to achieve calibrated states with low errors. While in the corrected phase characteristic, the spreading caused by the attenuator and phase bit error have been nearly reduced in all the range. For this particular example, a RMS amplitude error of 0.24 dB and RMS phase error of 1.73^o are achieved. Theoretically, due to quantization errors, it is expected an amplitude error of 0.13 dB RMS and phase error of 1.6^o RMS. The amplitude errors differences arise because the variance caused by the phase shifter on the gain.

On the other hand, the corrected gain and phase maps (see Figure 4.5) are obtained by the combination of 60 attenuation states and 64 phase states, together, each map is

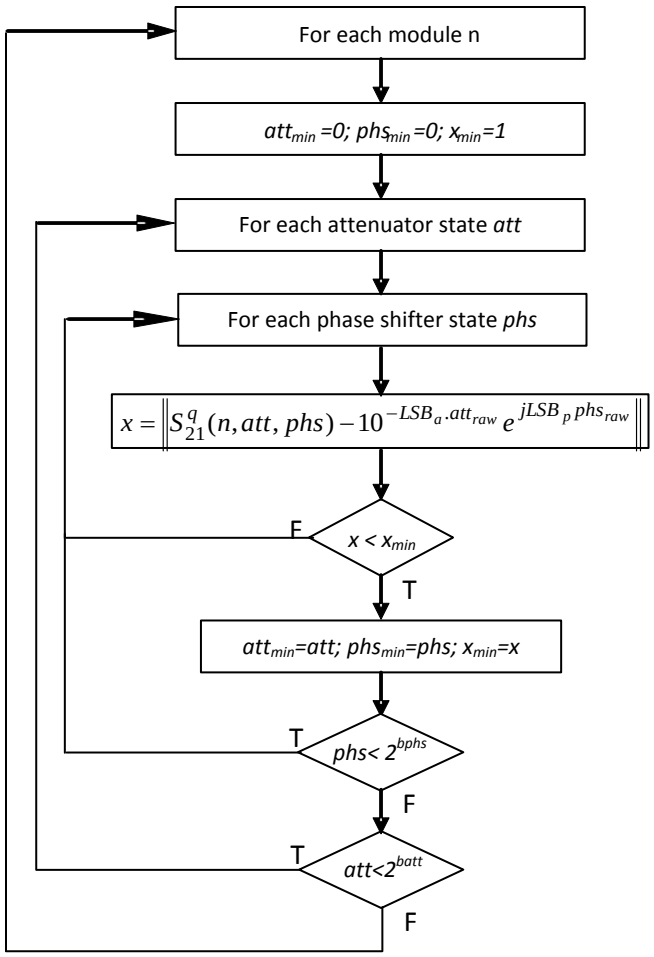

Figure 4.3: Amplitude and phase calibration algorithm for T/R modules.

comprised by 3840 states. After a comparative analysis between calibrated data and uncalibrated data, it was found that only 2944 of the original 4096 states were used in the creation of these maps. As result, there is a significant data reduction when elements are calibrated.

4.2.3 Element Characterization

In principle, it is desirable to measure all possible combinations of amplitude and phase states realized by the active elements in order to minimize the errors produced by the calibration process. However, full calibration of an active array is measurement intensive. It is common for array elements to have at least 6 bits at each digital attenuators and phase shifters, when are used together, they can provide 4096 combinations of amplitude

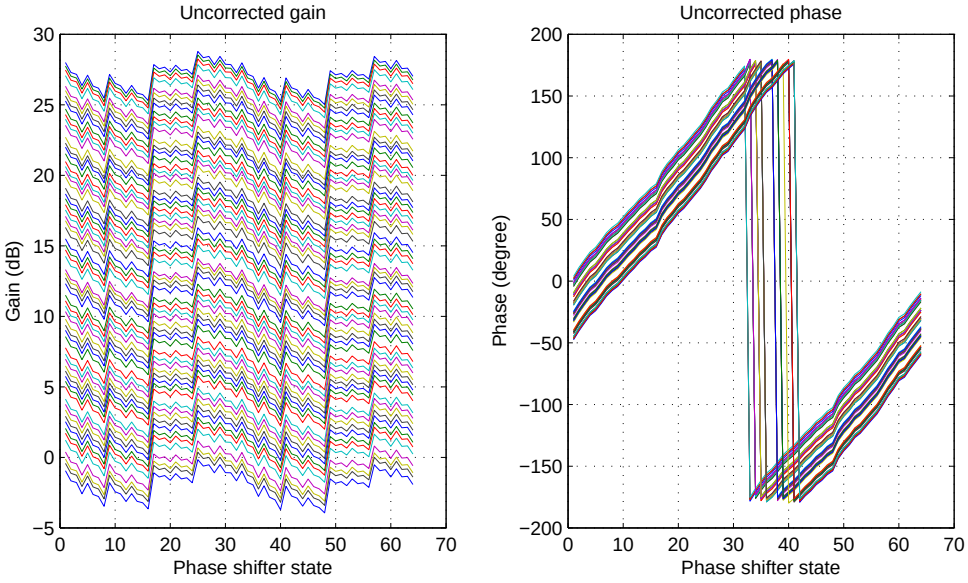

Figure 4.4: Raw gain and phase map for a X-band T/R module at 9.36 GHz.

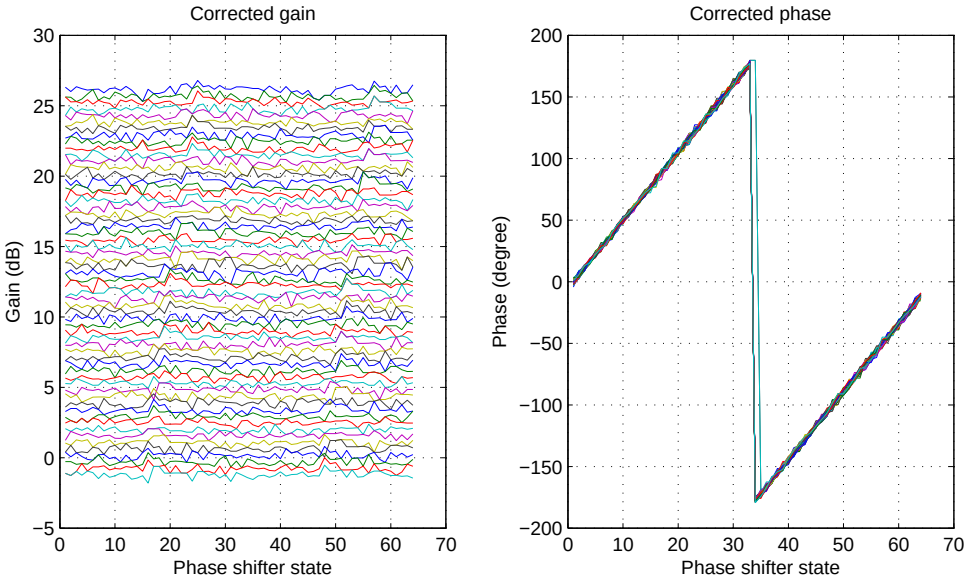

Figure 4.5: Calibrated gain and phase map for a X-band T/R module at 9.36 GHz.

and phase states per channel. In addition, measurements are realized at different frequency and temperature. As a result, thousands of measurements are required to fully characterize the performance of each element [63]. However, in practice, this procedure is avoided if the array is large, because it will result in a large number of measurements and an unacceptable long test time, affecting consequently the array test cost. To save time, the number of measurements are reduced and the omitted states are then recovered from the measurements.

In theory, the characterization could be done during the T/R modules production test, when they are isolated, allowing measurements at different temperatures [62]. But it can be also performed when modules are integrated on the system, connected to radiating elements and RF feed networks. In this case, measurements are taken with a near-field probe measurement system. A sampling probe is positioned in front of each element to be measured and amplitude and phase data are taken for that element, while other elements are terminated in match loads. For large arrays, the number of states to be measured from attenuators and phase shifters will depend on a trade-off between calibration error budget and test time [51]. While in moderate-size arrays, the measurements can be realized at cardinal states (states contained in the set 0,1,2,4,..2^{Nbits}) or through all states of each component [22, 57].

4.3 Calibration approach based on nearest state algorithm

Standard methods for array calibration assume that amplitude and phase characteristics of active elements have been calibrated in advance. Thus, array control computers only need to compute the amplitude and phase commands (attenuator and phase shifter raw states) for each module. Then, correction look-up tables in T/R modules translate the raw states into calibrated states. The data stored in the look-up tables is determined from measurements of the amplitude and phase behavior of each individual module; only data points that best approximate to ideal curves representing the ideal T/R module performance are selected. One disadvantage of this approach is that many amplitude and phase states are discarded during the creation of correction tables, reducing the ability to implement the desired excitation function with better amplitude and phase settings.

The problem of interest is to calibrate a phased array antenna in the presence of a RF beam former network with digital attenuators and phase shifters, focusing on the implementation of excitation functions with the lowest possible random errors. This goal can be accomplished if all the amplitude and phase settings measured from each element are available for the calibration. Optimum excitation settings are obtained if the calibration is performed using a nearest state algorithm. The algorithm searches across all amplitude and phase settings of each element for the values that best match the desired excitation coefficients for a particular beam. Settings for different beams are computed and then formatted into binary tables (beamtable) that are unique for each T/R module. To implement the array excitation, beamtables are stored in memory based look-up tables in the T/R modules, where the appropriated amplitude and phase settings for each desired beam are stored.

The proposed method assumes that gain and phase characteristics of radiating elements have been characterized through all attenuation and phase shifter states using a NF probe. Subsequently, these data can be used to compute the relative errors between elements (Eqn. 4.5) and ideal weighting (Eqn. 4.6) that is requered to implement the excitation function and correct the amplitude and phase differences among elements. Let's assume that the array has been calibrated by the above method. When (4.5) and (4.6) are used in (4.3), yields

$$S_{21}^{q}(n, att, phs) = v_{n}^{q} C u_{n_{ref}}^{q} \tag{4.11}$$

This quantity represents the implemented complex gain. Now, from (4.4), $S_{21}^{q}(n_{ref}, 0, 0) = Cu_{n_{ref}}^{q}$. Hence, it follows that

$$S_{21}^{q}(n, att, phs) = v_{n}^{q} S_{21}^{q}(n_{ref}, 0, 0) \tag{4.12}$$

Note that excitation coefficient is scaled by the gain of the element that has less gain in state zero. This condition allows the gain realized by the elements fall within the operation range of attenuators and phase shifters, or within the gain and phase range of each element. The values *att* and *phs* in the above formula are the states that must be found at each element to satisfy the equally (4.12). However, due to quantization effects the array

excitation will not be perfectly implemented. The goal of calibration is to find the proper settings that minimize the error between the implemented complex gain $S^q_{21}(n, att, phs)$ and the theoretical complex gain $S^q_{21,theo}(n)$, which depends on the desired aperture amplitude distribution function (a_n) and the scan angle (θ_0). Formally, this is expressed as

$$[att^q(n,\theta_0), phs^q(n,\theta_0)] = \underset{att,phs}{argmin} \parallel S^q_{21}(n, att, phs) - S^q_{21,theo}(n,\theta_0) \parallel \tag{4.13}$$

$$S^q_{21,theo}(n,\theta_0) = a_n e^{jnkdsin(\theta_0)} S^q_{21,ref}$$

$$|S^q_{21,ref}| \leq |S^q_{21}(n_{ref}, 0, 0)|$$

In fact, the expression (4.13) works for any scaling factor less than or equal to reference gain $S^q_{21}(n_{ref}, 0, 0)$, its value has been replaced by $S_{21,ref}$. The criteria to choose the reference gain depends on the operation mode. For receive mode, the criteria should be $|S_{21,ref}| \leq min(|S^q_{21}(n, 0, 0)|)$ to reduce the random excitation error and obtained better sidelobes levels. While in transmit mode, if the amplifiers need to operates in compression, the criteria should be $S_{21,ref} = max(S^q_{21}(n, 0, 0))$.

To find the array calibration settings, a nearest states algorithm is used. The algorithm searches in the measured data of each element, the best approximation for the attenuator and phase shifter states that minimizes the norm between the measured gain $S^q_{21}(n, att, phs)$ and theoretical gain $S_{21,theo}$ for that particular element. This process is represented algorithmically in Figure 4.6. This procedure gives two set of vectors $att^q(n,\theta_0)$ and $phs^q(n,\theta_0)$, which are quantized and formatted into a binary table (beamtable) that is unique to a particular T/R module.

RMS amplitude and phase errors between implemented excitation and theoretical excitation for each beam are computed as follow

$$\sigma_a(\theta_0) = \sqrt{\frac{1}{N}\sum_{n=1}^{N}\left(\frac{|S^q_{21}(n, att^q(n,\theta_0), phs^q(n,\theta_0))| - |S_{21,theo}(n,\theta_0)|}{|S_{21,theo}(n,\theta_0)|}\right)^2} \tag{4.14}$$

$$\sigma_a(\theta_0) = \sqrt{\frac{1}{N}\sum_{n=1}^{N}\left(\angle S^q_{21}(n, att^q(n,\theta_0), phs^q(n,\theta_0)) - \angle S_{21,theo}(n,\theta_0)\right)^2} \tag{4.15}$$

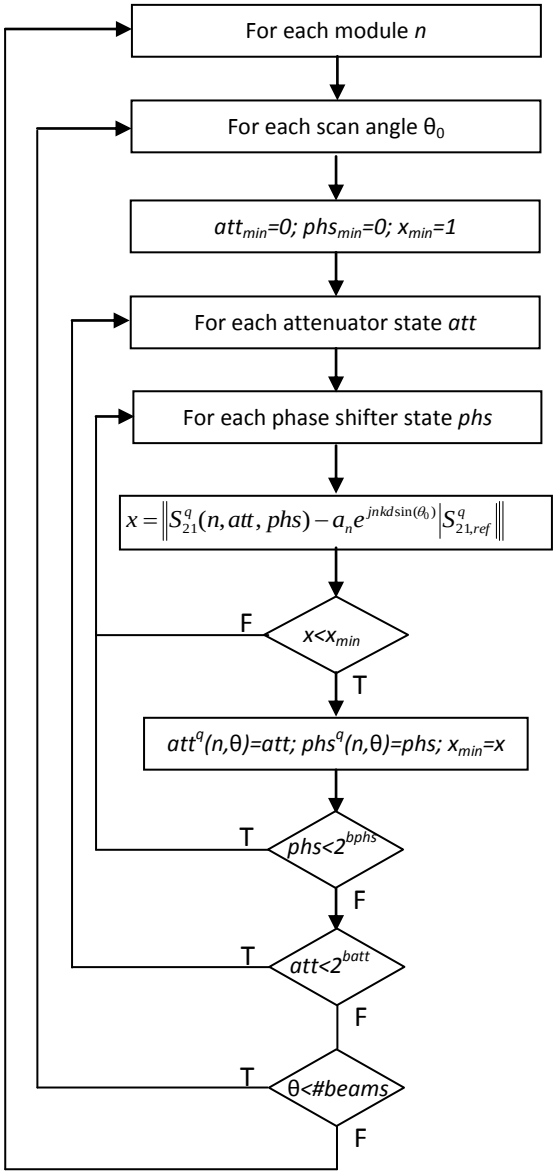

Figure 4.6: Amplitude and phase calibration algorithm for phase array system.

Theoretically, the amplitude and phase errors will depend on quantization errors created by the attenuators and phase shifters, respectively. Those values are given by following equations

$$\sigma_{a,theo} = \sqrt{\frac{LSB_a^2}{12} + std(LSB_a)^2} \tag{4.16}$$

$$\sigma_{a,theo} = \frac{LSB_p}{\sqrt{12}} \tag{4.17}$$

4.3.1 Pattern Prediction

Let it be assumed that the array has been calibrated by the above method, and the implemented array excitation for the nth element is proportional to the complex parameter $S_{21}^q(n, att, phs)$. If an average embedded element pattern, $f_{av}(\theta, \phi)$, can be determined, for example by far-field measurements, then the array radiation pattern can be computed from (4.2) as

$$f_a(\theta, \phi) = f_{av}(\theta, \phi) \sum_{n=1}^{N} S_{21}^q(n, att^q(n, \theta_0), phs^q(n, \theta_0)) e^{jnkdsin(\theta_0)} \tag{4.18}$$

4.3.2 Beamtable Format

The control electronic unit of each T/R module has 4K bytes (4096 x 16 bits) of RAM that is used for storing the beamtables of that particular element, as discussed in chapter [1]. The beamtables are arranged in memory blocks where calibration settings for different beams and operation modes are stored. To access the calibration settings, the memory blocks are configured in form of look-up tables, which looks up what the output should be for any given combination of input states. The number and size of beamtables that can be allocated in the memory depends on the number of beams, operation modes and temperatures tables. Table 4.1 summarizes the number of beamtables that are available for single and dual polarization when the array is calibrated for 128 and 256 beams. For example, a dual-polarized array with 256 beams, operating in both polarization used as minimum 4 different beamtables (one for each channel: RH, RV, TV and TH) for a single temperature. However, the memory size can allow the implementation of a maximum of 4096/(256)=16 beamtables, which can be used to calibrate the array at other temperatures.

Table 4.1: Number of beamtables available in a 4K Memory look up table

Mode	Number of beams	Number of channels	Max. number of beamtable	Max. number of beamtable per channel
single	128	2	32	1(T)+31(R)
dual	128	4	32	1(TH)+1(TV)+15(RV)+15(RH)
single	256	2	16	1(T)+15(R)
dual	256	4	16	1(TH)+1(TV)+7(RV)+7(RH)

For the particular case when the element memory is configured with 4 beamtables and 256 beams, the memory configuration and memory map are depicted in Figure 4.7 . The 4*256=1024 memory locations are addressed with only 10-bits of the 12-bits wide beam commands. The addressing command is concatenated as follows: two unused bits, one bit for T/R signal (operation mode), one bit for H/V signal (polarization), and 8-bits for the beamID (beam index), where, the bit T/R={0 for receive, 1 for transmit} and bit H/V={0 for horizontal, 1 for vertical} select the beamtable, while the $beamID = 0, 1, 2, ..., 255$ selects the desired beamsteering angle θ_0. Assuming the normal azimuth scanning range for the antenna is $\pm 45^o$ and that the beam sampling is uniformly distributed with angular increment $\Delta\theta = 90^o/(256-1) = 0.3529^o$. With these values, $beamID$ and θ_0 are related as

$$beamID = round\left(\frac{\theta_0 - \theta_{initial}}{\Delta\theta}\right)$$
$$\theta_0(beamID) = \theta_{initial} + \Delta\theta_0 beamID = -45 + 0.3529 beamID \tag{4.19}$$

The above formula generates the sequence $\theta_0(0:255) = \{$-45^o, -44.6471^o ,..., -0.1765^o , 0.1765^o,..., 44.6471^o, 45$^o\}$.

For the above example, the beamtable data is comprised of 1024 16-bit wide words. Each 16-bit words is the binary concatenation of 6 bits that specify the attenuator state, 6 bits that specify the phase shifter state, and bits H, V, T, and R, as it is indicated in Table 3.10. Based on memory configuration depicted in Figure 4.7, and the states obtained from (4.13), the beamtable data for the nth element is computed as follows:

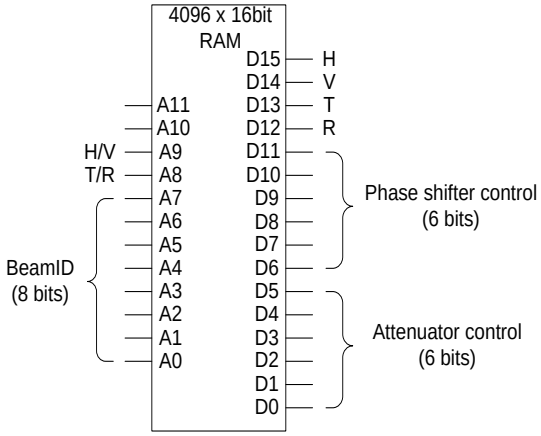

Beam Command

Unused[1:0]	T/H	H/V	BeamID[7:0]

T/H	H/V	BeamID	Address	Memory Map	Beam
0	0	0	000h	Beamtable for channel RV	-45
		255	0FFh		45
0	1	0	100h	Beamtable for channel RH	-45
		255	1FFh		45
1	0	0	200h	Beamtable for channel TV	-45
		255	2FFh		45
1	1	0	300h	Beamtable for channel TH	-45
		255	3FFh		45

Figure 4.7: Look up table configuration: Left: memory configuration. Right: memory map.

$$beamtable(n, address) = conc_2\{bit(H/V), \overline{H/V}, bit(T/R), \overline{T/R}, phs_2[5:0], att_2[5:0]\}$$

$$address = beamID + 256bit(T/H) + 512bit(H/V)$$

$$phs_2[5:0] = dec2bin(phs^q(n, beamID), 6)$$

$$att_2[5:0] = dec2bin(att^q(n, beamID), 6)$$

where $conc2$ is the concatenate function, $dec2bit$ is the function that converts decimal to binary numbers and q is the channel (TH, TV, RH and RV). Finally, the beamtable is transferred from the array controller to T/R module memories using the write memory command (see Table 3.10 in section 3.6.4.1).

Table 4.2: Beamtable data format

TRM command	beamtable length	beamtable(n)
16 bits	16 bits	1024x16 bit

4.3.3 Internal Temperature Compensation

The phased array system described in Chapter 3 is equipped with an inexpensive forced air cooling system to prevent the T/R modules from excessive heat. A voltage-controllable fan array that forces ambient air to circulate from the antenna base to the top, passing through the T/R modules is used. Although the cooling system seems adequate to regulate the heat of the active components, it has the disadvantage that system temperature varies with the ambient temperature (or weather condition). The problem with this is that changes in ambient temperature can causes drifts in the gain and phase of T/R modules [34]. As a result, the overall gain in both transmit and receive array is varied from their operating points, causing important changes in the radar parameters.

To ensure the gain and phase stability over ambient temperature, both transmit array and receive array should be calibrated at different temperatures. However, in many solid-state radars, the transmitters are calibrated to extract the maximum available power from power amplifiers. The problem that arises is when transmit modules operate in saturation; the gain drift cannot be compensated by adjusting the element gain. A solution to this problem is to make the assumption that transmit array gain is stable with temperature and attempt to compensate the two-way gain variation (Tx gain drift + Rx gain drift) with the receive array gain. In fact, for this approach to be valid, it must be assumed that the temperature drift is uniform all over the array.

In a phased array, the gain variations over temperature are caused generally by the RF solid-states devices used in the T/R modules. Both DC and RF characteristics (current, voltages, gain etc) of RF linear devices vary exponentially with temperature [64]. While gain in decibels and phase may vary quadratically [22] or linearly with temperature. Particularly in the phased array testbed described in Chapter 3, it was found in the RF component datasheets that the gain (in decibels dB) and phase variation over temperature vary linearly with temperature. Same behavior was observed experimentally during the test as well [65]. To model the gain, the measured gain in dB is converted to linear scale using exponential transformation. After transformation, one finds that gain varies exponentially with temperature.

Consider an active element that has been measured with a NF probe at different temperatures, the gain in linear scale as a function of temperature, t, can be described empirically by the equation

$$S_{21}^{q}(n, att, phs, t) = S_{21}^{q}(n, att, phs, t_0)e^{-(\alpha^q + j\beta^q)(t-t_0)} \tag{4.20}$$

where $S_{21}^{q}(n, att, phs, t_0)$ is the gain in the reference temperature t_0, α^q represents the gain variation coefficient (Neper/^{o}C), β^q represents the phase variation over temperature (radians/^{o}C). When measured gain (4.13) is expressed in dB, that is

$$|S_{21}^{q}(n, att, phs, t)| = 20 * log10_{10}(|S_{21}^{q}(n, att, phs, t_0)|) - A(t - t_0) \tag{4.21}$$

where $A = 20log_{10}(e)\alpha^q$ is the gain variation over temperature in dB/^{o}C . Note that the phase in (4.20) and gain in dB (4.21) vary linearly with temperature, as it is shown in Figure 4.13.

Now, let's consider that transmit gain variation is attributed to the receive channel and the gain drift can be compensated with the receive array. Then the modified receive array gain for the nth element is expressed as follow

$$S_{21}^{R}(n, att, phs, t)e^{-(\alpha^T + j\beta^T)(t-t_0)} = S_{21}^{R}(n, att, phs, t_0)e^{-(\alpha^R + \alpha^T + j\beta^R + \beta^T)(t-t_0)} \tag{4.22}$$

Using (4.22) and (4.13) , we can define an expression for estimating the attenuator and phase shifter states as a function of temperature for receive elements

$$[att^R(n, \theta_0, t), phs^R(n, \theta_0, t)] = \underset{att,phs}{argmin}||S_{21}^{R}(n, att, phs, t_0)e^{-(\alpha^R + \alpha^T + j\beta^R + \beta^T)(t-t_0)} - S_{21,theo}^{R}(n, \theta_0, t_0)|| \tag{4.23}$$

the quantity $S_{21,theo}^{R}(n, \theta, t_0)$ is defined as (4.13). The fact of keeping $S_{21,theo}^{R}(n, \theta, t_0)$ constant at any temperature in (4.23) obliges the adjustment of att and phs to compensate the gain drift produced by the factor $e^{-(\alpha^R + \alpha^T + j\beta^R + \beta^T)(t-t_0)}$.

4.4 Experimental Evaluation

4.4.1 Test Equipment Description

The phased array calibration and antenna pattern measurements were carried out using the near-field range system shown in Figure 4.8. The system consists of a linear scanner that carries an open-ended waveguide as a NF probe, and a Agilent E8362B network analyzer to measure the S-parameters. The lineal scanner is a product of Velmex inc having a travel range of 1.5 meters. The setup of the measurement equipment is shown in Figure 4.9. The array, network analyzer, and scanner controller are interfaced to a central computer, that in turn, controls them. The computer also provides timing and communication, processes the data, and records the measurements. The entire system is controlled by the user using a GUI developed in C language.

The linear scanner is controlled from the host computer via a RS232 interface. The NF probe position is controlled by commands that are generated by the computer and that are sent to the scanner controller. When the probe is placed in the desired location, the system can perform either single element measurements (i.e element characterization) or radiation pattern measurements. To do so, the host computer first enables the array elements and then sends trigger commands to E8362B network analyzer to perform standard S-parameter measurements. All measurements are realized in pulsing mode. Data is transferred to the computer via a 100 Mbps local area connection (LAN).

4.4.2 Scanner Alignment and Antenna Position Error Estimation

In order to minimize calibration errors, the linear positioner is parallel attached to the antenna support structure, with the near-field probe aligned to the center of the subarrays. The mechanical alignment is realized by hand using a webcam and image processing GUI developed in Matlab [66], see figure 4.10. The alignment procedure consists in positioning the webcam in front of each array elements and computing their positions in the array from snapshots that are taken at those particular positions. The location errors and offsets that are obtained from this procedure are used to correct any misalignment can exist between the array and scanner.

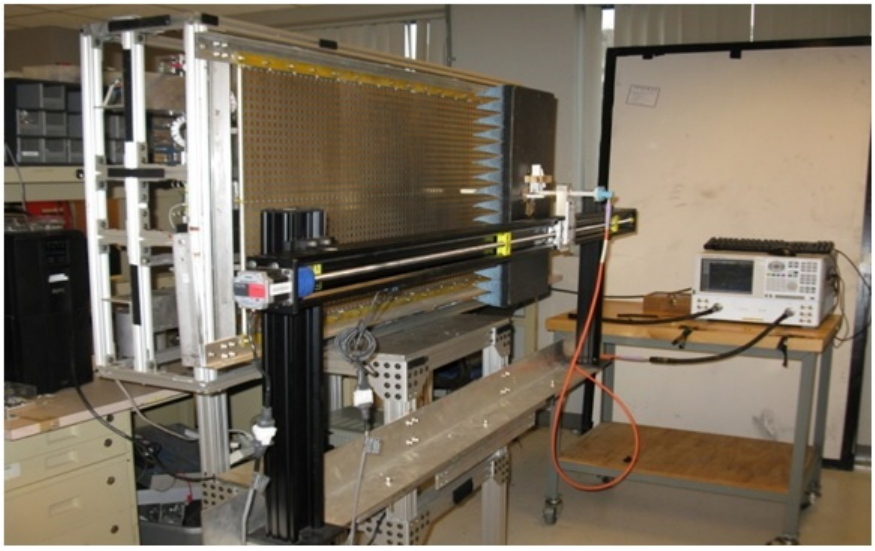

Figure 4.8: Near field probe test system.

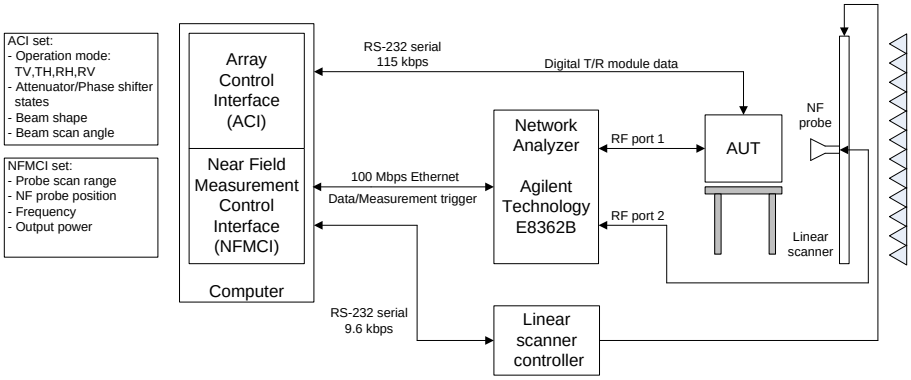

Figure 4.9: Measurement equipment setup for phased array calibration.

To measure the element position errors, first, the linear scanner automatically aligns the webcam with the first element of the array (i.e. the first element on the right hand side). This point is set as the antenna origin. Then, the webcam is moved in steps equal to the element spacing (d=17 mm), taking at each position a snapshot of each element, untill the last element is reached. Subsequently, the GUI processes the snapshots with a shape recognition algorithm, which recognizes the shape of microstrip patch antennas and computes the coordinates of their centroids from the image's center. The element location is determined when coordinates of the centroid are added to the theoretical element position.

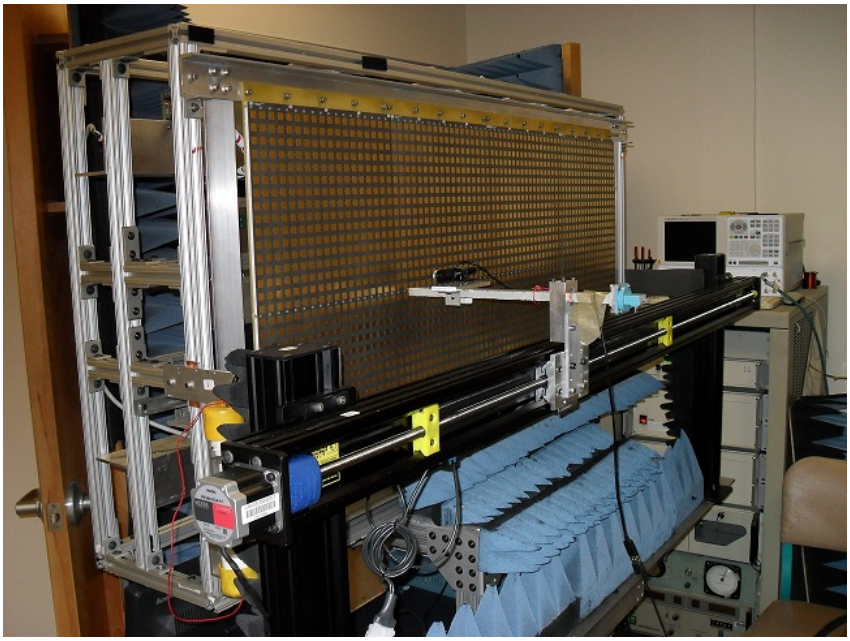

Figure 4.10: Webcam-based alignment control system

Figure 4.11 shows the example of misalignment between the array and scanner system that is obtained with the aforementioned GUI. In this particular case, the last element in the array (element 64) is 1.2 mm off in x direction (red curve) from the theoretical center; while in the y direction (blue curve) one panel is 0.8 mm off in height from the other antenna panels, this misalignment arises from fabrication defects in one of the antenna panels. Figure 4.11 also shows the discontinuities in the x direction that are produced by gaps between antenna panels. Based on this approach, a horizontal error of 0.20 mm RMS and vertical error of 0.33 mm RMS were found. The horizontal error produces in the system a phase error of 2.32^o RMS.

4.4.3 Temperature Characterization

The purpose of this test is to characterize the performance of the array elements as a function of ambient temperatures. Since the array is not equipped with a temperature control system that can hold a constant temperature in the array, it is necessary to estimate how the gain and phase of elements changes with temperature. Although ideally it is desirable to perform the array characterization in an environmental test chamber that

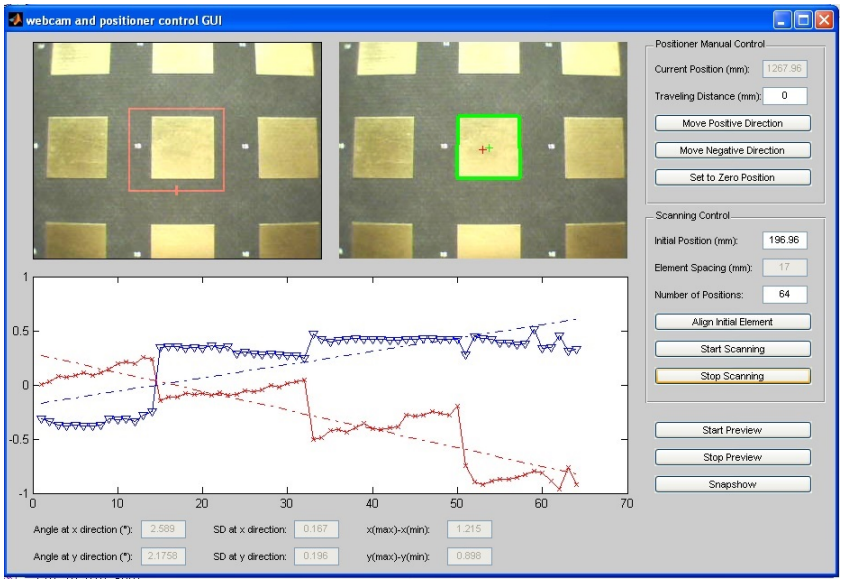

Figure 4.11: GUI that determine the element position errors and alignment errors

can emulate different ambient temperatures, such facility was not available for this test. However, it can be realized if the T/R module temperature can be varied externally, and if it is assumed that temperature dependence of manifold networks, cables, and passive array are negligible over the temperature range. In fact, passive components usually have low coefficients of thermal expansion that results in small changes in insertion phase with temperature compared to the insertion phase created by solid-state devices at the same temperature range. In this work, the T/R module temperature is controlled by adjusting the fan speed of a fan array system, which in turn controls the temperature of the airflow that passes through T/R modules.

The temperature characterization consists in measuring the S-parameter S_{21} from a calibrated array at different temperatures. To do this, first the array is calibrated at lower temperature, when the fan array operates at maximum speed; then temperature of T/R modules is varied in steps until it reaches the maximum temperature, that is when the fan array is off. At each temperature step, the parameter S_{21} of each active element is measured when module temperature reaches steady state. Figure 4.12 shows the temperature, gain and phase characteristics at different fan voltages as a function of time for a receive element, right after being turned on. The time to reach steady state depends on the initial

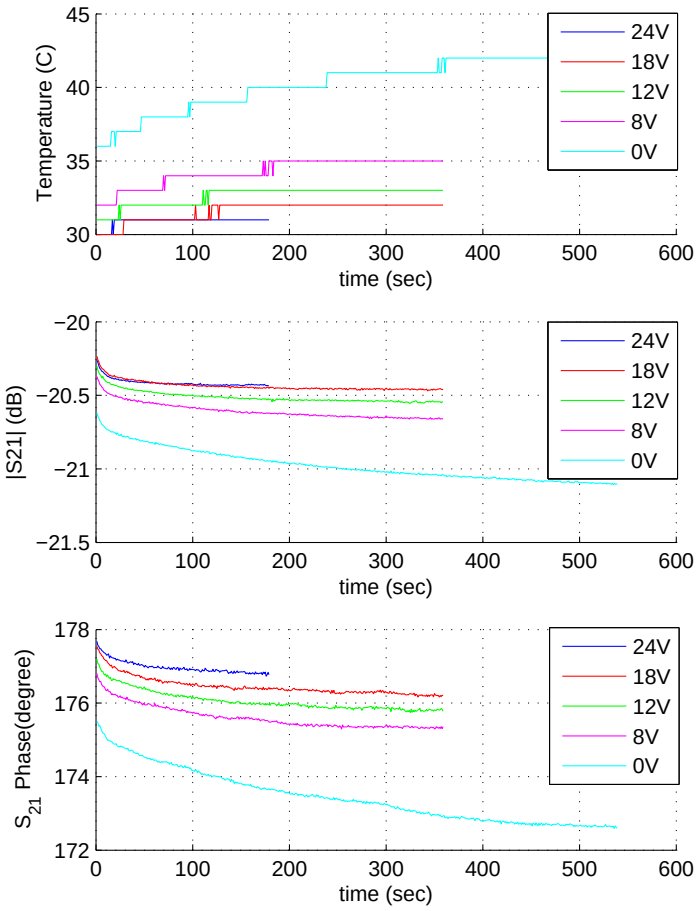

Figure 4.12: Measured temperature and Transmission coefficient S_{21} as a function of time and different fan voltages. Top: Temperature. Middle: S_{21} Magnitude. Bottom: S_{21} phase.

temperature, temperature constant, and pulse duty cycle. In this test, the time is between 60 sec to 500 sec.

The procedure to characterize the elements is described below:

1. Calibrate the array at low temperature, that is when fan speed is maximum.
2. Reduce the fan speeds to increase the temperature.
3. Place the NF probe in front the first element.

4. Pulse with a duty cycle of 30% the T/R module under test and read internal temperature. Repeat this step till steady-state temperature is reached. Then, measure the parameter $S_{21}(att, phs, t)$ with the network analyzer.
5. Move the NF probe to the next element and repeat steps 4 and 5 until last module is reached.
6. Repeat steps 2 to 5 until the fan speed is zero, point where the temperature is maximum.

It should be noted that, while in receive the temperature characterization is realized in the linear region, in transmit the characterization is realized using the power amplifiers in the saturation region. Figure 4.13 shows the average gain, phase and Tx saturation power characteristics versus module temperature for both Tx and Rx elements, at central frequency of 9.36 Ghz. Measurements are normalized to the temperature of 34 ^{o}C. According to the results, the receive gain and phase variation over temperature are 0.061 dB/^{o}C and 0.43 deg/^{o}C, respectively. The total gain loss is about 1.1 dB in the range. The gain variation over temperature is dominated specially by the thermal characteristics of three amplifiers (HMC441LP3 and HMC564LC4) used in the receive channel, the manufacturer specifies a typical gain variation of 0.2 dB/^{o}C for each component. In contrast, the Tx saturation power and Tx phase vary in at rate of 0.009 dB/^{o}C and 0.45 degree/^{o}C respectively, being the total power variation 0.14 dB in the range of interest. The small variation in the transmit saturation power is because the power amplifier is heavily compressed.

Based on above results, the gain for transmit and receive elements can be modeled using (4.20) or (4.21). For receive mode, $\alpha = A/(20 * log_{10}(e)) = 0.061/8.68 = 0.0079\ Neper/^oC$ and $\beta = 0.43 * \pi/180 = 0.0075\ radians/^oC$, thus the gain can be written as

$$S_{21}^R(n, att, phs, t) = S_{21}^R(n, att, phs, t_0)e^{-(0.0070+j0.0075)(t-t_0)} \tag{4.24}$$

$$|S_{21}^R(n, att, phs, t)|(dB) = 20log_{10}(|S_{21}^R(n, att, phs, t_0)|) - 0.061(t - t_0)$$

the reference gain $S_{21}^R(n, att, phs, t_0)$ is selected at temperature t_o. While for transmit mode, $\alpha = 0.001\ Neper/^oC$ and $\beta = 0.0079\ radians/^oC$. Hence, using (4.20) or (4.21), it follows that

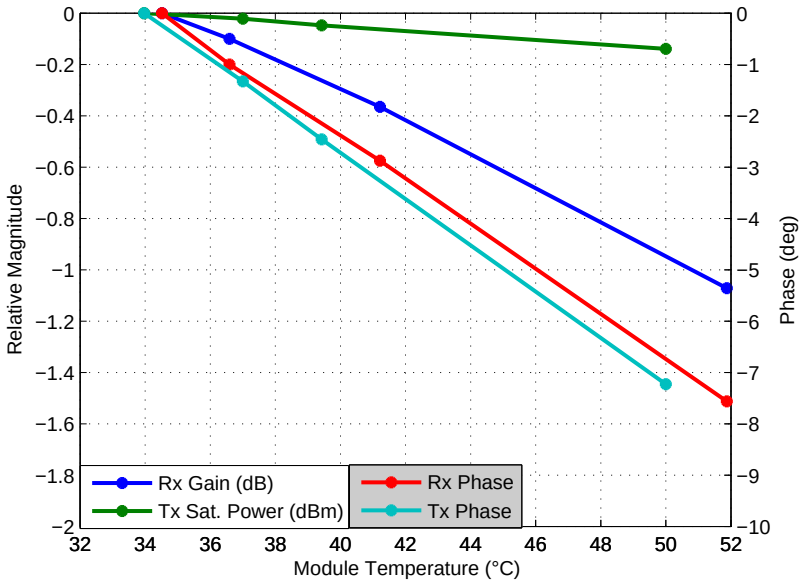

Figure 4.13: Relative gain, phase and saturation power performance versus module temperature.

$$S_{21}^{T}(n, att, phs, t) = S_{21}^{T}(n, att, phs, t_0)e^{-(0.001+j0.0079)(t-t_0)} \tag{4.25}$$

$$|S_{21}^{T}(n, att, phs, t)| = 20log_{10}(|S_{21}^{T}(n, att, phs, t_0)|) - 0.009(t - t_0)$$

Finally, although the gain was only modeled for the temperature range 34 ^{o}C - 52 ^{o}C, it is not clear if the linear characteristic of the gain in decibels can be extended to 0 ^{o}C . But assuming that the linear model is still valid for a temperature range from 0 ^{o}C to 54 ^{o}C, we will expect a Rx gain variation of 3.0 dB and Tx saturation power variation of 0.45 dBm into the range. These values suggest that the array will need an internal calibration system to correct the gain drift due to temperature changes.

4.4.4 Receive Array Calibration

In principle, it is desirable to measure all possible combinations of amplitude and phase states realized by the active elements in order to minimize the errors produced by the calibration process. But, the time to reach the steady-state temperature and time to measure the 4096 states (64x64) at difference frequencies of each element will result in unaccept-

able long test time. To reduce the characterization time, the number of measurements are reduced to 128 and the unmeasured states are recovered from measurements.

The characterization starts by first placing the NF probe in front of the subarray under test (SUT) and measuring the S_{21} parameter, with that element in receive mode and remaining array subarrays terminated in matched loads. To save time, the attenuator and phase shifter are only switched through a subset of 128 of the possible 4096 states, initiating the measurements with the attenuator in the state zero (0 dB) while the phase shifter is switched through each of its 64 states, and then setting the phase shifter to state zero (0^o) while switching the attenuator through each of its 64 states. The remaining 3968 states are obtained as follow:

$$S_{21}^q(n, att, phs, t_0) = \frac{S_{21}^q(n, att, 0, t_0) S_{21}^q(n, 0, phs, t_0)}{S_{21}^q(n, 0, 0, t_0)} \tag{4.26}$$

where q represents the channel (RH, or RV), n is the SUT index (n=1,2,3,..,64), att and phs are states defined in range from 0 to 63, and t_0 is the temperature index for calibration temperature. The parameters $S_{21}^q(n, att, 0, t_0)$, $S_{21}^q(n, 0, phs, t_0)$ and $S_{21}^q(n, 0, 0, t_0)$ represent three of the 128 measurements recorded for the subarray n at a specific frequency. This data reconstruction scheme allows the characterization time to be reduced by a factor of 32 compared to full measurements. Once the data is reconstructed and stored in individual files, the procedure is repeated with the next subarray until all the subarrays are measured. It should be noted that eq. 4.26 is an approximate formula that assumes that attenuators and phase shifters are perfectly matched at any states. Therefore, it is expected that reconstructed data is affected by small errors introduced by the approximation.

Following the above procedure, 128 files for the 64 elements were generated, 64 files for horizontal elements and 64 files for vertical elements. The files contain data at 10 different frequencies, from 9.31 GHz to 9.41 GHz. The data was taken using a separation distance of $4.4\lambda_0$ between the NF probe and antenna, where λ_0 is the wavelength at central frequency.

The next step consists in choosing a scaling factor for both polarizations that can be applied to the theoretical excitation distribution function. A common scaling factor allows that both polarizations have the same amplitude pattern at broadside; this in turn

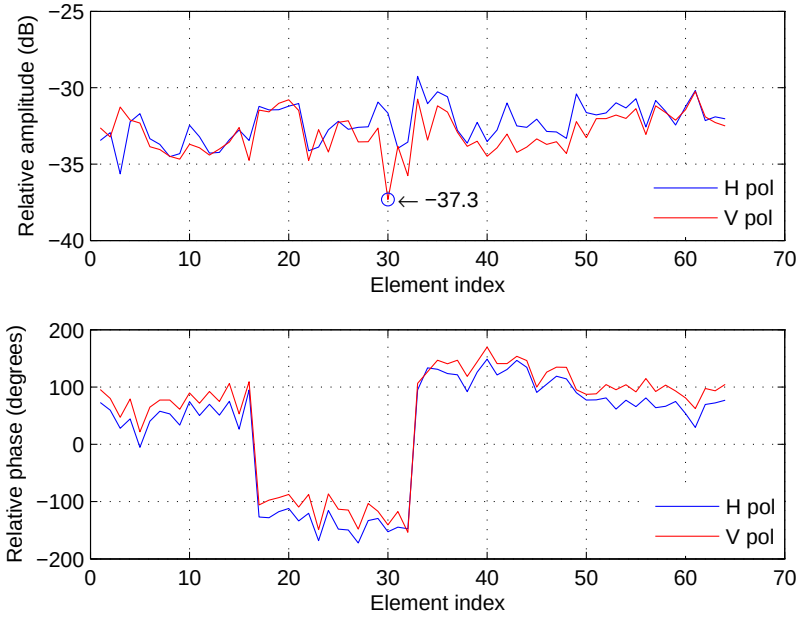

Figure 4.14: Measured transmission coefficient S_{21} for receive array at state zero. Top: Relative amplitude. Bottom: Relative phase

will allow the polarimetric calibration of vertical and horizontal channels. To choose this factor, it is necessary first to determine the lowest S_{21} among elements when attenuators and phase shifters are set to state zero. Figure 4.14 shows the measured amplitude and phase distribution for the transmission coefficient S_{21} at state zero across the array. It is important note that amplitude and phase disparities for a given polarization are caused by hardware differences among elements. While gain differences between polarization in a particular element is due to losses between T/R modules and radiators, which can be caused by some imperfection in T/R module connectors, antenna connectors, and loose interconnection cable. For the uncalibrated test array, the amplitude and phase variations at both polarizations are less than 1.3 dB RMS and 100.3^o RMS, respectively. In addition, the lowest amplitude value is -37.3 dB, which is found at the element 30. To minimize the RMS excitation error after calibration, it is necessary that the scaling factor should be less than or equal to lowest S_{21}; for this test, the chosen value is -39 dB.

The calibration is performed to implement a -25 dB $\overline{n}$=2 Taylor taper. Normalized amplitude coefficients are scaled by the scaling factor, and results are then used by the

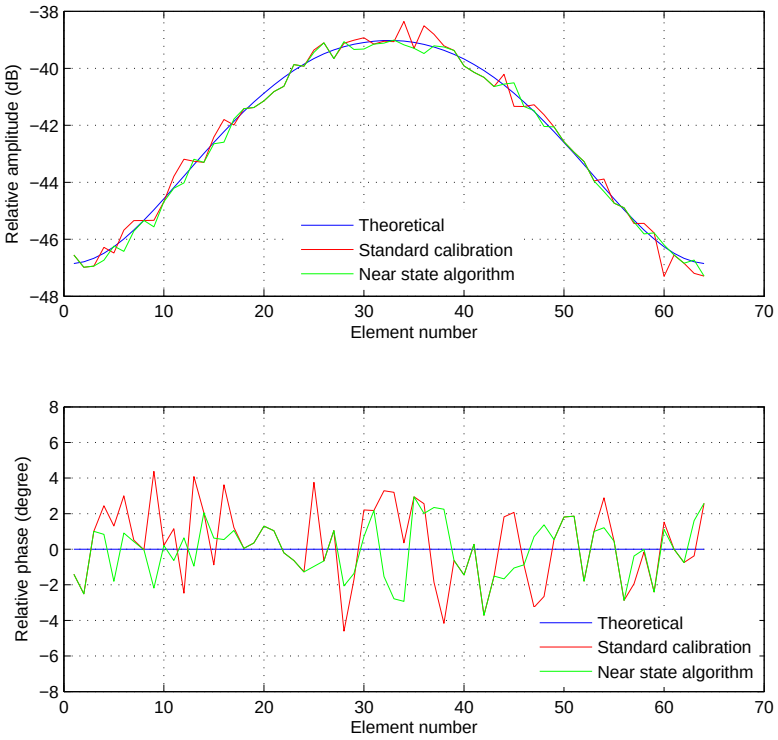

Figure 4.15: Comparison of calibrated transmition coefficiente S_{21} in receive mode . Top: Amplitude distribution. Bottom: Phase distribution

calibration algorithm to compute the element setting that implements the desired taper. For the purpose of demonstrating the improvement of RMS errors, the standard calibration is also implemented. Both calibrations are carried out at central frequency of 9.36 GHz. The amplitude and phase as determined by standard calibration and by the proposed approach are shown in figure 4.15 . The RMS errors, which are the main indicators of the performance, are shown in Table 4.3. The theoretical error were calculated from (4.16) and (4.17), using the measured values LSB_a=0.46 dB, $std(LSB_a)$=0.1671 dB, LSB_p= 5.51^o; while RMS errors for the other two methods were calculated using (4.14)-(4.17). Table 4.3 shows that RMS errors obtained from calibration based on nearest state algorithm are close to the theoretical values and better than the values obtained from standard calibration.

In order to evaluate the array calibration, the calibrated settings are loaded in the T/R modules to measure the far-field radiation patterns. In this case, the figure of merit is

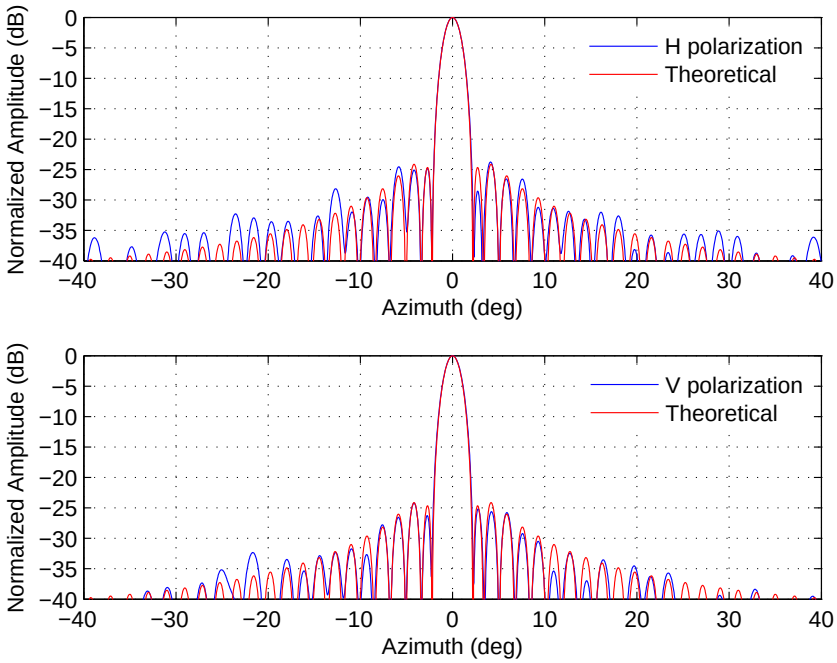

Figure 4.16: Theoretical and measured azimuth far field patterns at 9.36GHz, derived from Near-Field measurement. Top: H polarization. Bottom: V polarization.

how well the calibrated pattern approaches the theoretical pattern. In the experiment, the fields are measured in the near-field range. But they are transformed to far-field applying a Fourier transform. Additionally, an idealized probe correction is applied to data to remove the probe effects. The resulting normalized azimuth patterns and theoretical pattern in receive, for V and H polarization at 0^o scan angle are depicted in figure 4.16. The results are excellent based on the null locations and because there is not a large deviation in the peak sidelobes between measured and theoretical patterns. At 4.13^o, the increment in the larger sidelobes peak is 0.32 dB in the horizontal polarization and 0.76 dB in the vertical polarization.

Table 4.3: Comparison of RMS excitation errors for calibrated array in receive

Method	RMS amplitude error (dB)	RMS phase error (degrees)	Total error (σ)
Theoretical	0.21	1.59	0.037
Standard calibration	0.30	2.14	0.051
Nearest state algorithm	0.23	1.61	0.038

4.4.5 Transmit Array Calibration

The calibration goal for the transmit array is slightly different from the receive array. While in receive, the goal is to implement a Taylor-weighted amplitude taper that provides a radiation pattern with low sidelobes, in transmit the goal is to implement a uniform illumination using the maximum power available in the T/R modules. In order to use the maximum available output power, all transmit modules are operated in compression. This leads the array to lose the ability to control the gain. Having no gain control, the phase is the only parameter that needs to be characterized. To calibrate the transmit array with its modules in compression, an extra test is performed before the element characterization. The test consists in measuring the output power variations of each element versus the antenna input power with the NF probe. Test is done after setting the attenuator and phase shifter in the state zero. Measurements allow the determination of the minimum power (P_{in1dB}) that should be applied in the antenna input to operate the T/R modules under saturation. Once this boundary is found, an input power level greater than P_{in1dB} is applied to the antenna and the elements are characterized.

Figure 4.17 shows the average output power from 64 elements in both polarizations sensed with the NF probe versus the antenna input power. The standard deviation of the sensed output power was 0.92 dBm and 0.74 dBm for V and H polarization, respectively. The variance of these parameters is due in part to the interconnection losses between the T/R modules and the array elements, which is realized with push-on SMP connectors. The average (P_{in1dB}) is around 30 dBm. Above this point, any power level will be enough to saturate the modules.

For this experiment, the element characterization is performed using an input power of 35 dBm. The procedure used to measure the parameter S_{21} is similar to the receive elements. Although only the phase shifter should be characterized, the attenuator is also characterized to improve the phase resolution. The improvement in the phase steps is because the element insertion phase also changes as a function of the attenuation states, being its phase slope less than phase slope produced by phase shifter. As a result, the total phase can be controlled by adjusting both the attenuator and phase shifter. In contrast, in the standard calibration, the phase is only controlled by the phase shifters.

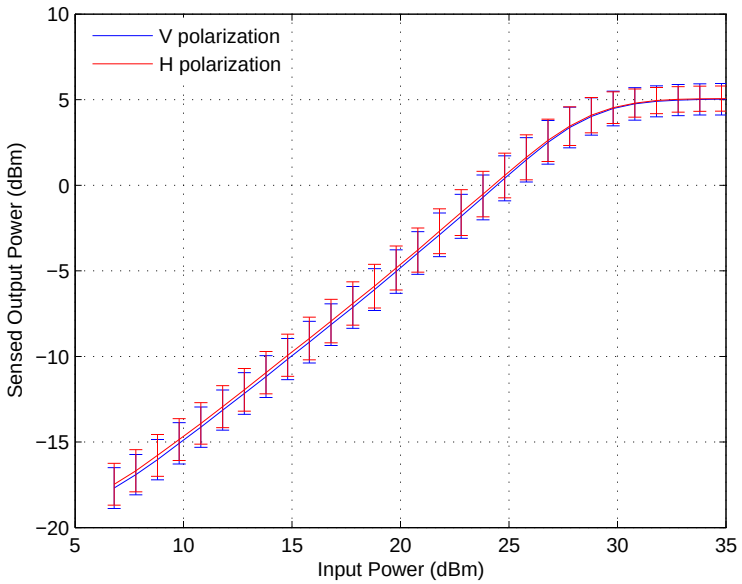

Figure 4.17: Average output power and error bars versus input power

In order to operate the array in compression, the scaling factor is chosen equal to the maximum S_{21} across the array. Figure 4.18 shows the corresponding amplitude (compressed gain) and phase distribution for the transmission coefficient S_{21} in both polarizations when measured in state zero. The amplitude errors are less than 0.89 dB RMS and the phase errors are less than 31.6^o RMS, while the maximum S_{21} is 1.3 dB.

After choosing the scaling factor, the nearest state algorithm is used to determinate the calibration settings that provide the uniform illumination to array. In addition, array calibration is performed using the standard calibration to compare the results obtained from both methods. The amplitude and phase settings for the vertical polarization obtained from the two calibration methods are depicted in Figure 4.19. The top graph shows that the amplitude distribution is not affected by the calibration as expected. While the lower graph shows that phase distribution obtained from the nearest state algorithm is better than the one obtained with the standard calibration. Table 4.4 shows that the RMS phase error obtained with nearest state algorithm is even better than the theoretical error (Calculated from phase shifter characteristic). The improvement is due to the extra phase shift created by the attenuator.

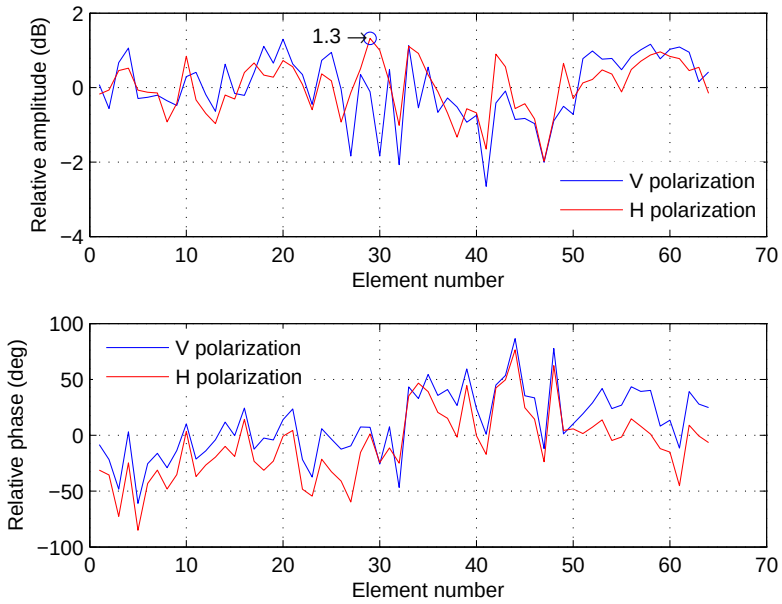

Figure 4.18: Measured transmition coefficiente S_{21} for transmit array at state zero. Top: Amplitude distribution. Bottom: Phase distribution

Table 4.4: Comparison of RMS excitation errors for calibrated array in transmit

Method	RMS amplitude error (dB)	RMS phase error (degrees)	Total error (σ)
Theoretical	-	1.59	0.102
Standard calibration	0.82	2.02	0.105
Nearest state algorithm	0.82	1.01	0.100

Unfortunately, due to laboratory safety issues, the radiation patterns from transmit array could not be measured in the near-field range. Rather, the patterns are predicted using (4.13). Figure 4.20 shows the predicted far-field radiation patterns at the central frequency 9.36 GHz. The patterns achieved peak sidelobe levels of -12.4 dB and -13.3 dB in the vertical and horizontal polarization respectively. The peak sidelobe level for the vertical polarization exceeds in 0.9 dB the expected value for a uniform distribution. This degradation is due to RMS amplitude errors of the implemented amplitude, which can not be calibrated.

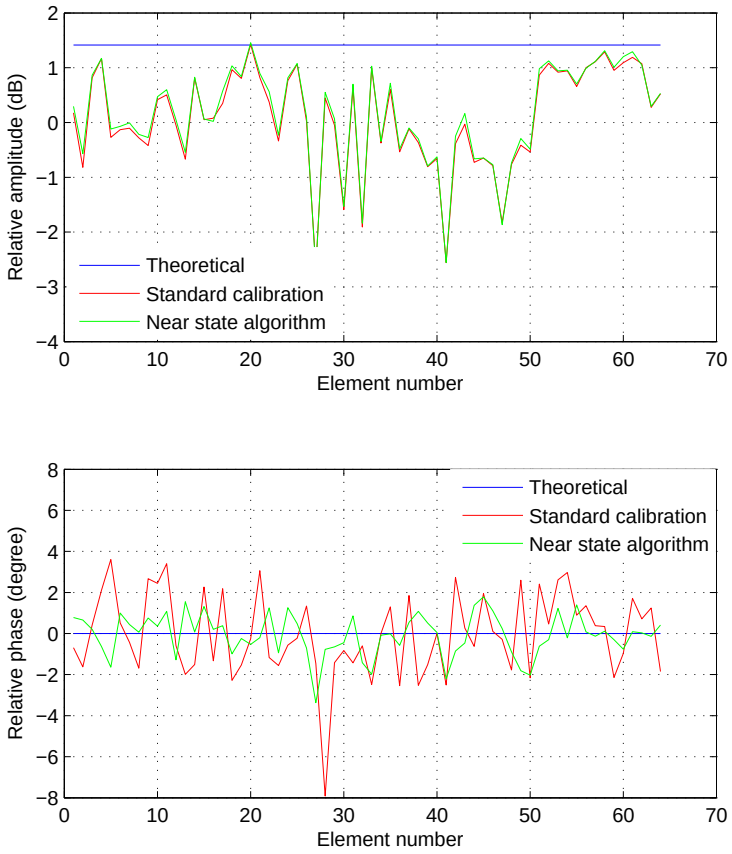

Figure 4.19: Comparison of calibrated transmission coefficient S_{21} in transmite mode. Top: Relative amplitude distribution. Bottom: Relative phase distribution.

4.5 Scanning performance

The purpose of this test is two-fold: first, to evaluate the array calibration at different scan angles. Second, to measure the array characteristic as a function of the scan angle. Part of this information will be useful to define the radar system equation. During the test, the array was calibrated such that it could generate 255 beams (using 25dB Taylor taper) at each polarization, ranging from -45^o to 45^o with uniform increment of 0.354^o. Calibration data is stored in the T/R module's beamtables in order to measure all beams in a single pass of the near-field scanner. Measurements in receive mode are only performed.

The procedure to measure the radiation pattern in a polarization is described below:

1. Calibrate the array for 255 beams and load the setting in the module's beamtables.

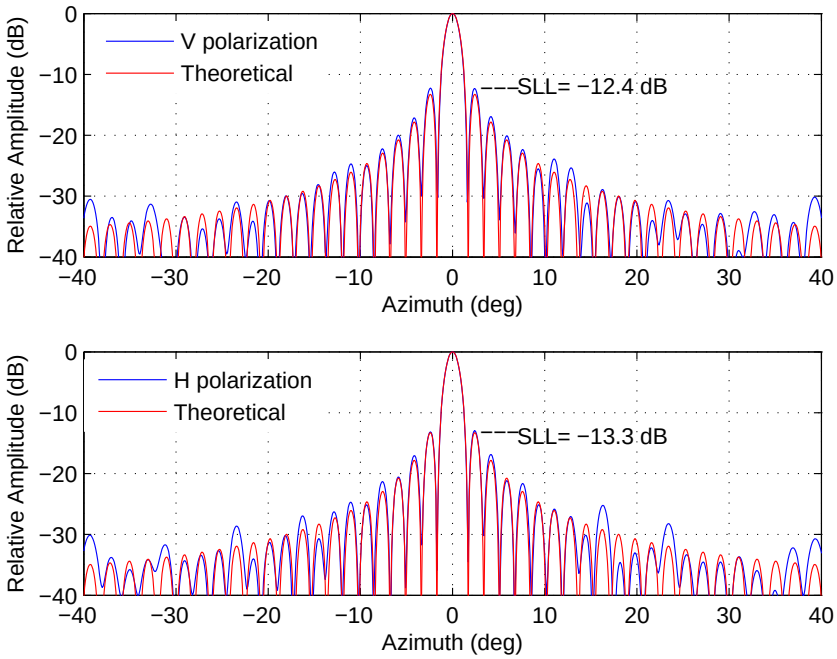

Figure 4.20: Theoretical and predicted azimuth far field patterns at 9.36 GHz. Top: V polarization. Bottom: H polarization.

2. Load sequence table for the first 8 beams (4 beams for receive and 4 beams for transmit). Transmit commands are loaded with settings that unable the transmit function.
3. Place the NF probe in front the first sampling position.
4. Pulse the array with a duty cycle of 30% until steady-state temperature is reached.
5. Measure the parameter S_{21} for each beam given by the sequence table
6. Load a sequence table for the next 4 beams repeat step 5 and 6 until the last table with the last beam is measured.
7. Move the NF probe to the next sampling position and repeat steps 5 to 7 until the last sampling position is reached.
8. Rotate 90^o the NF probe to measure the cross-polar component and return to step 2.
9. Transform near-field patterns to far-field pattern. Then, apply the theoretical probe correction.
10. Determine beamwidth, sidelobe level, and beam pointing accuracy for each beam.

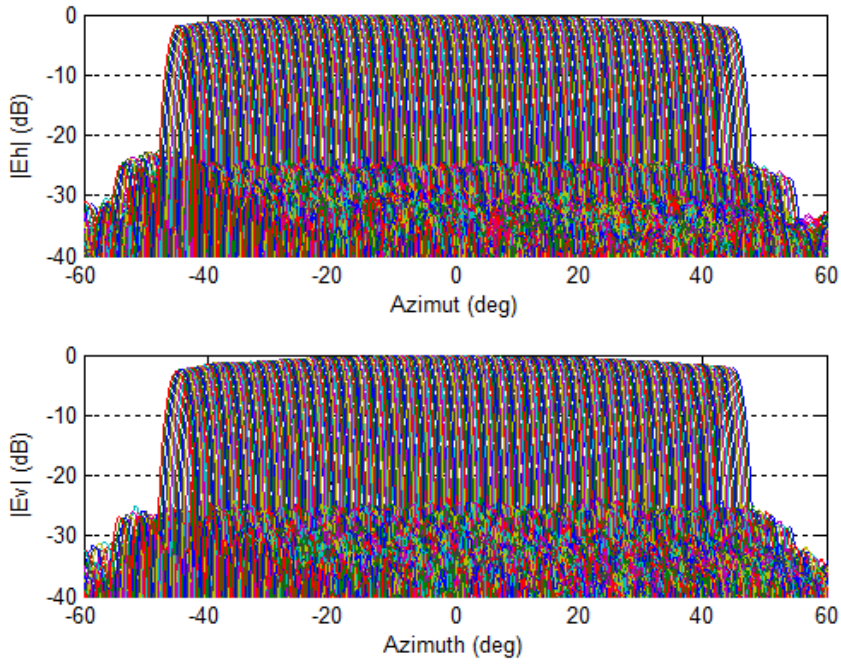

Figure 4.21: Overlay of 255 far field radiation pattern measurements, derived from Near-field measurements. Top: Horizontal polarization. Bottom: Vertical polarization

Figure 4.21 shows the measured far-field patterns (for 255 beams) at the azimuth plane for the main components of each polarization. Patterns have been normalized to the maximum gain at broadside. The density plot looks a little crowded, but one can clearly see how the scanned gain changes with scan angle. The scanned gain rolls off at larger scan angles because the element pattern rolls off.

Figure 4.22 and 4.23 show the co-polar and cross-polar patterns at azimuth plane for both H and V polarization, only 47 beams have been plotted to simplify the data visualization. It is important to note in both figures that calibration only works for the main components, and that the cross-polar patterns are always 30 dB lower than the co-polar patterns. These results corroborate the results of previous measurements that were obtained using element pattern measurements [67]. Additionally, Figure 4.22 and 4.23 also show the beamwidth broadening effect that occurs when the beam is steered off broadside.

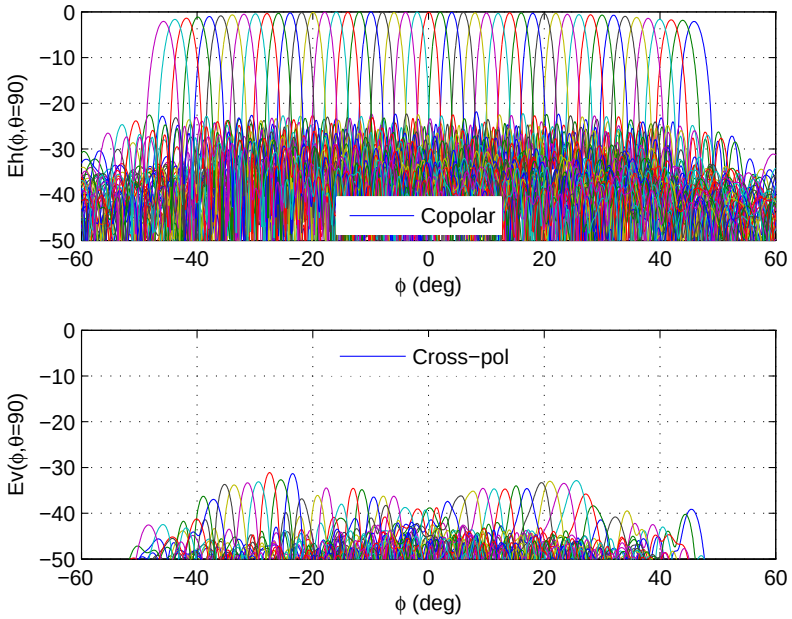

Figure 4.22: Overlay of 47 far field radiation patterns for receive mode, horizontal polarization. Top: Copolar pattern. Bottom: Cross polar pattern

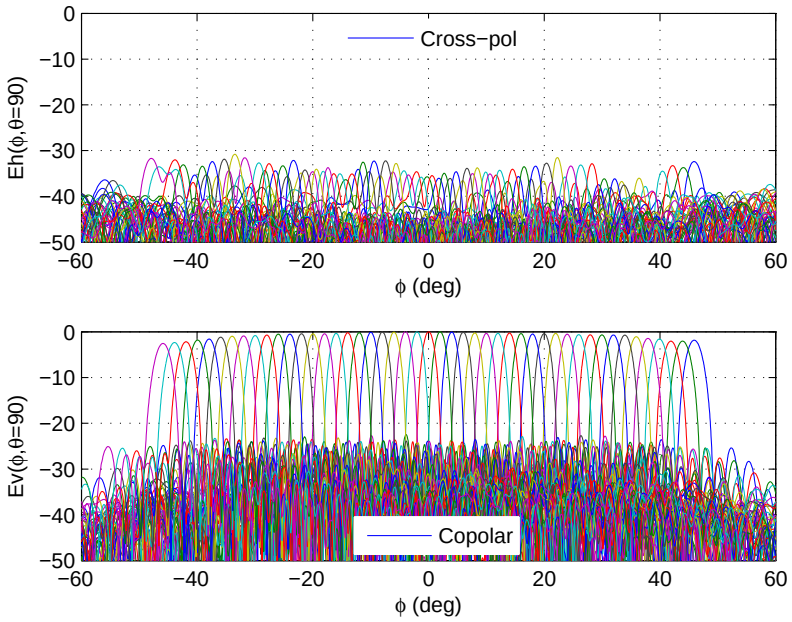

Figure 4.23: Overlay of 47 far field radiation patterns for receive mode, vertical polarization. Top: Cross polar pattern. Bottom: Copolar pattern

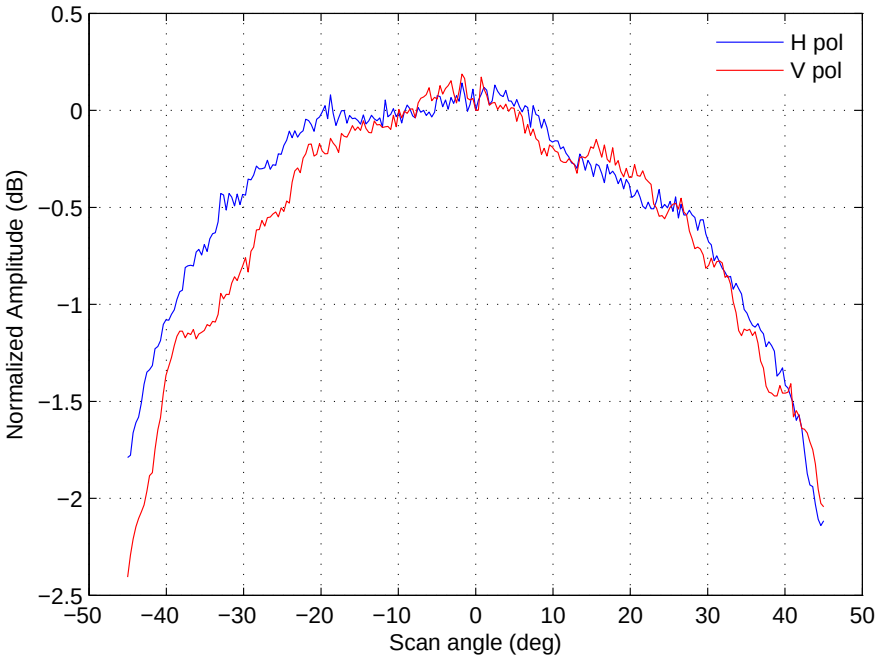

Figure 4.24: Measured gain envelope for receive horizontal and vertical polarization.

The scanning performance is verified by estimating the amplitude and phase of the main beam at the beam scan angle. The gain envelope (also called scanned gain or average active element pattern) for H and V polarization as a function of scan angle is depicted in Figure 4.24. The asymmetry in the plot about 45^o occurs due to the active element pattern roll-off, which depends on the mutual coupling and array tolerances (i.e. variations in the radiating elements or panel misalignment). The gain loss is less than 2.5 dB when the beam is steered to $\pm$ 45^o. The ripple present in the gain envelope is caused by the variance of the main beam peak due to excitation errors. The variance of the main beam peak is directly proportional to the amplitude mean error caused by attenuator quantization errors.

Figure 4.25 shows the main beam phase as function of the azimuth scan angle. The phase for H polarization is almost identical to the phase in V polarization.

4.5.1 Sidelobes

As mentioned above, the calibration goal in receive is to implement a -25 dB Taylor amplitude distribution with low random errors. This illumination creates theoretically a

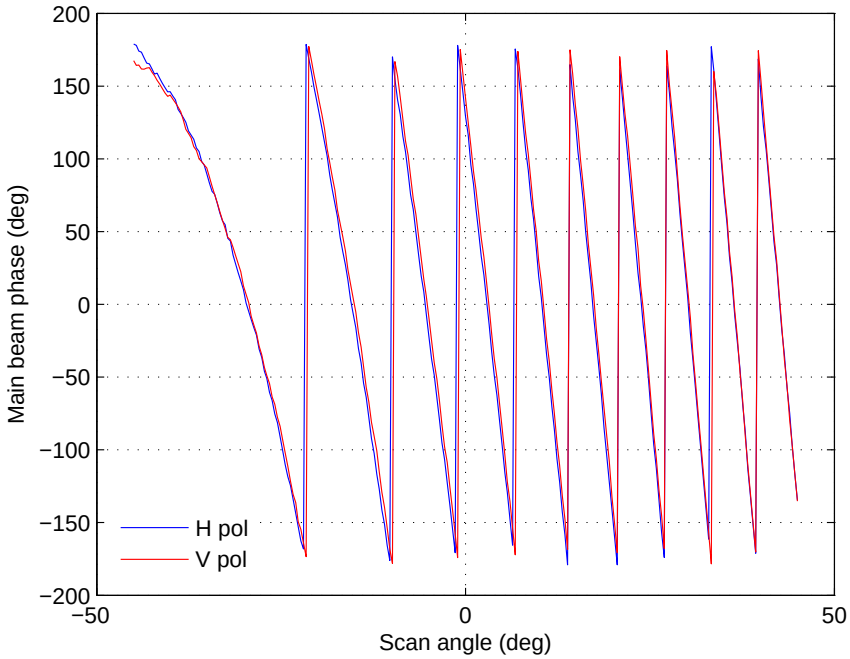

Figure 4.25: Measured phase for main beam peak in receive horizontal and vertical polarization.

radiation pattern having sidelobes that are always below -25 dB level. However, in practice when the beam is steered, some sidelobes can exceed the sidelobe level because of the element pattern roll off. The evaluation of maximum and first normalized sidelobe peaks at both polarizations as a function of scan angle for the calibrated array is shown in Figure 4.26. The sidelobes vary randomly with scan angle because the excitation errors change with the implementation of each beam. While the level for the first sidelobes is better that -24 dB in all the range, the maximum sidelobe increases up to -22 dB when the beam is steered to $\pm 45^o$. The increase is because the gain loss falls off about 2.5 dB at 45^o.

4.5.2 Beamwidth

The half power beamwidth at broadside of a phased array that uses a 25 dB $\overline{n} = 2$ Taylor taper is $\theta_{3dB}(\theta = 0) = 1.76^o$. When the beam is steered to scan angle θ_0, the scanned beamwidth is increased from the broadside beamwidth to $\theta_{3dB}(\theta_0) = \theta_{3dB}(\theta = 0)/cos(\theta)$. The measured and theoretical scanned beamwitdh as a function of the azimuth scan angle

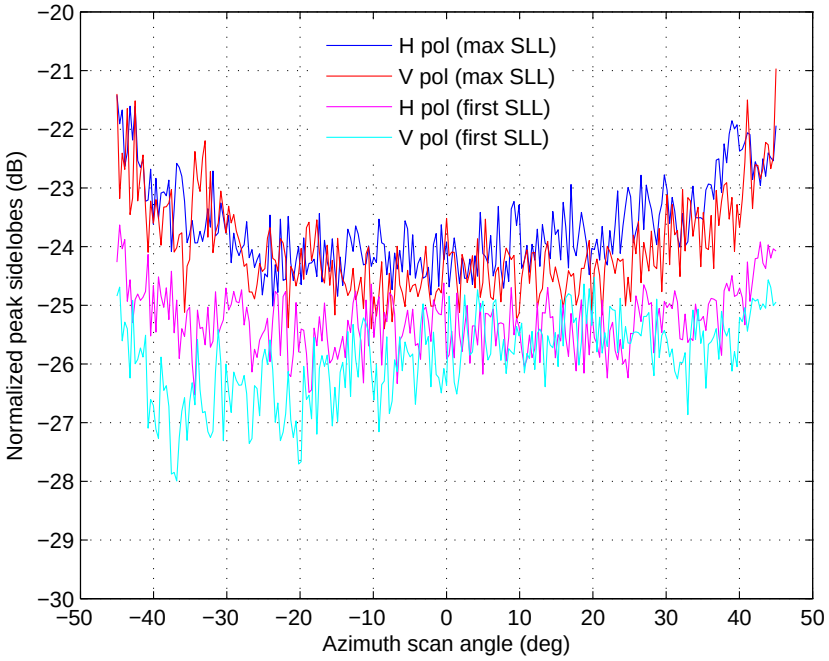

Figure 4.26: Measured sidelobe peaks versus azimuth scan angles.

are shown in Figure 4.27. The results are very good; the beamwidth performance with scanning is virtually identical. The maximum beamwidth is about 2.45^o at $\pm 45^o$, resulting in a 42.4% beam broadening.

4.5.3 Beam Pointing Error

Typically, beam-pointing errors are small in medium and large phased arrays, and when it is given as a fraction of beamwidth, its value increases proportionally with the variance of random errors. For the calibrated array using 255 beams and 0.354^o beam increments, the beam pointing error as a function of the azimuth scanning angle is shown in Figure 4.28. The variance of beam point error with scan angle is originated by excitation errors. In addition, it is noted an anti-symmetric behavior of pointing error, which does not have an explanation. The beam pointing error has a maximum value of 0.06^o and RMS error across the range of 0.0125^o, both values are small compared to beamwidth. The theoretical standard deviations are evaluated using the theoretical values given in Table 4.3 in the

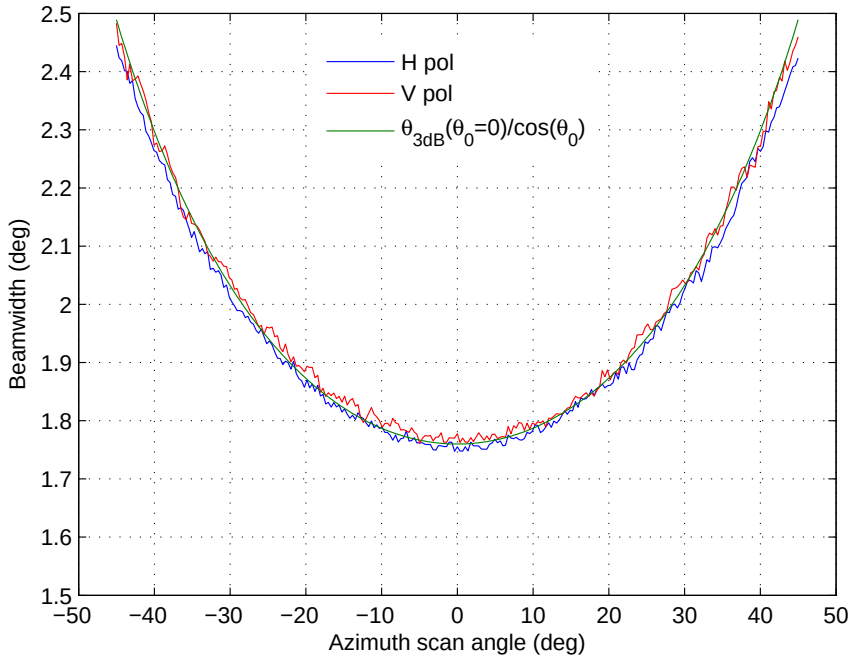

Figure 4.27: Comparison between theoretical and measured beamwith as a function of scan angle.

following equation [68]

$$\Delta\theta_{RMS} = \frac{2\sqrt{3(\sigma_\delta^2 + \sigma_\phi^2)}}{kdN^{3/2}} = \frac{2\sqrt{3(0.0245^2 + 0.0095^2)}}{196.03 * 17x10^{-3} * 64^{3/2}} = 5x10^{-5}rad = 0.0029^o$$

this value is very small compared to the measured value.

In order to demonstrate the minimum scan angle increment that can implemented by the system, the array is calibrated in the scanning range of $\pm 1^o$ using 255 beams with 0.025^o increments (2*RMS beam point error = 2*0.0125). The resulting error for the V polarization pattern is depicted in Figure 4.29. The plot shows that the beam pointing error does not excess the scan angle increment of 0.025^o. The result is interesting because the array can provide excellent pointing accuracy using 6 bit phased shifters with 5.625^o resolution steps.

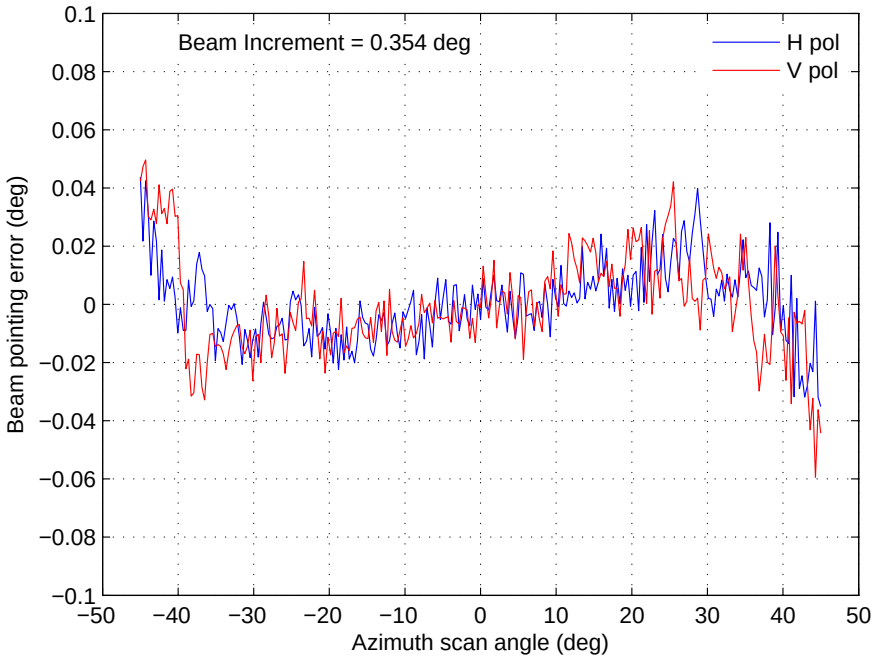

Figure 4.28: Measured beam pointing error as a function of scan angle, derived from patterns with scan angle increments of 0.354^o

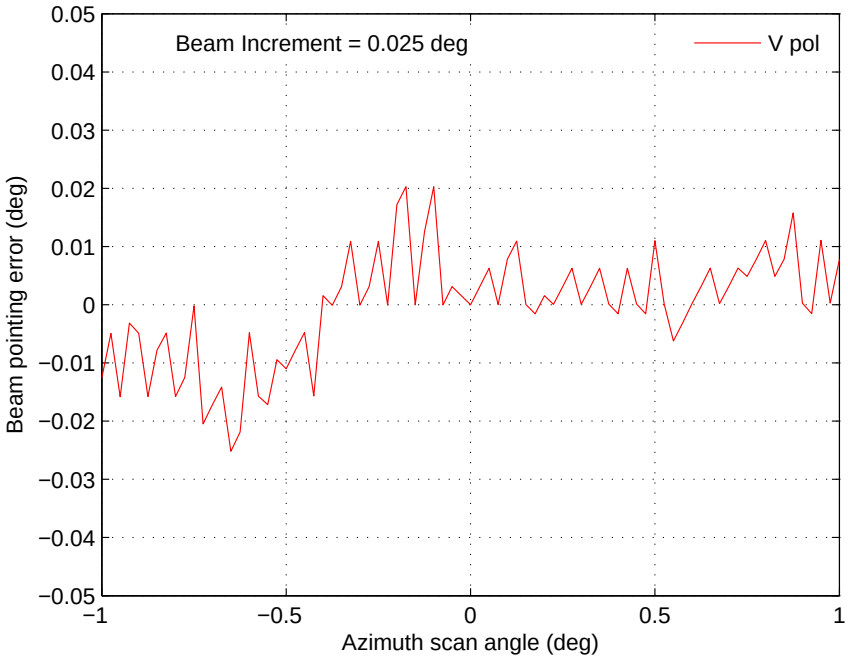

Figure 4.29: Measured beam pointing error as a function of scan angle, derived from patterns with scan angle increments of 0.0025^o.

4.5.4 Active Element Pattern and Pattern Prediction

The measurement of the average active element pattern is important because it can help to answers some questions that arise from the system, for example: are the transmit and receive average element patterns the same?, are the average active element pattern and scanned gain the same?, can the scanning performance predicted from measurements of the element pattern?. Answering the first question can help to demonstrate that all tests and results obtained from the receive array can be also applied to transmit array. Thus, one can avoid measuring the radiation patterns from the transmit array if one has no antenna range facilities to perform such measurements. The second and third question are investigated for the purpose of predicting the array performance.

In this test, the radiation patterns for 64 elements in both transmit and receive mode, and in H and V polarization were measured. At each mode, the near-field data for 64 elements is collected in a single pass of the near-field scanner. Then, the data was processed to obtain the far-field radiation patterns. The embedded element patterns for a set of 64 elements on each mode (RH, RV, TH, TV) are shown in Figure 4.30. The measurement frequency is 9.36 GHz and the azimuth range is $\pm 80^o$. Note that gain variations among patterns are due to hardware differences. Additionally, each element has a different embedded element pattern, which depends on the mutual coupling effect and element positions.

To calculate the average embedded element pattern, it was necessary to align the patterns at broadside so that the broadside response from all elements were the same. Then, at each angular position, the average was calculated. Figure 4.31 and 4.32 show the average embedded element pattern for transmit and receive, in V and H polarizations. The results demonstrate that patterns in transmit and receive are identical in both polarizations. In H polarization, the patterns have a null at around $\pm 62^o$, where a blind spot occurs. The blidness is created by the effecf of surfaces waves close to the position of the grating lobe [67]. While in V polarization, the patterns exhibit a smooth roll off that end at $\pm 90^o$.

The element pattern and mutual coupling effects are subsumed into the average embedded element pattern; which is an important design factor because it describes how the array performs with scan and whether blind angles exist. The overall radiated power is the product of average embedded element pattern and the isotropic array factor scanned to

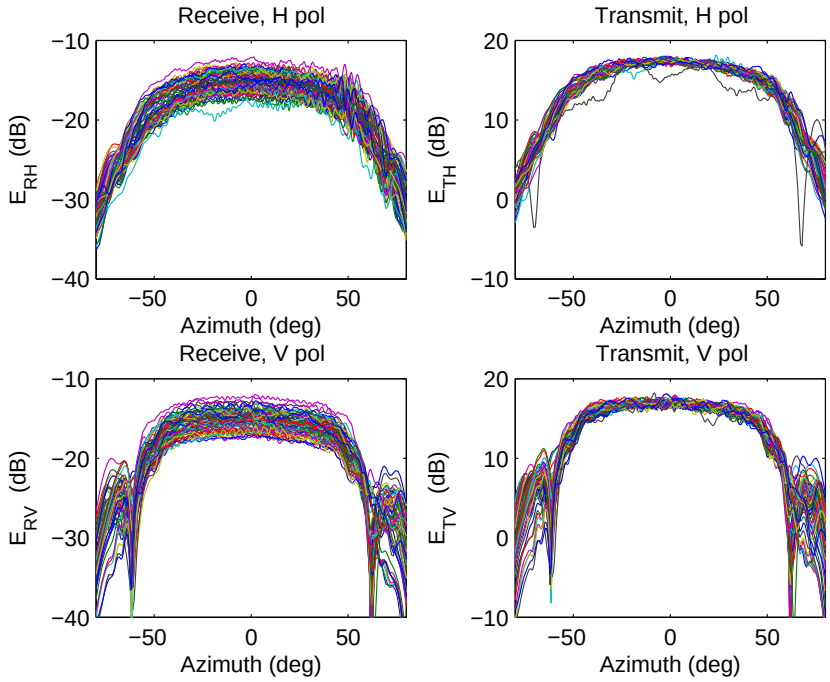

Figure 4.30: Overlay of 64 elements pattern measurements, derived from near-field measurements.

the proper angle (this is represented mathematically in 4.2). Since the average embedded element pattern is an envelope of array gain versus scan angles, its effect is similar to the term "scanned array gain" that has been obtained from a set of scanned radiation patterns when all elements are excited (see figure 4.24). Ideally, the terms "average embedded element pattern" and "scanned array gain" are the same. But in practice, they can differ if the scanned array gain is affected by random excitation errors.

The top graph of Figure 4.33 shows the comparison between the average embedded element pattern and scanned gain for the array in receive and H polarization, in the scanning range $\pm 45^o$ (data is also used in Figures 4.24 and 4.32). It is clear that both curves have the same behavior with scan angles, but the scanned gain is affected by ripples. The amplitude and angular position of each ripple depend on array size and quantization errors that are produced by attenuator and phase shifter settings. While the lower graph of Figure 4.33 shows the comparison between the average embedded element pattern and scanned gain in transmit and H polarization. Note that ripples in transmit are much lower than in receive in

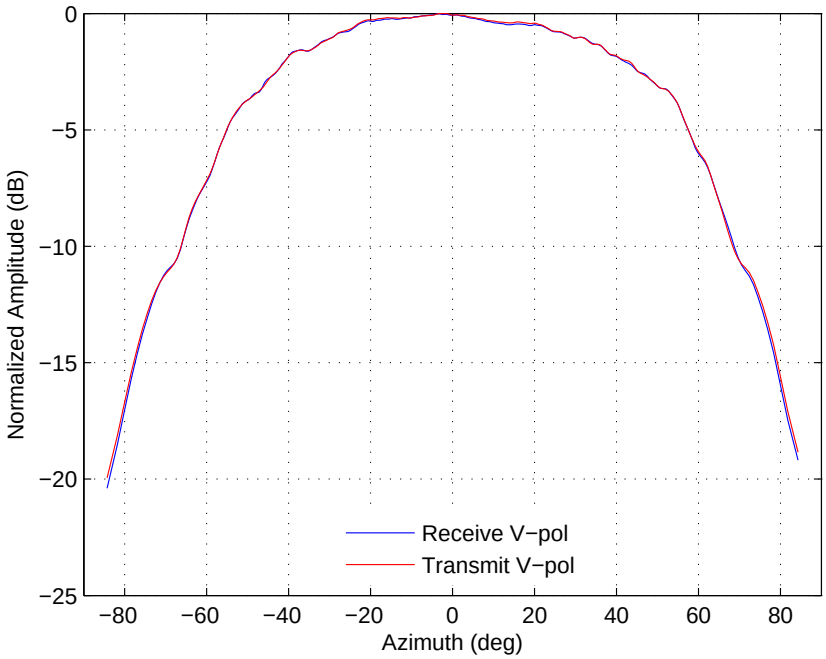

Figure 4.31: Average embedded element pattern for V polarization.

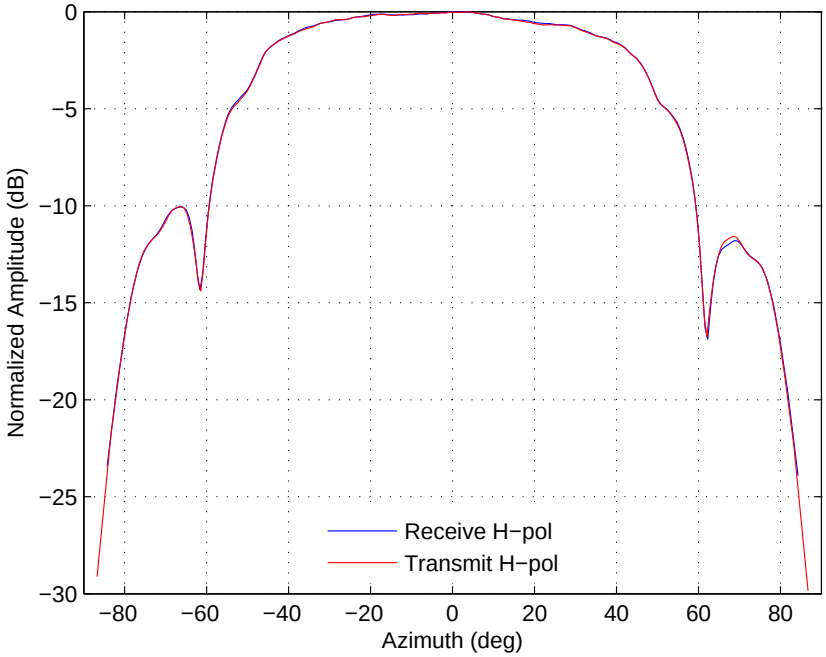

Figure 4.32: Average embedded element pattern for H polarization.

spite of having a larger RMS errors. The ripples are caused by variations in the amplitudes of the main beam with scan angle; the fractional error of the scanned gain at a specific scan angle with respect to the average gain is proportional to the mean amplitude error of elements, which depends on the attenuator quantization error. It should be pointed out that for large arrays this effect is negligible, but in small and medium-size phased array, the ripple effects can be notable. In transmit mode, on the other hand, the amplitude errors are large because the amplitude cannot be calibrated, but their variance with scan angle is almost negligible because modules operate in compression. As a result, the scanned gain presents low ripples with respect to receive mode.

The data shown in Figure 4.33 is important because it describes how the radar antenna gain (one-way gain) performs with scan angle. Ultimately, this data should be stored in a look-up table or should be fit to a curve in order to calibrate the radar system. Figure 4.34 shows how the radiation pattern is affected by the average embedded element pattern roll-off.

The average embedded element pattern can also be used to predict the radiation pattern and scanned gain of a phased array using (4.18). Typically, the radiation patterns of a phased array are measured in an antenna test facility before fielding the radar (or during radar calibration in the field). Once the radar is deployed, the patterns must be predicted routinely to verify that the array is operating within the specifications. This can be done during array maintenance. There are two scenarios where the pattern prediction can results necessary: first when the array is recalibrated, and second when the built-in-test system detects the presence of failed modules.

For the purpose of demonstrating the utility of pattern prediction, two examples are shown in Figure 4.35 and 4.36. In Figure 4.35, the comparison between measured and predicted radiation patterns at V polarization for a 0^o scan angle is shown. Measurements are made when there are not failed modules. The results are good based on the sidelobe level and null locations. In Figure 4.36, the comparison between measured and predicted scanned array gain is shown. The predicted curve is obtained after predicting 255 different beams (using eqn. (4.18)). Clearly, the agreement between measurement and prediction is

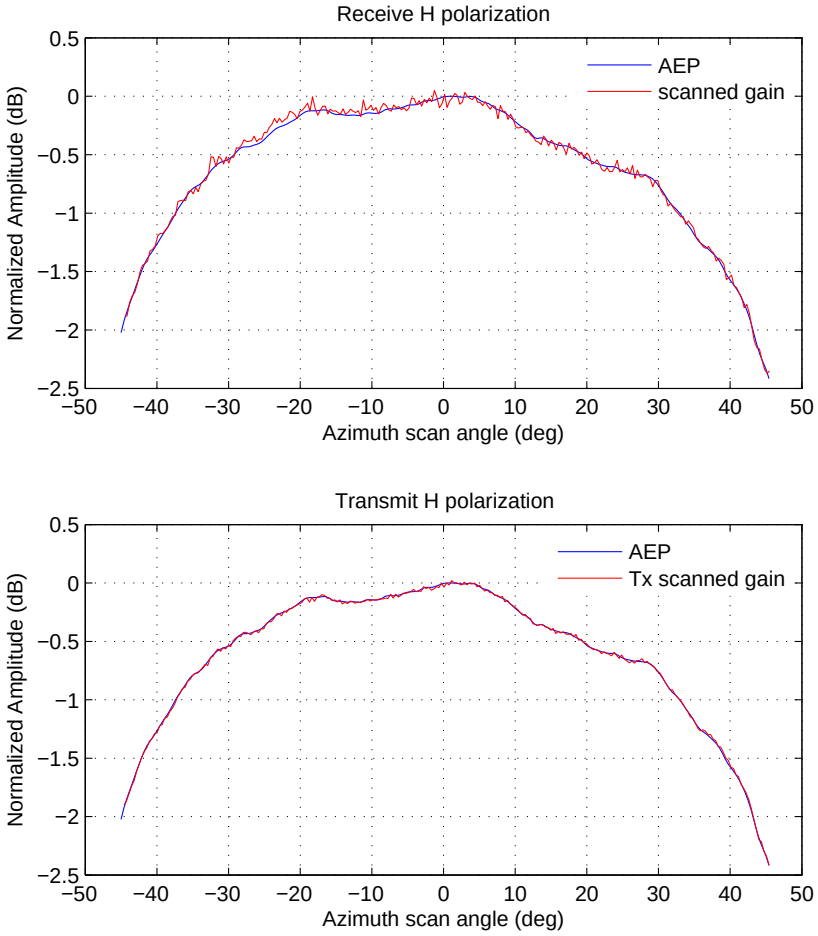

Figure 4.33: Comparison between average embedded element pattern and scanned gain in H polarization.

good in terms of roll off and ripples locations. An error of 0.042 dB RMS was calculated between the two data sets.

4.6 Temperature Compensation

In the temperature test described in section 4.3.3, the element characteristics were measured as a function of T/R module temperature, as it is shown in Figure 4.13. Results revealed that the gain in decibels (dB) and phase in both transmit and receive mode vary linearly with temperature. For the temperature range from 34^oC to 52^oC, the gain drift was 1.1 dB in receive and 0.16 dB in transmit. It is important to note that a radar system

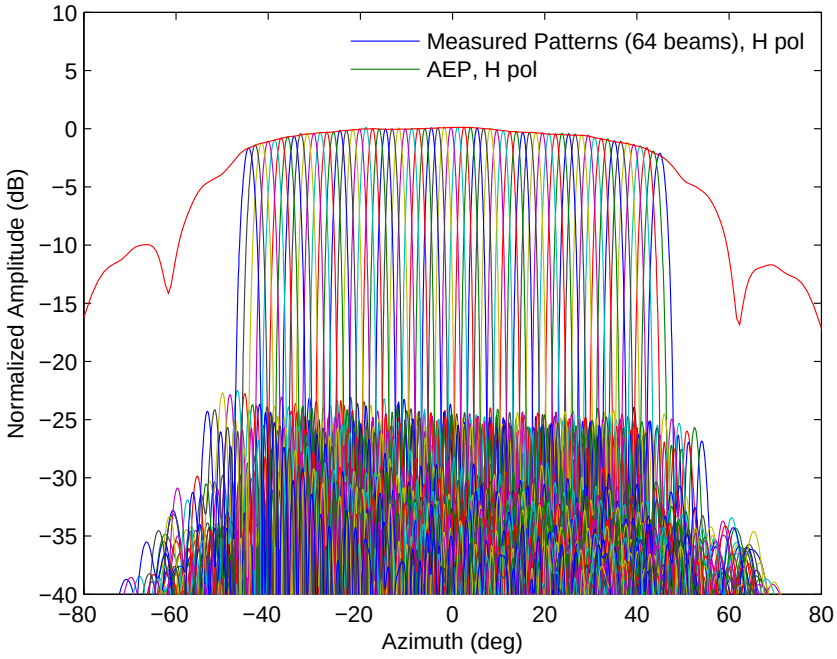

Figure 4.34: Overlay of average embedded element pattern (AEP) and 64 radiation pattern measurements.

using this array, in the same temperature range, will have a two-way antenna gain drift of 1.26 dB. However, the drift can even result in a larger value if the temperature range is extended. For example, a two-way gain variation of 3.64 dB can be obtained if the temperature is varied from 0^oC to 52^oC. Evidently this can cause problems of bias in the radar reflectivity measurements. To avoid the bias errors, the array gain must be calibrated for different temperatures.

To demonstrate the temperature compensation technique in the system, the receive array was calibrated for providing a constant gain in the range from 34^oC to 54^oC. We assumed that reference temperature is 34^oC and that 14 beamtables are enough to calibrate the array at 14 different temperatures. The two-way gain drift in dB of each module is given by

$$|\Delta S_{21}| = (A^R + A^T)(t_H - t_L) = (0.061 + 0.009)(54 - 34) = 1.4dB$$

where A^R and A^T are the gain variations over temperature in receive and transmit, respectably; which values have been characterized in section (4.4.3). For a look-up table with

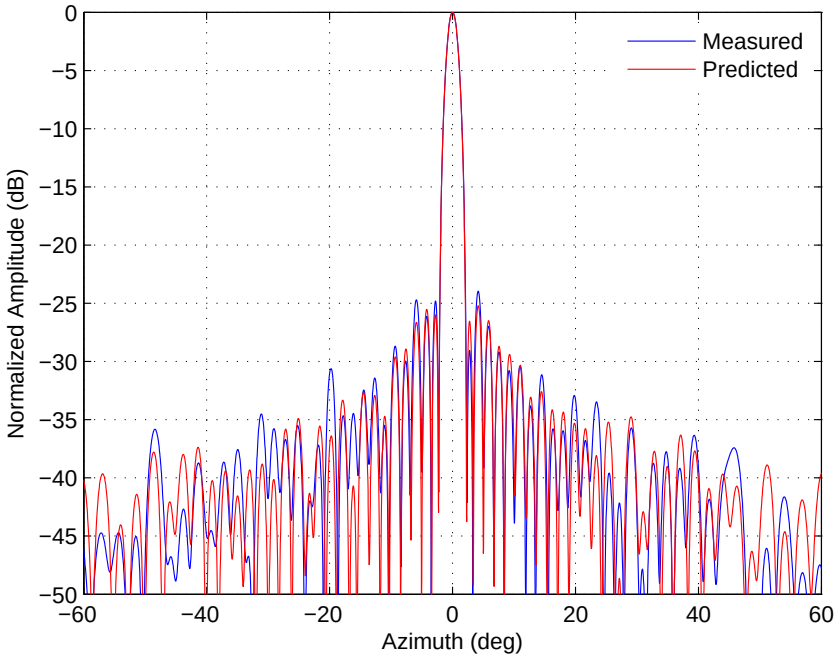

Figure 4.35: Comparison between measured and predicted radiation patterns at broadside.

14 beamtables, the gain increment between tables is $\Delta G = 1.4dB/14 = 0.1dB$; which implies that array gain is incremented in intervals of 0.1 dB. Similarly, the temperature step (temperature least significant bit) between beamtables is $LSB_{temp} = \Delta G/(A^R + A^T) = 0.1/(0.061 + 0.009) = 1.4286^oC$; which implies the array gain must be adjusted in temperature intervals of 1.4286 ^oC. Therefore, the beamtables are calculated for temperature values t= 34, 35.43, 36.86, 38.29, 39.71, 41.14, 42.57, 44, 45.43, 46.86, 48.29, 49.71, 51.14, 52.57. To select the beamtable, the average temperature of T/R modules must be computed. Then, the temperature index (t_n=0,1,2,...13) that address the beamtable is computed as

$$t_n = round\left(\frac{t - t_0}{LSB_{temp}}\right) = round\left(\frac{t - 34}{1.4286}\right)$$

where t is the average temperature in the T/R modules. The index t_n is calculated and formatted with other settings into binary commands by the array controller. Ultimately, these commands are broadcasted to T/R modules to control the beamtables.

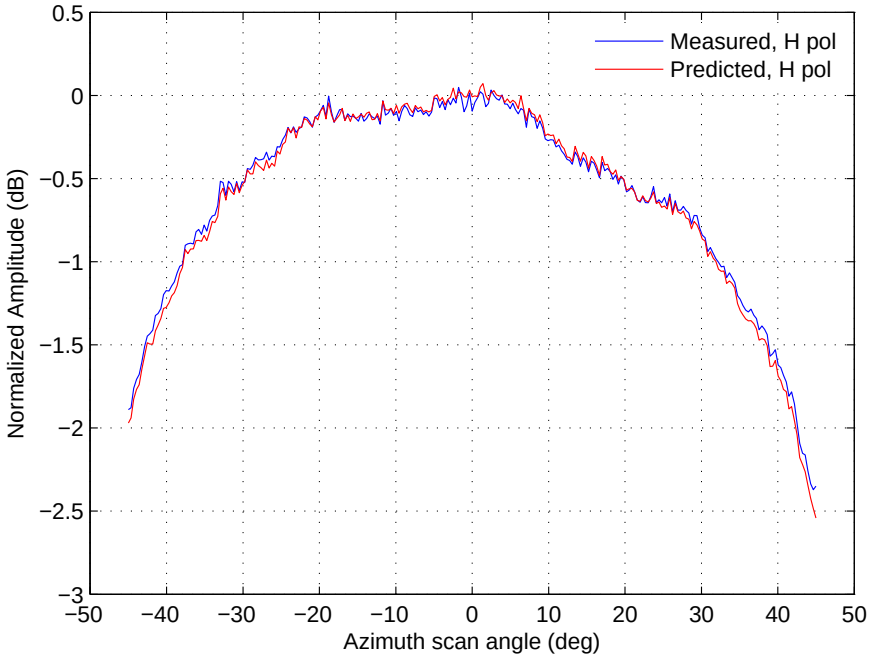

Figure 4.36: Comparison between measured and predicted scanned gain in receive H polarization.

To calibrate the array, one must choose a scaling factor at least 1.4 dB less than the lowest S_{21} at state zero (see Figure 4.14) As demonstrated in the section 4.4.4, an initial scaling factor of -39 dB was used to calibrate the receive array. However, to perform the temperature compensation here, the scaling factor is chosen to be -41 dB. Thus, any gain degradation due to temperature can be compensated by increasing element gains from -41 dB to -39 dB. Now, using the values computed in section 4.4.3, $\alpha_R = 0.007$ and $\alpha_T = 0.001$, in (4.23) and substituting, $t - t_0 = 1.4286 t_n$, the calibration algorithm for this problem is defined as

$$[att^R(n,\theta_0,t_n), phs^R(n,\theta_0,t_n)] = \underset{att,phs}{argmin}||S_{21}^R(n,att,phs,t_0)e^{-0.008(1.4286t_n)}$$

$$- S_{21,theo}^R(n,\theta_0,t_0)||$$

$$S_{21,theo}^R(n,\theta_0,t_0) = v_n S_{21,ref}^q = 10^{-41/20} a_n e^{jnkdsin(\theta_0)}$$

$$\text{for } t_n = 0,1,2,..13$$

For this test, the receive array at vertical polarization was used. Beamtables were created to implement 47 beams in the scanning range $\pm 46^oC$, using uniform beam increments of 2^oC. Here, the number of beams has been reduced to save time during the pattern measurements. A simulation was carried out to predicted the scanned gain and gain increment for each of the beamtables as shown in Figures 4.37 and 4.38, respectively. In Figure 4.37, each gain curve has been normalized by the broadside gain corresponding to beamtable t_0, which has been computed for the reference temperature 34^oC. Note that as the temperature index increases the scanned gain also increases, as expected. Therefore, the gain loss due to an increase of temperature can be compensated with an increase in the array gain. Figure 4.38, on the other hand, shows the relative gain increment of each beam with respect to the scanned gain at 34^oC (BTt_0). The predicted increment between curves, after averaging the 47 beams, was found close to the theoretical gain increment of 0.1 dB. The results indicate that despite the gain resolution steps of 0.5 dB (attenuator LSB) in the T/R modules, the array gain can be controlled in steps of 0.1 dB.

During the test, the temperature of T/R modules was adjusted arbitrary with the speed of the fan array. At each temperature (in steady-state), the radiation patterns were measured to evaluate the gain stability. The beamtables were selected by the computer after averaging the temperature in the T/R modules. Figure 4.39 shows the relative scanned gain obtained from radiation pattern measurements at 5 different temperatures (t = 34.1^oC, 36.9^oC, 38.5^oC, 46.0^oC, 51.0^oC) for the central frequency of 9.36 GHz. The calibration settings corresponding to the gain curves shown in the plot correspond with the data stored in beamtables t_0, t_2, t_3, t_8, and t_{12}. The fact that all the curves remain relatively at the same level at the testing temperatures demonstrates the temperature compensation technique

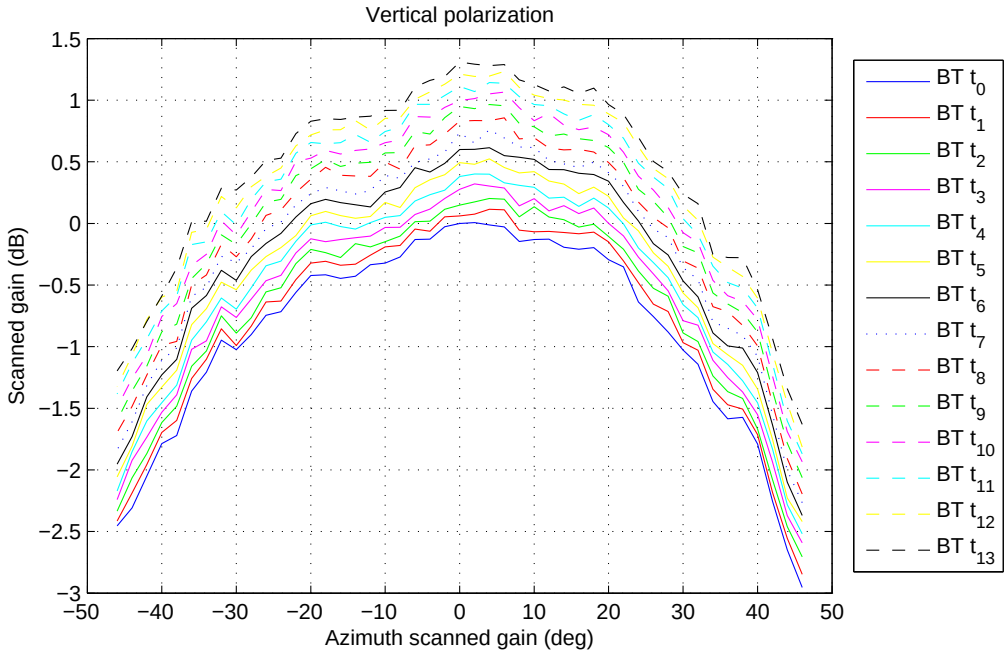

Figure 4.37: Predicted scanned gain for different beamtables as a function of scan angle.

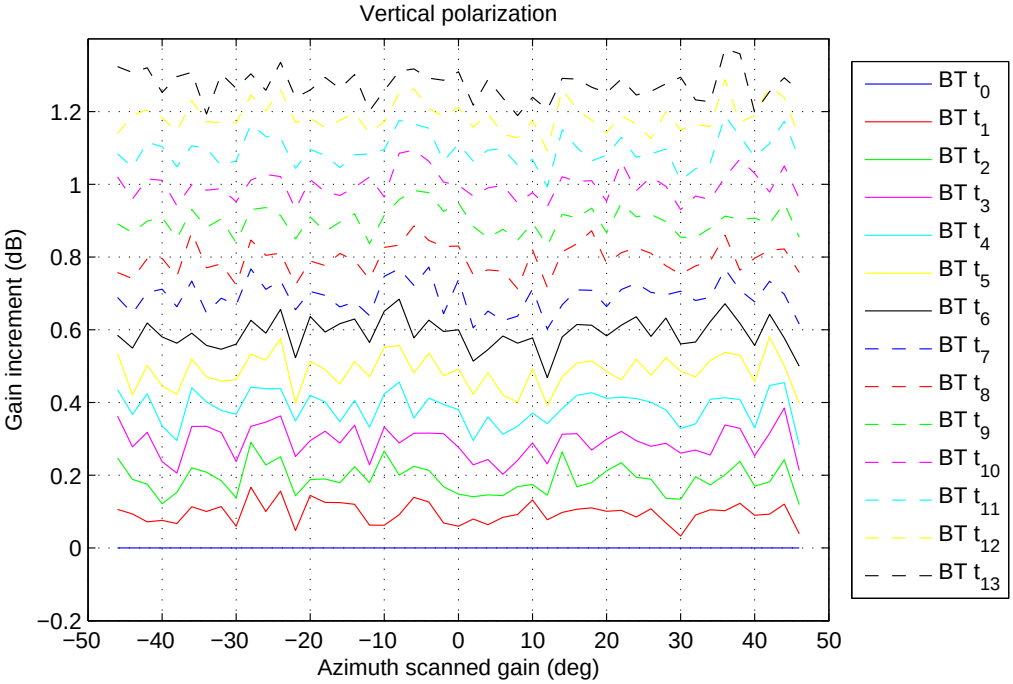

Figure 4.38: Predicted gain increment between beamtables t_n and t_0.

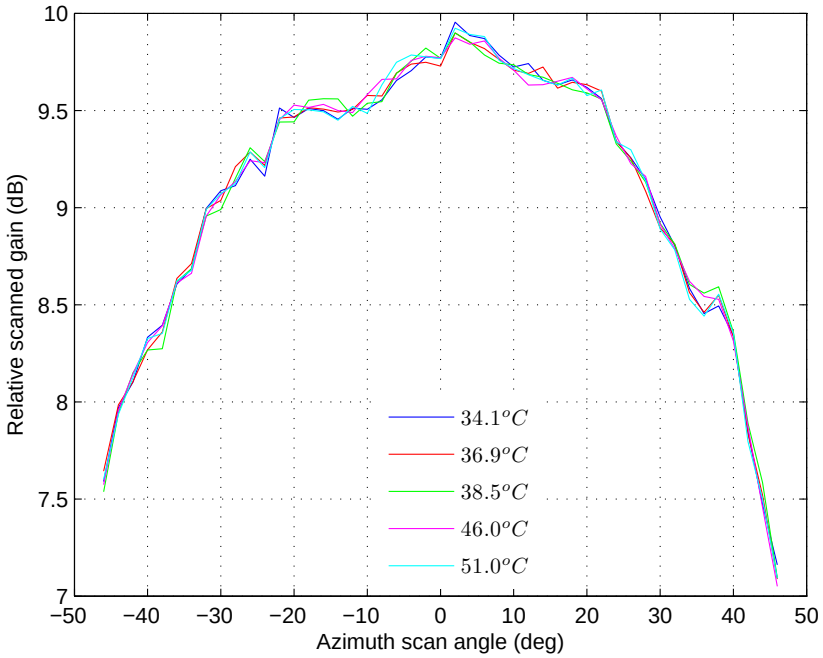

Figure 4.39: Scanned gain measuremenst at different temperatures. Derived from 47 patterns

works. To estimate the resulting gain drift, each gain curve is subtracted from the reference gain curve at 34.1^oC. Then, the resulting points are averaged to get the average gain drift over scan angle. The comparison of the average gain drift with and without temperature compensation is made Figure 4.40. The gain drift is quite low when the temperature compensation system is used, being 0.03 dB the maximum value obtained from the testing temperatures.

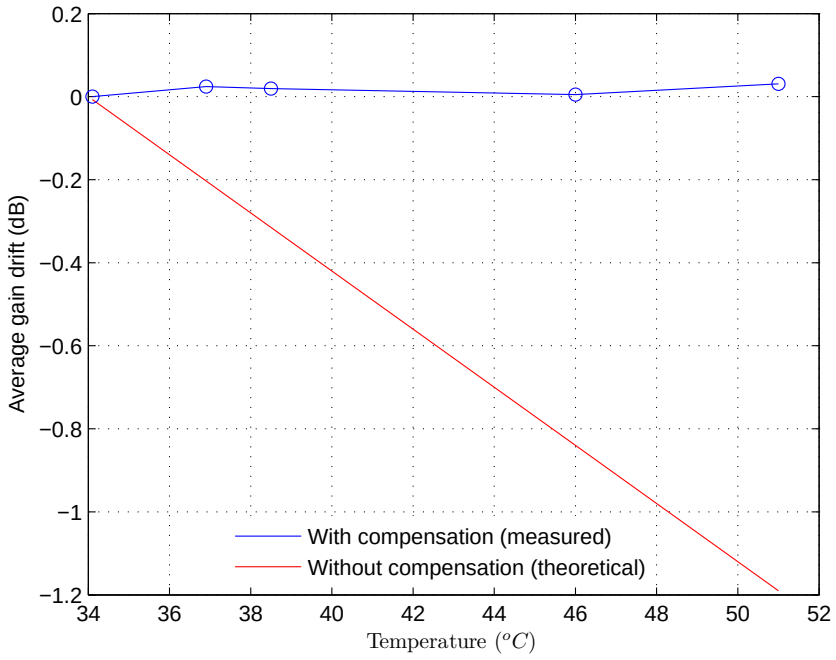

Figure 4.40: Gain drift with and without temperature compensation.

CHAPTER 5

INTERNAL CALIBRATION

5.1 Introduction

Weather radar systems require some level of calibration in order to estimate accurately the precipitation. There are basically two different approaches: the ground truth method and the engineering calibration [69]. The ground truth method tries to correlate the measurement obtained by the weather radar with the measurement obtained by an accurate ground sensor placed right below the volume observed by the radar. The engineering calibration is based on the use of the weather radar equation, which relates the features of radar subsystems to the reflectivity of the precipitation. This last approach is the most used method to calibrate weather radars.

In general, the engineering calibration requires the entire knowledge of the radar parameters to be able to perform the calibration. The parameter list include the transmit power, antenna gain, receiver gain, and system losses. Most of the time these parameters or their combined effect in a radar is not precisely known. The purpose of calibration is to determine directly or indirectly these parameters or their combined effect such that they can be included in the radar equation. A classic method for calibrating the radar parameters is to calibrate the receive power using a reference target of known radar cross section [70]. Usually, this external calibration method can only be realized one of few times during the radar deployment.

The other type of calibration, “internal calibration”, deals with variation over time of radar parameters. This may include, for example, the transmit power and receiver gain. Internal calibration can be performed using a ”calibration loop”, a special circuit that samples radar internal signals and measure gain variations. A calibration loop can be easily implemented in radars with single transceivers and single antennas, but its implementation in active phased array radar is more complex and costly because of the number of elements.

An example of this type of calibration is discussed in [11]. In this work, the calibration loop comprises several couplers and an N-way power divider connected to the test port of each T/R module.The system measures the characteristics of each individual element and uses the data for antenna gain monitoring, which is obtained by processing all measurements. Unfortunately, future low cost phased array radars may not be designed this feature as a way to reduce cost. For these systems, other techniques must be employed to monitor and calibrate the array gain.

Some of the problems that might affect the gain of a phase array are: external temperature, T/R module failures, and array excitation errors. The temperature and failures affect the radiated power and receive beamformer gain. Failures and excitation error reduce the antenna directivity gain in both transmit and receive. When all these effects are combined, the net effect can be so significant that it might lead to a degradation of the radar performance. Such degradation can cause a reduction in the transmitted and received power or create gain imbalance between polarization channels. Unless these effects are compensated, the precipitation measurements will be affected by a bias error. When this occurs, we should pay attention to the accuracy of the measurements. For precipitation estimation, it is desirable that weather radars provide an accuracy of 1 dB in reflectivity, 0.1 dB in differential reflectivity and low depolarization ratio.

Some of the problems affecting the stability of phased arrays can be compensated by hardware, for example, the gain variation due to temperature changes can be compensated by adjusting the element gain or by using a thermal control system. There are also some cases where neither of these solutions is appropriate for an array, either because the cost of thermal control or because elements operate at maximum gain to get the highest possible sensitivity, without leaving a gain margin to compensate the temperature. On the other hand, there also exist other problems that affect the radar stability and that cannot be compensated such as the failed modules. Systems like that, where temperature changes and failures can be not be compensated by hardware, the only possible solution to reduce the errors in radar measurements is to calibrate the radar system constant over time. For a phased array system, the radar constant (2.36) is given as

$$C_R = \left(\frac{1024ln(2)\lambda^2}{c\tau\pi^3|K|^2\theta_{3,br}\phi_{3,br}}\right)\left(\frac{l}{P_t G_{a,tx} G_{a,rx}}\right) \tag{5.1}$$

The first factor on the right side of (5.1) contains physical constants and system constants that are known and not necessary vary with system variations. The second factor contains parameters which vary over time, for example P_t might change because of component degradation in the up-converter, a way to track its degradation over time is by means a calibration loop in the transmit array input. Additionally, the second term includes the parameters $G_{a,rx}$ and $G_{a,tx}$, both with characteristics that depend on temperature and failures. The problem with the calibration of $G_{a,rx}$ and $G_{a,tx}$ is that both includes the effect of directivity gain, and it is clear that their values cannot be measured directly with an internal calibration network. The motivation of this work is to use the definition of $G_{a,rx}$ and $G_{a,tx}$ (equation 2.27) to estimate their degradation over time, for this purpose the performance of each array element must be measured with a low-cost calibration technique.

Usually, array elements are monitored and maintained by means of calibration signals that are injected into each element. The calibration signal can be injected through couplers and calibration networks [11, 71], or by coupling with external reference antennas [13], or even by mutual coupling between radiating elements [12]. The comparison of a previously measured (measurement in the field) and stored (factory measurement) data leads to the detection of failed modules or element gain variations. For low cost phase array systems, the signal injection technique most suitable, is the one based on mutual coupling because of the minimum hardware requirements. To obtain accurate measurements with this technique, the antenna environment in the field should be similar to the one found in the factory, without external interference that could affect the measurements. Unfortunately, in some systems, for example air cooled X-band phase array radars with flat radome covering the aperture, this condition is sometime difficult to meet because of the variant ambient temperature and precipitation. In fact, if the array calibration is performed at a temperature different from the calibration temperature, the comparison between data taken in the field and factory data will be affected by a bias. Unless this bias is removed, the calibration of elements with gain and phase drift will be affected by quantization errors. The precipita-

tion can also affect the array environment, for example the water accumulation over the array aperture can change the transmission and reflection properties of the radome [72], inducing error in the measurements. Based on the above limitations and array needs, the use of mutual coupling measurements as calibration technique for both array and radar are investigated.

This chapter describes and demonstrates experimentally several calibration techniques for both phased array antennas and phased array radars that take advantage of the inherent mutual coupling in an array. The technique is based on mutual coupling measurements that are made between the dummy elements and active elements of an array. Measurements are used to detect failed modules and gain variations due to temperature or aging components. Results from array diagnostic are used to calibrate both the array elements and radar system constant. Two internal calibration methods for radar are presented. The first method is based on the measurement of the antenna gain by mutual coupling measurements. The second method is based on a mathematical model that includes correction terms that are expressed as a function of T/R module temperature and the number of failed modules. The advantage of this model is that mutual coupling measurements are not needed to detect the gain drift during radar operations; therefore, the radar will not be distracted in performing calibration measurements. Phased array performance degradation due to temperature changes and failures is predicted and experimentally validated by means of measurements made to the scanned gain of an experimental phase array. It is shown that results obtained by correction constants are in good agreement with far-field measurements.

5.2 Theory

5.2.1 Monitoring and Calibration Technique

Before entering in service, all active phased array antennas should be calibrated in a test facility. The purpose of this calibration is to align the array elements and ensure the desired radiation pattern can be implemented. Once this process is completed, and after the array with other radar subsystems have been deployed in the field, the quality of this calibration must be monitored continuously over of the life of the system to ensure that the performance of each active elements hasn't change with time. In practice, this procedure

is performed by a monitoring and calibration system, sometimes called built-in-test. These systems have the purpose of ensuring that calibration aspect of the array elements that may change with time, for example gain and phase, can be monitored and even corrected when the array is deployed in the field; avoiding thus the use of external instruments and equipments for array calibration.

In general, a monitoring and calibration system requires a signal injection technique to monitor the aspects of actives components of an array. For the linear phased array used in this research, the injection technique is achieved by using the mutual coupling between active elements and passive elements. The phased array comprises of 64 active columns of elements and 4 passive columns of elements at each end. The purpose of the passive elements is to reduce the diffraction effect produced by the array edges. Two of these passive elements, one on each edge (see Figure 5.1), are used as reference antenna to transmit or receive the calibration signal. Figure 5.2. depicts the simplified block diagram of monitoring scheme for both transmit and receive array. For the receive array, the calibration pulse is transmitted from the passive element and received by one active element with other elements terminated. The voltage obtained at the array output represents the measurement of mutual coupling for the receive element, which is proportional to the gain of that particular element. In the transmit array, the calibration pulse is transmitted from one active element and received by one passive element. The voltage obtained at the passive element represents the measurement of mutual coupling for the transmitting element.

The requirements that the system must meet to successfully detect any change in active elements is that mutual coupling between array elements and passive element characteristics should not change with time. If this assumption can be made in the system, then any gain and phase deviation measured after initial calibration can be only attributed to the active elements.

During the initial calibration, the array elements are characterized by placing a near-field probe in front of each radiating element and measuring the signal path gain with a network analyzer, as it is explained in chapter 4. The signal path gain of an element includes the effect of RF manifold, cables, T/R module gain, radiating element, and free space mutual coupling. We have assumed that the gain (the transmission coefficient S_{21}

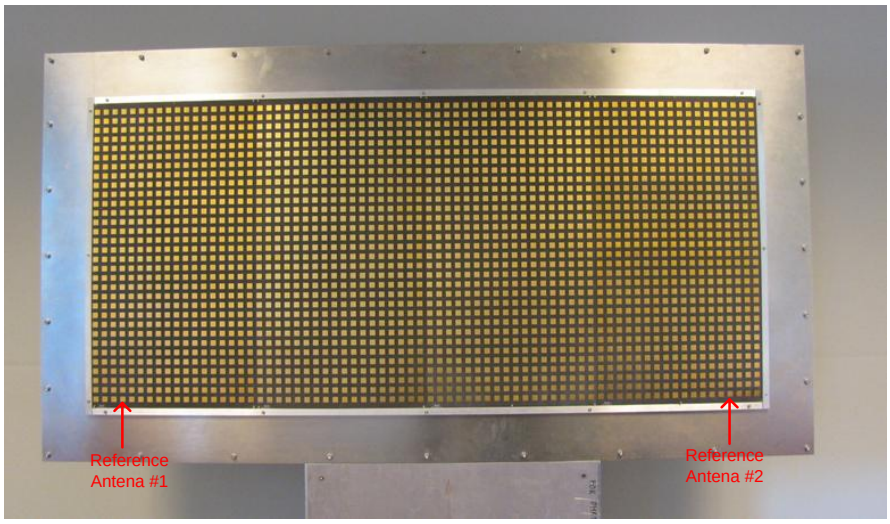

Figure 5.1: Location of reference passive elements on the array aperture.

measured using a network analyzer) is made up of a T/R module normalized complex gain, $W_n(att, phs)$, which depends on the attenuator and phase shifter states, att and phs respectively; the combined effects of RF manifold, RF cables, connectors, radiating element, and T/R module gain when $att = phs = 0$, denoted by the complex quantities u_n; and free space coupling between the radiating element and the sensing probe, denoted by C. Thus, the measured transmission coefficient can be expressed as

$$S_{21}^{q}(n, att, phs) = Cu_n^q W_n^q(att, phs) \tag{5.2}$$

where the superscript q denotes the operation mode on the driven element. For single polarization, $q = R$ (receive) or T (transmit). If the array elements are linear dual-polarized, then q denotes any of following modes: RH, RV, TH, and TH. When measurement are made with the attenuator and phased shifter are set in the zero state, it is assumed that $W_n(0, 0) = 1$, meaning that no insertion loss and insertion phase have been introduced by attenuator and phase shifters. Then, (2) can be reduced to

$$S_{21}^{q}(n, 0, 0) = Cu_n^q \tag{5.3}$$

The quantity $S_{21}^{q}(n, 0, 0)$ is a sample of the initial complex gain of the nth element, but scaled by coupling coefficient C. Next, consider the characteristics of the nth element is

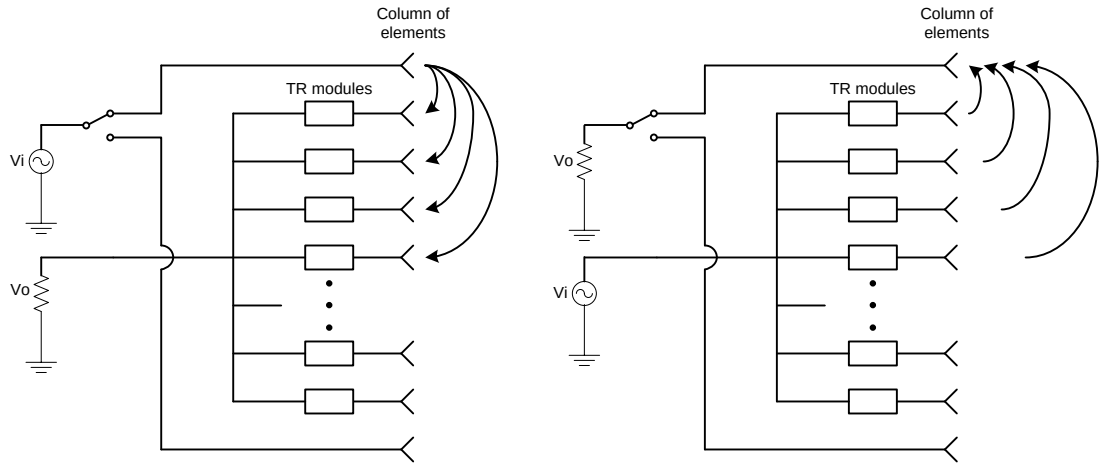

(a) Receive mode (b) Transmit mode

Figure 5.2: Simplified block diagram of monitoring technique based on mutual coupling measurements.

now measured using the mutual coupling from the passive element p. The mutual coupling transfer function $C^q_{m,p}$ can be expressed as

$$C^q_{n,p}(n, att, phs) = u^q_p M^q_{n,p} u^q_n W^q_n(att, phs)$$

or

$$C^q_{n,p}(n, 0, 0) = u^q_p M^q_{n,p} u^q_n \tag{5.4}$$

where u^q_p is insertion loss of the passive element p and $M_{n,p}$ represents the mutual coupling between radiating element n and p. This coupling mutual might include effects of coupling due to surface waves, free space coupling, and reflection. The quantity $C^q_{n,p}(n, 0, 0)$ also represents a sample of the initial complex gain of the nth element, but scaled by coefficient $M_{n,p}$ and u^q_p.

Denote any subsequent multiplicative change in transmit or receive element by K^q_n. Under the assumption that mutual coupling and passive element characteristic do no change with time, the subsequent mutual coupling transfer function measured by the passive element p is

$$C'^q_{n,p}(n, 0, 0) = K^q_n C^q_{n,p}(n, 0, 0) \tag{5.5}$$

Dividing this expression by the initial mutual coupling transfer function, we have

$$K_n^q = \frac{C_{n,p}^{'q}(n,0,0)}{C_{n,p}^{q}(n,0,0)} \tag{5.6}$$

This quantity represents the gain and phase deviation for the nth element. Note that if K_n^q is equal to unity, the element has retained its calibration. On the other hand, if $K_n^q = 0$, the element represents a faulty element. Any other value different from 0 and 1 will mean the element needs to be recalibrated. In general, K_n^q can be used to correct the deviation in the transmitters and receivers.

In an active phase array, it is likely that element characteristics tend to change over time due to aging or because the T/R module has been replaced. When this occurs, the actual characteristics of affected elements must be updated to accept the new changes. This can be done by multiplying the original transmission parameter by K_n^q, which gives

$$S_{21}^{'q}(n, att, phs) = K_n^q S_{21}^q(n, att, phs) \tag{5.7}$$

Because of the new characteristics, drifted elements needs to be calibrated to take into account the changes in the implementation of the element excitation. The calibration can be performed using the nearest state algorithm described in (section 4.3, equ. 4.13), that is

$$[att^q(n,\theta_0), phs^q(n,\theta_0)] = \underset{att,phs}{argmin} \parallel S_{21}^{'q}(n, att, phs) - S_{21,theo}^q(n,\theta_0) \parallel \tag{5.8}$$

where n represents the index of the drifted elements and $S_{21,theo}^q(n,\theta_0)$ is the transmission parameter that represents the desired excitation function. It should be pointed out that the use of (5.8) should be limited to those systems which performance is not temperature dependent. On the contrary, those systems for which performance is temperature dependent, for example in an air-cooled phased array system, it may happen that mutual coupling measurements will be made in the field at unspecified temperature. In this case, the gain drift caused by the temperature effect must be removed from the data to avoid quantization errors. The calibration of drifted elements can be performed using the approached described in (section 4.3.3, equ.4.23)

$$[att^R(n,\theta_0,t), phs^R(n,\theta_0,t)] = \underset{att,phs}{argmin} ||S_{21}^{'q}(n, att, phs, t)e^{-(\alpha^q+\beta^q)(t-t_0)} - S_{21,theo}^q(n,\theta_0,t_0)|| \tag{5.9}$$

where t is the monitoring temperature in the field, t_0 is the initial calibration temperature, α^q represents the amplitude variation coefficient (Neper/^{o}C), and β^q represents the phase variation over temperature (radians/^{o}C). Note that when monitoring and calibration temperature are the same, the expression (5.8) reduces to (5.9).

Once the recalibration is complete, the actual radiation pattern can be predicted to ensure if sidelobes meet the system requirements. The pattern prediction can be made by using the procedure described in (section 4.3.1 equ.4.18), that is

$$f_a(\theta,\phi) = f_{av}(\theta,\phi)\sum_{n=1}^{N} S_{21}^q(n, att^q, phs^q)e^{jnkdsin(\theta_0)} \tag{5.10}$$

where $f_a(\theta,\phi)$ is the average embedded element pattern and $S_{21}^q(n, att^q, phs^q)$ is the implemented excitation, which has been obtained using (5.8) or (5.9).

5.2.2 Radar Internal Calibration

Radars should be calibrated periodically to ensure that aspects of the system that tend to change over time do not affect the measurement accuracy. The calibration can be performed one or few times per day, or even every volume scan as the popular WSR-88D Radar [73]. In this process, internal and external methods are used to estimate the radar parameters that need calibration, results are then used for the radar to adjust the radar constant [74]. The internal method usually calibrates the transmit power and receiver gain by means a calibration loop at the antenna terminal. The external method typically uses the Sun as reference source to calibrate the receive antenna gain. This gain will be basically the same for the transmitting antenna if the radar uses a common antenna for both operations. Unfortunately, same reciprocity principle cannot be applied in active phased array radars if two different aperture illuminations and beamformer networks are used. This limitation leads to the need for developing a new calibration method to correct the gain of active phased array radars.

The calibration method presented below corrects the radar constant from variations that affect the beamformer and directive gain of air-cooled phased array radars. Since the transmit power depends on the beamformer gain, we can also say that the method corrects the transmit power indirectly. The method assumes the radar constant has been obtained by

the engineering approach using a reference target. Let's consider the initial radar constant C_{R0} is give as

$$C_{R0} = \left(\frac{1024ln(2)\lambda^2}{c\tau\pi^3|K|^2\theta_{3,br}\phi_{3,br}}\right)\left(\frac{l}{P_tG_{a,tx}(T_0,F_{rx0})G_{a,rx}(T_0,F_{rx0})}\right) \tag{5.11}$$

where T_0 is the average temperature of T/R modules, F_{t0} and F_{r0} are the number of failed modules in the array at the calibration time. Consider any subsequent multiplicative change (produced by temperature and failure) in the transmit gain and receive gain as C_{tx} and C_{rx} respectively. The subsequent radar constant after changes occur in the array will then has a value of

$$\begin{aligned} C_R &= \left(\frac{1024ln(2)\lambda^2}{c\tau\pi^3|K|^2\theta_{3,br}\phi_{3,br}}\right)\left(\frac{l}{P_tC_{tx}G_{a,tx}(T_0,F_{rx0})C_{rx}G_{a,rx}(T_0,F_{rx0})}\right) \\ &= \frac{C_{R0}}{C_{tx}C_{rx}} \end{aligned} \tag{5.12}$$

when this constant is expressed in dB, it can be writen as

$$C_R[dB] = C_{R0} - C_{tx}[dB] - C_{tx}[dB] \tag{5.13}$$

The purpose of the calibration is to estimate the values of C_{tx} and C_{rx} such that the radar constant can take into account the gain deviation that can caused by temperature changes and failures. Having this correction constants, the equivalent reflectivity can be estimated directly from the received power without bias errors. The value obtained in (5.13) can be used in (5.12) to estimate the equivalent radar reflective for a phased array radar that electronically scan in one dimension.

$$\begin{aligned} Z[dBZ] &= \overline{P_r}[dBm] + C_R[dB] + 20log(r[km]) + 10log(cos\theta_0) \\ &\quad -10log(g_{0n,rx}(\theta_0,0)g_{0n,tx}(\theta_0,0)) \end{aligned} \tag{5.14}$$

This equation also corrects for the scan loss produced by the element pattern and beam broadening effect when the beam has been steered away from broadside.

5.2.2.1 Calibration Based on Mutual Coupling Measurements

Consider an phased array of N elements as the one shown in Figure 2.1b. The array gain seen from the beamformer input (or output) terminal is proportional to the beamformer

gain and directivity gain of the array. If the array uses directive elements arranged in columns, the maximum gain can be expressed as in (2.27)

$$G_a = D_e D_y \frac{|\sum_{n=1}^{N} g_n|^2}{N} = D_e D_y |\sum_{n=1}^{N} g_{b,n}|^2 \tag{5.15}$$

where D_e is the element gain (given by equ. (2.10)), D_y is the directivity of a column, $g_{b,n} = g_n/\sqrt{(N)}$ is the signal gain of nth branch of the array, which includes the effects of RF manifolds, cables and T/R modules. Because D_e and D_y are constants, the antenna gain only depends on the sum of gains of all individual branches. Therefore, any change in the antenna gain can only be caused by changes in the gain of each branch, mainly in T/R modules, whose characteristics can be affected by temperature, aging components, and failures.

Now, denote the antenna gain when the radar is calibrated with the reference target at temperature T_0 as G'_{a0}. This is the antenna gain that will be obtained right after the radar calibration using mutual coupling measurements, and that will be used always as reference data. Let's now assume a multiplicative change in the antenna gain as C_a, the gain obtained from mutual coupling measurements can be written as

$$G'_a = C_a G'_{a0} \tag{5.16}$$

Dividing the current gain by the reference gain value, and using (5.15), we obtain the next ratio

$$C_a = \frac{G'_a}{G'_{a0}} = \frac{|\sum_{n=1}^{N} g'_{b,n}|^2}{|\sum_{n=1}^{N} g'_{b0,n}|^2} \tag{5.17}$$

This ratio can be used to estimate the gain deviations in the transmit or receive arrays. The complex gain of each branch is directly proportional to the values obtained by mutual coupling in (5.7), therefore they can be defined as

$$g'_{b0,n} = S'_{21,0}(n, att, phs) = K_{n0} S_{21}(n, att, phs) \tag{5.18}$$
$$g'_{b,n} = S'_{21}(n, att, phs) = K_n S_{21}(n, att, phs)$$

Note that $S_{21}(n, att, phs)$ is measured during the array calibration using a near-field probe, while K_{n0} and K_n are the gain drift of each element obtained from mutual coupling

measurements at two different times, one during the radar calibration and the other during the array monitoring. When this procedure is applied to both transmit and receive arrays, we can find the gain calibration constant for both arrays, which are defined as

$$C_{a,tx} = \frac{G'_{a,tx}}{G'_{a0,tx}} = \frac{|\sum_{n=1}^{N} g'_{btx,n}|^2}{|\sum_{n=1}^{N} g'_{btx0,n}|^2} \tag{5.19}$$

$$C_{a,rx} = \frac{G'_{a,rx}}{G'_{a0,rx}} = \frac{|\sum_{n=1}^{N} g'_{brx,n}|^2}{|\sum_{n=1}^{N} g'_{brx0,n}|^2} \tag{5.20}$$

These two values should be used in (5.13) to correct the radar constant.

5.2.2.2 Calibration Based on a Deterministic Model

Next, consider the phased array system of N-element shown in Figure 5.3a. Each radiating element is fed by a T/R module with gain $g_n = A_n.g_{max}$, where A_n is the normalized excitation coefficient controlling the amplitude and phase of the nth radiating element, and g_{max} is the T/R module maximum gain. Figure 5.3b shows the equivalent bock diagram of Figure 5.3a, one can assume the directive gain is only controlled by excitation coefficients A_n and that the beamformer gain is only controlled by the T/R module gain. Particularly, the directive gain of a linear array is defined in (2.7) as

$$D_x = \frac{|\sum_{n=1}^{N} A_n|^2}{\sum_{n=1}^{N} A_n^2} = \epsilon_T N \tag{5.21}$$

where

$$\epsilon_T = \frac{1}{N} \frac{|\sum_{n=1}^{N} A_n|^2}{\sum_{n=1}^{N} A_n^2} \tag{5.22}$$

is the tapering efficiency of the aperture. Its value is always less than or equals to 1. It should be mentioned that (5.21) gives the maximum directivity of an array for a certain value of ϵ_T, coinciding when there are not failed elements. Subsequently, from (5.21), the directivity of an array with failed elements can be written as

$$D_x = \epsilon_T (N - F) \tag{5.23}$$

where F is the number of failures in the array. The above equation shows that array directivity tends to decrease when the number of failures increases.

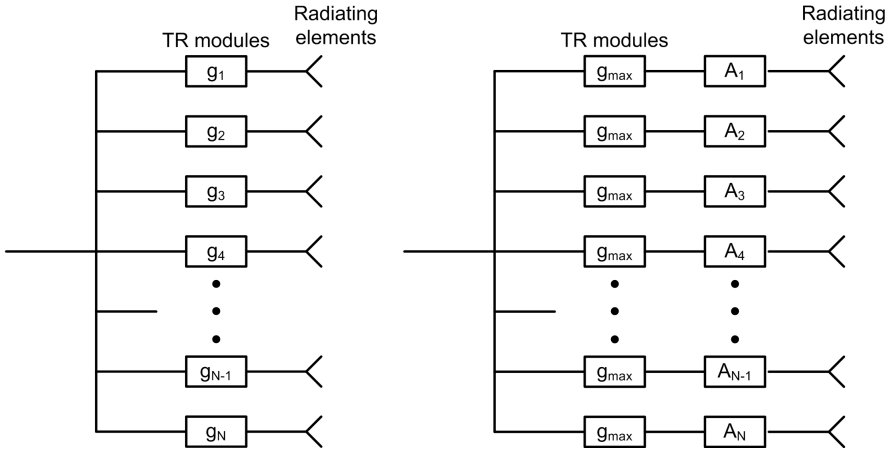

(a) Original diagram (b) Equivalent diagram

Figure 5.3: Block diagram of an active phased array with tapered amplitude distribution.

In the case of the beamformer network, the maximum gain is defined in 2.19 as

$$G_{BF} = \frac{\sum_{n=1}^{N} g_{max}^2}{N} = \frac{g_{max}^2 N}{N} \tag{5.24}$$

When in the presence of failures, the beamformer gain can be expressed as

$$G_{BF} = \frac{g_{max}^2 (N - F)}{N} \tag{5.25}$$

At this point, it should be clear that T/R module gain is temperature dependent and that this dependence can be found by characterizing the T/R module at different temperatures. We have demonstrated experimentally that the gain characteristic can be written as (3.20)

$$g_{max} = g_{max0} e^{-(\alpha + j\beta)(T - T_0)} \tag{5.26}$$

where g_{max0} is the maximum gain of a T/R module at reference temperature T_0, T is the actual temperature of T/R modules, α represents the gain variation coefficient (Neper/^{o}C), and β represents the phase variation over temperature (radians/^{o}C). When (5.26) is substituted in (5.25) and the phase is omitted, we obtained that

$$G_{BF} = \frac{g_{max0}^2 e^{-2\alpha(T - T_0)} (N - F)}{N} \tag{5.27}$$

Having the array directivity and beamformer gain, we can derivate the total gain for a phased array that scan in one dimension as

$$G_a(T,F) = D_e D_y D_x G_{BF} = \epsilon_T D_e D_y g_{max0}^2 e^{-2\alpha(T-T_0)} \frac{(N-F)^2}{N} \tag{5.28}$$

The antenna gain depends on the number of failures and actual temperature of T/R modules. It should be noted that this equation assumes that temperature gradient between T/R modules is zero, which implies that all T/R modules have almost the same temperature. Because, in reality, the temperature among T/R modules can be a slightly different, we must assume that T and T_0 are the average temperatures in the T/R modules.

During radar calibration, using the reference target, it is important to read the temperature of each T/R module and compute its average value. Denote this temperature value as T_0. Additionally, mutual coupling measurements should be taken and data compared with the factory measurements to quantify the number of failures at the calibration time. Denote this value as F_0. Consequently, from 5.28,the initial antenna gain when the radar is calibrated at temperature $T = T_0$ will yield

$$G_{a0}(T_0,F_0) = \epsilon_T D_e D_y g_{max0}^2 \frac{(N-F_0)^2}{N} \tag{5.29}$$

The ratio between the actual gain (5.28) and the initial gain (5.29) gives the gain deviation in the array, that is

$$C_a = \frac{G_a(T,F)}{G_{a0}(T_0,F_0)} \tag{5.30}$$

For the transmit and receive array, the above ratio yields the values

$$C_{rx} = e^{-2\alpha_r x(T-T_0)} \frac{(N-F_{rx})^2}{(N-F_{rx0})^2} \tag{5.31}$$

$$C_{tx} = e^{-2\alpha_t x(T-T_0)} \frac{(N-F_{tx})^2}{(N-F_{tx0})^2} \tag{5.32}$$

These are the two calibration constant that we need to calibrate the radar constant in (5.12), or in (5.13) if they are expressed in decibels (dB)

$$C_{rx}[dB] = -20\alpha_{rx} log(e)(T-T_0) + 20log(N-F_{rx}) - 20 * log(N-F_{rx0}) \tag{5.33}$$

$$C_{tx}[dB] = -20\alpha_{tx} log(e)(T-T_0) + 20log(N-F_{tx}) - 20 * log(N-F_{tx0}) \tag{5.34}$$

The first term on right side of (5.33) and (5.34) represents the gain deviation caused by temperature changes in T/R modules. The other two terms represents the gain loss caused by increase of the number of failures in the array. The advantaged of using these

expressions is that each effect can be calibrated independently, and at different times. We should expect that because the failure rate in a phased array is typically small, the gain correction due to this effect shouldn't be updated so often. On the contrary, due to the T/R module temperature depends on outdoor ambient temperature and this varies in a wide range of values during the day and year, the calibration due to this effect should be performed continuously, for example every volume scan according to the temperature read from T/R modules sensors.

5.3 Experimental Results

5.3.1 Phased Array Calibration by Mutual Coupling Measurements

The experimental phased array used in this test is the one described in the Chapter 3. The calibration was performed in an improvised anechoic chamber that was built to reduce the reflections from walls and other objects within the test facility. The initial calibration is performed using the technique described in Chapter 4, the purpose of this calibration is to align elements and implement the desired excitation function. Once this procedure is complete, the mutual coupling between actives and reference passive elements is recorded using a network analyzer. Measurements are made by enabling each module, one at a time, with the attenuator and phased shifter set at zero states, and measuring the complex gain (transmission parameter S_{21}) between the array input/output terminal and passive elements at the selected frequency of 9.36 GHz. The T/R modules, instrument, and measurements are controlled by a GUI-based program running in windows computer, where the measured data is stored.

To demonstrate the calibration technique in the experimental array, the mutual coupling was measured in the receive array under two different scenarios, one right after the array calibration to record the factory data, and another when some elements in the array have suffered of intentional gain and phase drifts. To simulate the performance monitoring in the field, measurements in the two scenarios were performed at different temperatures, being 29 ^{o}C at first test and 37 ^{o}C at the second test. These temperature values are the average temperatures measured in the T/R modules. Figure 5.4 shows the insertion loss and insertion phase obtained in the two tests from mutual coupling measurements made from

one passive element. The passive element is located next to the first active element in the array. Figure 5.4a shows how the magnitude of mutual coupling decreases with the increase of separation distance between the passive and active elements in both curves. Ideally, one should expect a smooth exponential curve, but because the electrical misalignment between active elements at the state zero, the mutual coupling exhibits the behavior shown in the plot. Additionally, the temperature drift creates a small bias between the two data. While in Figure 5.4a the element suffering of gain drift cannot be distinguished, the phase shown in Figure 5.4b reveals those elements that need to be recalibrated.

The gain and phase deviation in the elements are obtained from the ratio of the two mutual coupling measurements, calculating the parameter K_n with (5.6). The amplitude and phase of K_n as a function of the element number are shown in Figure 5.5. The results show that elements 2, 4, 8, 16, 32, 48, and 64 exhibit a large gain and phase deviation with respect to others elements. In Figure 5.5a, there is a bias of 0.86 dB in all data, which is caused by the temperature change. The large error between the gain deviation and bias level in the last 24 elements (from element 40 to 64) is due to the low mutual coupling and low signal to noise ratio in this region. This problem could have been avoided if the mutual coupling measurements for elements 32 to 64 had been made from the closer passive element (element next to element 64). Similar effect can be observed in Figure 5.5b, the data has a bias of approximately 4.2^o, and errors between phase deviation and bias level increase for the last 24 elements.

The elements 2, 4, 8, 16, 32, 48, and 64 are calibrated using the equation (5.9), with α=0.007 Neper/^{o}C and β=0.38^o/^{o}C (both constants were determined experimentally in Chapter 4). Additionally, the actual characteristics of aforementioned elements were computed using (5.7) and results then used in (5.9). The calibration's goal was to implement the array excitation using a -25 dB Taylor distribution. The amplitude and phase distribution determined by the initial excitation, monitored excitation with errors (after using (5.7)), and recalibrated excitation (after error correction) are shows in Figure 5.6. Values are determined at frequency of 9.36 GHz. The gain and phase drift is strongly corrected in most of the elements, except for element 64, which still has a large difference between the initial and calibrated excitation, being the error of 3.1 dB in gain and 11.9^o in phase.

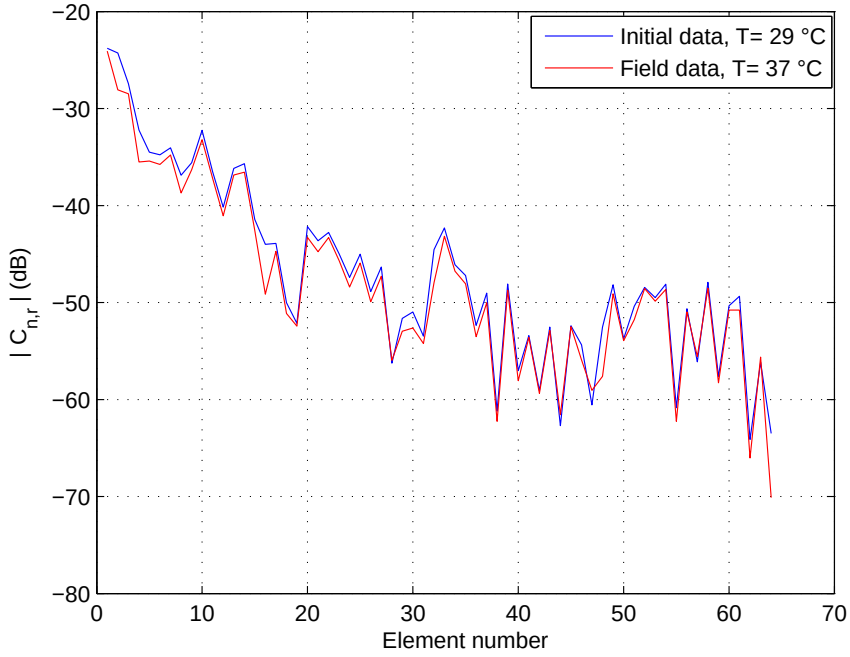

(a)

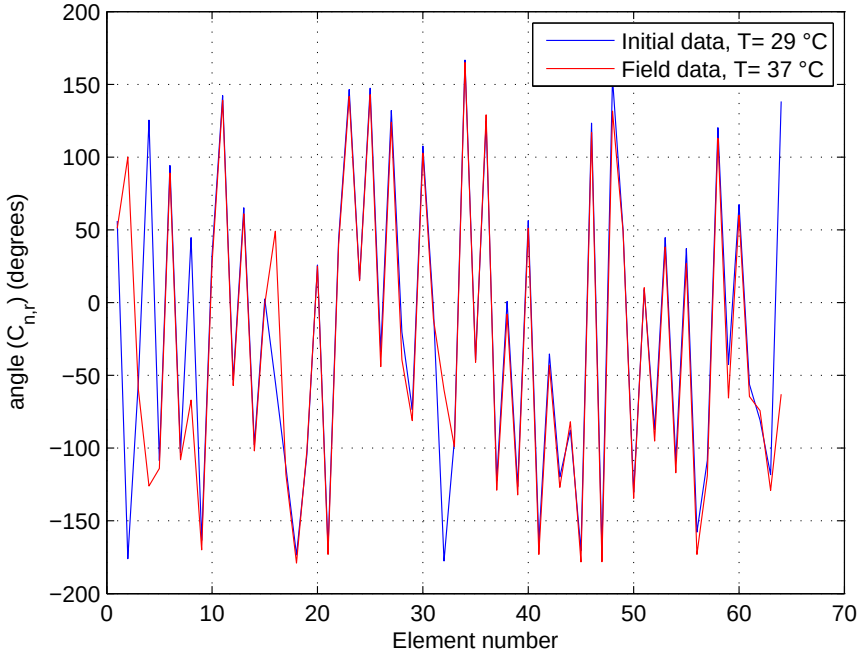

(b)

Figure 5.4: Comparison of mutual coupling measurements, at two different temperatures, obtained before and after calibration errors. a) Insertion loss. b) Insertion phase.

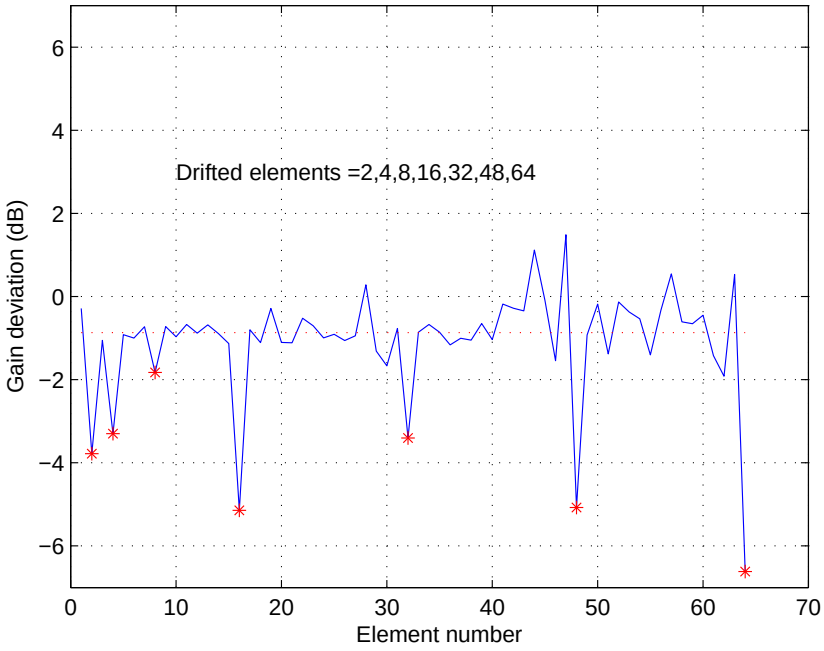

(a)

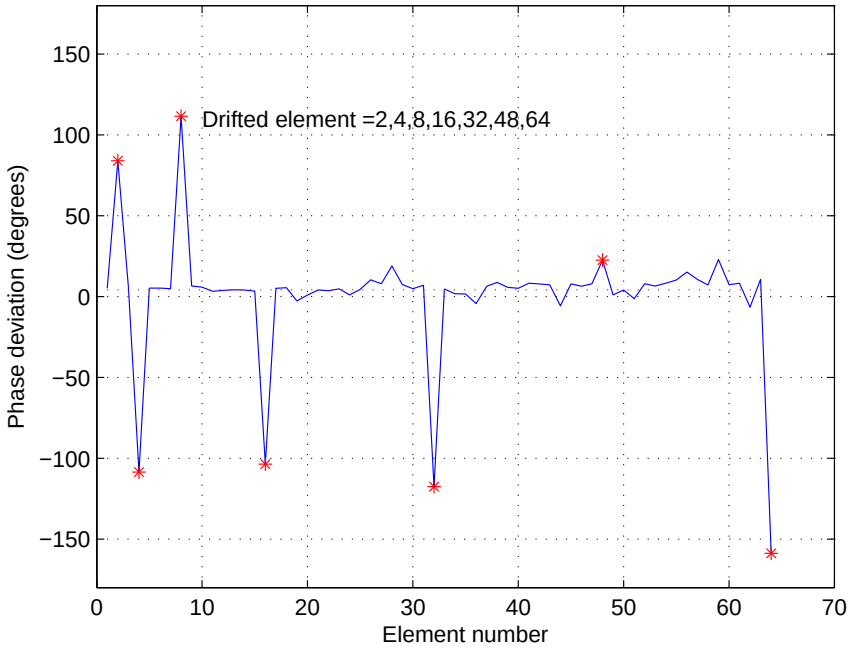

(b)

Figure 5.5: Gain and phase deviation detected by using mutual coupling technique. a) Gain deviation. b) Phase deviation.

These differences are because the mutual coupling in the last element is quite low and its measurement could be affected by the noise floor.

Other way to evaluate the calibration technique is to measure the far-field radiation patterns created by the array. For this test, the array is calibrated to implement 47 beams in receive, from -45^o to +45^o using 1^o increment step. Figure 5.7 shows the resulting radiation patterns when the beam is steered to broadside for the three excitations shown in Figure 5.6. The results show why the calibration in a phased array must maintained, it is clear that elements with calibration errors tend to increase the random errors in the excitation, and this in turn also increase the sidelobes. Once the array is recalibrated, the sidelobes return to their initial state, below 25 dB. The performance of normalized sidelobe and beamwidth as a function of scan angle are show in Figure 5.8 and 5.9, respectively. The sidelobe and beamwidth degradation in an array with random errors was improved after element recalibration for all scan angles.

Radiation pattern measurements are useful in the verification of antenna parameters such as sidelobes and beamwidth. For fielded phased array radars, it is important to measure the radiation patterns after failures occur or after element calibration, to ensure that antenna parameters meet the radar specifications. In practice, the measurements are carried out at the radar site using external antennas and instrumentation. However, they are sometimes impractical or difficult to implement in the field because ground multipath. This limitation motivates the use of other alternate methods to perform this task. To attend this need, we use the results from calibration test based on mutual coupling measurements to predict the far-field radiation pattern. Figure 5.10 shows the radiation pattern for a re-calibrated array as determined by far-field measurements and by prediction using (5.10). A very good match is obtained for the main lobe and the first sidelobes. There are some differences in the far sidelobes at the -35 dB level, which can be attributed to excitation errors created by mutual coupling.

5.3.2 Gain Calibration Due to T/R Module Failures

T/R module failures can be caused due to damaged components in either transmit or receive channel. Amplifiers are one of the most common causes of failures, leading

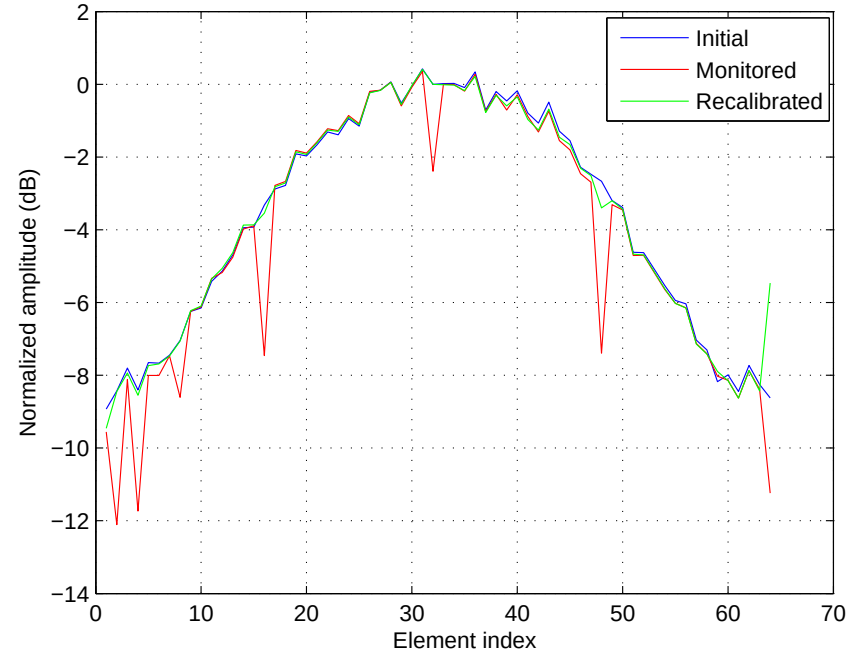

(a)

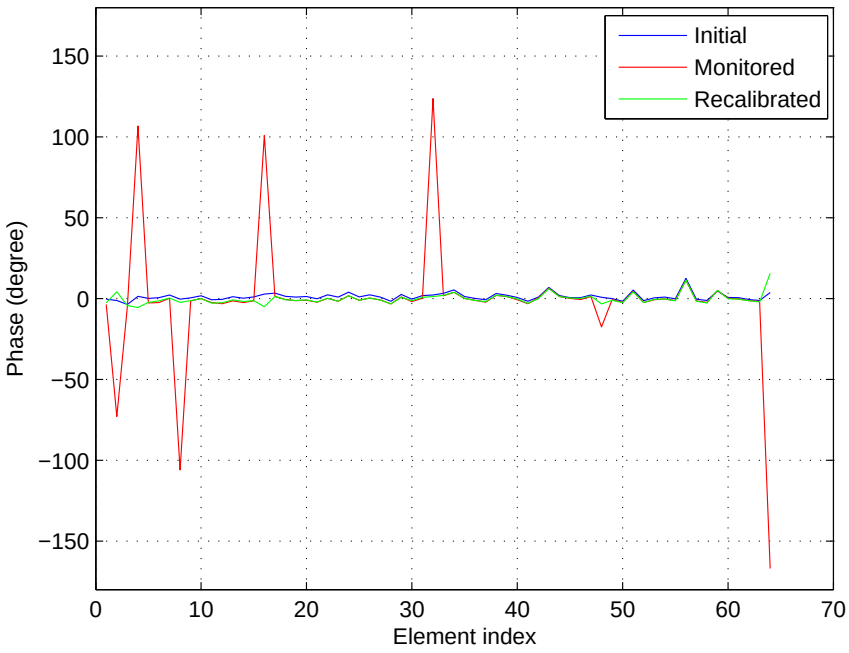

(b)

Figure 5.6: Amplitude and phase distributions in the array, obtained after initial calibration, errors occur, and recalibration. a) Amplitude distribution. b) Phase distribution.

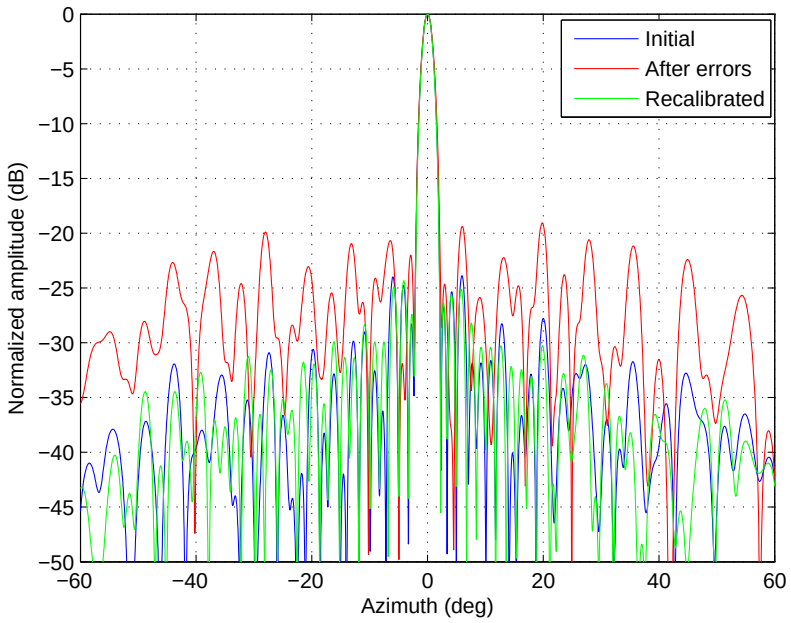

Figure 5.7: Comparison of radiation patterns measured at the initial calibration, after error occurs, and after element calibration.

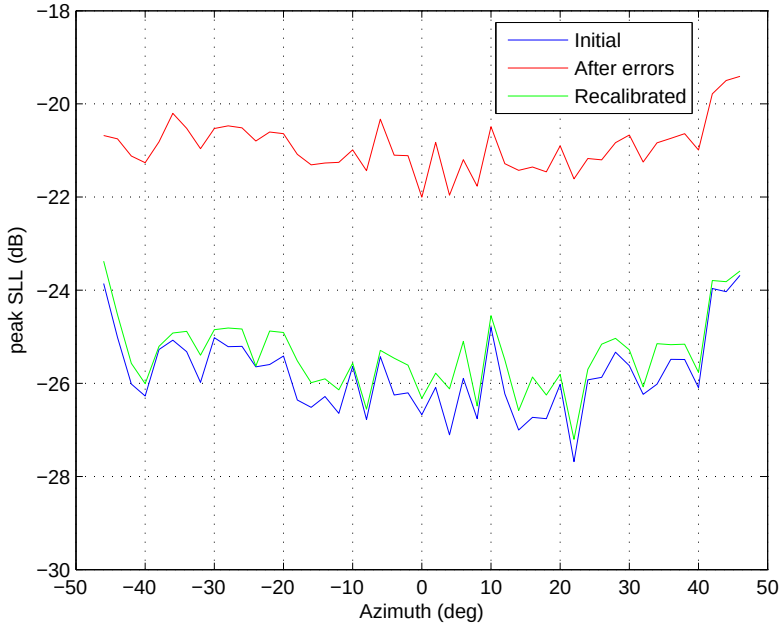

Figure 5.8: Measurements of sidelobes at the initial calibration, after error occurs, and after element calibration, obtained from measured radiation patterns.

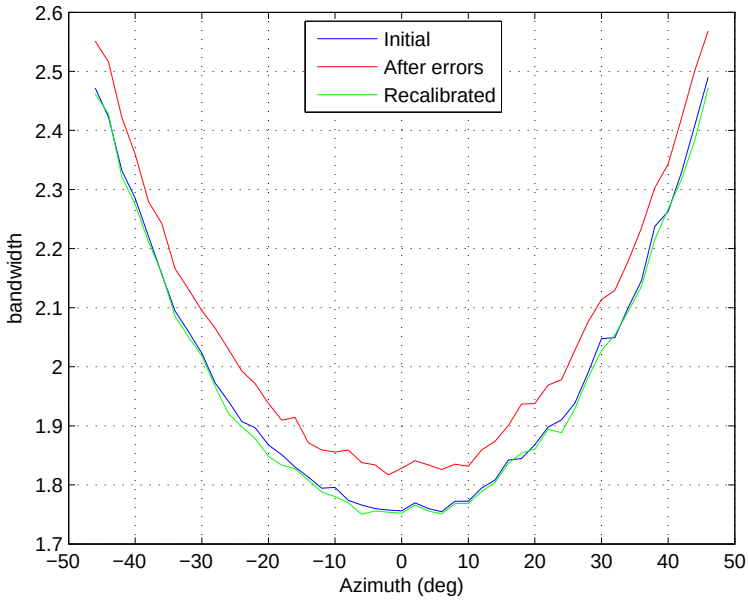

Figure 5.9: Measurements of beamwidth at the initial calibration, after error occurs, and after element calibration, obtained from measured radiation patterns.

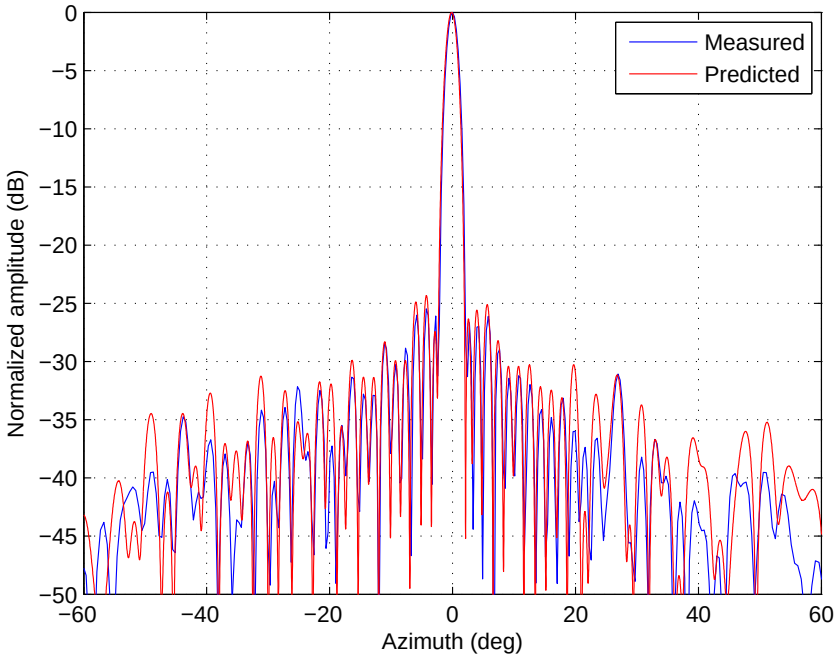

Figure 5.10: Comparision of far-field radiation pattern obtained from near-field measurements and after prediction with mutual coupling measurements.

to extinction of the signal and cease of operation in an radiating element. The effect of failures is to reduce the antenna gain and effective transmit power, and to raise the sidelobes. To retain the benefit of graceful degradation, arrays are usually operated with acceptable number of failed elements. Element with failed modules will be replaced when only a significant amount of modules have failed. In the particular case of a weather radar, the system will need to estimate the gain degradation caused by the antenna and to use the results to maintain the radar calibration.

The failure rate for T/R modules in the experimental phased array was estimated through a statistical analysis, giving as result a rate of 2.5 million per hours for both transmit and receive functions [6]. Assuming the radar can operates 24 hours per day and 365 day per year, and assuming that duty cycle is 30% (30% of the time the array is transmitting and other 70% is receiving), we can find that after 5 years, the failure percentage can be 8% in receive and 3% in transmit. For a 64 element array, these percentages corresponds to 5 and 3 failures in receive and transmit, respectively. The low number of failures suggests that gain calibration due to failure effects does not need to be performed so often.

Since the number of failures increases gradually over time, we have decided to demonstrate experimentally how the antenna gain will change with the increase of failures. The tests were only performed in receive mode because the methodology is the same for transmit mode. Failures are simulated by turning off the amplifiers in the "failed module" during mutual coupling measurements. Failed modules were chosen randomly, corresponding to the numbers: 4, 7, 11, 20, 32, 51, and 59.

Figure 5.11 shows the amplitude of the mutual coupling measurements made from one passive element before and after the failure occurs. Measurements were obtained at a fixed temperature, after calibrating the receive modules with a uniform amplitude distribution. Note the large difference in gain in the locations of failed elements. Theoretically, the gain differences should be larger than -50 dB, but because of the noise floor in the system, mutual coupling measurements lower than -75 dB are not possible. Therefore, the failed elements that are closer to the reference passive element present a larger gain difference than those that are farther away. This effect can be observed after computing the ratio K_n between the two set of data, as shown in Figure 5.12. Since the noise tends to introduce errors in the

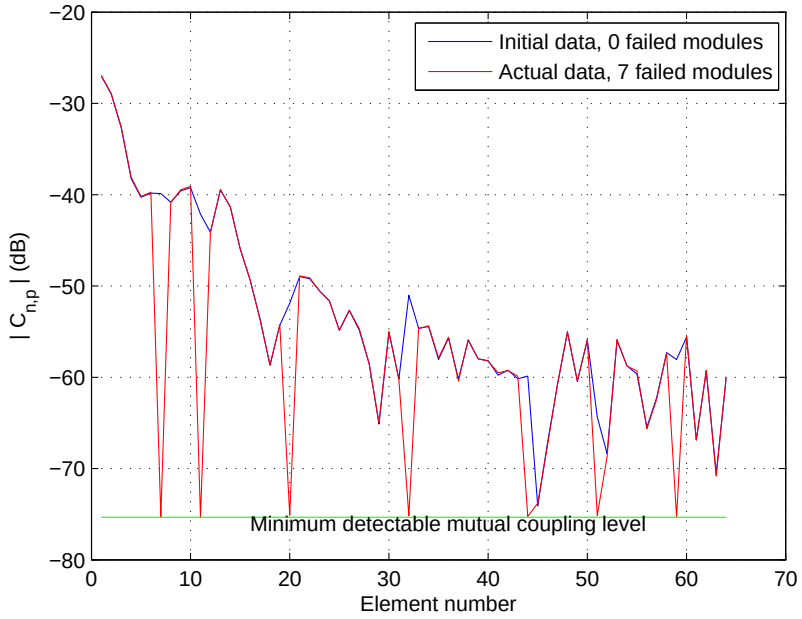

Figure 5.11: Mutual coupling measurements before and after T/R module failures.

measurements of farther elements, the actual gain of faulty elements cannot be estimated with accuracy. However, the measurement errors can be avoided if a threshold is applied to the data and only data below this reference is replaced by zeros.

Once the threshold operation is complete, the resulting data is used in (5.7) to compute gain of each element. Figure 5.13 shows the resulting normalized gain distribution for a -25 dB Taylor function. The threshold operation also allows the actual number of failures can be determined, for example, by counting the number of elements having a zero gain. Subsequently, both results were used by the two proposed methods to compute the gain deviation. Furthermore, in order to verify the results, the radiation patterns from the experimental array were measured with and without failed elements. Initially, the array was calibrated with zero failures, then 47 radiation patterns at different scan angles were measured and used to determine the scanned gain. This procedure was repeated 4 times for different sets of failed modules. In the end, the computed gain deviation (from proposed methods) and initial scanned gain (with zero failures) were used to predict the scanned gain for the cases when the array has failed modules. As described in (5.33), the actual gain can be obtained as

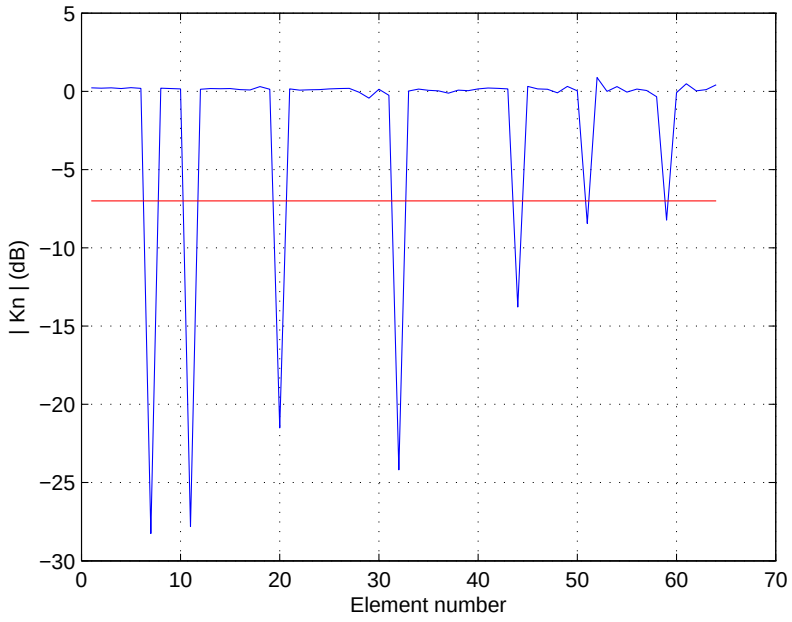

Figure 5.12: Gain deviation in an array with 7 failed elements.

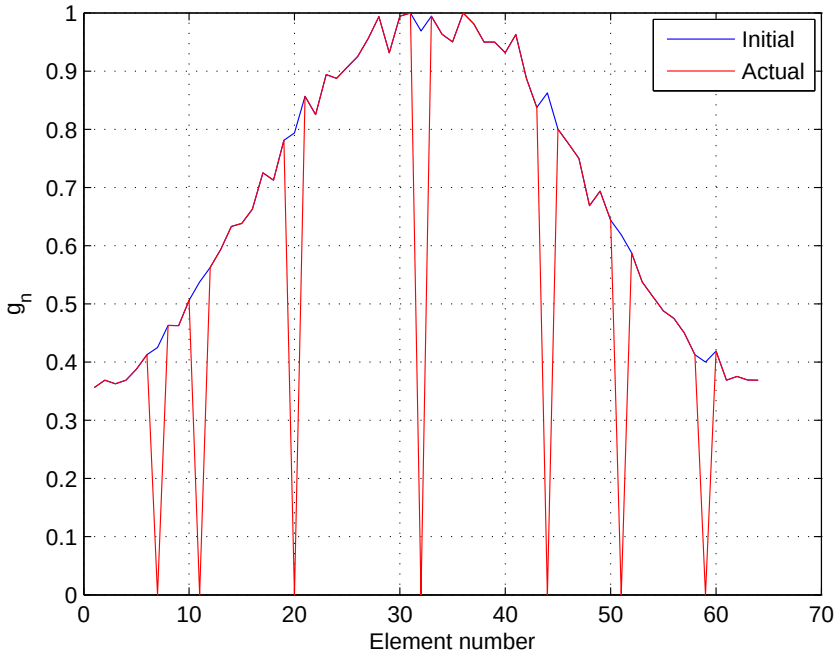

Figure 5.13: Gain distribution before and after failures.

$$G'_{rx}(\theta, F) = C_{rx}(F) G'_{rx0}(\theta, F_0) \tag{5.35}$$

Comparisons of scanned gain obtained from far-field measurements with mutual coupling measurements (equ. 5.20) and deterministic model (equ. 5.33) are shown in Figures 5.14 and 5.15, respectively. Measurements were obtained from receive array using the horizontal polarization, at a constant temperature of 29^oC. Note the receive gain loss with 7 failures is approximately 1 dB for all scan angles, corresponding to a bias error of 1 dB in the equivalent radar reflectivity if the radar constant is not corrected. When Figure 5.14 and 5.15 are compared, one found that results obtained from deterministic model are slightly more accurate than results obtained from mutual coupling measurements. Table 5.1 indicates the gain deviation and error as determined by the mutual coupling measurements and by deterministic model. In both cases, the error in the gain deviation with respect to the measured deviation don't exceed the 1.4%.

The above tests assume that initial number of failures in the array is zero. However, it might also occur that a phased array radar can present a certain number of failures from the beginning, before radar operation. Subsequently, when new failures appear, the actual gain drift must be computed with respect to initial gain with failures. To give an example, consider the case when the array has initially 3 failures (element number =11,32,51) and we wish to estimate the gain drift when number of failures in the system has increased to 5 and 7. Using (5.33) at $T = T_0$, we found that the gain drift $C_{rx}(F = 5)$= -0.28 dB and $C_{rx}(F = 7)$= -0.48 dB, next, the predicted gain is obtained as

$$G'_{rx}(\theta, F = 5, 7) = C_{rx}(F) G'_{rx0}(\theta, F_0 = 3) \tag{5.36}$$

Table 5.1: Gain deviation due to element failures obtained from radiation pattern measurements, mutual coupling method, and deterministic model

Failed element number	# of failures	Gain deviation, C_{rx} (dB)			Error in the gain (%)	
		MCM	Det. model	measured	MCM	Det. model
11	1	-0.19	-0.14	-0.13	1.37	0.07
11,32,51	3	-0.43	-0.42	-0.44	0.26	0.59
7,11,20,32,51	5	-0.69	-0.71	-0.73	1.06	0.64
7,11,20,32,44,51,59	7	-0.96	-1.01	-1.01	1.16	0.17

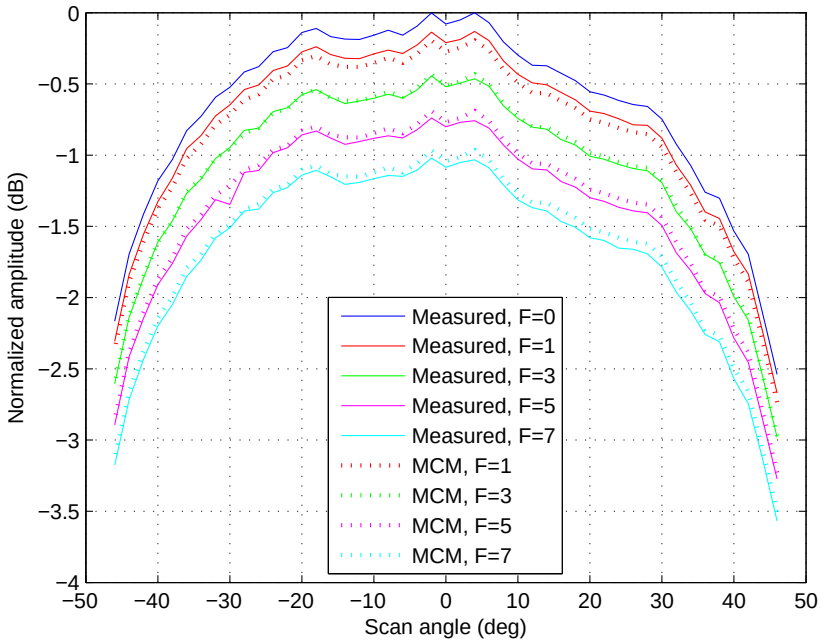

Figure 5.14: Comparison of scanned gain under different failure condition, obtained by radiation pattern measurements and by prediction using mutual coupling measurements.

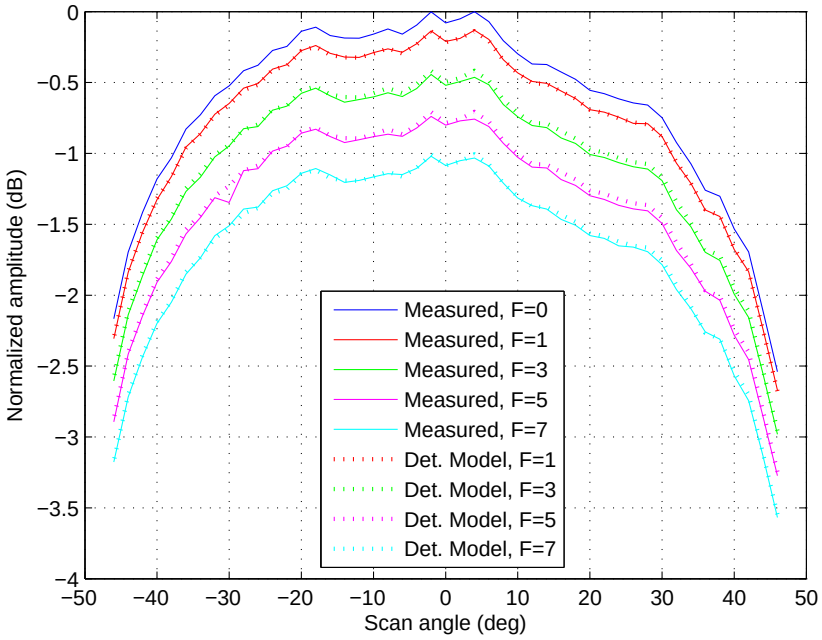

Figure 5.15: Comparison of scanned gain under different failure condition, obtained by radiation pattern measurements and by prediction using deterministic model.

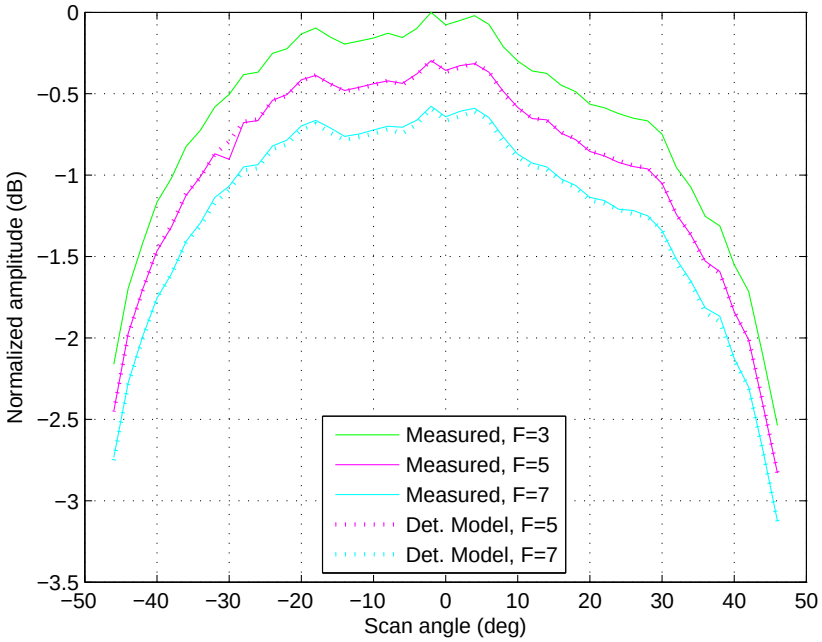

Figure 5.16: Comparison of scanned gain for the case of an array with initial failures, obtained by far-field radiation pattern and by prediction using deterministic model.

Figure 5.16 shows the scanned gain as determined by far-field measurements and by prediction based on the deterministic model when the initial array has 3 failures and actual array has 5 and 7 failures. We found again a very good match between the measured and predicted gain. The result demonstrates that gain estimation must be based on the initial number of failures, the number than can be found using mutual coupling measurements after radar calibration.

Failures not only affect the gain of an array, it also increases the sidelobe in a radiation pattern. Figure 5.17 shows how sidelobes are affected by the failed elements given in Table 5.1. The data corresponds to the maximum sidelobe, which can occur at any azimuth angle. Note that a small number of failures produce a large change in the sidelobes. For example, when the beam is at broadside, the sidelobe is raised from -24 dB to -19 dB, point where the array has 3 failed elements. Because of the small number of elements in the array (64 elements), the sidelobes tends to increase rapidly after a few failures, something that does not occur on a large phased array with thousand of elements.

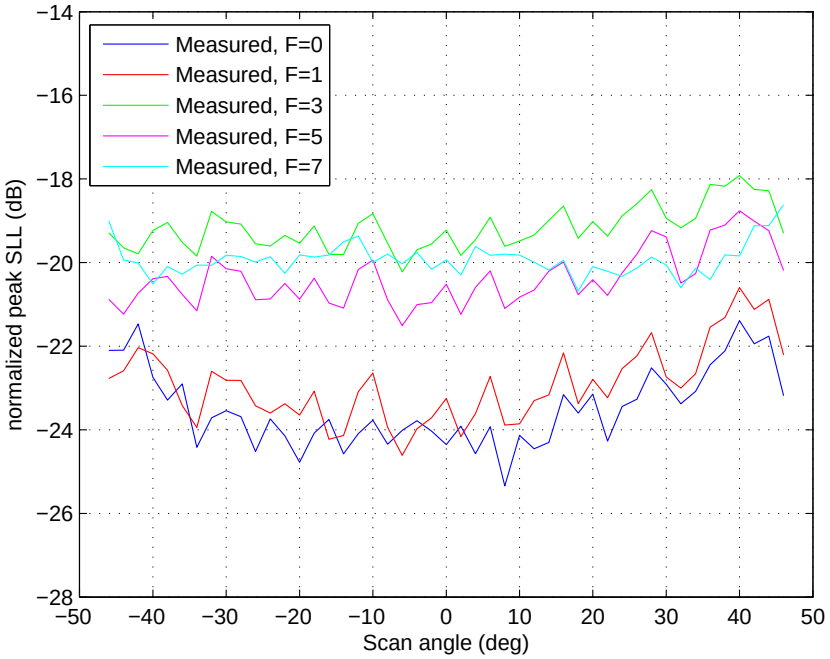

Figure 5.17: Maximum sidelobe level for a -25 dB Taylor pattern under different failure conditions.

5.3.3 Gain Calibration Due to Temperature Changes

To demonstrate the gain calibration technique by temperature, the scanned gain obtained by scanning the beam was measured at different temperatures by means of a near-field scanner, then for each operating temperature, the mutual coupling measurements were recorded. Subsequently, gain deviations were computed from mutual coupling measurements using the two proposed methods. Validation of results is made by comparison to those obtained from radiation pattern measurements.

For this test, mutual coupling measurements are obtained from two element passives as shown in Figure 5.18. Curves are given 5 different temperatures. The coupling from elements 1 to 32 were measured from the passive element adjacent to element 1, while coupling from elements 33 to 64 were measured from passive element adjacent to element 64. Measurements were performed in receive mode after calibrating the array with an uniform amplitude distribution. Figure 5.19 shows the respective temperature distribution across T/R modules for each operating temperature. Each temperature curve follows an

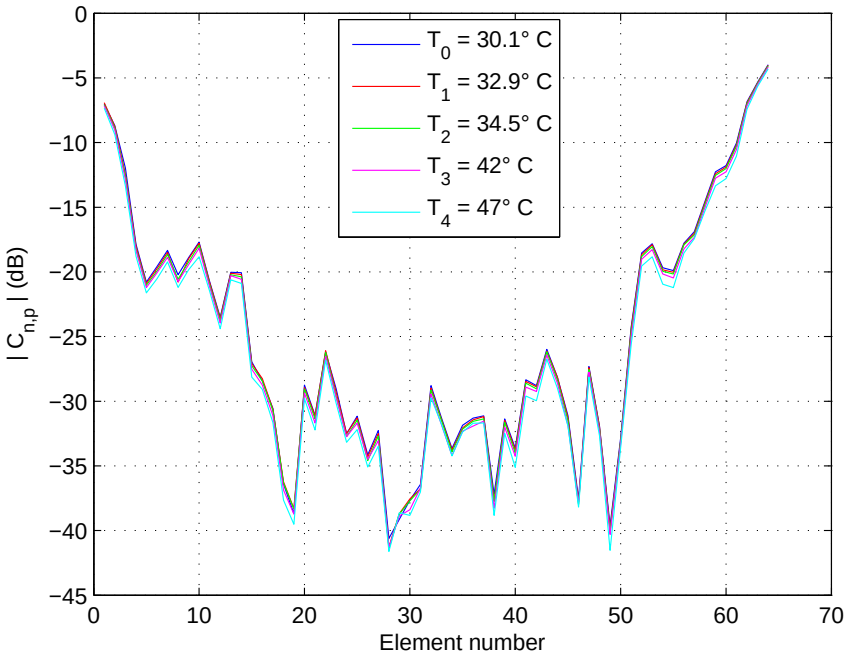

Figure 5.18: Mutual coupling measurements obtained at different operating temperatures using two passive elements.

uniform distribution with means T_0=30.1 ^{o}C, T_1=32.9 ^{o}C, T_2=34.5 ^{o}C ,T_3=42 ^{o}C, and T_4=47 ^{o}C, and mean standard deviation of 0.86 ^{o}C.

As described in section 5.2.2.1, the calibration uses the comparison of a previously measured data with a reference data for detecting gain variations. In this test, we have considered as the reference data, the measurements taken at temperature 30.1 ^{o}C. The mutual coupling ratio K_n between the actual data (data at temperatures T_1, T_2, T_3, and T_4) and reference data (data at temperature T_0) as a function of element number is shown in Figure 5.20. As expected, an increase in the T/R module temperature causes a decrease in the gain of each element, reducing the intensity of mutual coupling between the active and passive elements. The coupling reduction produces a negative shift in the parameter K_n that is equal to the gain drift in each element.

Having obtained the parameter K_n, the subsequent gain drift at each temperature is computed using (5.18) and (5.20). Additionally, the gain drift is computed by using the deterministic model (5.33), after considering no failures in the array, and using α_{rx}=0.007.

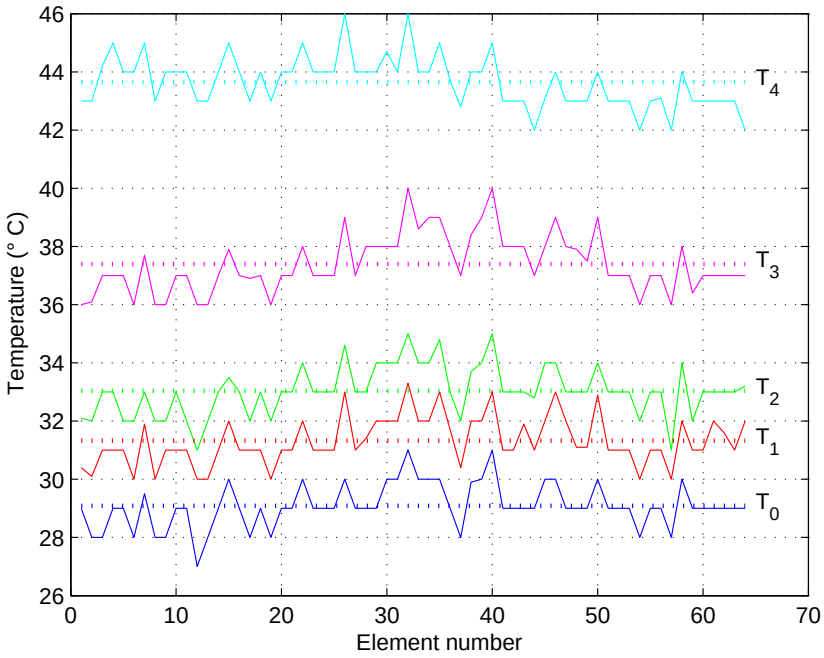

Figure 5.19: Temperature distribution along the T/R modules for different operating temperatures.

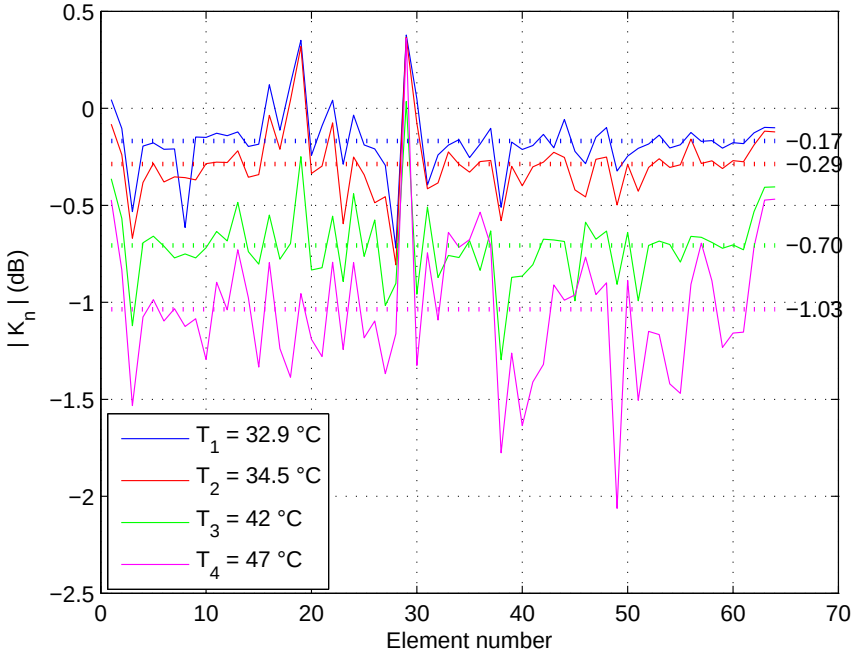

Figure 5.20: Gain deviation obtained at different operating temperatures using mutual coupling technique.

The calibration constant for the receive array is given as

$$C_{rx}[dB] = -0.0608(T - 30.1)$$

Results obtained from both methods were used to predict the array scanned gain at each operating temperature. Comparisons of scanned gains obtained by mutual coupling measurements and deterministic model with obtained by far-field radiation pattern measurements are shown in Figure 5.21 and 5.22. In most cases, the predicted results are in good agreement with measurements. While at temperature 47 ^{o}C there are some differences at certain scan angles. These differences are caused by two reasons: the increase of random errors in the excitation and by failures that occurs in some T/R modules. Failures in T/R modules are caused by the thermal protection circuits in the voltage linear regulators that feed the amplifiers. It has been observed specifically in 3 T/R modules that voltage regulator tends to cut-off the output current when temperatures reach values higher than 50 ^{o}C. Since the scanned gain measurement with the near-field scanner take about 40 minutes, it is possible that affected modules can be switching between"on" and "off" states. Table 5.2 summaries the gain drift measured and computed by the two proposed methods, as well as the errors obtained by each methods. The estimated errors are quite low, providing evidence that both methods work very well to monitor the gain drift caused by temperature changes.

Table 5.2: Gain deviation due to temperature changes

Initial temperature ^oC	Actual temperature ^oC	Gain deviation, C_{rx} (dB)			Error in the gain (%)	
		MCM	Det. model	measured	MCM	Det. model
30.1	32.9	-0.17	-0.170	-0.15	0.20	0.21
30.1	34.5	-0.29	-0.27	-0.23	0.66	0.39
30.1	42	-0.72	-0.73	-0.67	0.60	0.68
30.1	47	-1.04	-1.03	-1.07	0.30	0.40

5.3.4 Gain Calibration Due to Temperature Changes and T/R Module Failures

The gain deviation due to temperature changes and failures was also investigated. The test was realized at a temperature 41^{o}C simulating 5 faulty elements (module numbers =

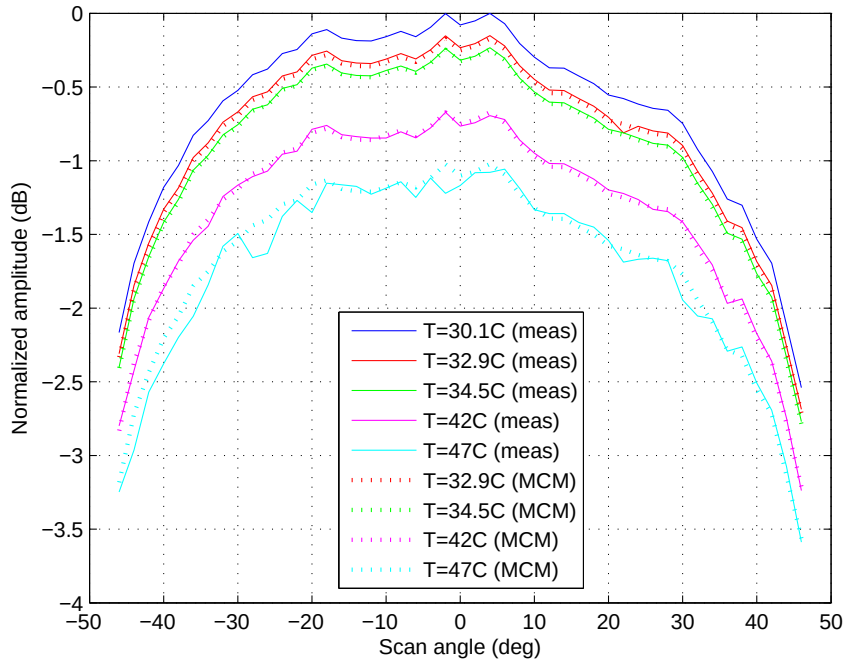

Figure 5.21: Scanned gain at different operating temperatures, obtained by radiation pattern measurements and by prediction using mutual coupling measurements.

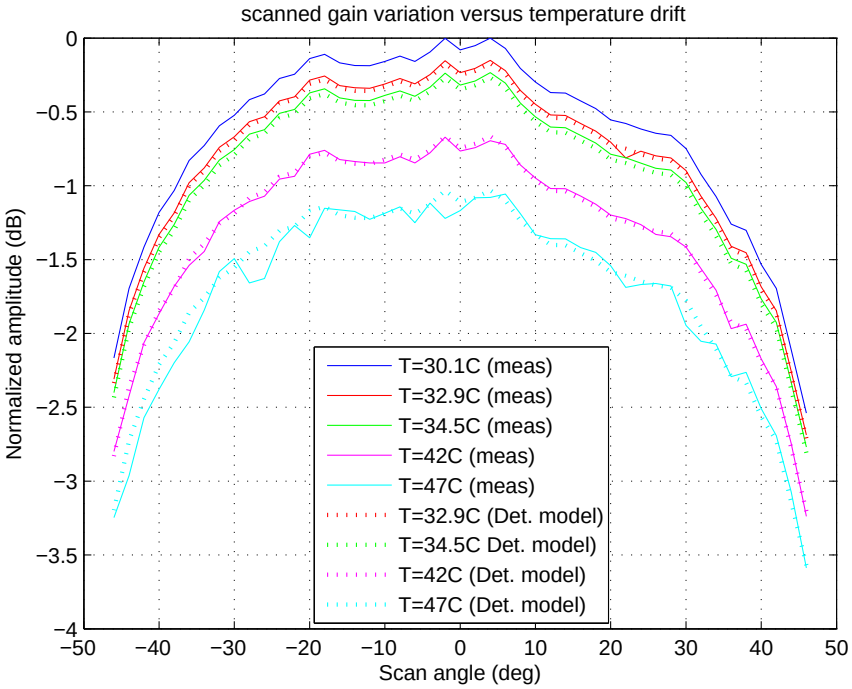

Figure 5.22: Scanned gain at different operating temperatures, obtained by radiation pattern measurements and by prediction using deterministic model.

7, 11, 20, 32 and 51) in the array. It has been assumed as reference data, the data obtained from an array operating with zero failures at temperature of 30.1 ^{o}C. For each temperature, receive pattern measurements were made at 47 different scan angles in the range $\pm 45^{o}$, results were then used to estimate scanned gain in the scanning range. Subsequently, mutual coupling measurements were made to estimate the gain drift and number of failures. Figure 5.23 shows the comparison of the initial scanned gain with actual scanned gain affected by failure and temperature changes, as determined by measures and by prediction using the two proposed methods. Results from this comparison are shown in Table 5.3. The measured and predicted gain are matched fairly well over most of the scan range, the error obtained from prediction using mutual coupling method and deterministic model are 0.2% and 0.6%, respectively.

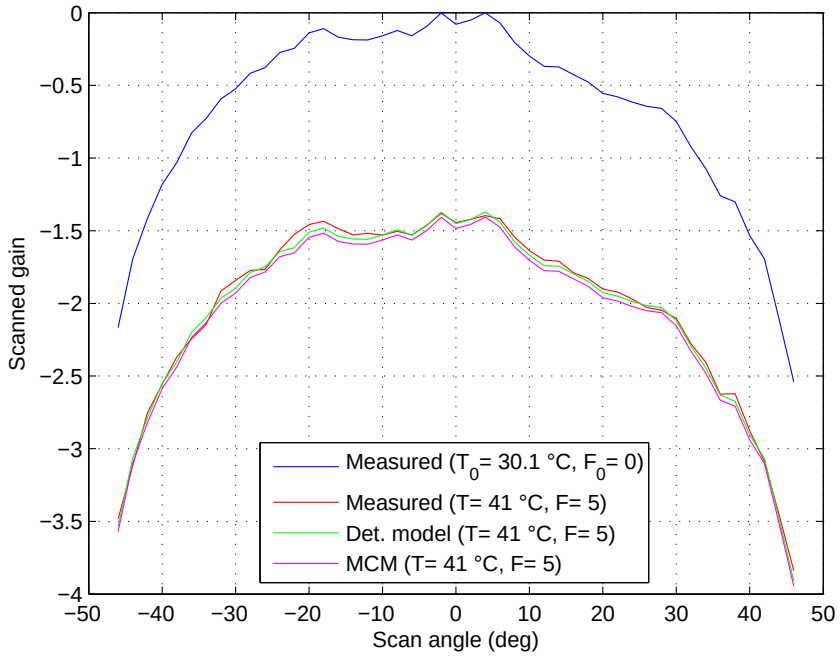

Figure 5.23: Effects of temperature and failures on the scanned gain. Curves obtained by radiation pattern measurements, by prediction using mutual coupling method, and by deterministic model.

Table 5.3: Gain deviation due to temperature changes and failed elements

Actual temperature ^oC	# of failures	Gain deviation, C_{rx} (dB)			Error in the gain (%)	
		MCM	Det. model	measured	MCM	Det. model
41	5	-1.40	-1.37	-1.35	0.2	0.6

CHAPTER 6

SUMMARY AND CONCLUSION

Benefits of dense networks of short-range X-band weather radars using mechanically steered dishes has been recognized in the past 10 years. The need to improve radar capabilities in order to provide early warning of hazardous weather phenomena, and the need to provide more reliable and cost-effect radar systems have led to the consideration of using the phased array as an alternative technology to mechanically steered antennas. A drawback of phased array systems are their high cost, making them too expensive for civil application. For the concept of dense networks of phased array radar to be an economically feasible alternative, the radar must be built at dramatically lower cost than current phased array systems. A feasible solution is to use the phase-tilt array architecture, which performs electronic scanning in azimuth direction and mechanical scanning in elevation direction.

The first part of this dissertation describes the design and implementation of a beamforming network and beam steering control system that enable the development of low-cost low-power phase-tilt radars. A detailed, system-oriented description of the electrical requirements, design, test, and performance of different subsystems were given.

A summary of the most important results and findings in this part of the dissertation are as follows:

- The phase-tilt array architecture reduces cost because it uses a reduced number of low-cost T/R modules in the array aperture. T/R modules make up about 50% of overall system cost. Additionally, a significant cost reduction have been achieved in the fabrication of other array subsystems by integrating in a single printed circuit board (called backplane) the design of RF power distribution networks, DC power network, control network. The cost has been reduced over other architectures through increased integration of subsystems and reduced wiring, accounting for about 6% of total array cost.

- T/R module design approach is based on radar system specifications and calibration requirements. Modules are designed in individual boards to reduce maintenance cost and provide low cost replacement parts. They also use their own housing to reduce coupling between adjacent modules, which allows the investigation of mutual coupling as calibration technique. The fabrication and assembly is realized in arrayed panels to ensure low-cost manufacturing. The cost of each module is approximate $ 350 dollars (in year 2010) at high volume production. Within the module cost, the digital phased shifter is the dominant factor, accounting for about 25% of current module cost. Module test was very intense and time consuming. Measurements were realized at an automated test station that was specifically designed for this project. The key parameters, the transmit peak power, noise figure and the isolation between antenna polarization ports met the design requirements. Additionally, the modules presented a low settling time. Switch characteristics allows the phased array to theoretically achieve pulse repetition frequencies up to 100 KHz, making it suitable for a wide range of radar applications.
- Considerable simplification in the integration of various subsystems with T/R modules have been obtained by means of a hybrid backplane architecture, an interconnect interface widely used in computer systems to make reliable and high speed connections between several daughter cards. The backplanes are composed of two RF power distribution networks, a DC power network, and a control and communication bus. These subsystems have been incorporated into a low-cost multilayer printed circuit board. The board allows the interconnection of 16 T/R modules to a common communication bus and power distribution system without using cables. T/R modules are plugged into the backplane in their appropriate slots, according T/R module address. The connection between T/R modules and RF manifold is realized through RF coaxial cables. The advantages of using a backplane architecture is that it reduces cost (i.e. reduce material and manufacturing process steps), reduce wiring complexity and space, simplifies array integration, and allows the implementation of high-speed communication buses.

- One of the most important results coming from the beam steering control design was the implementation of a high-speed bus based on a LVDS multidrop backplane architecture. The bus is capable of driving up to 32 T/R modules in parallel when two backplanes are cascaded. It also allows data transmission speeds up to 100 Mbps. The communication speed is 10 times higher than the communication speed obtained in most phased arrays using RS485 and RS422 standards. Buses are designed with a pair of microstrip lines and with terminations at the ends to eliminate reflections caused by the mismatch between the transmission lines and loads. Tests made in a heavily load backplane with 32 modules using a 25 Mbps serial transmission resulted in a zero-error communication.
- A new control architecture for the beam steering system of a phased array radar was designed and implemented. The control is based on a distributed system, which has a central controller and several element controllers at the level of each T/R module. The central controller generates beam commands and element controllers translate them into calibrated settings allowing the implementation of the desired excitation. The control differs from others architectures in that all element controllers are controlled in parallel and synchronously by the central controller, and that non computing units are used. In addition, element controllers can be controlled individually or simultaneously by means of unicast or broadcast commands. Advantages of this architecture include real time rapid update, high steering throughput, decreased complexity, and reduced hardware cost. Some of these features enable the implementation of adaptive scan and beam multiplexing scan strategy with a widely range of PRF and pulse width. Another feature is that sequence table enables the implementation of a variety of different pulse schemes.
- Element controllers are implemented in a low-cost small FPGA incorporated in the T/R modules. The design is based on a state-machine with a programmable sequence table and pre-stored calibration look-up table. The sequence table stores the beam commands (scan angle + pulse scheme) to be used for the radar at a specific beam. Look-up table translates the command indicated by the sequence table into control

signals for phase shifter, attenuator, T/R switches, polarizations switches and amplifier bias. Each T/R module has a unique look-up table, which contains calibrated data for different operation modes, temperature or even frequencies. Control of sequence table, memory and registers is realized through commands. A list of commands with their description have been presented.

The second study has addressed a method to perform the initial calibration of phased arrays. The conventional method of setting the phase and amplitude in a phased array system is through calibration look-up tables that are stored locally at each T/R module. These tables store calibration offsets or calibrated settings that correct the errors created by attenuators and phased shifters. This method does not always provide the best available setting for a given element excitation. The third chapter has addressed a calibration algorithm that provides better calibration settings than the standard calibration. The algorithm searches in the raw data of each element the best amplitude and phase settings that minimize the random errors in the excitation. The settings are obtained as a function of module, scan angle, and temperature. These data are organized and stored into calibration tables, called "beamtables", in the array control computer, which transfers them to T/R modules each time the radar is turned on or is in idle mode. Additionally, array radiation patterns can be calculated from the calibration settings, the known array element positions, and a known embedded element pattern.

A summary of the most important results and findings in this part of the dissertation are as follows:

- The power of the calibration technique has been demonstrated by calibrating successfully a phased array system in both receive and transmit mode. The criteria used to choose the gain scaling factor for the calibration algorithm at each mode depends on the antenna operation mode. In receive, the gain scaling factor should be chosen less than or equal to the minimum gain found across elements (having the attenuators and phase shifters are loaded with all zeros) in order to implement the desired excitation function with low random errors. This condition allows achievement of errors that are approximately close to theoretical errors. On the other hand, in transmit, the

gain scaling factor should be chosen equal to the maximum gain found across the elements. This condition ensures that elements will operate in compression. Results have shown that when attenuator's insertion phase is considered into the calibration, a RMS phase error better than the theoretical error is obtained.

- Radiation pattern measurements obtained from calibrated array are in good agreement with both theoretical and predicted patterns. Results indicate that radiation patterns can be calculated directly from calibration settings if the embedded element pattern is known. This method may be applicable to predict the radiation patterns of a fielded phased array after internal calibration.
- Both measured and predicted patterns have been used to determine the array scanning performance. Comparisons of scanned gains obtained by measurements, by prediction, and by average embedded element pattern are made. It has been observed the presence of ripples on the scanned gain in both receive and transmit array, being most noticeable in receive than in transmit, although the latter had higher excitation errors. These ripples are caused by the variation of amplitude errors with scan angles. Particularly, in transmit there are not variations in the amplitude errors with scanning because the elements operates in compression. For that reason, the ripples are quite small in the scanned gain.
- Array characteristics as beamwidth, sidelobes, and beam pointing errors have been measured are different scan angles in order to evaluate the quality of the calibration process. The beamwidth performance is in good agreement with the theory. Sidelobe level for beams close to broadside corresponds with the designed value, however its value increases when the beam is scanned away from broadside because of the scanning loss, being the maximum value equal to -21 dB at 45^o. Beam pointing errors less than 0.06^o has been obtained.
- An open loop calibration technique that compensates for the two-way antenna gain drift caused by temperature changes is also presented. The technique is applicable to phased arrays that have transmit modules operating in compression. Because the gain cannot be adjusted in the transmit array, the compensation is realized in the

receive array. Gain compensation has been demonstrated experimentally at several temperatures. Results show that the gain drift obtained after compensation is less than 0.05 dB.

The third study has addressed a technique that uses mutual coupling measurements for both monitoring and calibration of phase array systems. The technique takes advantage of the inherent mutual coupling between the active elements and passive elements of an array to measure the characteristics of active elements. The only two requirements of the technique is that characteristics of passive elements and mutual coupling between radiating elements must not change over time. It has been demonstrated successfully that mutual coupling measurements can be used to monitor and maintain the calibration of an array. In general, experiments has been conduced to estimate gain variations in the elements that may be caused by temperature changes, aging, or even replaced modules. Results have been used to calibrate the array elements when they suffers of excitation errors, and to calibrate the radar constant when the array suffers of temperature and failures effects. The approach has the advantage of low cost and easy implementation. The added circuit complexity is also minimal.

A summary of the most important results and findings in this part of the dissertation are as follows:

- The theory associated with monitoring and calibration of phased arrays that are susceptible to temperature changes has been discussed and demonstrated experimentally. The calibration concept uses the comparison of two mutual coupling measurements, one obtained during the monitoring task, the other one obtained during initial array calibration, to determine calibration errors that occur in the elements over time. It has been demonstrated that when two measurements are made at different temperatures, the calibration constant is affected by a bias error that is exponentially proportional to the temperature drift. The proposed calibration algorithm removes the bias caused by the temperature and corrects the characteristics of uncalibrated elements according to the calibration constant. Test results indicate that both gain and phase drift can be calibrated with good accuracy if the signal-to-noise ratio is

the appropriated. Radiation pattern measurements confirmed that sidelobe level and beamwidth are within the expected values after calibration procedure.

- The accuracy of the mutual coupling measurements are affected by the signal-to-noise ratio resulting from the coupling between the active elements and passive elements, as the separation distance increases, the signal-to-noise ratio decreases and accuracy decreases. In a small linear phased array, the accuracy of calibration can be improved by using two passive elements, one on each edge of the array, and measuring each half of the antenna with the closer passive element.
- Results obtained by mutual coupling measurements can be used with the initial array excitation function, and a known embedded element pattern to predict the array radiation pattern. It has been shown that prediction results are in good agreement with conventional far-field measurements. This method may prove to be very useful in the maintenance of future low cost phased array radars where the radiation patterns must be monitored routinely to insure that they meet the radar specifications. In particular, small phased arrays are more susceptible to failures than large phased array, the effect of failures is to reduce the antenna directivity and rise the sidelobes. The antenna degradation can only be determined by measuring the antenna radiation pattern. The pattern prediction by mutual coupling measurements can be a viable alternative for performing this task.
- An experimental investigation of temperature and failures effects in an air-cooled, phased array antenna has been made. It was shown that losses in receive gain can be approximately 1 dB when the array has 7 failed modules. Similarly, the gain deviation is 1 dB when the antenna is affected by a temperature change of 17 ^{o}C. Combining both effects, the net gain deviation in receive can be equal to 2 dB. Unless this deviation and transmit gain deviation is compensated, the equivalent reflectivity measured by the radar will be affected by a bias error larger than 2 dB.
- The potential for radar calibration based on mutual coupling measurements has been demonstrated. Two methods that effectively estimate the antenna gain deviation due to temperature changes and failures are presented. The first method is based on the

comparison of the actual antenna gain with the initial antenna gain measured during the external calibration of the radar. Each gain depends on the individual gains of each array branch, which are obtained by mutual coupling measurements. The second method is based on a mathematical model that takes into account the temperature characteristic of T/R modules and the number of failures presents in the array. The number of failures is estimated by mutual coupling measurements. The calibration constants obtained from these methods correct the combined losses that occur in the beamformer networks and antenna directivity. Two calibration constants, one for transmit array and one for receive array, are defined to correct the radar system constant. It was also shown that calibration constants can be used with the embedded element pattern to predict the scanned gain of an array.

- Various calibration tests made under different operating temperatures and failures conditions were shown. Results indicate that gain deviation can be accurately estimated using any of the two proposed methods. Predicted scanned gains are in good agreement with far-field measurements. Residual errors are less than 1.4 % in the mutual coupling method and less than 0.7% in the mathematical model. Besides accuracy, the mathematical model has the advantage that non mutual coupling measurements are needed to calibrate the gain during radar operations. It is assumed that calibration term due to failures is updated only after the array maintenance, when there is not precipitation, while calibration term due to temperature should be updated more often, for example, every scan sector after reading the temperature from T/R modules.
- The calibration techniques based on mutual coupling measurements prove to be a viable alternative to conventional techniques. Their accuracy, reduced cost and reduced complexity makes them a good candidate for use in low-cost X-band phased array radars.

APPENDIX A

T/R MODULE SCHEMATIC

This appendix provides the following circuit board schematics:

- RF circuit diagram
- Voltage regulators diagram
- Digital circuit and 30 pin header diagram

This appendix also includes the bill of material for T/R module

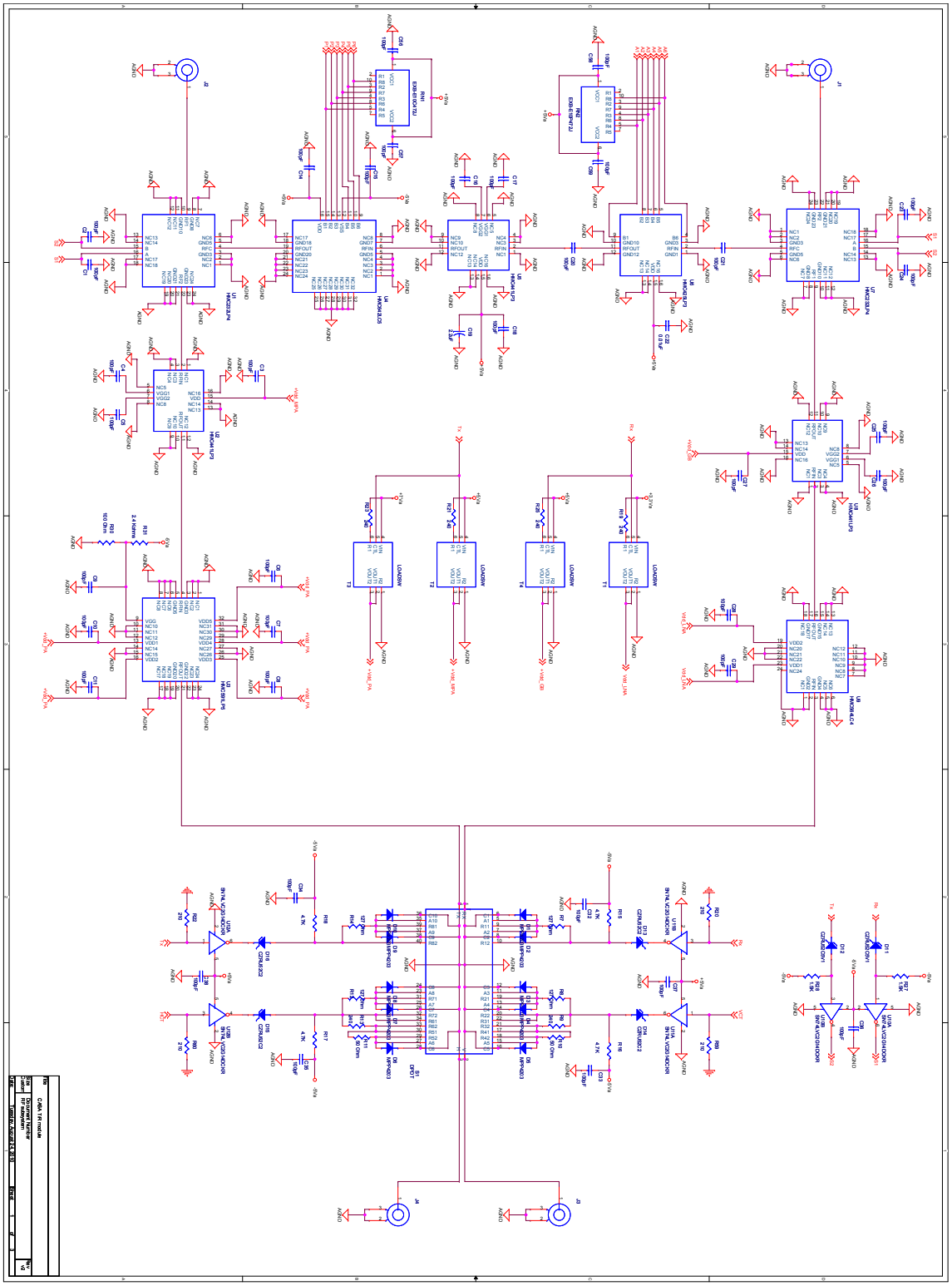

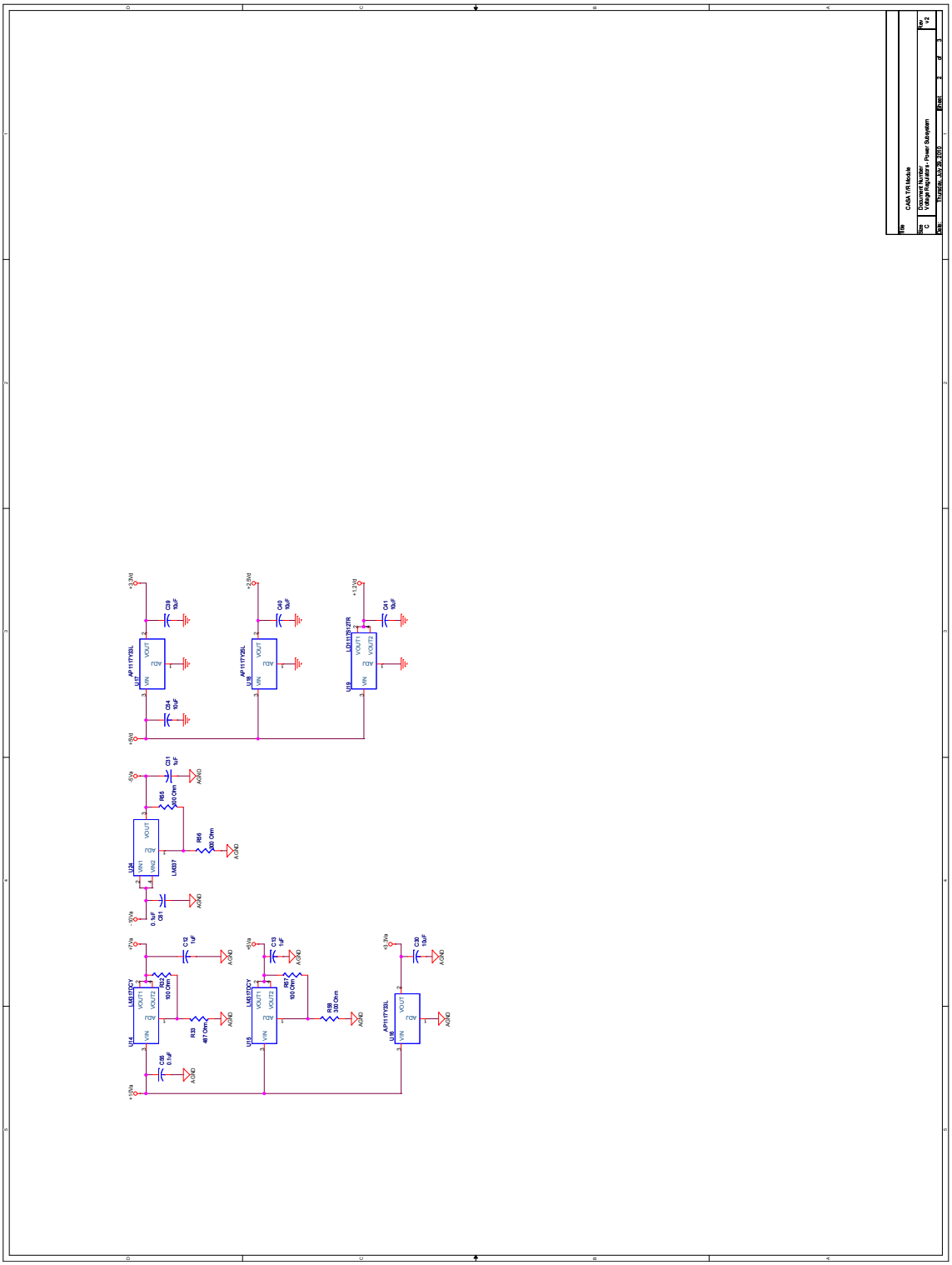
Title
CASA TIR Module
Size
C
Document Number
Power Schematic
Rev
V2
Date:
Tuesday, July 28, 2020
Sheet
2
of
3

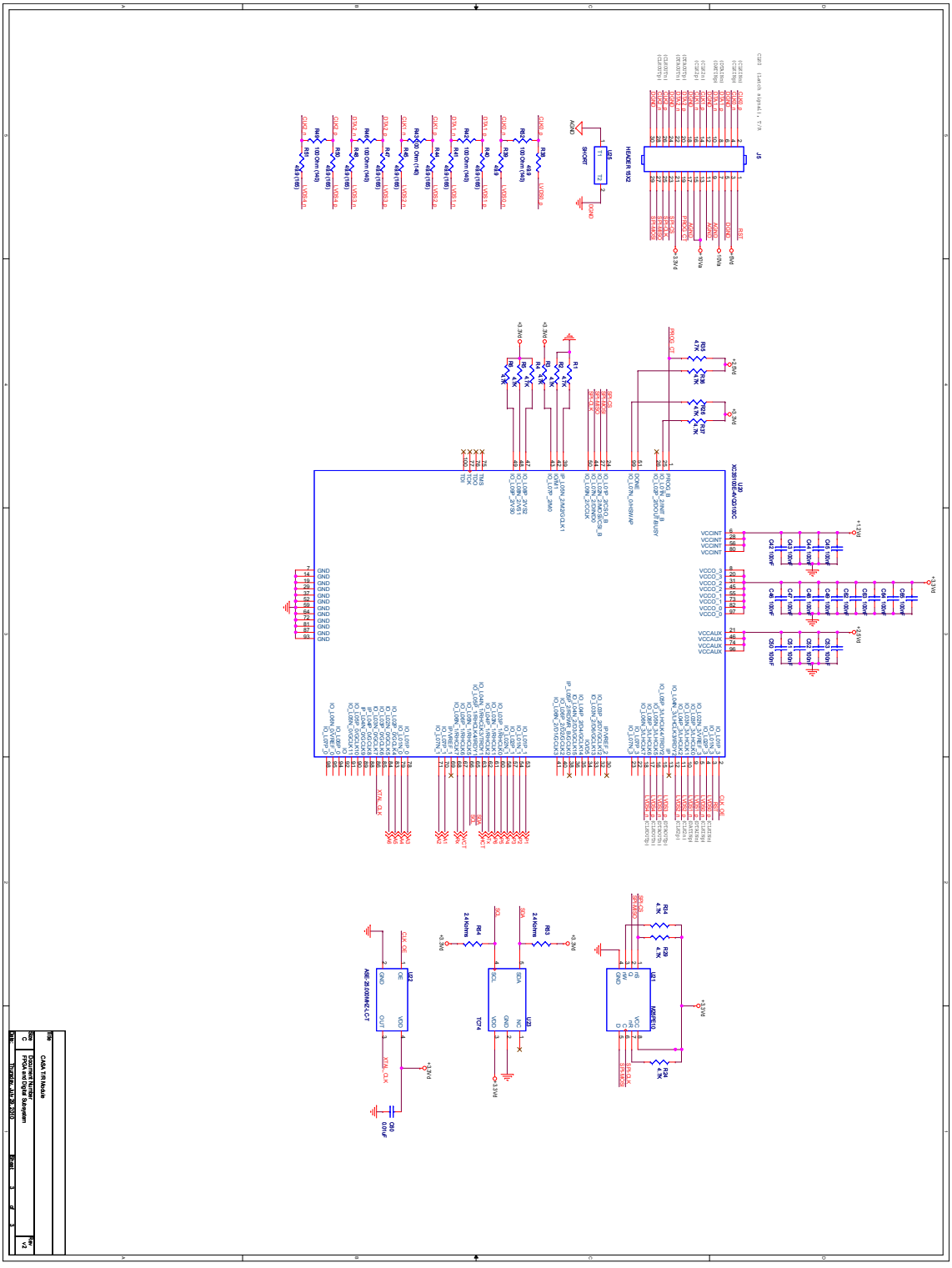
CAMA TIM Module
Document Number
FPGA and Digital Subsystem
Thursday, July 29, 2010
Rev
V2
Sheet
5
of
5
SIZE
C
HEADER 80X2
XC3S1200E-4FG320C
ABS-30.000MHZ-LC-T
TC74
MCP6L91

Revised: Wednesday, March 25, 2009
Revision: v2

Item	Quantity	Reference	Value	Part Number	Description	Distributor	Dist Part Number	
1	36	C1,C2,C3,C4,C5,C6,C7,C8,C9,C10,C11,C14,C15,C16,C17,C18,C20,C21,C23, C24,C25,C26,C27,C28,C29,C32,C33,C34,C35,C36,C37,C38,C56,C57,C58,C59	100pF	ECJ-0EB1E682K	CAP 100PF 25V CERAMIC X7R 0402	Digi-Key	PCC1702CT-ND	
2	2	C12,C31	1uF	TCA1C105M8R	CAP TANT 1UF 16V 20% SMD	Digi-Key	511-1466-1-ND	
3	1	C13	1uF	TCA1C106M8R	CAP TANT 10UF 16V 20% SMD	Digi-Key	511-1473-1-ND	
4	1	C19	2.2uF	TCA1C225M8R	CAP TANTALUM 2.2UF 16V 20%, 1206 SMD	Digi-Key	511-1469-1-ND	
5	2	C22,C60	0.01uF	ECJ-1VB1E103K	CAP 10000PF 25V CERM X7R 0603	Digi-Key	PCC1763CT-ND	
6	5	C30,C39,C40,C41,C54	10uF	TCA1C106M8R	CAP TANT 10UF 16V 20% SMD	Digi-Key	511-1473-1-ND	
7	16	C42,C43,C44,C45,C46,C47,C48,C49,C50,C51,C52,C53,C62,C63,C64,C65	100nF	ECJ-0EB1A104K	CAP .1UF 10V CERAMIC X5R 0402	Digi-Key	PCC2146CT-ND	
8	2	C55,C61	0.1uF	F971V104MAA	CAP TANTALUM 0.1UF 35V 20% SMD	Digi-Key	493-2431-1-ND	
9	2	D11,D12	CZRU52C5V1	CZRU52C5V1	DIODE ZENER 150MW 5.1V 0603	Digi-Key	641-1029-1-ND	
10	4	D13,D14,D15,D16	CZRU52C2	CZRU52C2	DIODE ZENER 150MW 2V 0603	Digi-Key	641-1019-1-ND	
11	2	J1,J2	SMA	142-0761-851	CONN JACK SMA 50 OHMS PC MOUNT	Digi-Key	J800-ND	
12	1	J5	HEADER 15X2	TFML-115-01-S-D-RA	CONN HEADR .05" 30POS DL T/H R/A	Digi-Key	SAM8263-ND	
13	1	RN1	EXB-E10C472J	EXB-E10C472J	RES NETWRK 4.7K OHM 8RES10PN SMD	Digi-Key	U8472CT-ND	
14	1	RN2	EXB-E10P472J	EXB-E10P472J	RES NETWRK 4.7K OHM 8RES10PN SMD	Digi-Key	U8472CT-ND	
15	13	R1,R2,R3,R4,R5,R6,R24,R26,R29,R34,R35,R36,R37	4.7K	ERJ-2GEJ472X	RES 4.7K OHM 1/10W 5% 0402 SMD	Digi-Key	P4.7KJCT-ND	
16	4	R7,R8,R12,R14	127 Ohm	RC1206FR-07127RL	RES 127 OHM 1/4W 1% 1206 SMD	Digi-Key	311-127FRCT-ND	
17	5	R9,R13,R19,R21,R25	200	ESR03EZPJ241	RES 200 OHM 1/5W 5% 0603 SMD	Digi-Key	RHM240DCT-ND	
18	4	R15,R16,R17,R18	4.7K	ERJ-2GEJ472X	RES 4.7K OHM 1/10W 5% 0603 SMD	Digi-Key	P4.7KJCT-ND	
19	4	R20,R22,R59,R60	210	ERJ-2RKF2100X	RES 210 OHM 1/16W 1% 0402 SMD	Digi-Key	P210LCT-ND	
20	1	R23	200	ERJ-P06J201V	RES 200 OHM 1/4W 5% 0805 SMD	Digi-Key	P200ADCT-ND	
21	2	R27,R28	1.5K	ERJ-2GEJ152X	RES 1.5K OHM 1/10W 5% 0603 SMD	Digi-Key	P1.5KJCT-ND	
22	1	R30	100 Ohm	MCR01MZPJ101	RES 100 OHM 1/16W 5% 0402 SMD	Digi-Key	RHM100JCT-ND	
23	3	R31,R53,R54	2.4 Kohms	ERJ-3GEYJ242V	RES 2.4K OHM 1/10W 5% 0603 SMD	Digi-Key	P2.4KGCT-ND	
24	3	R32,R55,R57	100 Ohm	ERJ-3GEYJ101V	RES 100 OHM 1/10W 5% 0603 SMD	Digi-Key	P100GCT-ND	
25	1	R33	487 Ohm	ERJ-3EKF4870V	RES 464 OHM 1/10W 5% 0603 SMD	Digi-Key	P487HCT-ND	
26	2	R38,R39	49.9 Ohm	ERJ-2RKF49R9X	RES 49.9 OHM 1/16W 1% 0402 SMD	Digi-Key	P49.9LCT-ND	
27	8	R40,R41,R44,R45,R47,R48,R50,R51	49.9 Ohm	ERJ-2RKF49R9X	RES 49.9 OHM 1/16W 1% 0402 SMD	Digi-Key	P49.9LCT-ND	
28	5	R42,R43,R46,R49,R52	100 Ohm	MCR01MZPJ101	RES 100 OHM 1/16W 5% 0402 SMD	Digi-Key	RHM100JCT-ND	No connect
29	2	R56,R58	300 Ohm	ERJ-3GEYJ301V	RES 300 OHM 1/10W 5% 0603 SMD	Digi-Key	P300GCT-ND	
30	4	T1,T2,T3,T4	LOADSW	FDC6331L	Integrated Load Switch	Digi-Key	FDC6331LCT-ND	
31	3	U10,U11,U12	SN74LVC2G14DCKR	SN74LVC2G14DCKR	IC INVERTER DUAL	Digi-Key	296-13011-1-ND	
32	2	U14,U15	LM317DCY	LM317DCYR	IC VOLT REG POS ADJ SOT-223-4	Digi-Key	296-12602-1-ND	
33	2	U16,U17	AP1117Y33L	AP1117Y33L	IC REG LDO 1.0A 3.3V SOT89-3L	Digi-Key	AP1117Y33LDICT-ND	
34	1	U18	AP1117Y25L	AP1117Y25L	IC REG LDO 1.0A 2.5V SOT89-3L	Digi-Key	AP1117Y25LDICT-ND	
35	1	U19	LD1117S12TR	LD1117S12TR	IC REG LDO POS 800MA 1.2V SOT223	Digi-Key	497-4240-2-ND	
36	1	U20	XC3S100E-4VQG100C	XC3S100E-4VQG100C	IC SPARTAN-3E FPGA 100K 100VTQFP	Digi-Key	122-1479-ND	
37	1	U21	M25PE10	M25PE10-VMN6P	IC SERIAL FLASH 1MBIT LV SO-8N	Digi-Key	M25PE10-VMN6P-ND	
38	1	U22	ASE-25.000MHZ-LC-T	ASE-25.000MHZ-LC-T	OSCILLATOR 25.000 MHZ 3.3V SMD	Digi-Key	535-9568-1-ND	
39	1	U23	TC74	TC74A0-5.0VCTTR	IC DGTL THERM SENSOR	Digi-Key	TC74A0-5.0VCTCT-ND	
40	1	U24	LM337	LM337IMP/NOPB	IC VREG NEGATIVE ADJ 1A SOT223	Digi-Key	LM337IMPCT-ND	
9	10	D1,D2,D3,D4,D5,D6,D7,D8,D9,D10	MPP4203	MPP4203	SM PIN diode	Microsemi	MPP4203	
13	2	J3,J4	SMP	P606-6CC	CONN JACK SMA 50 OHMS PC MOUNT	Tensolite	P606-6CC	
20	2	R10,R11	50 Ohm	RC3-0402PW50R0J	RES 50 OHM 1/16W 1% 0402 SMD	IMS-Resistor	RC3-0402PW50R0J	
35	2	U1,U7	HMC232LP4	HMC232LP4	GaAs MMIC SPDT Non-Reflective Switch	Hittite	HMC232LP4	
36	3	U2,U5,U8	HMC441LP3	HMC441LP3	GaAs MMIC Medium power Amplifier	Hittite	HMC441LP3	
37	1	U3	HMC591LP5	HMC591LP5	GaAs MMIC Power Amplifier	Hittite	HMC591LP5	
38	1	U4	HMC642LC5	HMC642LC5	GaAs MMIC 6-Bit Digital Phase Shifter	Hittite	HMC642LC5	
39	1	U6	HMC425LP3	HMC425LP3	GaAs MMIC 6-Bit Digital Attenuator	Hittite	HMC425LP3	
40	1	U9	HMC564LC4	HMC564LC4	GaAS MMIC Low Noise Amplifier	Hittite	HMC564LC4	

T/R module cost

Item	Quantity	Value	Distributor	Dist Part Number	Unit price					unit price of T/R module (only parts)				
					1	10	100	500	1000	1	10	100	500	1000
1	36	100pF	Digi-Key	PCC1702CT-ND	0.18	0.114	0.0409	0.02088	0.01476	6.48	4.104	1.4724	0.75168	0.53136
2	2	1uF	Digi-Key	511-1466-1-ND	0.33	0.283	0.247	0.195	0.1625	0.66	0.566	0.494	0.39	0.325
3	1	10uF	Digi-Key	511-1473-1-ND	0.33	0.283	0.247	0.195	0.1625	0.33	0.283	0.247	0.195	0.1625
4	1	2.2uF	Digi-Key	511-1469-1-ND	0.33	0.283	0.247	0.195	0.1625	0.33	0.283	0.247	0.195	0.1625
5	2	0.01uF	Digi-Key	PCC1763CT-ND	0.33	0.283	0.247	0.195	0.1625	0.66	0.566	0.494	0.39	0.325
6	5	10uF	Digi-Key	511-1473-1-ND	0.33	0.283	0.247	0.195	0.1625	1.65	1.415	1.235	0.975	0.8125
7	16	100nF	Digi-Key	PCC2146CT-ND	0.0033	0.033	0.0117	0.00598	0.00423	0.0528	0.528	0.1872	0.09568	0.06768
8	2	0.1uF	Digi-Key	493-2431-1-ND	0.0394	0.394	0.3377	0.2814	0.22512	0.0788	0.788	0.6754	0.5628	0.45024
9	2	CZRU52C5V1	Digi-Key	641-1029-1-ND	0.46	0.333	0.1961	0.1184	0.0925	0.92	0.666	0.3922	0.2368	0.185
10	4	CZRU52C2	Digi-Key	641-1019-1-ND	0.53	0.378	0.226	0.1344	0.105	2.12	1.512	0.904	0.5376	0.42
11	2	SMA	Digi-Key	J800-ND	8.45	7.524	5.5278	4.29994	3.83875	16.9	15.048	11.0556	8.59988	7.6775
12	1	HEADER 15X2	Digi-Key	SAM8263-ND	5.21	3.764	3.088	2.75	2.702	5.21	3.764	3.088	2.75	2.702
13	1	EXB-E10C472J	Digi-Key	U8472CT-ND	0.42	0.389	0.315	0.262	0.21	0.42	0.389	0.315	0.262	0.21
14	1	EXB-E10P472J	Digi-Key	U8472CT-ND	0.42	0.389	0.315	0.262	0.21	0.42	0.389	0.315	0.262	0.21
15	13	4.7K	Digi-Key	P4.7KJCT-ND	0.08	0.081	0.0436	0.0251	0.01711	1.04	1.053	0.5668	0.3263	0.22243
16	4	127 Ohm	Digi-Key	311-127FRCT-ND	0.088	0.082	0.0444	0.02545	0.1737	0.352	0.328	0.1776	0.1018	0.6948
17	5	200	Digi-Key	RHM240DCT-ND	0.142	0.142	0.0746	0.0439	0.02996	0.71	0.71	0.373	0.2195	0.1498
18	4	4.7K	Digi-Key	P4.7KJCT-ND	0.08	0.081	0.0436	0.0251	0.01711	0.32	0.324	0.1744	0.1004	0.06844
19	4	210	Digi-Key	P210LCT-ND	0.08	0.081	0.0436	0.0251	0.01711	0.32	0.324	0.1744	0.1004	0.06844
20	1	200	Digi-Key	P200ADCT-ND	0.0165	0.165	0.0986	0.058	0.0348	0.0165	0.165	0.0986	0.058	0.0348
21	2	1.5K	Digi-Key	P1.5KJCT-ND	0.08	0.081	0.0436	0.0251	0.01711	0.16	0.162	0.0872	0.0502	0.03422
22	1	100 Ohm	Digi-Key	RHM100JCT-ND	0.074	0.0398	0.0398	0.02285	0.0156	0.074	0.0398	0.0398	0.02285	0.0156
23	3	2.4 Kohms	Digi-Key	P2.4KGCT-ND	0.08	0.081	0.0436	0.0251	0.01711	0.24	0.243	0.1308	0.0753	0.05133
24	3	100 Ohm	Digi-Key	P100GCT-ND	0.08	0.081	0.0436	0.0251	0.01711	0.24	0.243	0.1308	0.0753	0.05133
25	1	487 Ohm	Digi-Key	P487HCT-ND	0.08	0.081	0.0436	0.0251	0.01711	0.08	0.081	0.0436	0.0251	0.01711
26	2	49.9	Digi-Key	P49.9LCT-ND	0.098	0.098	0.053	0.0304	0.02074	0.196	0.196	0.106	0.0608	0.04148
27	8	49.9	Digi-Key	P49.9LCT-ND	0.098	0.098	0.053	0.0304	0.02074	0.784	0.784	0.424	0.2432	0.16592
28	5	100 Ohm (140)	Digi-Key	RHM100JCT-ND	0.074	0.0398	0.0398	0.02285	0.0156	0.37	0.199	0.199	0.11425	0.078
29	2	300 Ohm	Digi-Key	P300GCT-ND	0.071	0.071	0.0382	0.02195	0.01499	0.142	0.142	0.0764	0.0439	0.02998
30	4	LOADSW	Digi-Key	FDC6331LCT-ND	0.78	0.582	0.4365	0.2716	0.25802	0.69	0.6	0.49	1.0864	1.03208
31	3	SN74LVC2G14DCKR	Digi-Key	296-13011-1-ND	0.4	0.4	0.24	0.1328	0.112	1.2	1.2	0.72	0.346	0.277
32	2	LM317DCY	Digi-Key	296-12602-1-ND	0.62	0.62	0.3465	0.2156	0.20484	1.24	1.24	0.693	0.4312	0.40968
33	2	AP1117Y33L	Digi-Key	AP1117Y33LDICT-ND	0.95	0.95	0.63	0.525	0.42	1.9	1.9	1.26	1.05	0.84
34	1	AP1117Y25L	Digi-Key	AP1117Y25LDICT-ND	0.95	0.95	0.63	0.525	0.42	0.95	0.95	0.63	0.525	0.42
35	1	LD1117S12TR	Digi-Key	497-4240-2-ND	0.77	0.595	0.51	0.425	0.34	0.77	0.595	0.51	0.425	0.34
36	1	XC3S100E-4VQG100C	Digi-Key	122-1479-ND	9.48	9.48	9.48	9.48	9.48	9.48	9.48	9.48	9.48	9.48
37	1	M25PE10	Digi-Key	M25PE10-VMN6P-ND	2.1	1.65	1.4	1.15	0.875	2.1	1.65	1.4	1.15	0.875
38	1	ASE-25.000MHZ-LC-T	Digi-Key	535-9568-1-ND	3.47	3.21	2.2275	1.881	1.881	3.47	3.21	2.2275	1.881	1.881
39	1	TC74	Digi-Key	TC74A0-5.0VCTCT-ND	1.34	1.34	1.08	1.08	0.98	1.34	1.34	1.08	1.08	0.98
40	1	LM337	Digi-Key	LM337IMPCT-ND	1.86	1.86	1.02	0.78	0.78	1.86	1.86	1.02	0.78	0.78
41	10	MPP4203	Microsemi	MPP4203	1.2	1.2	1.2	1.2	1.2	12	12	12	12	12
42	2	SMP	Tensolite	P606-6CC	16.54	16.54	13.4	13.4	13.4	33.08	33.08	26.8	26.8	26.8
43	2	50 Ohm	SOTA	S0202AF50R0FEB	4.16	4.16	4.16	2.79	2.25	8.32	8.32	8.32	5.58	4.5
44	2	HMC232LP4	Hittite	HMC232LP4	30.51	30.51	27.25	27.25	23.37	61.02	61.02	54.5	54.5	46.74
45	3	HMC441LP3	Hittite	HMC441LP3	18.28	18.28	16.33	16.33	12.52	54.84	54.84	48.99	48.99	37.56
46	1	HMC591LP5	Hittite	HMC591LP5	45.05	45.05	40.23	40.23	35.11	45.05	45.05	40.23	40.23	35.11
47	1	HMC642LC5	Hittite	HMC642LC5	121.95	121.95	108.88	108.88	84.67	121.95	121.95	108.88	108.88	84.67
48	1	HMC425LP3	Hittite	HMC425LP3	12.23	12.92	10.92	10.92	9.18	12.23	12.92	10.92	10.92	9.18
49	1	HMC564LC4	Hittite	HMC564LC4	20.94	20.94	18.7	18.7	15.91	20.94	20.94	18.7	18.7	15.91
										435.7061	429.4398	372.7747	362.6553	305.7497

		Unit cost of T/R module				
Item	Distributor	1	10	100	500	1000
T/R module parts	various	435.7061	429.4398	372.7747	362.6553	305.7497
Board	Cirexx	880	186.5	36.8	23.5	21.9
Assembly	Cirexx	500	20.71	6.3	5	4.85
Enclousure	Emachine	36	22	12	10	8
		1851.7061	658.6498	427.8747	401.1553	340.4997

APPENDIX B

BACKPLANE

This appendix provides the bill of material and cost model for the backplane board.

B.1 Bill of material

Item	Quantity	Part	Part Number	Description	Distributor	Dist Part Number	Package	Type
1	8	10A01-T	10A01-T	RECTIFIER 50V 10A R-6	Digi-Key	10A01CT-ND	R-6	Through-holes
2	18	SOCKET 15X2	SFML-115-T1-S-D	CONN HEADR .05" 30POS DL T/H R/A	Digi-Key	SAM8243-ND	CONN30SCK	Through-holes
3	34	SMA	142-0711-201	CONN JACK SMA 50 OHMS PC MOUNT	Digi-Key	J819-ND	SMA conn	Surface Mount
4	1	HEADER 12POS	10-84-4120	MALE CONN HEADER 12POS .084 VERT TIN	Digi-Key	WM1261-ND	CONN12	Through-holes
5	1	HEADER 6POS	10-84-4060	MALE CONN HEADER 6POS .084 VERT TIN	Digikey	WM1259-ND	CONN2	Through-holes
6	1	HEADER 2POS	10-84-4020	MALE CONN HEADER 2POS .084 VERT TIN	Digi-Key	WM1256-ND	CONN2	Through-holes
7	10	43 Ohms	CRCW040243R0FKED	RES 43.0 OHM 1/16W 1% 0402 SMD	Digi-key	541-43.0LCT-ND	SMD_402	Surface Mount
8	30	50 Ohms	RC3-0402PW50R0J	RES 50 OHM 1/16W 1% 0402 SMD	IMS-Resistor	RC3-0402PW50R0J	SMD_402	Surface Mount

B.2 Component costs

					Unit price					Unit price of backplane (only parts)				
Item	Quantity	Part	Distributor	Dist Part Number	1	10	100	500	1000	1	10	100	500	1000
1	8	10A01-T	Digi-Key	10A01CT-ND	0.74	0.578	0.495	0.462	0.462	5.92	4.624	3.696	3.696	3.696
2	18	SOCKET 15X2	Digi-Key	SAM8243-ND	4.95	3.51	2.88	2.565	2.52	63.18	51.84	45.36	45.36	45.36
3	34	SMA	Digi-Key	J819-ND	4.55	4.052	2.9772	2.3156	2.0675	137.768	101.2248	70.295	70.295	70.295
4	1	HEADER 12POS	Digi-Key	WM1261-ND	2.19	1.931	1.2873	1.0298	0.85473	2.19	1.931	1.2873	1.0298	0.85473
5	1	HEADER 6POS	Digikey	WM1259-ND	1.35	1.195	0.7968	0.6374	0.52904	1.35	1.195	0.7968	0.6374	0.52904
6	1	HEADER 2POS	Digi-Key	WM1256-ND	0.6	0.53	0.3533	0.2826	0.23456	0.6	0.53	0.3533	0.2826	0.23456
8	10	43 Ohms	Digi-key	541-43.0LCT-ND	0.0083	0.083	0.0444	0.0255	0.0174	0.83	0.444	0.174	0.174	0.174
7	30	50 Ohms	IMS-Resistor	RC3-0402PW50R0J	0.79	0.69	0.59	0.5	0.35	20.7	17.7	10.5	10.5	10.5
										232.538	179.4888	132.4624	131.9748	131.6433

B.3 Cost model

Item	Distributor	1	10	100	500	1000
Backplane parts	Various	232.538	179.4888	132.4624	131.9748	131.6433
Fabrication	Cirexx	1000	580	296	274	270
Assembly	Cirexx	1058	180.7	62.6	61	60
Total		2290.538	940.1888	491.0624	466.9748	461.6433

BIBLIOGRAPHY

[1] N. R. C. (NRC), *Weather Technology Beyond NEXRAD*. Washington, DC: National Academy Press., 2002.

[2] R. A. Maddox, J. Zhang, J. Gourley, and K. W. Howard, "Weather radar coverage over the contiguous united states," *Weather and Forecasting*, vol. 4, pp. 927 – 934, Aug. 2002.

[3] D. McLaughlin, D. P. adn V. Chandrasekar, B. Philips, and e. a. J. Kurose, "Short-wavelength technology and the potential for distributed networks of small radar systems," *Bulletin American Meteorological Society*, vol. 90, pp. 1797 – 1817, Dec. 2009.

[4] N. R. C. (NRC), *Evaluation of the Multifunction Phased Array Radar Planning Process*. Washington, DC: National Academy Press., 2008.

[5] M. E. Weber, J. Y. N. Cho, J. S. Herd, and J. M. Flavin, "The next-generation multimission u.s. surveillance radar network," *Bulletin American Meteorological Society*, vol. 88, pp. 1739 – 1751, Nov. 2007.

[6] J. Salazar, *The feasibility of low-cost, dual-polarized, Phase-Tilt Antenna Arrays for dense radar networks*. PhD thesis, University of Massachusetts, Amherst, 2012. Doctoral Dissertations.

[7] D. McLaughlin, E. Knapp, Y. Wang, and V. Chandrasekar, "Distributed weather radar using x-band active arrays," in *IEEE Aerospace and Electronic Systems Magazine*, pp. 21 – 26, July 2009.

[8] E. D. Cohen, "Active electronically scanned arrays," in *IEEE MTT-S International Microwave Symposium Diges*, (San Diego, CA), pp. 1323–1326, May 1994.

[9] A. Agrawal and E. Holzman, "Active phased array design for high reliability," *IEEE Transactions on Aerospace and Electronic Systems*, vol. 35, pp. 1204 –1211, Oct. 1999.

[10] R. C. Kley, W. P. Hull, and F. D. Lamb, "Solid state phased array SSPA performance," in *IEEE International Radar Conference*, (Arlington, VA), pp. 298–303, May 1990.

[11] J. Closa, "Internal calibration processing and processor normalization." `https://earth.esa.int/calval/proceedings/asar/asar_10.pdf`. Earth Observation Department, ESA-ESRIN. Italy.

[12] H. M. Aumann, A. J. Fenn, and F. G. Willwerth, "Phased array antenna calibration and pattern prediction using mutual coupling measurements," *IEEE Trans. Antennas Propagation*, vol. 37, pp. 844–850, July 1989.

[13] M. Sarcione and et al, "The design, development and testing of the thaad (theater high altitude area defense) solid state phased array (formerly ground based radar," in *IEEE International Symposium on Phased Array Systems and Technology*, (Boston, MA), pp. 260–265, Oct. 1996.

[14] T. Y. Yu, M. B. Orescain, C. D. Curtis, D. S. Zrnic, and D. E. Forsyth, "Beam multiplexing using the phased-array weather radar," *Journal of atmosferic and oceanic technology*, vol. 24, pp. 616 – 626, Apr. 2007.

[15] R. J. Mailloux, *Phased Array Antenna Handbook*. Norwood, MA: Artech House, 2005.

[16] R. S. Elliott, *Antenna Theory and Design*. Hoboken, NJ: John Wiley and Sons. Inc, 2003.

[17] J. Allen and B. Diamond, "Mutual coupling in array antennas." `http://www.dtic.mil/dtic/tr/fulltext/u2/648153.pdf`, 10 1966. MIT Lincoln Laboratoy. Technical Report.

[18] D. Pozar, "The active element pattern," *IEEE Transactions on Antennas and Propagation*, vol. 4, pp. 1176 – 1178, Aug. 1994.

[19] M. Skolnik, *Introduction to Radar Systems*. New York, NY: McGraw Hill, 2002.

[20] G. Zhang, R. J. Doviak, D. S. Zrnic, J. Crain, D. Staiman, and Y. Al-Rashid, "Phased array radar polarimetry for weather sensing: A theoretical formulation for bias corrections," *IEEE Transactions on Geoscience and Remote Sensing*, vol. 47, pp. 3679–3689, Nov. 2009.

[21] L. Lei, G. Zhang, and R. Doviak, "Bias correction for polarimetric phased-array radar with idealized aperture and patch antenna elements," *IEEE Transactions on Geoscience and Remote Sensing*, vol. 51, pp. 473–486, June 2012.

[22] N. Chamberlain and G., "The UAVSAR Transmit / Receive module," in *IEEE Aerospace Conference*, (Big Sky, MT), pp. 1–15, 2008.

[23] Y.-L. Desnos, C. Buck, J. Guijarro, J.-L. Suchail, R. Torres, and E. Attema, "Asar envisats advanced synthetic aperture radar." `http://www.esa.int/esapub/bulletin/bullet102/Desnos102.pdf/`, May 2000. ESA bulletin.

[24] B. Grafmuller, A. Herschlein, and C.Fischer, "The terrasar-x antenna system," in *IEEE International Radar Conference*, (Munich), pp. 202 – 205, May 2005.

[25] P. Snoeij, R. Torres, D. Geudtner, M. Brown, P. Deghaye, and et al., "Sentinel-1 instrument overview." `https://earth.esa.int/documents/10174/233696/2-Sentinel-1_Instrument_Overview.pdf/`, June 2012. The 4th international workshop on adc=vances in SAR oceanography.

[26] H. Wilden, O.Saalmann, B. Poppelreuter, and O. Peters, "A radar frontend with time steered array antenna for pamir," in *EuRAD Radar Conference*, (Munich), pp. 202 – 205, Oct. 2007.

[27] A. Puzella and R. Alm, "Air-cooled, active transmit/receive panel array," in *IEEE Radar conference*, (Rome), pp. 1 – 6, May 2008.

[28] G. Sadowy, C. Andricos, and S. Durden, "A dual-polarized mm-wave active array feed for the second generation rain." `http://esto.nasa.gov/conferences/estc-2002/Papers/B2P3(Sadowy).pdf/`, June 2002. Earth Science Technology Conference.

[29] W. Hull, "Aesa diagnostics in operational environments," in *Proceedings of the IEEE National Radar Conference*, (Dallas, TX), pp. 107 – 112, June 1989.

[30] A. DeLuca, J. E. Gentry, D. L. Thomas, N. R. Landry, and A. K. Agrawal, "Phased array antenna with distributed beam steering." Patent US 5339086, June 1994. US 5339086.

[31] T. Waldron, S. Chin, and R. Naster, "Distributed beamsteering control of phased array radars," *Microwave Journal*, vol. 29, pp. 133–136, 09 1986.

[32] J. Salazar, R. Medina, E. Knap, and D. McLaughlin, "Phase-tilt array antenna design for dense distributed radar networks for weather sensing," in *2008 IEEE InternationalGeoscience and Remote Sensing Symposium*, (Boston, MA), pp. 318– 321, July 2008.

[33] A. Krishnamurthy, "Design of an fpga-based array formatter for casa phase-tilt radar system," Master's thesis, University of Massachusetts - Amherst, 2011.

[34] R. Medina, E. Knap, J. Salazar, and D. McLaughlin, "T/R module for CASA phase-tilt radar antenna array"," in *42nd European Microwave Conference (EuRad)*, (Amsterdam, Netherland), pp. 1293 – 1296, Oct. 2012.

[35] T. C. Cheston, "Phased arrays for radars," *IEEE Spectrum*, vol. 5, pp. 102 – 111, Nov. 1968.

[36] A. K. Agrawal and E. L. Holzman, "Beamformer architectures for active phased-array radar antennas," in *IEEE International Radar Conference*, vol. 47, pp. 1888 – 1899, May 1999.

[37] J. K. Hsiao, "Array sidelobes, error tolerance, gain, and beamwidth." `http://www.dtic.mil/dtic/tr/fulltext/u2/a147004.pdf`, 09 1984. Naval Research Laboratory, Washington, DC.

[38] D. N. McQuiddy and et al, "Transmit/receive module technology for x-band active array radar," *Proceedings of IEEE*, vol. 79, no. 3, pp. 308–341, 1991.

[39] J. Frank and J. D. Richards, *Phased Array Radar Antennas, in Radar Handbook, Skolnik M. I.* New York: McGraw-Hill, 2008.

[40] C. Aixin and W. Peng, "Design of beam steering system in phased array based on dsp," in *3rd IEEE International Symposium on Microwave, Antenna, Propagation and EMC Technologies for Wireless Communications*, (Beijing), pp. 608–611, Oct. 2009.

[41] Z. Chen, J. Liu, and L. Li, "Design of scalable beam steering system of phased array radar," in *IEEE CIE International Conference on radar*, (Chengdu), pp. 1153 – 1156, Oct. 2011.

[42] A. Agrawa, R. Clark, and J. Komiak, "T/R module architecture tradeoffs for phased array antennas," in *IEEE MTT-S International Microwave Symposium Diges*, (San Fransisco, CA), pp. 995 – 998, June 1996.

[43] J. D. Harrop, "Solid-state, active-phased arrays - some aspects of receiver design." http://www.dtic.mil/dtic/tr/fulltext/u2/a275893.pdf, 02 1994. Naval surface warfare center Dahlgren Div Va.

[44] W. Doherty and R. Joos, "PIN diode circuit designers handbook," 1999. Microsemi Corporation.

[45] Texas Instruments , "Basic design considerations for backplanes." http://www.ti.com/lit/an/szza016b/szza016b.pdf, 06 2001. Application Report.

[46] T. Instruments, "LVDS owners manual." http://www.ti.com/lit/ml/snla187/snla187.pdf, 2008. Manual.

[47] K. Mitzner, *Complete PCB Design Using OrCAD Capture and PCB Editor*. Burlington, MA: Newnes, 06 2009.

[48] J. J. Alter, J. P. Letellier, and J. M. Willey, "Programmable beam transform and beam steering control system for a phased array radar antenna." Patent US 5008680, Apr. 1991.

[49] R. Sundararaman, "Implementation of optimized 6-bit phase angle calculation from phase gradients for T/R modules in active phased array radars using FPGA," in *International Conference on Control, Automation, Communication and Energy Conservation*, (Perundurai, Tamilnadu), pp. 1–8, June 2009.

[50] R. Herveille, "TLatticeMico32 i2c (Master)." http://www.http://opencores.org/project,i2c, July 2003. Application note.

[51] J. K. Mulcahey and M. G. Sarcione, "Calibration and diagnostics of the thaad solid state phased array in a planar nearfield facility," in *IEEE International Symposium on Phased Array Systems and Technology*, pp. 322 – 326, Oct. 1996.

[52] A. J. Fenn, F. G. Willwerth, and H. M. A. , "Displaced phase center antenna near field measurements for space based radar applications," in *Phased Arrays Symposium Procedure*, (Bedford, MA), pp. 303–318, Aug. 1985.

[53] J. Patel, C. F. du Toit, and V. G. Karasack, "Nearfield calibration method used for phased array antennas containing tunable phase shifters." Patent US 6771216, Ago 2004.

[54] H. M. Aumann and F. G. Willwerth, "Phased array calibration by adaptive nulling." http://www.dtic.mil/cgi-bin/GetTRDoc?AD=ADA238562, 05 1991. MIT Lincoln Laboratoy. Technical Report.

[55] H. M. Aumann and F. G. Willwerth, "Phased array calibration using measured element patterns,"

[56] T. Takahashi, Y. Konishi, S. Makino, H. Ohmine, and H. Nakagur, "Fast measurement technique for phased array calibration," *IEEE Trans. Antennas Propagation*, vol. 56, no. 07, pp. 1888 – 1899, 2008.

[57] N. Chamberlain, C. Andricos, A. Berkun, K. Kumley, V. Krimskiy, R. Hodges, and S. Spitz, "Transmit / Receive module development for large aperture L-band phased array," in *IEEE Aerospace Conference*, (Big Sky, MT), pp. 1093–1103, 2005.

[58] U. Hackenberg, M. Adolph, H. Dreher, H. Ott, R. Reber, R. Rieger, and B. Schweizer, "Polarisation agile, highly accurate T/R module for synthetic aperture radar," in *33rd European Microwave Conference*, (Munich, Germany), pp. 875–878, Oct. 2003.

[59] D. Kelley and W. Stutzman, "Array antenna pattern modeling methods that include mutual coupling effects," *IEEE Trans. Antennas Propagation*, vol. 41, no. 12, pp. 1625–1632, 1993.

[60] C. A. Balanis, *Antenna Theory: Analysis and Design*. New York: John Wiley and Sons, 1997.

[61] H. M. Aumann and F. G. Willwerth, "Intermediate frequency transmit/receive modules for low sidelobe phased array application," in *IEEE National Radar Conference*, (Ann Arbor, Michigan), pp. 33–37, Oct. 1988.

[62] M. Lorcher and H. Brugger, "Advanced RF sensors for SAR earth observation using high precision T/R-modules," in *3rd International APSAR Conference*, (Seoul), pp. 1–6, Sep 2011.

[63] Agilent Technologies, "Optimizing throughput in transmit/receive module test." `http://cp.literature.agilent.com/litweb/pdf/5990-7526EN.pdf`, 04 2011. Application Note.

[64] R. Anholt and S. Swirhun, "Experimental investigation of the temperature dependence of GaAs FET equivalent circuits," in *IEEE Transactions on electron device*, pp. 2029 – 2036, 1992.

[65] J. Salazar, R. Medina, E. Knap, and D. McLaughlin, "Calibration and validation of the CASA phased array antenna'," in *9th European Microwave Conference (EuMic)*, (Amsterdam, Netherland), pp. 614 – 617, Oct. 2012.

[66] M. Mathworks, "Matlab – the language of technical computing." `http://www.mathworks.com/products/matlab/`, 1994.

[67] J. Salazar, R. Medina, E. Knap, and D. McLaughlin, "Low cost x-band dual polarization phased array antenna: Scanning performance'," in *42nd European Microwave Conference (EuRad)*, (Amsterdam, Netherland), pp. 425 – 428, Oct. 2012.

[68] K. Carver, W. Cooper, and W. Stutzman

[69] F. Gekat, M. Hille, H. Niese, and M. Pool, "Accuracy of the engineering calibration of weather radars," in *IEEE International Geoscience and Remote Sensing Symposium (IGARSS)*, (Honolulu, HI), pp. 1096 – 1099, July 2010.

[70] D. Atlas, "Radar calibration: some simple approaches," *Bulletin American Meteorological Society*, vol. 83, pp. 1313– 1316, Sept. 2002.

[71] K. M. Lee, R. S. Chu, and S. C. Liu, "A performance monitoring/fault isolation and correction system of a phased array antenna using transmission-line signal injection with phase toggling method," in *Antennas and Propagation Society International Symposium*, (Chicago, IL), pp. 429 – 432, July 1992.

[72] J. L. Salazar, P. Siqueira, J. Trabal, and E. Knap, "Performance of the wet radomes for phased-array weather radars: Evaluation and applications," in *Radar Conference(EuRAD)*, (Amsterdam), pp. 341 – 344, Oct. 2012.

[73] S. Hunter, "Wsr-88d radar rainfall estimation: Capabilities,limitations and potential improvements." `http://www.srh.noaa.gov/mrx/research/precip/precip.php`, 1996. NWA Digest, 20 (4), 2636.

[74] J. C. Hubbert, V. N. Bringi, and D. Brunkow, "Studies of the polarimetric covariance matrix. part i: Calibration methodology," *Journal of Atmospheric and Oceanic Technology*, vol. 20, pp. 696–706, May 2003.